EUROPEAN UNION
European Structural and Investment Funds
Operational Programme Research,
Development and Education

MŠMT
MINISTRY OF EDUCATION,
YOUTH AND SPORTS

INTER-EXCELLENCE

SILESIAN
UNIVERSITY
INSTITUTE OF PHYSICS
IN OPAVA

ISBN 978-80-7510-576-9
ISSN 2336-5668

Proceedings of RAGtime 23–25: Workshops on black holes and neutron stars

Z. Stuchlík, G. Török, V. Karas,
D. Lančová, editors

Proceedings of

RAGtime 23–25: Workshops on black holes and neutron stars

6–10 September / 10–14 October /
27 November–1 December /'21/'22/'23
Opava, Czech Republic

Editors:
Z. Stuchlík, G. Török,
V. Karas,
D. Lančová

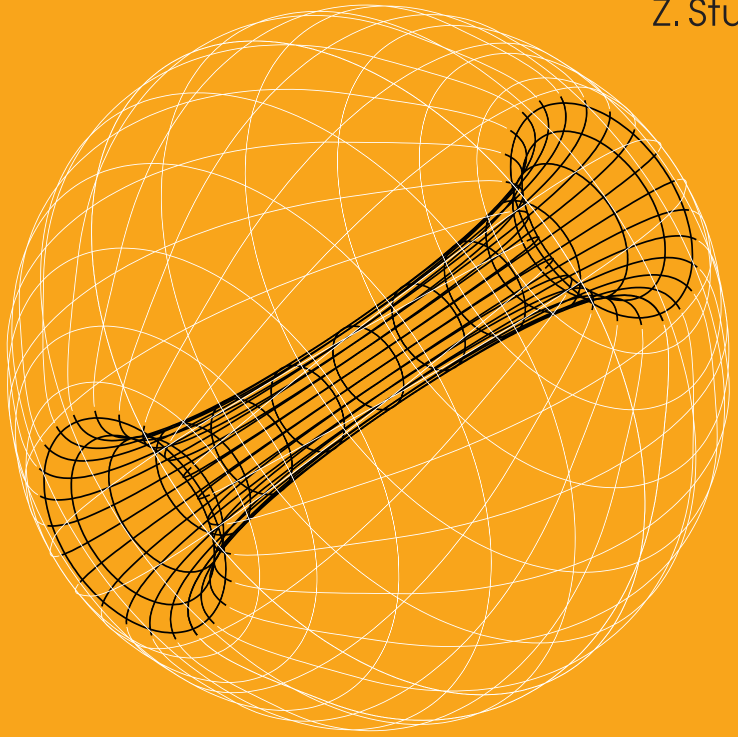

SILESIAN UNIVERSITY IN OPAVA

Publications of the Institute of Physics No. 10

Proceedings of RAGtime 23–25:
Workshops on black holes and neutron stars

6–10 Sep., 10–14 Oct., 27 Nov.–1 Dec.
2021/2022/2023
Opava
Czech Republic

Z. Stuchlík, G. Török, V. Karas and D. Lančová, editors

Opava 2023

Annotation: In this Proceedings, the talks presented during workshops *RAGtime 23–25: Workshops on black holes and neutron stars, 6–10 Sep., 10–14 Oct., 27 Nov.–1 Dec. 2021/2022/2023, Opava, Czech Republic* are collected.

ISBN 978-80-7510-576-9

PREFACE

The Proceedings collects contributions from three RAGtime meetings in 2021, 2022 and 2023. Most of the presented results have been obtained thanks to the collaboration of the research groups at the Silesian University in Opava, the Astronomical Institute of the Czech Academy of Science, the Faculty of Mathematics and Physics of the Charles University in Prague, Department of Theoretical Physics and Astrophysics of the Masaryk University in Brno, and furthermore our colleagues at many other foreign institutions. The RAGtime participants from a wide international community have represented University of Oxford, Nicolaus Copernicus Astronomical Center in Warsaw, Goethe University of Frankfurt, Observatoire de Paris, Max Planck Institute in Garching, The Joint Institute for Nuclear Research in Dubna, The Ulugh Beg Astronomical Institute in Tashkent, The International Space Science Institute in Bern, Osservatorio Astronomico di Roma, University of Cologne, and several others. The contributions are listed in the order in which they were finally accepted for publication.

We thank the Editorial Board members for their valuable advice and assistance, all the authors for the careful preparation of their contributions, and our referees for their perfect work. We are also indebted to the Ministry of Education of the Czech Republic and the European Social Fund in the Czech Republic for providing financial support for the workshops and participants' activities, namely within the INTER-EXCELLENCE project No. LTI17018, the ESF projects No. CZ.02.2.69/0.0/0.0/18_058/0010238, CZ.02.2.69/0.0/0.0/18_056/0013364, CZ.02.2.69/0.0/0.0/18_054/0014696, and the internal grants of the Silesian University in Opava (SGS) awarded to the Institute of Physics during the period 2021-2023.

Opava, December 2023

Z. Stuchlík, G. Török, V. Karas and D. Lančová
editors

CONTENTS

Proceedings of *RAGtime 23–25*
Z. Stuchlík, G. Török, V. Karas and D. Lančová, editors, Silesian University in Opava, 2023, pp. i–ii

25 years of RAGtime: Foreword by the director

Zdeněk Stuchlík

Director of the Institute of Physics in Opava

The RAGtime meeting organised in the year 2023 reached the “celebration” number 25. This is a good reason to look back and follow its history.

The idea to each year organise a meeting of scientists and students involved in relativistic astrophysics at the Silesian University in Opava came to my mind at the end of the 20th century. At those times, a group of scientists and their students, who were focusing their research on the processes around compact objects such as black holes and neutron stars, was established at the Institute of Physics, Faculty of Philosophy and Science, Silesian University in Opava. Because of this Relativistic Astrophysics Group (RAG), I invented the name of RAGtime Meetings, and our student Jakub Říčan composed the RAGtime hymn, in fact, a ragtime song with Silesian motives, which is sometimes used even in the recent times. For my decision to organise such a meeting each year, I found strong support from my teachers and colleagues from the Institute of Theoretical Physics at the Faculty of Mathematics and Physics, Charles University in Prague, Jiří Bičák and Jiří Langer, and from my good friends Marek Abramowicz from the Chalmers University of Technology in Gothenburg and John C. Miller from the University of Oxford, who promised support in establishing an interesting program for these meetings. I have to stress that both Marek and John are playing very important roles in RAGtime meetings at the present time.

We started with the RAGtime Meeting in 1999 with the strong contribution of Standa Hledík, who prepared the format of the contributed papers for the meetings; Standa and I prepared the logo.

It soon became clear that the RAGtime was a very useful idea, as the extent and the scientific relevance of the RAGtime meetings quickly increased, and the content covered many of the most relevant aspects of relativistic astrophysics and cosmology, including the black hole and neutron star physics in many theoretical aspects, with their relation to observational phenomena including the participation on the preparation of important cosmic projects organised under ESA, as ATHENA, eXTP, and others. In the beginning, the pure General Relativistic framework for gravity was considered, along with the Maxwellian framework for the electromagnetic phenomena, but soon, many alternative theories of gravity entered the play, along with various variants of non-linear electrodynamics. Soon after the start of the RAGtime meetings, my students and later my collaborators (Gabo Török, Jan Schee, Jirka Kovář, Petr Slaný, Martin Urbanec, Martin Petrásek, Tomáš Pecháček and others) had an important role in the preparation of the meetings, at the present time strong support also comes from younger colleagues (Debora Lančová, Martin Kološ, Arman

978-80-7510-576-9

Tursunov and others). In preparation for the program of the meetings, an important role was played very soon by people from closely collaborating institutes. Namely Vladimír Karas from the Astronomical Institute, Academy of Science of Czech Republic, and his colleagues Michal Bursa and Jiří Horák, Włodek Kluźniak from the Copernicus Centre Warsaw, Bodo Ahmedov from the Tashkent University, and finally Remo Ruffini and Jorge Rueda from the ECRANET. I would like to thank them for their significant help in establishing very interesting scientific programs for the RAGtime Meetings.

I would like to thank very much all of the colleagues and students who helped in the preparations and organisation of the RAGtime meetings and all of the participants who helped to keep very high standards of the content of the Contributed Papers. I am sure that the RAGtime meetings have strong potential to significantly contribute to the future development of extremely exciting and fascinating research in the area of relativistic astrophysics.

Proceedings of *RAGtime 23–25*
Z. Stuchlík, G. Török, V. Karas and D. Lančová, editors, Silesian University in Opava, 2023, p. iii

Dedication to Jiří Langer

With gratitude and respect, we dedicate this volume to the memory of our unforgettable colleague, doc. RNDr. Jiří Langer, CSc. Those who knew him will surely retain and pass on at least some of what they admired about his personality. He not only instilled in us how to do science and teach science, honestly, but also influenced our thinking as a connoisseur of art, philosophy and history, a translator, a helpful friend and an excellent companion. I firmly believe that his erudition, insight, wit, humour, humanity and refinement, though inimitable, will be preserved for future generations, at least in this form.

Both his friends, among whom I immodestly count myself, and those who were not fortunate enough to know Jiří personally, can find several personal memories of Jiří in the obituary on the website of the Silesian University in Opava (available in Czech at www.slu.cz/phys/cz/aktuality/15/193), and a very nice memorial article in PMFA 65(3), 2020, pp. 185190 (available in Czech at www.dml.cz/handle/10338.dmlcz/148358).

On behalf of the local organising committee,

Stanislav Hledík

978-80-7510-576-9

Proceedings of *RAGtime 23–25*
Z. Stuchlík, G. Török, V. Karas and D. Lančová, editors, Silesian University in Opava, 2023, pp. 1–11

Tidal deformability of ultracompact Schwarzschild stars and their approach to the black hole limit

Camilo Posada

Institute of Physics in Opava, Silesian University in Opava,
Bezručovo nám. 13, CZ-746 01 Opava, Czech Republic
`camilo.posada@physics.slu.cz`

ABSTRACT
A well-known result in general relativity is that the tidal Love numbers of black holes vanish. In contrast, different configurations of a black hole may have non-vanishing Love numbers. For instance, it has been conjectured recently that the Love number of generic exotic compact objects (ECOs) shows a logarithmic behaviour. Here, we analyse the ultracompact Schwarzschild star, which allows the compactness to cross and go beyond the Buchdahl limit. This Schwarzschild star has been shown to be a good black hole mimicker. Moreover, it has been found that the Love number of these objects approaches zero as their compactness approaches the black hole limit. Here, we complement those results by showing that the Love number for these configurations follows an exponentially decaying behaviour rather than the logarithmic behaviour proposed for generic ECOs.

Keywords: Tidal deformability – interior solutions – black hole mimicker – gravastar

1 INTRODUCTION

Black holes (BHs) are one of the most intriguing predictions of Einstein's classical general relativity (GR). Beyond their elegant mathematical structure (Chandrasekhar, 1985), they are also the main candidates to explain most of the astrophysical observations (Celotti et al., 1999). Nevertheless, besides their curvature singularity in the interior geometry, which is believed will be "removed" by a consistent quantum theory of gravity, BHs present certain paradoxes which remain puzzling. For instance, the interior geometry of mathematical BHs shows some unphysical behaviour, such as the closed timelike geodesics in the Kerr spacetime (Hawking and Ellis, 1973). On the other hand, the event horizon is at the root of the so-called "information paradox", which remains one of the central problems in black hole physics (Wald, 2001).

As a consequence of the BH paradoxes, a number of models of "regular BHs" or "BH mimickers" (also known as exotic compact objects (ECOs)) have been proposed in the

978-80-7510-576-9

literature (see, e.g. Cardoso and Pani (2019) and references therein). Regular BHs are constructed with different non-singular interiors, but in such a way that they reproduce the well-known geometries of BH solutions in GR. For instance, the gravitational condensate star, or gravastar (Mazur and Mottola, 2001, 2004), is composed of a non-singular de Sitter interior with negative pressure $p = -\epsilon$, but with positive vacuum energy $\epsilon > 0$, which is matched to the exterior Schwarzschild solution with $p = \epsilon = 0$. The "gluing" of both geometries was done by introducing an infinitesimal thin shell of ultra-stiff matter.

In connection with gravastars, Mazur and Mottola (2015) revisited the well-known Schwarzschild's interior solution with uniform density, or *Schwarzschild star* (see e.g. Glendenning (2000)). The Schwarzschild star manifests a divergence in the central pressure when its compactness reaches the Buchdahl bound $M/R = 4/9$. The importance of this limit relies on the fact that it is independent of the equation of state (EOS) of the configuration, as shown by Buchdahl (1959), under the assumption of isotropic pressure, positive energy density and monotonically decreasing with the distance r. Thus, the Schwarschild star represents a toy model which saturates the Buchdahl bound and should be considered as the limiting case of an ultra-stiff EOS; incidentally, configurations with compactness higher than 4/9 have usually been assumed as unphysical.

Nevertheless, some interesting features become apparent when one considers the Schwarzschild star beyond the Buchdahl limit, $R_\mathrm{S} < R < (9/8)R_\mathrm{S}$, where $R_\mathrm{S} \equiv 2M$. First of all, the pole where the pressure is divergent moves out from the origin up to a surface of radius $R_0 = 3R\sqrt{1 - (4/9)(R/M)} < R$ and a regular interior region with negative pressure emerges naturally in the regime $0 < r < R_0$; meanwhile the pressure remains positive in the region $R_0 < r < R$. In the limit when $R_0 \to R_\mathrm{S}^-$, from below, and $R \to R_\mathrm{S}^+$, from above, the ultracompact Schwarzschild star becomes essentially the gravastar proposed by Mazur and Mottola (2015). It is important to remark that the Schwarzschild star *evades* the Buchdahl limit by having an anisotropic stress at the surface R_0. In the limiting case when $R_0 = R = R_\mathrm{S}$, the interior static de Sitter is matched to the exterior Schwarzschild geometry through a boundary layer located at their respective horizons $R_\mathrm{S} = H$, where H is related to the de Sitter energy density by $\epsilon = 3H^2/(8\pi)$. Furthermore, there is a discontinuity $[\kappa]$ in the surface gravities, which produces a surface tension $\tau_s = 1/(8\pi R_\mathrm{S})$ and incidentally a δ-function stress tensor which replaces the BH horizon.

Some of the physical properties and observational signatures of the ultracompact Schwarzschild stars have been studied recently in the literature. For instance, a time-dependent model was proposed by Beltracchi and Gondolo (2019). On the other hand, these configurations seem to be stable against radial oscillations (Posada and Chirenti, 2019). The analysis of axial modes was carried out in Konoplya et al. (2019), where it was found that the Schwarzschild stars are stable against axial perturbations. Moreover, the Schwarzschild star can "mimic" very well the gravitational wave response of a BH at $l = 2$ and higher multipoles because it approaches the Schwarzschild BH spectrum as closely as possible. This is due to the fact that the null surface R_0 provides the same boundary conditions for the quasi-normal modes as for the case of a BH. An extension to the anisotropic case using the minimal geometric deformation (MGD) was developed by Ovalle et al. (2019).

An early model for a slowly rotating ultracompact Schwarzschild star was proposed by Posada (2017) using the Hartle-Thorne framework (Hartle, 1967; Hartle and Thorne, 1968).

However, the results reported there are marred by a wrong assumption in the regime beyond the Buchdahl limit after making a coordinate transformation. This proposal has been surpassed recently by Beltracchi et al. (2021), where they developed a model for a slowly rotating gravastar to second order in the rotation. These authors found that the exterior metric to a slowly rotating gravastar is precisely that of the Kerr spacetime. Therefore, it is impossible to tell a gravastar from a Kerr BH by any observation, such as accretion disk processes or light ring images.

An alternative for, potentially distinguishing ECOs from BHs is through their tidal deformability. A compelling result in GR is that the tidal Love numbers of Schwarzschild BHs are zero (Damour and Nagar, 2009; Binnington and Poisson, 2009; Hui et al., 2021; Chia, 2021; Charalambous et al., 2021; Poisson, 2021). On the other hand, it has been found that the Love numbers of general ECOs scale as $k \sim 1/\log\xi$, where ξ is a parameter which measures how much the object deviates from the BH geometry (Cardoso et al., 2017). Recently Chirenti et al. (2020) studied the tidal Love number of ultracompact Schwarzschild stars, below and beyond the Buchdahl limit. These authors found that the Love number of these configurations tends to zero as the compactness approaches the BH limit. Thus, they concluded that the vanishing of the Love number is not a unique property of BHs. Instead, it's a consequence of the approach to the Schwarzschild limit.

In this paper, we will review the main results of the tidal deformability of ultracompact Schwarzschild stars presented by Chirenti et al. (2020). As an addition to those results, we will show that the tidal Love number k_2 for ultracompact Schwarzschild stars does not follow the $1/\log\xi$ proposed by Cardoso et al. (2017). Instead, we found that k_2 decays exponentially as a function of the compactness.

2 TIDAL DEFORMABILITY

2.1 General formulation

The tidal Love number quantifies the deformations of the quadrupole moments of a star induced by external fields, which are connected through the relation (Hinderer, 2008; Damour and Nagar, 2009)

$$Q_{ij} = -\frac{2k_2R^5}{3}E_{ij} \equiv -\Lambda\, E_{ij}\,, \tag{1}$$

where k_2 is the Love number and Λ is the tidal deformability. It is conventional to introduce the dimensionless tidal deformability

$$\bar{\Lambda} = \Lambda/M^5 = 2k_2/\left(3C^5\right)\,, \tag{2}$$

here $C \equiv M/R$ denotes the compactness of the configuration. Following Damour and Nagar (2009), the unperturbed spacetime of a nonrotating star is described, generally, by the standard metric

$$\mathrm{d}s^2 = -e^{\nu(r)}\mathrm{d}t^2 + e^{\lambda(r)}\mathrm{d}r^2 + r^2\mathrm{d}\Omega^2\,, \tag{3}$$

and the even-parity metric perturbation $H = H_0 = H_2$ is governed by the following equation

$$\frac{\mathrm{d}^2 H}{\mathrm{d}r^2} + C_1(r)\frac{\mathrm{d}H}{\mathrm{d}r} + C_0(r)H = 0\,, \tag{4}$$

where the coefficients C_1 and C_0 are given by

$$C_1(r) = \frac{2}{r} + e^{\lambda}\left[\frac{2m}{r^2} + 4\pi r\,(p - \epsilon)\right], \tag{5}$$

$$C_0(r) = e^{\lambda}\left[-\frac{l(l+1)}{r^2} + 4\pi(\epsilon + p)\frac{\mathrm{d}\epsilon}{\mathrm{d}p} + 4\pi(5\epsilon + 9p)\right] - \left(\frac{\mathrm{d}\nu}{\mathrm{d}r}\right)^2 . \tag{6}$$

In order to simplify the form of the perturbation equation (4), it is conventional to introduce the logarithmic derivative $h(r) \equiv (r/H)\mathrm{d}H/\mathrm{d}r$. Substituting $h(r)$ into Eq. (4), we obtain a Riccati-type equation in the form (Damour and Nagar, 2009)

$$r\frac{\mathrm{d}h}{\mathrm{d}r} + h(h-1) + rC_1 h + r^2 C_0 = 0\,, \tag{7}$$

with the regular solution near the origin, $h(r) \simeq l$. Finally, the Love number k_2 can be determined using the following expression

$$\begin{aligned} k_2(C, h_R) = \frac{8}{5}&(1-2C)^2 C^5\,[2C(h_R - 1) - h_R + 2] \times \Big\{2C\big[4(h_R + 1)C^4 \\ &+(6h_R - 4)C^3 + (26 - 22h_R)C^2 + 3(5h_R - 8)C - 3h_R + 6\big] \\ &+ 3(1-2C)^2\,[2C(h_R - 1) - h_R + 2]\log(1 - 2C)\Big\}^{-1}, \end{aligned} \tag{8}$$

where h_R is the value of h at the surface $r = R$.

2.2 Schwarzschild stars

In this section, we discuss the homogeneous configurations with constant density. Although uniform-density stars are only an approximation for a realistic compact object, they are useful toy models which are described by Schwarzschild's interior solution (Glendenning, 2000). Moreover, there are various reasons to consider them in detail (see, e.g. Harrison et al., 1965).

The tidal Love number for constant-density stars, or Schwarzschild stars, was studied by Damour and Nagar (2009); Postnikov et al. (2010); Chan et al. (2015) and more recently by Chirenti et al. (2020). The details of the computation were discussed in these papers, so we refer the reader to those works.

The interior Schwarzschild solution describes a configuration of constant energy density ϵ. For convenience, it can be written in terms of the auxiliary function y (Chandrasekhar and Miller, 1974; Posada and Chirenti, 2019; Chirenti et al., 2020) defined as

$$y^2 = 1 - \left(\frac{r}{\alpha}\right)^2, \quad \text{with} \quad \alpha^2 = \frac{3}{8\pi\epsilon} \equiv \frac{R^3}{R_S}\,, \tag{9}$$

where R is the radius of the star and $R_S \equiv 2M$ is the Schwarzschild radius. The function y is defined in the range $[1, y_1]$ where $y_1 \equiv y(R)$ is the corresponding value at the surface. The interior metric functions are given by

$$\mathrm{e}^{\nu} = \frac{1}{4}(3y_1 - y)^2 \quad \text{and} \quad \mathrm{e}^{\lambda} = \frac{1}{y^2}\,, \tag{10}$$

which match continuously, at the surface $r = R$, with the exterior Schwarzschild solution. The pressure p in the interior is found to be

$$p = \epsilon\left(\frac{y - y_1}{3y_1 - y}\right)\,, \tag{11}$$

which vanishes at the surface $r = R$. The central pressure diverges when the compactness reaches the Buchdahl bound $M/R = 4/9$ (Buchdahl, 1959).

It is convenient to introduce a new coordinate x given by (Chandrasekhar and Miller, 1974)

$$x \equiv 1 - y = 1 - \sqrt{1 - \left(\frac{r}{\alpha}\right)^2}\,, \tag{12}$$

which is defined in the range $[0, x_1]$ where $x_1 = 1 - y_1 \equiv x(R)$, which depends on the compactness. The interior metric functions (10) take the form

$$\mathrm{e}^{\nu(x)} = \frac{1}{4}(k + x)^2, \quad \text{and} \quad \mathrm{e}^{\lambda(x)} = \frac{1}{(1 - x)^2}\,, \tag{13}$$

and the pressure (11) reads now

$$p = \epsilon\left(\frac{1 - x - y_1}{\kappa + x}\right), \tag{14}$$

where the constant κ is defined as

$$\kappa \equiv 3y_1 - 1\,. \tag{15}$$

Note that $\kappa > 0$ when $C < 4/9$, and, $-1 < \kappa \leq 0$ in the regime beyond Buchdahl. Note that Eq. (14), has a regular singular point at $x_0 \equiv -\kappa$. The careful analysis of this singularity for the computation of the Love number was done in Chirenti et al. (2020), so we refer the reader to that paper for more details.

The same singular point appears when one considers the extension of the ultracompact Schwarzschild star to slow rotation, using the equations derived by Hartle (Chandrasekhar and Miller, 1974; Posada, 2017). However, the results presented by Posada (2017) are marred after assuming, wrongly, an absolute value of κ when the compactness goes beyond the Buchdahl limit [1].

---

[1] The author acknowledges Emil Mottola and Philip Beltracchi for calling his attention to this point.

3 TIDAL DEFORMABILITY OF ULTRACOMPACT SCHWARZSCHILD STARS

In this section, we summarise the results of the tidal deformability of ultracompact Schwarschild stars reported by Chirenti et al. (2020). We used the transformation (12) in the perturbation equation (7), which facilitates the computation when the compactness goes beyond the Buchdahl bound. Profiles of the solutions to the perturbation equation for certain values of the compactness are presented in Figs. 1 and 2 in Chirenti et al. (2020). Of particular interest is the value of k_2 at the Buchdahl limit, which was found to be $\kappa_2^{\text{Buch}} = 0.0017103$, which is in excellent agreement with the result reported by Damour and Nagar (2009).

The value of k_2 is computed in the following way; the structure equations (13)–(14) are substituted into the coefficients (5) and (6), which consequently determine Eq. (7). Given the condition at the origin $h(r) = l$, one solves numerically Eq. (7) for $h(r)^{-}$, in the interior of the star, from the center (or, rather, some cutoff value, $r_0 = 10^{-7}$), outwards up to the surface $r = R$. Some care must be taken here regarding the constant density condition. Note that Eq. (6) contains a term in the form $(\epsilon + p)(d\epsilon/dp)$ which vanishes in the limit $\epsilon =$ constant. Given the discontinuity of the density at the surface, this term contributes a $\delta-$function which must be taken into account to obtain h_R^{+} (see the discussion in Damour and Nagar (2009); Postnikov et al. (2010)). This correction is given by

$$h_R^{+} = h_R^{-} - \left(\frac{4\pi R^3 \epsilon}{M}\right)^{-} , \tag{16}$$

which gives

$$h_R^{+} = h_R^{-} - 3 \, . \tag{17}$$

In Fig. 1, we show the profile of the tidal Love number k_2, as a function of the compactness M/R, for Schwarzschild stars below and beyond the Buchdahl limit (Chirenti et al., 2020). The inset shows a zoom of the region near the Buchdahl limit up to the Schwarzschild radius. The results of k_2 for $C \leq 4/9$ are in very good agreement with those reported by Damour and Nagar (2009). Note how k_2 approaches continuously to zero as the compactness approaches the Schwarzschild limit. Stars with compactness bigger than $4/9$ show a region of negative pressure in the interval $x \in [0, x_0]$ with $x_0 = -\kappa$. In the limit when $C \rightarrow 1/2$ from above, and $x_0 \rightarrow x_1$ from below, the central region of negative pressure covers the whole interior of the star. Thus, in this limit, the ultracompact Schwarzschild star becomes essentially the gravastar (Mazur and Mottola, 2015).

Note the striking “quenching”, in three orders of magnitude, of the tidal Love number, for ultracompact Schwarzschild stars, from 0.75, for $C \rightarrow 0$, to 0.0017103 at the Buchdahl bound, and the subsequent approach to zero as the compactness approaches $1/2$. This rapid quenching of k_2 clearly indicates that these configurations do not follow the logarithmic behaviour suggested by Cardoso et al. (2017) as a “generic feature” of ECOs with an exterior geometry arbitrarily close to the BH geometry. To see this, in Fig. 2, we show the same results shown in Fig. 1, but we also include the fit, which we model as an exponentially

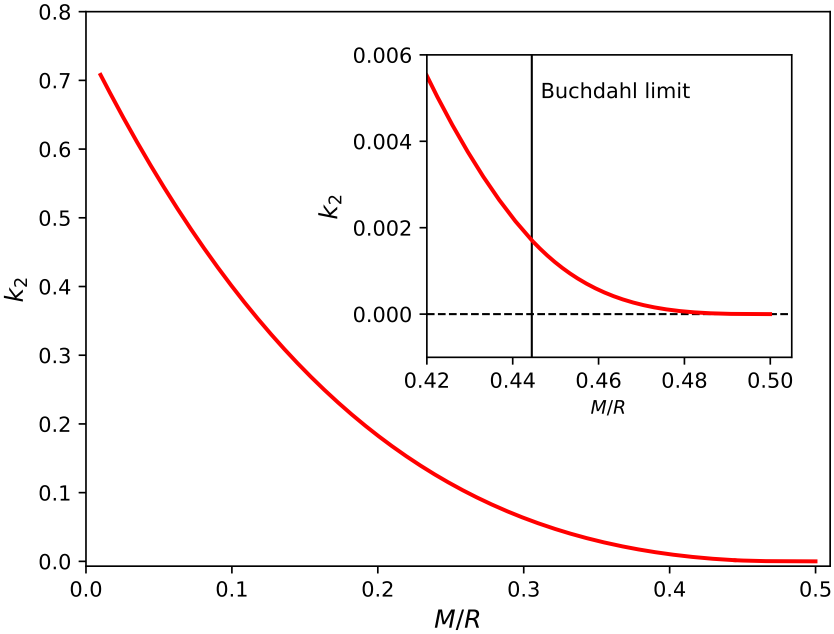

Figure 1. Tidal Love number k_2, as a function of the compactness, for Schwarzschild stars below and beyond the Buchdahl limit. Note how k_2 approaches smoothly and continuously to zero, as the compactness approaches the Schwarzschild limit (figure adapted from Chirenti et al. (2020)).

decaying function in the form

$$k_2 = a\left[1 - e^{-b(C-0.5)}\right] + d, \tag{18}$$

where the fitted coefficients are shown in the label of Fig. 2. We found that the R-squared value for this fitting model is $R^2 = 0.999429$, which shows that the exponentially decaying model is a good one. Note that in reference Chirenti et al. (2020), this fitting was overlooked, so here we are complementing those results.

Finally, in Fig. 3 we show in log-scale the tidal Love number as a function of the compactness, and we also include the Post-Minkowskian (PM) expansion for constant density stars introduced by Chan et al. (2015). Note that for configurations with low compactness (Newtonian limit), the PM approximation is in good agreement with our results. However, when the compactness approaches the Buchdahl limit, the differences between both results increase. This difference is expected, considering that near the Buchdahl limit, we are entering into the strong gravity zone. Thus, the PM expansion is not a good approximation; in the strong gravity regime, we require the full general relativistic computation. In reference Chirenti et al. (2020), figure 4 shows a similar log-scale for k_2, together with the PM ap-

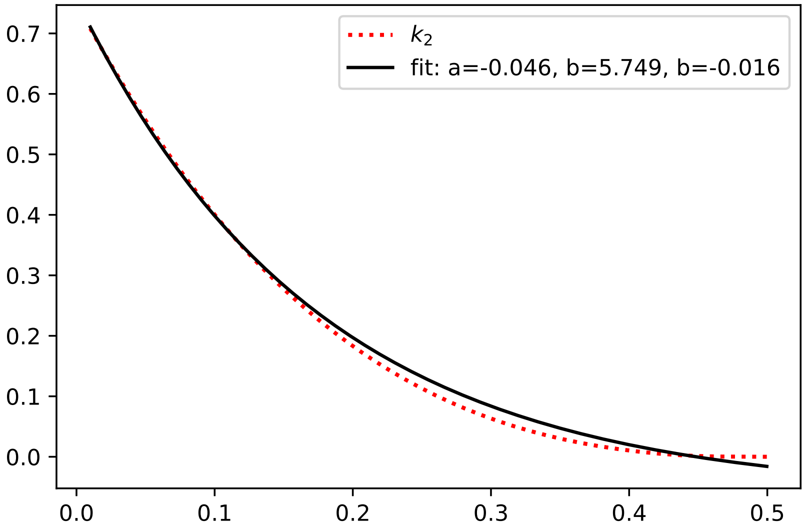

Figure 2. Same results as in Fig. 1, but we also present the fit in a black solid curve. We consider an exponentially decaying model in the form: $a\left[1 - e^{-b(C-0.5)}\right] + d$. The corresponding coefficients are shown in the label.

proximation. After the publication of that paper, the author found that the plot was marred due to a typo in the PM expansion. However, this error does not affect the results of k_2.

4 DISCUSSION

The Schwarzschild interior solution with constant density, or Schwarzschild star, remains an interesting and simple example of an exact solution to Einstein's equations for a perfect fluid. One of the most remarkable features of this model only discovered recently, is that it allows for compactness to cross beyond the Buchdahl limit. Moreover, these configurations can approach arbitrarily close to the Schwarzschild radius, where they become essentially the gravastar.

It has been found that the Love number k_2 of the ultracompact Schwarzschild stars is a smooth and continuous function of the compactness, and it approaches zero as the compactness approaches the BH limit 1/2. Thus, one can conclude that the result $k_2 \to 0$ is not an exclusive property of BHs but rather a consequence of the compactness approaching the Schwarzschild limit.

We found that the Love number of ultracompact Schwarzschild stars does not follow the logarithmic behaviour conjectured by Cardoso et al. (2017) for generic ECOs. Instead,

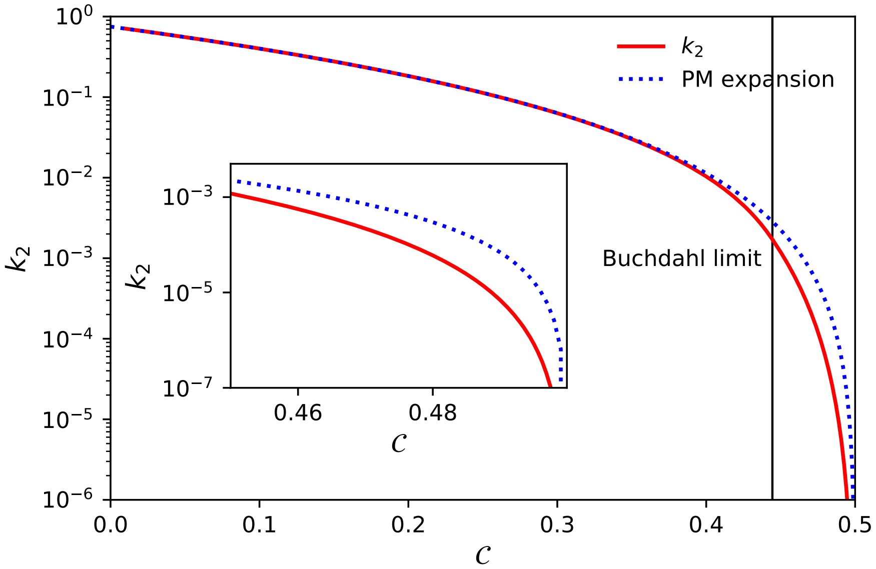

Figure 3. Same as Fig. 1, but in log-scale to emphasise the approach to the Schwarzschild limit. For comparison, we also show the Post-Minkowskian approximation for constant density stars presented in Chan et al. (2015). In the Newtonian limit, both approaches are in good agreement. In the strong gravity zone, near the Buchdahl limit, the deviations start to grow as expected.

we found that k_2 decreases rapidly with compactness, following an exponentially decaying behaviour. Therefore, we believe that the conclusions drawn by Cardoso et al. (2017), regarding the behaviour of k_2 for ECOs, are too restrictive considering that they studied only 4 types of ECOs, namely, thin-shell gravastar, boson stars, wormholes and some kind of anisotropic stars.

ACKNOWLEDGEMENTS

The author acknowledges the support of the Institute of Physics in Opava and its Research Centre for Theoretical Physics and Astrophysics.

REFERENCES

Beltracchi, P. and Gondolo, P. (2019), An exact time-dependent interior Schwarzschild solution, *Phys. Rev. D*, **99**(8), p. 084021, arXiv: `1902.07827`.

Beltracchi, P., Gondolo, P. and Mottola, E. (2021), Slowly rotating gravastars, arXiv: `2107.00762`.

Binnington, T. and Poisson, E. (2009), Relativistic theory of tidal Love numbers, *Phys. Rev. D*, **80**, p. 084018, arXiv: `0906.1366`.

Buchdahl, H. A. (1959), General Relativistic Fluid Spheres, *Phys. Rev.*, **116**, pp. 1027–1034.

Cardoso, V., Franzin, E., Maselli, A., Pani, P. and Raposo, G. (2017), Testing strong-field gravity with tidal Love numbers, *Phys. Rev. D*, **95**(8), p. 084014, [Addendum: Phys.Rev.D 95, 089901 (2017)], arXiv: `1701.01116`.

Cardoso, V. and Pani, P. (2019), Testing the nature of dark compact objects: a status report, *Living Rev. Rel.*, **22**(1), p. 4, arXiv: `1904.05363`.

Celotti, A., Miller, J. C. and Sciama, D. W. (1999), Astrophysical evidence for the existence of black holes: Topical review, *Class. Quant. Grav.*, **16**, p. A3, arXiv: `astro-ph/9912186`.

Chan, T. K., Chan, A. P. O. and Leung, P. T. (2015), I-Love relations for incompressible stars and realistic stars, *Phys. Rev.*, **D91**(4), p. 044017, arXiv: `1411.7141`.

Chandrasekhar, S. (1985), *The mathematical theory of black holes*, Oxford University Press.

Chandrasekhar, S. and Miller, J. C. (1974), On slowly rotating homogeneous masses in general relativity, *Mon. Not. Roy. Astron. Soc.*, **167**, p. 63.

Charalambous, P., Dubovsky, S. and Ivanov, M. M. (2021), On the Vanishing of Love Numbers for Kerr Black Holes, *JHEP*, **05**, p. 038, arXiv: `2102.08917`.

Chia, H. S. (2021), Tidal deformation and dissipation of rotating black holes, *Phys. Rev. D*, **104**(2), p. 024013, arXiv: `2010.07300`.

Chirenti, C., Posada, C. and Guedes, V. (2020), Where is Love? Tidal deformability in the black hole compactness limit, *Class. Quant. Grav.*, **37**(19), p. 195017, arXiv: `2005.10794`.

Damour, T. and Nagar, A. (2009), Relativistic tidal properties of neutron stars, *Phys. Rev.*, **D80**, p. 084035, arXiv: `0906.0096`.

Glendenning, N. K. (2000), *Compact stars: Nuclear physics, particle physics, and general relativity*, Springer, 2nd. edition.

Harrison, B. K., Thorne, K. S., Wakano, M. and Wheeler, J. A. (1965), *Gravitation theory and gravitational collapse*, The University of Chicago Press.

Hartle, J. B. (1967), Slowly rotating relativistic stars. 1. Equations of structure, *Astrophys. J.*, **150**, pp. 1005–1029.

Hartle, J. B. and Thorne, K. S. (1968), Slowly Rotating Relativistic Stars. II. Models for Neutron Stars and Supermassive Stars, *Astrophys. J.*, **153**, p. 807.

Hawking, S. W. and Ellis, G. F. R. (1973), *The Large Scale Structure of Space-Time*, Cambridge Monographs on Mathematical Physics, Cambridge University Press.

Hinderer, T. (2008), Tidal Love numbers of neutron stars, *Astrophys. J.*, **677**, pp. 1216–1220, arXiv: `0711.2420`.

Hui, L., Joyce, A., Penco, R., Santoni, L. and Solomon, A. R. (2021), Static response and Love numbers of Schwarzschild black holes, *JCAP*, **04**, p. 052, arXiv: `2010.00593`.

Konoplya, R. A., Posada, C., Stuchlík, Z. and Zhidenko, A. (2019), Stable Schwarzschild stars as black-hole mimickers, *Phys. Rev. D*, **100**(4), p. 044027, arXiv: `1905.08097`.

Mazur, P. O. and Mottola, E. (2001), Gravitational condensate stars: An alternative to black holes, arXiv: `gr-qc/0109035`.

Mazur, P. O. and Mottola, E. (2004), Gravitational vacuum condensate stars, *Proc. Nat. Acad. Sci.*, **101**, pp. 9545–9550, arXiv: `gr-qc/0407075`.

Mazur, P. O. and Mottola, E. (2015), Surface tension and negative pressure interior of a non-singular black hole, *Class. Quant. Grav.*, **32**(21), p. 215024, arXiv: `1501.03806`.

Ovalle, J., Posada, C. and Stuchlík, Z. (2019), Anisotropic ultracompact Schwarzschild star by gravitational decoupling, *Class. Quant. Grav.*, **36**(20), p. 205010, arXiv: `1905.12452`.

Poisson, E. (2021), Tidally induced multipole moments of a nonrotating black hole vanish to all post-Newtonian orders, *Phys. Rev. D*, **104**(10), p. 104062, arXiv: `2108.07328`.

Posada, C. (2017), Slowly rotating supercompact Schwarzschild stars, *Mon. Not. Roy. Astron. Soc.*, **468**(2), pp. 2128–2139, arXiv: `1612.05290`.

Posada, C. and Chirenti, C. (2019), On the radial stability of ultra compact Schwarzschild stars beyond the Buchdahl limit, *Class. Quant. Grav.*, **36**, p. 065004, arXiv: `1811.09589`.

Postnikov, S., Prakash, M. and Lattimer, J. M. (2010), Tidal Love Numbers of Neutron and Self-Bound Quark Stars, *Phys. Rev. D*, **82**, p. 024016, arXiv: `1004.5098`.

Wald, R. M. (2001), The thermodynamics of black holes, *Living Rev. Rel.*, **4**, p. 6, arXiv: `gr-qc/9912119`.

Proceedings of *RAGtime 23–25*
Z. Stuchlík, G. Török, V. Karas and D. Lančová, editors, Silesian University in Opava, 2023, pp. 13–19

Astrophysical black holes embedded in organized magnetic fields

Case of a nonvanishing electric charge

Vladimír Karas

Astronomical Institute, Czech Academy of Sciences, Boční II 1401,
CZ-14100 Prague, Czech Republic
`vladimir.karas@asu.cas.cz`

ABSTRACT
Large-scale magnetic fields pervade the cosmic environment where the astrophysical black holes are often embedded and influenced by mutual interaction. In this contribution, we outline the appropriate mathematical framework to describe magnetized black holes within General Relativity, and we show several examples of how these can be employed in the astrophysical context. In particular, we examine the magnetized black hole metric in terms of an exact solution of electro-vacuum Einstein-Maxwell equations under the influence of a non-vanishing electric charge. New effects emerge: the expulsion of the magnetic flux out of the black-hole horizon depends on the intensity of the imposed magnetic field.

Keywords: Black holes – electromagnetic fields – general relativity

1 INTRODUCTION

Astrophysical black holes are cosmic objects that can be mathematically described by a set of Einstein-Maxwell equations (e.g., Romero and Vila, 2014). Various formulations of the Uniqueness Theorems express in a rigorous way the conditions under which the black hole solutions exist, and they constrain the parameter space that is necessary to specify different cases (Wald, 1984). It turns out that classical black holes are described by a small number of such parameters, in particular, the mass, electric (or magnetic) charge, and angular momentum (spin). Black holes do not support their own magnetic field except the gravito-magnetically induced components in the rotating, charged Kerr-Newman metric.

However, astrophysical black holes are embedded in a magnetic field of external origin, which then interacts with the internal properties of the black hole (Ruffini and Wilson, 1975). In the case of very strong magnetic intensity, the magnetic field even contributes to the spacetime metric. In the present contribution, we examine the interesting properties of such an electrically charged, magnetized, rotating black hole. To this end, we employ the solution originally derived in the 1970s by means of Ernst magnetization techniques

978-80-7510-576-9

(Ernst and Wild, 1976) and demonstrate its interesting features in terms of magnetic flux threading different regions of the black hole horizon or an entire hemisphere (see Bičák and Hejda (2015), and further references cited therein).

We limit our discussion to axially symmetric and stationary solutions. These are vacuum, asymptotically non-flat solutions, where the influence of plasma is ignored, but the effects of strong gravity are taken into account.

2 MAGNETIZED BLACK HOLES WITH SPIN AND CHARGE

We can write the system of mutually coupled Einstein-Maxwell partial differential equations (Chandrasekhar, 1983),

$$R_{\mu\nu} - \tfrac{1}{2} R g_{\mu\nu} = 8\pi T_{\mu\nu}, \tag{1}$$

where the source term $T_{\mu\nu}$ is of purely electromagnetic origin,

$$T^{\alpha\beta} \equiv T^{\alpha\beta}_{\mathrm{EMG}} = \frac{1}{4\pi}\left(F^{\alpha\mu}F^{\beta}_{\mu} - \frac{1}{4}F^{\mu\nu}F_{\mu\nu}g^{\alpha\beta}\right), \tag{2}$$

$$T^{\mu\nu}{}_{;\nu} = -F^{\mu\alpha}j_{\alpha}, \qquad F^{\mu\nu}{}_{;\nu} = 4\pi j^{\mu}, \qquad {}^{\star}F^{\mu\nu}{}_{;\nu} = 4\pi \mathcal{M}^{\mu}, \tag{3}$$

and ${}^{\star}F_{\mu\nu} \equiv \tfrac{1}{2}\varepsilon_{\mu\nu}{}^{\rho\sigma}F_{\rho\sigma}$. We will consider the spacetime solutions for the metric that satisfies the electro-vacuum case with a regular event horizon under the constraints of axial symmetry and stationarity,

$$\mathrm{d}s^2 = f^{-1}\left[e^{2\gamma}\left(\mathrm{d}z^2 + \mathrm{d}\rho^2\right) + \rho^2\,\mathrm{d}\phi^2\right] - f\left(\mathrm{d}t - \omega\,\mathrm{d}\phi\right)^2, \tag{4}$$

with f, ω, and γ being functions of z and ρ only. Hereafter, instead of the canonical cylindrical form (4), we will also employ the spheroidal coordinates r and θ when convenient. In the weak electromagnetic field approximation, the electromagnetic (test) field is supposed to reside in the background of a rotating black hole, e.g., Kerr metric or a weakly charged Kerr metric (e.g., Wald, 1984; Gal'tsov, 1986). As an example, in such an asymptotically flat spacetime, the axial Killing vector $\partial_{\phi}(\equiv \tilde{\xi})$ generates a uniform magnetic field, whereas the field vanishes asymptotically for the time-like Killing vector $\partial_t(\equiv \xi)$. These two solutions are known as the Wald's field, i.e.

$$\boldsymbol{F} = \tfrac{1}{2}B_0\left(\mathbf{d}\tilde{\xi} + \tfrac{2J}{M}\,\mathbf{d}\xi\right) \tag{5}$$

in Wald (1974) notation. Magnetic flux surfaces are defined,

$$4\pi\Phi_{\mathrm{m}} = \int_S \boldsymbol{F} \;=\; \text{const.} \tag{6}$$

Magnetic and electric (Lorentz) forces are then given in terms of the particle's mass m, its four-velocity $\boldsymbol{u}$, and magnetic and electric charges, q_{m} and q_{e}, respectively:

$$m\dot{\boldsymbol{u}} = q_{\mathrm{m}}{}^{\star}\boldsymbol{F}.\boldsymbol{u}, \qquad m\dot{\boldsymbol{u}} = q_{\mathrm{e}}\boldsymbol{F}.\boldsymbol{u}. \tag{7}$$

Magnetic field lines are determined by

$$\frac{\mathrm{d}r}{\mathrm{d}\theta}=\frac{B_r}{B_\theta},\qquad \frac{\mathrm{d}r}{\mathrm{d}\phi}=\frac{B_r}{B_\phi},\tag{8}$$

in a perfect analogy with classical electromagnetism. We will employ the above-given quantities in our discussion further below.

Magnetic (electric) lines of force are defined by the direction of Lorentz force that acts on electric (magnetic) charges,

$$\frac{\mathrm{d}u^\mu}{\mathrm{d}\tau}\propto {}^\star F^\mu_{\ \nu}\,u^\nu,\qquad \frac{\mathrm{d}u^\mu}{\mathrm{d}\tau}\propto F^\mu_{\ \nu}\,u^\nu.\tag{9}$$

Therefore, in an axially symmetric system, the equation for magnetic lines takes a lucid form,

$$\frac{\mathrm{d}r}{\mathrm{d}\theta}=-\frac{F_{\theta\phi}}{F_{r\phi}},\qquad \frac{\mathrm{d}r}{\mathrm{d}\phi}=\frac{F_{\theta\phi}}{F_{r\theta}},\tag{10}$$

that is in correspondence with eq. (8).

Let us now turn our attention to the case of a strong magnetic field, where we cannot ignore its influence on the spacetime metric. The latter is not necessarily flat in the asymptotical spatial region far from the black hole (Ernst and Wild, 1976; Karas and Vokrouhlický, 1991).

As an example, we can consider magnetized Kerr-Newman black hole metric expressed in the form (García Díaz, 1985)

$$\mathrm{d}s^2 \;=\; |\Lambda|^2\,\Sigma\left(\Delta^{-1}\,\mathrm{d}r^2+\,\mathrm{d}\theta^2-\Delta A^{-1}\,\mathrm{d}t^2\right)+|\Lambda|^{-2}\,\Sigma^{-1}A\sin^2\theta\,(\,\mathrm{d}\phi-\omega\,\mathrm{d}t)^2\,,\tag{11}$$

where $\Sigma=r^2{+}a^2\cos^2\theta$, $\Delta=r^2{-}2Mr{+}a^2{+}e^2$, $A=\left(r^2+a^2\right)^2{-}\Delta a^2\sin^2\theta$ are functions from the Kerr-Newman metric. The outer horizon is located at radius $r{\equiv}r_+=1{+}\left(1-a^2-e^2\right)^{1/2}$, like in an unmagnetized case, and the horizon existence is restricted to the range of parameters $a^2{+}e^2\leq 1$. Let us emphasise that, in the magnetized case, the traditional Kerr-Newman parameters a and e are *not identical* with the black hole total spin and electric charge, as we will see further below. Moreover, because of the asymptotically non-flat nature of the spacetime, the Komar-type angular momentum and electric charge (as well as the black hole mass) have to be defined by integration over the horizon sphere rather than at radial infinity.

The magnetization function $\Lambda=1+\beta\Phi-\frac{1}{4}\beta^2\mathcal{E}$, in terms of the Ernst potentials $\Phi\,(r,\theta)$ and $\mathcal{E}\,(r,\theta)$, reads

$$\Sigma\Phi=ear\sin^2\theta-\mathrm{i}e\left(r^2+a^2\right)\cos\theta,\tag{12}$$

$$\begin{aligned}\Sigma\mathcal{E}=&-A\sin^2\theta-e^2\left(a^2+r^2\cos^2\theta\right)\\&+2\mathrm{i}a\left[\Sigma\left(3-\cos^2\theta\right)+a^2\sin^4\theta-re^2\sin^2\theta\right]\cos\theta.\end{aligned}\tag{13}$$

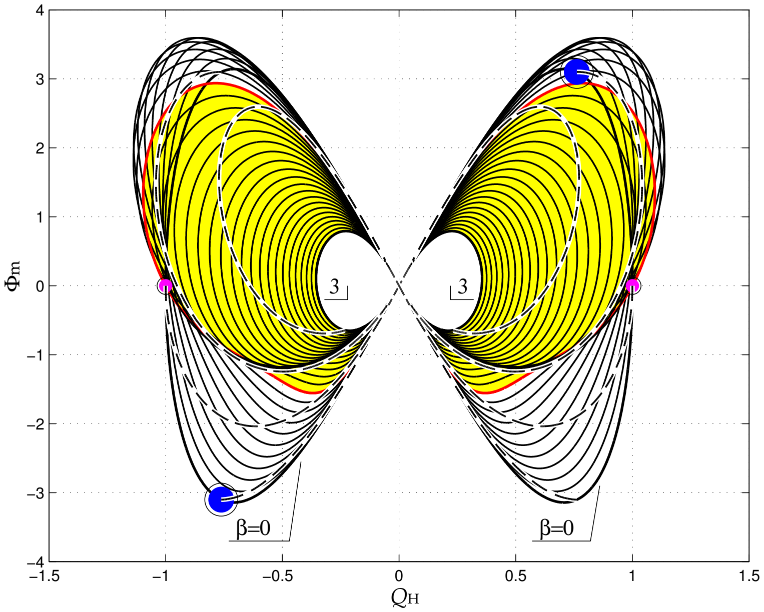

Figure 1. The "butterfly diagram" shows the magnetic flux Φ_{m} of magnetized Kerr-Newman black hole with $a^2 + e^2 = 1$ as a function of the total electric charge Q_{H}. Solid curves correspond to a constant value of the dimensionless magnetization parameter $\beta = BM$ ($\beta = 0$ is the case of an unmagnetized Kerr-Newman black hole). The area of the plot with ultra-strong magnetization is bounded by $\beta = 1$ (red curve) and emphasized by yellow colour in the plot. The lines of a constant ratio of a/e and varying β are also plotted (dashed; the cases of $a/e = \pm 0.85$ and 0 are shown); some distinctive combinations of the parameters a, e are emphasized by colour points.

The corresponding components of the electromagnetic field can be written conveniently with respect to orthonormal LNRF components,

$$H_{(r)} + \mathrm{i}E_{(r)} = A^{-1/2} \sin^{-1}\theta \, \Phi'_{,\theta}, \tag{14}$$

$$H_{(\theta)} + \mathrm{i}E_{(\theta)} = -(\Delta/A)^{1/2} \sin^{-1}\theta \, \Phi'_{,r}, \tag{15}$$

where $\Phi'(r,\theta) = \Lambda^{-1}\left(\Phi - \frac{1}{2}\beta\mathcal{E}\right)$. The total electric charge Q_{H} is

$$Q_{\mathrm{H}} = -\left|\Lambda_0\right|^2 \, \Im\mathrm{m}\, \Phi'\left(r_+, 0\right), \tag{16}$$

and the magnetic flux $\Phi_{\mathrm{m}}(\theta)$ across a cap placed in an axisymmetric position on the horizon is

$$\Phi_{\mathrm{m}} = 2\pi \left|\Lambda_0\right|^2 \, \Re\mathrm{e}\, \Phi'\left(r_+, \bar{\theta}\right)\Big|_{\bar{\theta}=0}^{\theta}, \tag{17}$$

where $\Lambda_0 = \Lambda(\theta = 0)$. The adopted notation indicates subtraction of the Ernst potential values $\Phi'\left(r_+, \bar{\theta}\right)$ taken at $\bar{\theta} \to \theta$ and $\bar{\theta} \to 0$.

At this point, it is interesting to mention that the span of the azimuthal coordinate in the magnetized solution must be rescaled by the multiplication factor Λ_0 in order to avoid a conical singularity on the symmetry axis (Hiscock, 1981):

$$\Lambda_0 = \left[1 + \tfrac{3}{2}\beta^2 e^2 + 2\beta^3 ae + \beta^4\left(\tfrac{1}{16}e^4 + a^2\right)\right]^{1/2}. \tag{18}$$

This rescaling procedure effectively leads to the increase of the horizon surface area, and thereby also magnetic flux across the horizon (Karas, 1988). In Figure 1, the magnetic flux across the entire black hole hemisphere in Kerr-Newman strongly magnetized black hole solution, $\Phi_{\rm m}(\theta = \pi/2)$, is shown as a function of electric charge on the horizon, $Q_{\rm H}$ (additional details can be found in Karas and Budinová (2000); Karas et al. (2019)).

Cases of intersection of the $\beta =$ const curves with $F = 0$ and non-zero charge, $Q_{\rm H} \neq 0$, correspond to the vanishing angular momentum of the black hole, $J = 0$. This property is rather different from the behaviour of weakly magnetized black holes with only a test magnetic field imposed on them. On the other hand, this exact solution does not allow us to study the effects of the misalignment of the magnetic field with respect to the rotation axis, which is so far possible only in the test-field approximation or by numerical techniques. Let us also note that it may be interesting to consider the magnetic flux also in other spacetime metrics for comparison and better understanding of the underlying processes (see, e.g., Gutsunaev and Manko (1988); Kovář et al. (2012); Khan and Chen (2023); Vrba et al. (2023), and further references cited therein).

3 CONCLUSIONS

We discussed the magnetic flux across the event horizon of a magnetized rotating black hole and the associated electric charge within the framework of the *exact solution* of mutually coupled Einstein-Maxwell equations. To this end, we adopted Ernst and Wild (1976) spacetime, which represents an axially symmetric, stationary solution that corresponds, in a straightforward manner, to the Wald (1974) solution of an asymptotically uniform magnetic field imposed on the background of Kerr metric. On the other hand, in the limit of small black hole mass, zero angular momentum and strong magnetic intensity, the adopted solution goes over to the cosmological solution of Melvin universe (Melvin, 1964). The latter represents an asymptotically non-flat ‘geon’ that is maintained in the static configuration by the gravitational effect of the magnetic field acting upon itself. In other words, this means that our discussion is appropriate for the limit of ultra-strong magnetic fields that might be possibly relevant in the conditions of early Universe (Beskin et al., 2015). On the other hand, we think that this extreme situation does not bring any qualitatively new phenomena into the discussion of the magnetic Penrose process, which has been recently discussed in the context of weakly magnetized black holes (Karas and Stuchlík, 2023).

We elaborated a detailed graphical representation of magnetic flux which exhibits an intricate structure as a function of the space-time parameters. This has allowed us to position specific configurations, such as those with vanishing angular momentum or vanishing electric charge. The corresponding combinations of the model parameters are different from the case of weak magnetic field limit because of strong-gravity effects. Let us note that ultra-strong magnetic fields are expected to affect processes on molecular and atomic scales in the conditions when the magnetic energy density becomes comparable to the binding energy density (Lai, 2015).

ACKNOWLEDGEMENTS

The author thanks the referee for careful reading of the original version of the manuscript and for helpful suggestions towards improvements at several points. The author acknowledges continued support from the Czech Science Foundation EXPRO grant titled "Accreting black holes in the new era of X-ray polarimetry missions", No. 21-06825X.

REFERENCES

Beskin, V. S., Balogh, A., Falanga, M. and Treumann, R. A. (2015), Magnetic fields at largest universal strengths: Overview, *Space Science Reviews*, **191**(1-4), pp. 1–12.

Bičák, J. and Hejda, F. (2015), Near-horizon description of extremal magnetized stationary black holes and meissner effect, *Physical Review D*, **92**(10), p. 104006.

Chandrasekhar, S. (1983), *The Mathematical Theory of Black Holes*, Oxford University Press.

Ernst, F. J. and Wild, W. J. (1976), Kerr black holes in a magnetic universe, *Journal of Mathematical Physics*, **17**(2), pp. 182–184.

Gal'tsov, D. V. (1986), *Particles and Fields around Black Holes*, Moscow University Press.

García Díaz, A. (1985), Magnetic generalization of the kerr–newman metric, *Journal of Mathematical Physics*, **26**(1), pp. 155–156.

Gutsunaev, T. I. and Manko, V. S. (1988), On a family of solutions of the einstein-maxwell equations, *General Relativity and Gravitation*, **20**(4), pp. 327–335.

Hiscock, W. A. (1981), On black holes in magnetic universes, *Journal of Mathematical Physics*, **22**(8), pp. 1828–1833.

Karas, V. (1988), Magnetic fluxes across black holes. exact models, *Bulletin of the Astronomical Institute of Czechoslovakia*, **39**.

Karas, V. and Budinová, Z. (2000), Magnetic fluxes across black holes in a strong magnetic field regime, *Physica Scripta*, **61**(2), pp. 253–256.

Karas, V. and Stuchlík, Z. (2023), Magnetized black holes: Interplay between charge and rotation, *Universe*, **9**(6), p. 267.

Karas, V., Svoboda, J. and Zajacek, M. (2019), Selected chapters on active galactic nuclei as relativistic systems, *arXiv preprint arXiv:1901.06507*.

Karas, V. and Vokrouhlický, D. (1991), On interpretation of the magnetized kerr–newman black hole, *Journal of Mathematical Physics*, **32**(3), pp. 714–716.

Khan, S. U. and Chen, Z.-M. (2023), Charged particle dynamics in black hole split monopole magnetosphere, *The European Physical Journal C*, **83**(8).

Kovář, J., Kopáček, O., Karas, V. and Kojima, Y. (2012), Regular and chaotic orbits near a massive magnetic dipole, *Classical and Quantum Gravity*, **30**(2), p. 025010.

Lai, D. (2015), Physics in very strong magnetic fields, *Space Science Reviews*, **191**(1-4), pp. 13–25.

Melvin, M. (1964), Pure magnetic and electric geons, *Physics Letters*, **8**(1), pp. 65–68.

Romero, G. E. and Vila, G. S. (2014), *Introduction to Black Hole Astrophysics*, Springer Berlin Heidelberg.

Ruffini, R. and Wilson, J. R. (1975), Relativistic magnetohydrodynamical effects of plasma accreting into a black hole, *Physical Review D*, **12**(10), pp. 2959–2962.

Vrba, J., Rayimbaev, J., Stuchlik, Z. and Ahmedov, B. (2023), Charged particles motion and quasiperiodic oscillation in simpson–visser spacetime in the presence of external magnetic fields, *The European Physical Journal C*, **83**(9).

Wald, R. M. (1974), Black hole in a uniform magnetic field, *Physical Review D*, **10**(6), pp. 1680–1685.

Wald, R. M. (1984), *General Relativity*, University of Chicago Press.

Proceedings of *RAGtime 23–25*
Z. Stuchlík, G. Török, V. Karas and D. Lančová, editors, Silesian University in Opava, 2023, pp. 21–27

Charged particles on resonant orbits around Schwarzschild black hole

Martin Kološ[1,a] and Misbah Shahzadi[2,b]

[1]Institute of Physics, Silesian University in Opava,
Bezručovo nám.13, CZ-74601 Opava, Czech Republic
[2]Department of Mathematics, COMSATS University Islamabad,
Lahore Campus, 54000 Lahore, Pakistan
[a]`martin.kolos@physics.slu.cz`
[b]`misbahshahzadi51@gmail.com`

ABSTRACT
We explore the dynamics of test particles on perturbed circular orbits in the equatorial plane of a Schwarzschild black hole in search of resonant effects. The nonlinear bond between radial and vertical oscillatory modes is given by Lorentz electromagnetic force acting on charged particles in the uniform magnetic field. When the perturbation of the circular orbit is large enough, strong, persistent 2:1 resonance between radial and vertical modes develops.

Keywords: Black hole – resonances – particle dynamics – magnetic field

1 INTRODUCTION

The microquasars are binary systems composed of a black hole (BH) and a companion (donor) star, and Quasi-Periodic Oscillations (QPOs) are periodic changes in X-ray photons flux in these systems (Remillard and McClintock, 2006). QPOs cover a wide range of frequencies, from low-frequency QPOs (∼ 30 Hz) to high-frequency QPOs (∼ 500 Hz). The QPOs are still unresolved phenomena, but the connection to particle orbital frequency at the innermost stable circular orbit (ISCO) (∼200 Hz for $10M_\odot$ BH) is frequently assumed (Török et al., 2005). Most high-frequency QPOs in BHs are detected with twin peaks with a frequency ratio ∼3:2; obviously, some resonance phenomena in the BH accretion disk are present. In this proceeding, we will simulate accretion disk resonances using simple charged test particle dynamics as a model for plasma around BH.

2 CHARGED PARTICLE DYNAMICS

We consider a BH of a mass M described by the Schwarzschild metric

$$\mathrm{d}s^2 = -f(r)\,\mathrm{d}t^2 + f^{-1}(r)\,\mathrm{d}r^2 + r^2\left(\mathrm{d}\theta^2 + \sin^2\theta\mathrm{d}\phi^2\right), \qquad f(r) = 1 - \frac{2M}{r}, \tag{1}$$

978-80-7510-576-9

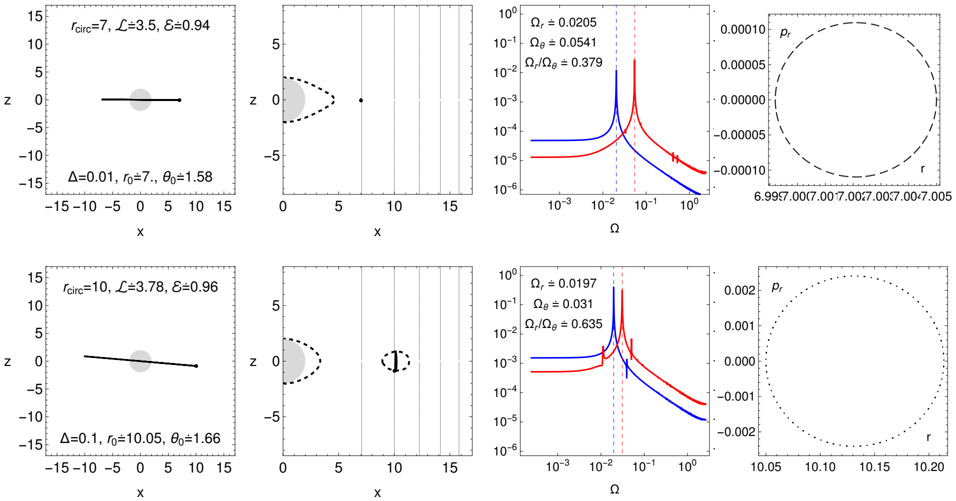

Figure 1. Charged particle oscillations around circular orbit with very weak magnetic field influence $\mathcal{B} = 10^{-5}$. We see particle trajectories in x-z plane (first column) with BH as a grey disk, projection in x-z plane (second column) with dashed energetic boundary, Fourier spectra (third column) for radial r and vertical θ coordinates with frequency ratios, dashed vertical lines pointing maxima, Poincaré surface of section (fourth column) for equatorial plane crossing. The first row of figures is for small perturbation $\triangle = 0.01$ from circular orbit, where only main frequencies are present, and the second row is for larger perturbation $\triangle = 0.1$, where we can see higher harmonic in the spectra.

where $f(r)$ is the lapse function. Let the BH be immersed into an external uniform magnetic field, given by electromagnetic four-potential (Wald, 1974)

$$A_\phi = \frac{B}{2}\, r^2 \sin^2\theta. \tag{2}$$

Hereafter, we put $M = 1$, i.e., we use dimensionless radial coordinate r (and time coordinate t).

The equations of motion for a charged particle with mass m and electric charge q can be obtained using the Hamiltonian formalism

$$\frac{\mathrm{d}x^\mu}{\mathrm{d}\zeta} = \frac{\partial H}{\partial \pi_\mu}, \quad \frac{\mathrm{d}\pi_\mu}{\mathrm{d}\zeta} = -\frac{\partial H}{\partial x^\mu}, \qquad H = \frac{1}{2} g^{\alpha\beta}(\pi_\alpha - qA_\alpha)(\pi_\beta - qA_\beta) + \frac{m^2}{2} = 0, \tag{3}$$

where the kinematical four-momentum $p^\mu = mu^\mu = \mathrm{d}x^\mu/\mathrm{d}\zeta$ is related to the generalized (canonical) four-momentum π^μ by the relation $\pi^\mu = p^\mu + qA^\mu$. The affine parameter ζ of the particle is related to its proper time τ by the relation $\zeta = \tau/m$.

Due to the symmetries of the Schwarzschild spacetime (1) and the magnetic field (2), one can easily find the conserved quantities that are particle energy and axial angular momentum and magnetic field parameters $\mathcal{B}$

$$\mathcal{E} = \frac{E}{m} = -\frac{\pi_t}{m} = -g_{tt}u^t, \quad \mathcal{L} = \frac{L}{m} = \frac{\pi_\phi}{m} = g_{\phi\phi}u^\phi + \frac{q}{m}A_\phi, \qquad \mathcal{B} = \frac{qB}{2m}, \tag{4}$$

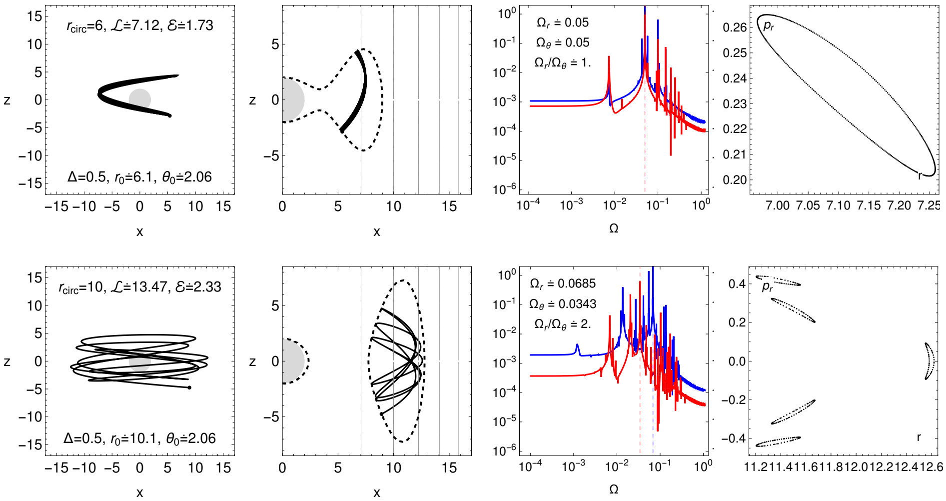

Figure 2. Charged particle oscillations around circular orbit in stronger magnetic field influence $\mathcal{B} = 0.1$, similar to Fig. 1. In the first row of figures, the motion has complicated Fourier spectra, but the main frequency peaks are in resonant ratio $\Omega_r/\Omega_\theta \sim 1$. The trajectory in the second row is close to chaotic motion, but the main peak frequencies are still in resonant ratio $\Omega_r/\Omega_\theta \sim 2$, which appear frequently in our numerical experiment.

which reflects a relative relationship between Lorentz and gravitational forces. Using such symmetries, one can rewrite the Hamiltonian (3) in the form

$$H = \frac{1}{2}g^{rr}p_r^2 + \frac{1}{2}g^{\theta\theta}p_\theta^2 + \frac{1}{2}g^{tt}E^2 + \frac{1}{2}g^{\phi\phi}\left(L - qA_\phi\right)^2 + \frac{1}{2}m^2. \tag{5}$$

Energetic boundary for particle motion can be expressed from the equation (5)

$$\mathcal{E}^2 = V_{\text{eff}}\,(r,\theta) \quad (\text{for } p_r = p_\theta = 0)\,. \tag{6}$$

We introduced effective potential for charged particles $V_{\text{eff}}(r,\theta)$ by the relation

$$V_{\text{eff}}\,(r,\theta) \equiv -g_{tt}\left[g^{\phi\phi}\left(\mathcal{L} - \frac{q}{m}A_\phi\right)^2 + 1\right]. \tag{7}$$

The effective potential $V_{\text{eff}}\,(r,\theta)$ combines the influence of gravity potential (g_{tt} term) with the influence of central force potential given by the specific angular momentum $\mathcal{L}$ and electromagnetic potential energy given by qA_ϕ.

A detailed description of charged particle dynamics around BH can be found for the uniform magnetic field in Galtsov and Petukhov (1978); Karas and Vokrouhlicky (1990); Frolov and Shoom (2010); Kološ et al. (2015); Kopáček and Karas (2018) or for more realistic parabolic BH magnetosphere in Kološ et al. (2023).

If a charged test particle is slightly displaced from the equilibrium position located in a minimum of the effective potential $V_{\text{eff}}\,(r,\theta)$ at r_0 and $\theta_0 = \pi/2$, corresponding to a stable

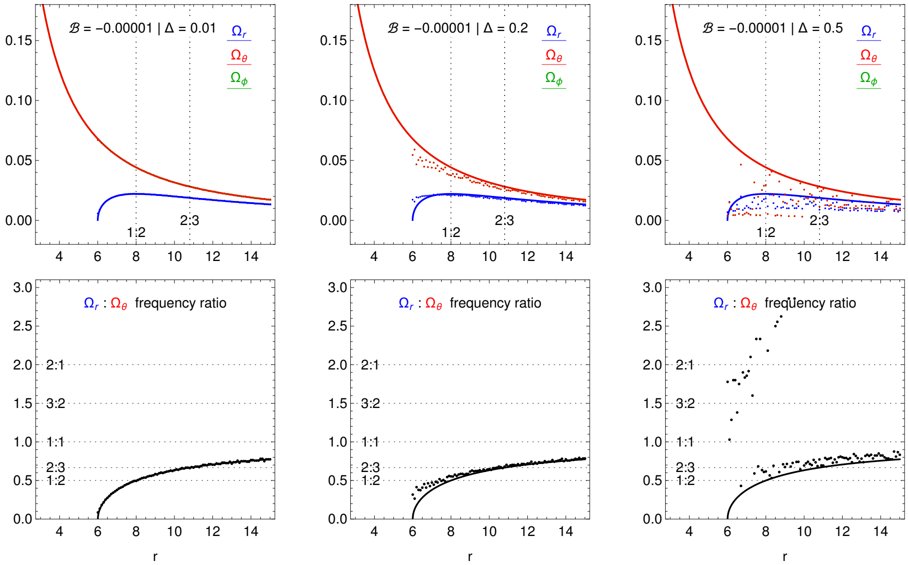

Figure 3. Test particle orbital frequencies (first row), and the ratio of radial and vertical frequencies (second row) with weak electromagnetic influence ($\mathcal{B} = -10^{-5}$). For small circular orbit perturbation $\triangle = 0.01$, the numerically calculated frequencies (individual dots) from perturbed orbit exactly follow the analytic frequencies (solid curves) given by effective potential minima. For large perturbation $\triangle = 0.5$, the numerical frequencies are detached from the analytical one. Different resonant radii (vertical dotted lines in the first row and horizontal dotted lines in the second row) are plotted, but no clustering around them can be reported.

circular orbit, the particle will start to oscillate around the minimum realising thus epicyclic motion governed by linear harmonic oscillations with the radial Ω_r, vertical Ω_θ, and axial Ω_ϕ frequencies (Wald, 1984)

$$\Omega_r^2 = \frac{1}{2}\frac{f^2(r)}{\mathcal{E}^2(r)}\frac{\partial^2 V_{\rm eff}}{\partial r^2}, \quad \Omega_\theta^2 = \frac{1}{2}\frac{f(r)}{r^2\mathcal{E}^2(r)}\frac{\partial^2 V_{\rm eff}}{\partial \theta^2}, \quad \Omega_\phi^2 = \frac{\mathcal{L}^2(r)}{g_{\phi\phi}^2}\frac{f^2(r)}{\mathcal{E}^2(r)}. \tag{8}$$

3 RESONANCES FOR PERTURBED CIRCULAR ORBIT

A thin Keplerian accretion disk model is given by a dense set of particles on a circular orbit where gravity is perfectly compensated by centrifugal force. In our case of charged test particles, the Lorentz force from an external uniform magnetic field will also be taken into account. To simulate resonances in the accretion disk around BH, we randomly perturb all particles on the circular orbits in radial δr and vertical direction $\delta\theta$. For all different circular

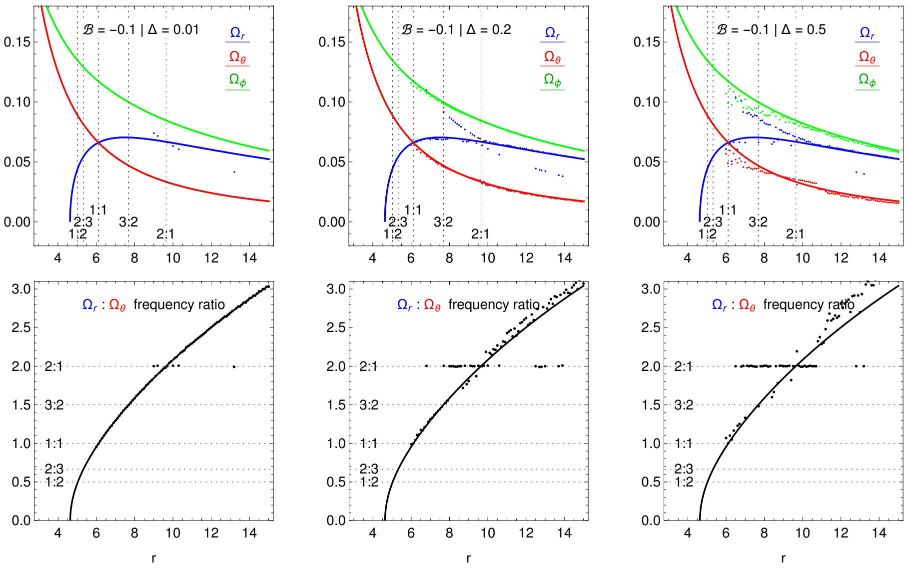

Figure 4. Charged particle orbital frequencies (first row) and the frequency ratio (second row) with stronger magnetic field influence $\mathcal{B} = -0.1$, similar to Fig. 3. When the circular orbit is only slightly perturbed $\triangle = 0.1$, the numerical and analytical frequencies coincide for almost all the points with only a few 2:1 resonant exceptions. The number of trajectories with a 2:1 resonant ratio grows with circular orbit perturbation, reaching more than 50% for $\triangle = 0.5$ value.

orbits from the Keplerian disk, the total perturbation $\triangle$ will remain the same

$$r = r_{\text{circ}} + \delta r, \quad \theta = \pi/2 + \delta\theta, \qquad \triangle = \sqrt{\delta r^2 + \delta\theta^2}. \tag{9}$$

As it has been demonstrated in Fig. 3, when the perturbation δ is small, the main peak frequency calculated from particle trajectory using Fourier transform coinciding with analytically calculated frequencies for small circular orbit perturbation (8). When the perturbation is large enough and when the nonlinear electromagnetic bound between r and θ oscillatory modes is present, the particle trajectory main frequency peaks are likely to be in resonant ratios 2:1, see Fig. 4.

While resonant ratios between oscillatory modes might appear coincidental for a single particle orbit, they become statistically significant when considering the dense set of circular orbits covering the entire Keplerian disk. When perturbed, the charged particles are likely to orbit around BH in 2:1 resonance between $\Omega_r : \Omega_\theta$ modes as demonstrated in Figs. 3 and 4.

The parametric resonance model (Abramowicz and Kluźniak, 2004) is given by formula

$$\frac{\Omega_r}{\Omega_\theta} = \frac{2}{n}, \quad n = 1, 2, 3, \ldots, \tag{10}$$

where the strongest resonances can be expected for small n. For the observed QPOs signal, a 3:2 resonance has been reported and not a 2:1 resonance. However, this discrepancy could be explained by the fact that we do not observe Ω_r and Ω_θ directly, but we observe their combinations

$$\Omega_r : \Omega_\theta = 2 : 1 \quad \rightarrow \quad \Omega_r + \Omega_\theta : \Omega_r = 3 : 2. \tag{11}$$

We currently have no direct explanation for the 2:1 resonance and why we do not observe stronger 1:1 or weaker 3:2 resonances, even though they are allowed in our model for charged particle dynamics. The effective potential for a charged particle has a special shape, it has Z_2 symmetry ($V_{\text{eff}}\,(x, z)$ is the same above $z > 0$ and below $z < 0$ the equatorial plane), which could be one of the possible explanations for the observed strong 2:1 resonance. Another explanation could come from the Kolmogorov-Arnold-Moser (KAM) theorem. If we can express our system as having the regular part H_0 and a perturbative part H_p, with perturbation parameter ϵ, then the Hamiltonian can be expressed as

$$H = H_0 + \epsilon H_\text{p}. \tag{12}$$

According to the KAM theorem, only nonresonant tori will survive small ϵ perturbation, while the resonant tori will be destroyed. For two degrees of freedom system, as is our particle dynamics in an axially symmetric model, one will have

$$k_1\,\Omega_r + k_2\,\Omega_\theta = 0, \quad k_1 + k_2 < 4, \tag{13}$$

and hence around the resonant elliptic point (minima in effective potential), we can not construct Birkhoff normal form if $k_1 + k_2 > 4$ (Tabor, 1989). The condition (13) is correct only for 1:1, 1:2, and 2:1 resonances but not $3 : 2$ and could explain why 3:2 resonance between Ω_r and Ω_θ is not observed in our model.

4 CONCLUSIONS

In our numerical experiment with charged particle dynamics around magnetized Schwarzschild BH, we have demonstrated the existence of 2:1 resonance, which could be related to observed QPO within the parametric resonance model. It is still an open question, whether these 2:1 resonances are unique to our test particle model, and if 2:1 will appear in other systems. In the future, we would like to explore other nonlinear models, like string-loop, spinning particle dynamics, and test particle motion in modified BH spacetimes.

ACKNOWLEDGEMENTS

This work was supported by Czech Science Foundation Grant (GAČR) No. 23-07043S. We also thank the internal grant of Silesian University, SGS/30/2023: Dynamics of structures in strong gravomagnetic fields of compact objects modeled in the framework of Einstein or alternative theories of gravity.

REFERENCES

Abramowicz, M. A. and Kluźniak, W. (2004), Interpreting black hole QPOs, in P. Kaaret, F. K. Lamb and J. H. Swank, editors, *X-ray Timing 2003: Rossi and Beyond*, volume 714 of *American Institute of Physics Conference Series*, pp. 21–28, arXiv: `astro-ph/0312396`.

Frolov, V. P. and Shoom, A. A. (2010), Motion of charged particles near a weakly magnetized Schwarzschild black hole, *Phys. Rev. D* , **82**(8), 084034, arXiv: `1008.2985`.

Galtsov, D. V. and Petukhov, V. I. (1978), Black hole in an external magnetic field., *Zhurnal Eksperimentalnoi i Teoreticheskoi Fiziki*, **74**, pp. 801–818.

Karas, V. and Vokrouhlicky, D. (1990), Test particle motion around a magnetised Schwarzschild black hole, *Classical and Quantum Gravity*, **7**(3), pp. 391–398.

Kološ, M., Stuchlík, Z. and Tursunov, A. (2015), Quasi-harmonic oscillatory motion of charged particles around a Schwarzschild black hole immersed in a uniform magnetic field, *Classical and Quantum Gravity*, **32**(16), 165009, arXiv: `1506.06799`.

Kološ, M., Shahzadi, M. and Tursunov, A. (2023), Charged particle dynamics in parabolic magnetosphere around Schwarzschild black hole, *European Physical Journal C*, **83**(4), 323.

Kopáček, O. and Karas, V. (2018), Near-horizon Structure of Escape Zones of Electrically Charged Particles around Weakly Magnetized Rotating Black Hole, *The Astrophysical Journal* , **853**, 53, arXiv: `1801.01576`.

Remillard, R. A. and McClintock, J. E. (2006), X-Ray Properties of Black-Hole Binaries, *Annual Review of Astronomy and Astrophysics*, **44**, pp. 49–92, arXiv: `astro-ph/0606352`.

Tabor, M. (1989), *Chaos and Integrability in Nonlinear Dynamics: An Introduction, WileyInterscience.*

Török, G., Abramowicz, M. A., Kluźniak, W. and Stuchlík, Z. (2005), The orbital resonance model for twin peak kHz quasi periodic oscillations in microquasars, *Astronomy and Astrophysics* , **436**, pp. 1–8.

Wald, R. M. (1974), Black hole in a uniform magnetic field, *Phys. Rev. D* , **10**, pp. 1680–1685.

Wald, R. M. (1984), *General relativity*, University of Chicago Press, Chicago.

Proceedings of *RAGtime 23–25*
Z. Stuchlík, G. Török, V. Karas and D. Lančová, editors, Silesian University in Opava, 2023, pp. 29–39

Growth of orbital resonances around a black hole surrounded by matter

Michal Stratený[1,2,a] and Georgios Lukes-Gerakopoulos[1,b]

[1]Astronomical Institute of the Academy of Sciences of the Czech Republic,
Boční II 1401/1a, CZ-141 31 Prague, Czech Republic
[2]Institute of Theoretical Physics, Faculty of Mathematics and Physics,
Charles University, CZ-180 00 Prague, Czech Republic
[a]`strateny.m@gmail.com`
[b]`gglukes@gmail.com`

ABSTRACT
This work studies the dynamics of geodesic motion within a curved spacetime around a Schwarzschild black hole, perturbed by a gravitational field of a far axisymmetric distribution of mass enclosing the system. This spacetime can serve as a versatile model for a diverse range of astrophysical scenarios and, in particular, for extreme mass ratio inspirals as in our work. We show that the system is non-integrable by employing Poincaré surface of section and rotation numbers. By utilising the rotation numbers, the widths of resonances are calculated, which are then used in establishing the relation between the underlying perturbation parameter driving the system from integrability and the quadrupole parameter characterising the perturbed metric. This relation allows us to estimate the phase shift caused by the resonance during an inspiral.

Keywords: Geodesic motion – black holes – chaos

1 INTRODUCTION

Even if the Kerr black hole solution of the Einstein field equation is a vacuum one (Kerr, 1963), astrophysical black holes are surrounded by matter distributions. Therefore, a curved spacetime describing a Schwarzschild black hole perturbed by the gravitational field of a far axisymmetric distribution is of interest since it can serve as a model for a diverse range of physical scenarios. For instance, massive black holes located in the centres of galaxies are often surrounded by dense nuclear star clusters and other molecular and dust structures (Genzel et al., 2010). Furthermore, alternative sources of external matter can come from more exotic sources, such as dark matter or scalar fields (Hannuksela et al., 2020; Ferreira et al., 2017).

In the close vicinity of these primary massive black holes, we expect that stellar compact objects are trapped by the gravitational field of the primaries. While such a secondary

978-80-7510-576-9

object orbits the primary one, it loses energy and angular momentum in the form of gravitational waves. This loss leads the secondary to inspiral towards the primary, creating an extreme mass ratio inspiral (EMRI). These gravitational waves peak in the mHz frequency band and are expected to be observed by the next generation of gravitational-wave observatories (Berry et al., 2019; Amaro-Seoane et al., 2017; Polcar et al., 2022).

The perturbation of a Schwarzschild black hole by the surrounding matter can have observational implications on the evolution of an EMRI. In particular, a key aspect of geodesic motion in the Schwarzschild spacetime is its integrability. However, by perturbing the spacetime, the system is no longer entirely symmetrical, which results in the loss of integrals of motion. The insufficient number of integrals of motion leads to non-integrability, which allows chaotic behaviour to emerge.

We focus mainly on resonances, parts of the phase space where two or more characteristic frequencies of the system match in integer ratios. These regions are key parts of the study of chaos because the chaotic behaviour emerges there. There are studies (see, e.g., Lukes-Gerakopoulos and Witzany, 2022 and references therein) showing that such regions can have an observational impact on the gravitational waves emitted during an EMRI since a resonance crossing is expected to cause a dephasing of the gravitational waveforms. Hence, investigating the strength and the growth of the resonances is important for the preparation of the gravitational waveforms needed to detect the signal from an EMRI (Babak et al., 2017).

The article is organised as follows: in section 2, we introduce the properties of the studied spacetime, some cardinal theoretical elements of non-integrable systems, and some tools to study these systems. Section 3 showcases our numerical results obtained from the computation of geodesic motion within the studied curved spacetime. Section 4 discusses our main findings. Note that geometric units are employed throughout the article $G = c = 1$. Greek letters denote the indices corresponding to spacetime. The metric signature is chosen as $(- + + +)$.

2 GEODESIC MOTION AND CHAOS

This work studies geodesic motion in curved spacetime introduced by Polcar et al. (2022), who outlined its derivation. This metric expresses a spacetime around a non-spinning black hole of mass M encircled by a rotating gravitating ring with mass $\mathcal{M}_r$ at a radius $r_r \gg M$ much larger than the black hole horizon. The gravitational field near the black hole is influenced by the tidal effects caused by the presence of the ring. The resulting spacetime is static and axisymmetric, while the multipole structure of the ring is truncated to the leading quadrupolar order. In Schwarzschild-like coordinates (t, r, θ, ϕ), the resulting metric is given by the line element:

$$\begin{aligned} \mathrm{d}s^2_{r \ll r_r} = &-\left(1 - \frac{2M}{r}\right)(1 + 2\nu_{\mathrm{Q}})\,\mathrm{d}t^2 + \frac{1 + 2\chi_{\mathrm{Q}} - 2\nu_{\mathrm{Q}}}{1 - 2M/r}\,\mathrm{d}r^2 \\ &+ (1 - 2\nu_{\mathrm{Q}})r^2\left[(1 + 2\chi_{\mathrm{Q}})\,\mathrm{d}\theta^2 + \sin^2\theta\,\mathrm{d}\phi^2\right], \end{aligned} \tag{1}$$

$$\nu_{\mathcal{Q}} \equiv \frac{\mathcal{Q}}{4}\left[r(2M-r)\sin^2\theta + 2(M-r)^2\cos^2\theta - 6M^2\right], \tag{2a}$$

$$\chi_{\mathcal{Q}} \equiv \mathcal{Q}M(M-r)\sin^2\theta, \tag{2b}$$

with $\mathcal{Q} \equiv \mathcal{M}_r/r_r^3$ representing the quadrupole perturbation parameter. It should be noted that metric (1) is valid only for $r \ll r_r$ and assumes non-compact rings, i.e. $\mathcal{M}_r \ll r_r$. Especially, it neglects all terms starting from $\mathcal{O}\left(r_r^{-4}\right)$ and $\mathcal{O}\left(\mathcal{M}_r^2\right)$.

The Hamiltonian function governing the geodesic evolution of the system is:

$$\mathcal{H} = \frac{1}{2}g^{\mu\nu}p_\mu p_\nu = -\frac{1}{2}m^2, \tag{3}$$

where m is the mass of the secondary body, while one of Hamilton's equations reads

$$\frac{\mathrm{d}p_\kappa}{\mathrm{d}\tau} = -\frac{\partial\mathcal{H}}{\partial q^\kappa} = -\frac{1}{2}g_{\mu\nu,\kappa}p^\mu p^\nu, \tag{4}$$

where τ is the proper time, and we utilised that the canonical momenta are independent of the generalised coordinates; therefore, only the metric tensor will contribute to the derivative with respect to generalised coordinates. This implies that if the metric tensor is independent of a particular generalised coordinate, the conjugate momentum associated with that coordinate is conserved and considered an integral of motion. This observation corresponds with Noether's theorem, which states that symmetries of a system give rise to the existence of integrals of motion. Furthermore, it implies the presence of a Killing vector field in the differential geometry.

The initial system exhibits four degrees of freedom; however, if we examine the form of the metric (1), we see that it does not depend on the time variable t and the azimuthal angle ϕ. The conjugate momentum associated with the time coordinate is denoted as $p_t \equiv -E$ and it has the meaning of the *total energy*, whereas the conjugate momentum related to the azimuthal angle is denoted as $p_\phi \equiv L$ and it has the meaning of a *angular momentum* (see, e.g. Misner et al., 1973). Both quantities are referenced with respect to an observer standing at infinity. These symmetries allow us to reduce our system to a two-degrees-of-freedom problem solely described by coordinates r and θ. The reduced Hamiltonian of this system takes the following form:

$$\mathcal{H} = \frac{1}{2}\left(\frac{(p_r)^2}{g_{rr}} + \frac{(p_\theta)^2}{g_{\theta\theta}} + \frac{E^2}{g_{tt}} + \frac{L^2}{g_{\phi\phi}}\right). \tag{5}$$

Because of the Liouville-Arnold theorem (Arnold, 1989), in the reduced Hamiltonian system of two degrees of freedom, the bounded motion takes place on a two-dimensional invariant torus with two fundamental frequencies. We can distinguish the nature of the motion by the ratio of these fundamental frequencies $\omega = \omega^1/\omega^2$. If ω is irrational, the motion on the torus is quasiperiodic. In this case, the quasiperiodic orbit densely covers the torus over an infinite amount of time and does not return to its initial state from where it started within a finite period. If ω is rational, the torus is called resonant, and the motion is periodic. For a detailed analysis of the resonance condition, we refer to Lukes-Gerakopoulos and Witzany (2022).

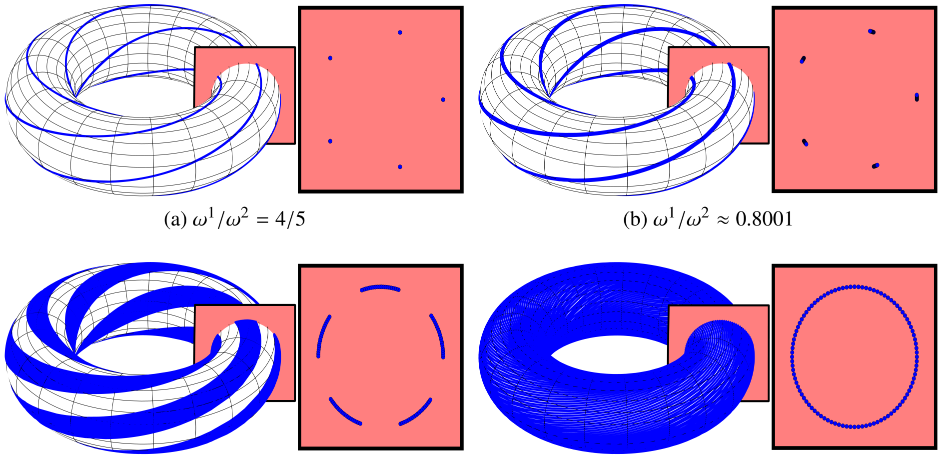

(a) $\omega^1/\omega^2 = 4/5$

(b) $\omega^1/\omega^2 \approx 0.8001$

(c) $\omega^1/\omega^2 \approx 0.801$

(d) $\omega^1/\omega^2 \approx 0.81$

Figure 1. An illustration of a resonant (a) torus and three quasiperiodic ones (b,c,d) in a two-degree of freedom system. The trajectories on the tori are depicted in blue, while the Poincaré surfaces of the section are in red. Each trajectory undergoes calculations until the motion intersects the Poincaré surface of the section for a total of 100 occurrences. The resonant trajectory, located in the upper left plot, exhibits a resonant ratio expressed as $\omega^1/\omega^2 = 4/5$, representing the fundamental frequency of the small circle over the large circle. In contrast, the remaining trajectories represent non-resonant trajectories, characterised by ratios that deviate from the resonant ratio and are of an irrational nature. Over time, the non-resonant trajectories asymptotically trace out the torus cross-section.

Let us consider an integrable system that undergoes perturbation, causing it to lose its integrability enabling chaos to occur. The transition from integrable two degrees of freedom systems to non-integrable ones is governed by two fundamental theorems: the Kolmogorov-Arnold-Moser theorem (abbreviated as the KAM theorem) and the Poincaré-Birkhoff theorem (for detailed references see Iro (2016)). According to the KAM theorem, the non-resonant torus survives for small perturbations. These tori are called KAM tori. Furthermore, Poincaré-Birkhoff's theorem states that in spaces where there is a resonant torus, an even number of periodic trajectories survive; half of them are stable and half unstable.

To study the dynamics of a two-degree-of-freedom Hamiltonian system, the symplecticity of the system allows us to reduce the 4-dimensional phase space to a two-dimensional section in it, known as *Poincaré surface of section*. In order to achieve that, we have to find a section through the tori foliation where the Hamiltonian flow is transverse. A schematic of such a section is shown in Fig. 1, where it is shown how the motion on torii is mapped on the surface of the section. In particular, Fig. 1(a) shows how a periodic orbit on a resonance torus is mapped on the surface of the section, while Figs. 1(a)-(c) show how quasiperiodic orbits on non-resonance tori are mapped on the surface of the section. To computationally create a Poincaré section, one must integrate the equations of motion and identify the constant of the motion that remains fixed, as well as the section condition that reflects

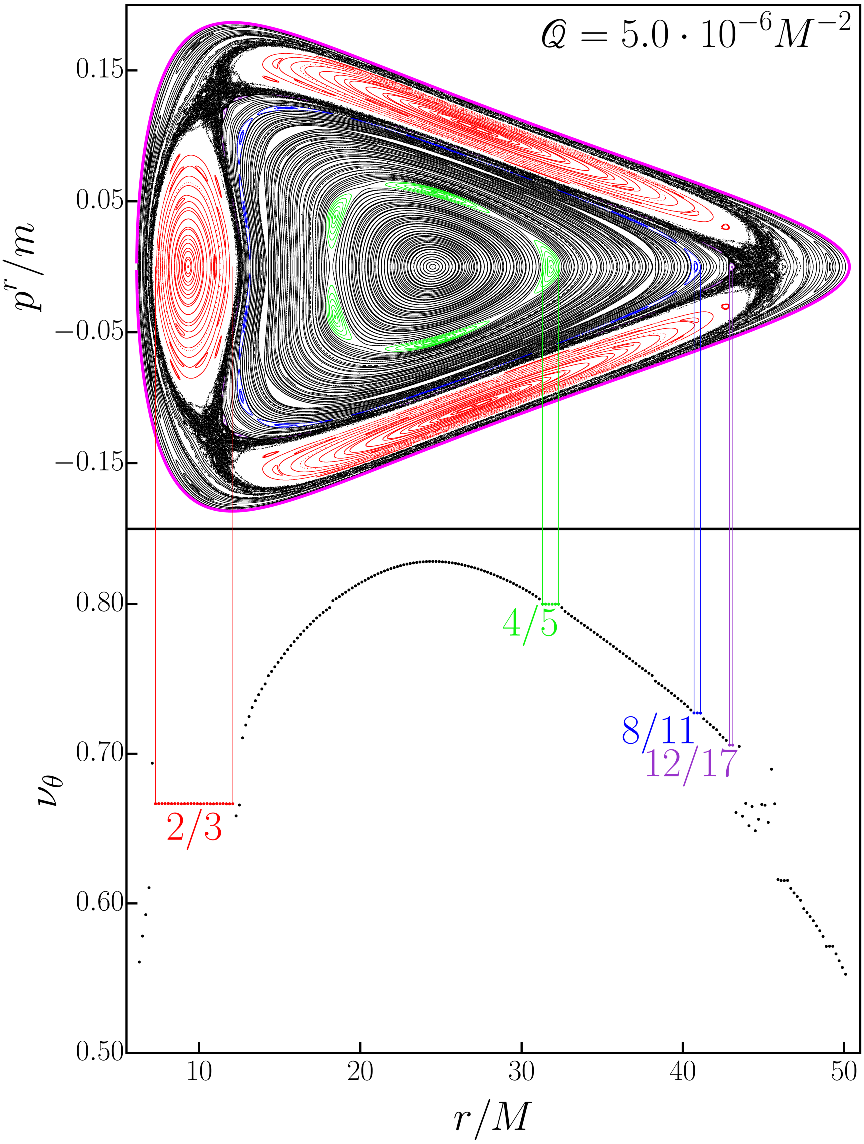

Figure 2. The top figure displays a Poincaré surface of the section, while the bottom figure shows the corresponding rotation curve computed along the $p^r/m = 0$ line. The dominant resonances are prominently marked in both figures, along with their ratios of fundamental frequencies. The parameters taken are $L = 4.0mM$, $E = 0.98m$, $\theta[0] = \pi/2$ and $r[0] \in (6.298M; 50.098M)$ with step size $0.2M$.

the symmetries of the system. Only two remaining phase-space coordinates are recorded once the trajectory passes through this section of the surface. After a sufficient number of crossings have been recorded, the results can be plotted.

The system we study exhibits reflection symmetry along the equatorial plane; thus, in order to ensure that the chosen section intersects the Hamiltonian flow perpendicularly, we set the Poincaré surface of the section as the equatorial plane (i.e. $\theta \equiv \pi/2$). Additionally, we only consider points intersecting the surface of a section from a specific direction, which we choose to be $u^\theta > 0$. Therefore, we are left with the two remaining phase coordinates, r and p^r, which we record (Fig. 2). The accessibility for the motion region on the Poincaré surface of a section is determined by Eq. (5) (see, e.g., Polcar et al., 2019). We represent the boundary curve of the accessible region as a thick magenta curve in Fig. 2.

Resonances are parts of the phase space where the non-integrable behaviour emerges. Therefore, having methods to identify these zones effectively would be advantageous. In systems with two degrees of freedom, we might take advantage of the Poincaré surface of a section to evaluate the rotation number ν_ϑ (for further details, see e.g. Lukes-Gerakopoulos and Witzany, 2022; Voglis et al., 1990). Assuming we have already produced a Poincaré surface of a section of the system, we must first distinguish the centre of the main island of stability, represented by a fixed point $\mathbf{x}_s$ on the Poincaré section, around which most invariant curves are nested. Next, we evaluate rotation angle, defined as the angle between two vectors originating from $\mathbf{x}_s$ and pointing towards two consecutive points on the Poincaré surface of section:

$$\vartheta_i := ang[(\mathbf{x}_{i+1} - \mathbf{x}_c)\,;(\mathbf{x}_i - \mathbf{x}_c)]. \tag{6}$$

The angle value spectrum has to be restricted to a proper interval so there is no discontinuity in the spectrum (Voglis et al., 1990). The *rotation number* is then obtained as the average of these rotation angles as follows:

$$\nu_\vartheta = \lim_{N\to\infty} \frac{1}{2\pi N} \sum_{i=1}^{N} \vartheta_i. \tag{7}$$

In the limit, $N \to \infty$, the calculated rotation number (7) corresponds to the ratio of two fundamental frequencies ω^1/ω^2. For finite N, the inaccuracy of calculations is approximately equal to (Voglis et al., 1990):

$$\delta_\vartheta = \frac{\Delta}{N}, \text{ where } 0 < \Delta < 1. \tag{8}$$

Hence, in order to obtain more precise values of rotation numbers, it is necessary to record more rotation angles. Typically, we have calculated the trajectory for our numerical results until 35000 rotation angles have been recorded.

The plot of rotation numbers ν_ϑ as a function of distance from the main island's centre is referred to as a *rotation curve*. The rotation curve is strictly monotonic for integrable systems as one advances away from the centre $\mathbf{x}_s$. In contrast, for perturbed non-integrable systems, the curve maintains qualitative similarity to the unperturbed one, except in the vicinity of the resonances where it exhibits significant changes. The resonance curve starts to fluctuate randomly in chaotic layers at the resonance (Fig. 2). Moreover, within the Birhoff chain, stable regions known as islands of stability appear as plateaus with constant values in the rotation curve (Fig. 2).

The *width of a resonance* is a useful measure as it can be related to the perturbation parameter ϵ driving the system away from integrability. It can be shown that the relation between the width of the resonance and the perturbation parameter of two degrees of freedom system, as provided by Lukes-Gerakopoulos and Witzany (2022) (further details are given by Arnold et al., 2007) can be expressed as:

$$w := 4\sqrt{\frac{\alpha}{\beta}}\sqrt{\epsilon}, \tag{9}$$

where w denotes the width of the resonance and α, β are positive parameters. By taking the logarithm of the equation (9), we obtain:

$$\log w(\mathcal{Q}) = \frac{1}{2}\log \epsilon(\mathcal{Q}) + \log 4\sqrt{\frac{\alpha}{\beta}}, \tag{10}$$

where we emphasise that on the right-hand side of the equation, only ϵ is dependent on $\mathcal{Q}$ as α and β are positive parameters. Therefore, by plotting the width of the resonance with respect to the quadrupole perturbation parameter on a logarithmic scale and performing the linear regression, we are able to quantify the relation between ϵ and $\mathcal{Q}$. The aforementioned linear regression takes the following form:

$$\log \frac{w(\mathcal{Q})}{M} = A \cdot \log \mathcal{Q}M^2 + B. \tag{11}$$

Thus, by comparing the equations (10) and (11), we obtain the following power law expression for the perturbation parameter:

$$\epsilon = (\mathcal{Q}M^2)^{2A}. \tag{12}$$

3 NUMERICAL EXAMPLES

In this section, we aim to employ the theoretical concepts introduced in the previous section to examine the orbital resonances in the spacetime described by the metric (1). For our numerical calculations, we kept fixed $E = 0.98m$, $L = 4.0mM$, and the initial conditions were chosen along the $p^r/m = 0$ line in the Poincaré surface of section.

Fig. 2 showcases the Poincaré section along with the corresponding rotation curve. In the particular figure, it is evident that the presence of a chaotic layer is not negligible; therefore, one must be cautious in using the widths of resonances in such cases. Namely, prominent chaotic layers, in general, tend to distort the width of resonance since we depart from the pendulum approximation used in establishing the relation 9; thus, these data points cannot be used in the linear regression analysis. Nonetheless, Fig. 2 serves as a valuable example wherein all four resonances are discernible.

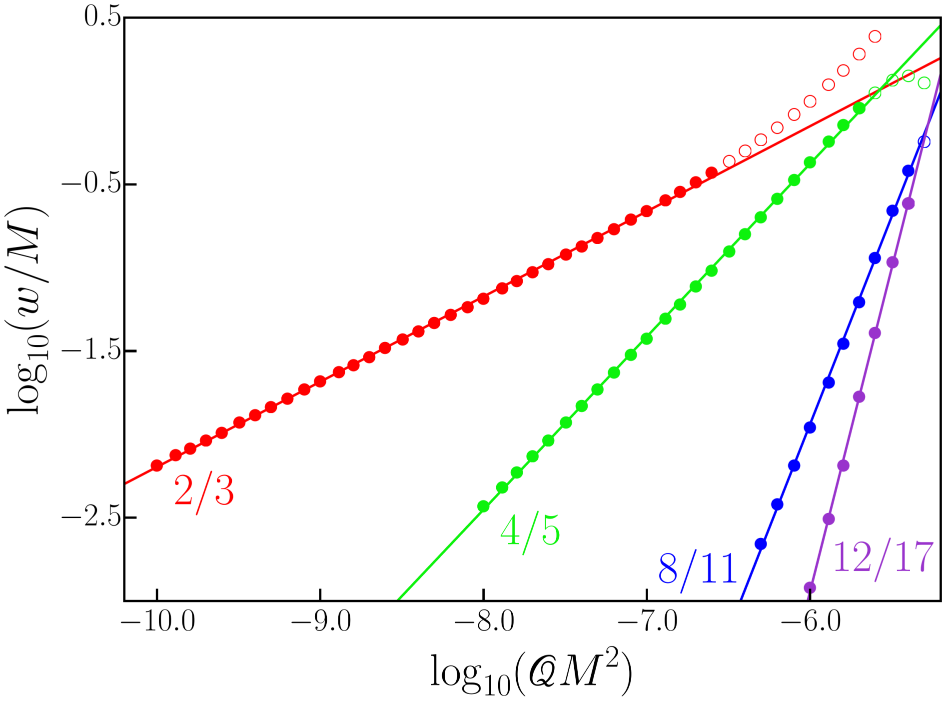

Figure 3. Logarithmic plot of widths of resonances with respect to the quadrupole perturbation parameter. The figure omits the error bars as their size is smaller than the plot symbols (the relative error was maintained below 1%).

Resonance	**Parameter A**	**Parameter B**	**Power law**
2/3	0.511 ± 0.002	2.91 ± 0.01	$\epsilon = \mathcal{Q}M^2$
4/5	1.038 ± 0.004	5.85 ± 0.03	$\epsilon = \mathcal{Q}^2 M^4$
8/11	2.491 ± 0.027	13.01 ± 0.16	$\epsilon = \mathcal{Q}^5 M^{10}$
12/17	3.880 ± 0.040	20.34 ± 0.23	$\epsilon = \mathcal{Q}^8 M^{16}$

Table 1. Results of resonance growth with respect to quadrupole perturbation parameter.

For several values of the quadrupole perturbation parameter, the widths of the four most prominent resonances were recorded. The results can be seen in Fig. 3 where a linear regression is applied. During the linear regression, certain data points were omitted (marked in a particular figure with empty circles). This exclusion is due to those points corresponding to the quadrupole perturbation parameter, where a prominent chaotic layer surrounds the particular resonance. Table 1 provides a summary of the power laws for the studied resonances. We see from the table 1 that the relation between the quadrupole perturbation parameter $\mathcal{Q}$ and the perturbation parameter ϵ is not uniform and differs for each resonance. This is not in agreement with previous studies (Lukes-Gerakopoulos and Witzany, 2022; Zelenka et al., 2020; Mukherjee et al., 2023), which indicated one single relation. Therefore, we verified that the validity of such a relation is not necessarily global and can differ from resonance to resonance in the phase space.

4 DISCUSSION

Apart from the energy and the L, in the Schwarzschild case, there is the total angular momentum constant. The total angular momentum is not constant of motion after the quadrupole perturbation is imposed. The absence of this constant drives the system away from integrability. For small perturbation values, a total angular momentum-like quantity should oscillate around an averaged value (Polcar et al., 2022; Kerachian et al., 2023). We speculate that the order $O(Q^n)$ at which the Poisson bracket of this quantity with the Hamiltonian departs from zero near each resonance should correspond to the value we are finding. However, this speculation is yet to be investigated. What we can deduce from the obtained results is that each resonance appears to be driven from a different order in the perturbation. Moreover, it appears that the value of n in $O(Q^n)$ grows as the denominator in the resonance ratio increases.

The values of the quadrupole perturbation parameter, like $\mathcal{Q} = 10^{-7}M^2$, used in this work were slightly exaggerated. Namely, by taking into account that the quadrupole perturbation parameter is defined as $\mathcal{Q} \equiv \mathcal{M}_r/r_r^3$, the radius of the gravitating ring should be, for instance, at $r_r = 100M$ and the mass of the ring should be $\mathcal{M}_r = 0.1M$, which implies that the mass of the accreting matter in the near vicinity of the primary black hole corresponds to a significant fraction of its mass. However, the findings remain interesting, even if they do not correspond to probable astrophysical scenarios, for which $\mathcal{Q}$ should be much smaller since they provide an insight into the influence of the accreting matter on the resonances. With respect to the perturbation parameter and $\mathcal{Q}$ relation, the only astrophysically relevant resonance is 2/3, rendering the remaining resonances negligible. Thus, it is possible to utilise the linear relation between the perturbation parameter and the quadrupole perturbation parameter in most regions of the phase space.

ACKNOWLEDGEMENTS

M.S. and G.L-G have been supported by the fellowship Lumina Quaeruntur No. LQ1000-32102 of the Czech Academy of Sciences. We would like to thank Vojtěch Witzany for his remarks.

REFERENCES

Amaro-Seoane, P., Audley, H., Babak, S. et al. (LISA) (2017), Laser Interferometer Space Antenna, *arXiv e-prints*, arXiv: `1702.00786`.

Arnold, V. I. (1989), *Mathematical Methods of Classical Mechanics*, Springer, New York, first edition, ISBN 978-0387968902.

Arnold, V. I., Kozlov, V. V. and Neishtadt, A. (2007), *Mathematical Aspects of Classical and Celestial Mechanics*, Encyclopaedia of Mathematical Sciences, Springer Berlin Heidelberg, ISBN 9783540489269.

Babak, S., Gair, J., Sesana, A., Barausse, E., Sopuerta, C. F., Berry, C. P. L., Berti, E., Amaro-Seoane, P., Petiteau, A. and Klein, A. (2017), Science with the space-based interferometer lisa. v. extreme mass-ratio inspirals, *Phys. Rev. D*, **95**, p. 103012, URL `https://link.aps.org/doi/10.1103/PhysRevD.95.103012`.

Berry, C. P. L., Hughes, S. A., Sopuerta, C. F., Chua, A. J. K., Heffernan, A., Holley-Bockelmann, K., Mihaylov, D. P., Miller, M. C. and Sesana, A. (2019), The unique potential of extreme mass-ratio inspirals for gravitational-wave astronomy, arXiv: `1903.03686`.

Ferreira, M. C., Macedo, C. F. B. and Cardoso, V. (2017), Orbital fingerprints of ultralight scalar fields around black holes, *Phys. Rev. D*, **96**, p. 083017, URL `https://link.aps.org/doi/10.1103/PhysRevD.96.083017`.

Genzel, R., Eisenhauer, F. and Gillessen, S. (2010), The galactic center massive black hole and nuclear star cluster, *Rev. Mod. Phys.*, **82**, pp. 3121–3195, URL `https://link.aps.org/doi/10.1103/RevModPhys.82.3121`.

Hannuksela, O. A., Ng, K. C. Y. and Li, T. G. F. (2020), Extreme dark matter tests with extreme mass ratio inspirals, *Phys. Rev. D*, **102**, p. 103022, URL `https://link.aps.org/doi/10.1103/PhysRevD.102.103022`.

Iro, H. (2016), *Modern Approach To Classical Mechanics*, World Scientific Publishing Co. Pte. Ltd., Singapore, second edition, ISBN 978-9814704113.

Kerachian, M., Polcar, L., Skoupý, V., Efthymiopoulos, C. and Lukes-Gerakopoulos, G. (2023), Action-Angle formalism for extreme mass ratio inspirals in Kerr spacetime, *arXiv e-prints*, arXiv:2301.08150, arXiv: `2301.08150`.

Kerr, R. P. (1963), Gravitational Field of a Spinning Mass as an Example of Algebraically Special Metrics, *Physical Review Letters*, **11**(5), pp. 237–238.

Lukes-Gerakopoulos, G. and Witzany, V. (2022), *Nonlinear Effects in EMRI Dynamics and Their Imprints on Gravitational Waves*, pp. 1625–1668, Springer Nature Singapore, Singapore, ISBN 978-981-16-4306-4, URL `https://doi.org/10.1007/978-981-16-4306-4_42`.

Misner, C. W., Thorne, K. S. and Wheeler, J. A. (1973), *Gravitation*, W. H. Freeman, San Francisco, ISBN 978-0-7167-0344-0, 978-0-691-17779-3.

Mukherjee, S., Kopáček, O. and Lukes-Gerakopoulos, G. (2023), Resonance crossing of a charged body in a magnetized Kerr background: An analog of extreme mass ratio inspiral, *Physical Review D*, **107**(6), 064005, arXiv: `2206.10302`.

Polcar, L., Suková, P. and Semerák, O. (2019), Free Motion around Black Holes with Disks or Rings: Between Integrability and Chaos–V, *Astrophys. J.*, **877**(1), p. 16, arXiv: `1905.07646`.

Polcar, L. c. v., Lukes-Gerakopoulos, G. and Witzany, V. c. v. (2022), Extreme mass ratio inspirals into black holes surrounded by matter, *Phys. Rev. D*, **106**, p. 044069, URL `https://link.aps.org/doi/10.1103/PhysRevD.106.044069`.

Voglis, N., Contopoulos, G. and Efthymiopoulos, C. (1990), Detection of ordered and chaotic motion using the dynamical spectra, *Impact of Modern Dynamics in Astronomy, Colloquium 172 of the*

International Astronomical Union, **73**, pp. 211–220.

Zelenka, O., Lukes-Gerakopoulos, G., Witzany, V. and Kopáček, O. (2020), Growth of resonances and chaos for a spinning test particle in the Schwarzschild background, *Phys. Rev. D*, **101**(2), p. 024037, arXiv: `1911.00414`.

Proceedings of *RAGtime 23–25*
Z. Stuchlík, G. Török, V. Karas and D. Lančová, editors, Silesian University in Opava, 2023, pp. 41–45

Aurora on pulsar planets

Miljenko Čemeljić[1,2,3,a] and Jacobo Varela[4]

[1]Research Centre for Computational Physics and Data Processing,
Institute of Physics, Silesian University in Opava, Bezručovo nám. 13,
CZ-746 01 Opava, Czech Republic,
[2]Nicolaus Copernicus Astronomical Center, Bartycka 18, 00-716,
Warszaw, Poland,
[3]Academia Sinica, Institute of Astronomy and Astrophysics,
P.O. Box 23-141, Taipei 106, Taiwan
[4]Universidad Carlos III de Madrid, Leganes 28911, Spain
[a]`miki@camk.edu.pl`

ABSTRACT
Exoplanets were long anticipated, but the discovery of the first such planet in an orbit around a pulsar came as a surprise. The only method for the detection of such planets is the precise timing method, relying on pulsars being precise clocks. In analogy with auroral emission from planets in our solar system, we suggest that planets around pulsars could also exhibit auroras. This would provide an additional method for observation of pulsar planets and conditions in the pulsar wind through emissions in visible wavelength (aurora) and cyclotron radiation in radio wavelengths. We present the first setup for magnetohydrodynamic (MHD) simulations of star-planet magnetospheric interaction for pulsar planets and the preliminary results.

Keywords: Magnetohydrodynamics – reconnection – energy dissipation – resistivity – numerical simulations – PLUTO – KORAL

1 INTRODUCTION

The first ever discovered exoplanets were found serendipitously, around the millisecond pulsar PSR 1257+12 (Wolszczan and Frail, 1992): one with $0.02M_\oplus$ and other two super-Earth planets with $4M_\oplus$ (Wolszczan, 1994). Only a 0.5% of known pulsars have a planetary companion, which could be formed around a main sequence star and later captured by a pulsar, or formed in the disk around the pulsar.

Because of their extremely stable rotation, the millisecond pulsars provide a very accurate timing method, of the order of 10^{-18} s^{-1} (Lorimer, 2008) in the arrival time of the pulses to the observer. Irregularities in the pulsar time profile are a measure of (one or more) planet masses orbiting the pulsar.

Using our setup developed for star-planet magnetospheric interaction, which was used for Solar system planets and exoplanets, we perform simulations for pulsar-planet systems.

978-80-7510-576-9

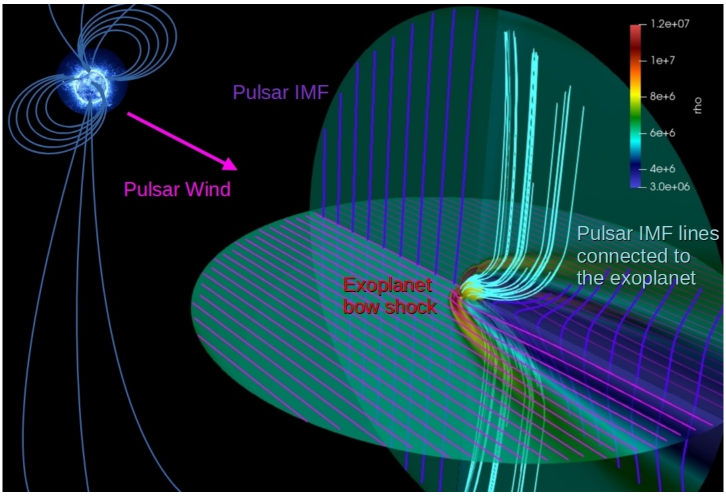

Figure 1. Pulsar-planet system in our simulation with conducting planet surface. The density is shown in a color scale and interplanetary magnetic field (IMF) with blue lines. Induced magnetic field lines at the planet dayside, which form during the piling-up of the IMF lines, are shown with cyan lines. The pulsar wind is shown with the violet lines, and its direction is indicated with an arrow. The pulsar itself is not a part of the simulation. It is assumed beyond the outer boundary of the simulation domain, which is inside the two intersecting bright circles.

Since the planetary magnetic field could be nonexistent or overwhelmed by the large pulsar field, we investigate the cases of non-magnetic planets.

2 NUMERICAL SETUP

For our simulations, we use the PLUTO code (Mignone et al., 2007). Our setup, which is almost identical to the setup presented in Varela et al. (2018), is presented in Fig. 1. The only difference stems from the assumption of non-magnetic planets, as the conducting or ferromagnetic planetary surface is set with the inner boundary specified in a slightly different, simpler way: we do not set a soft coupling region previously used atop the planet's surface to facilitate the flow towards the planet surface. The radial component of the magnetic field is set to zero, and the polar and azimuthal components are set to be smoothly absorbed by copying the values from the last active zone to the boundary ghost zone. Also, in the ferromagnetic case, the azimuthal component of the magnetic field changes the sign at the inner boundary. We neglect the anticipated relativistic nature of the pulsar wind, relegating it to future work.

We use a three-dimensional uniform spherical grid, with 128 radial cells, 48 cells in the polar angle $\theta \in [0, \pi]$ and 96 cells in the azimuthal angle $\phi \in [0, 2\pi]$. Our computational domain is between two spherical shells around the planet, representing the inner $R_{\mathrm{in}} = 1$ and outer boundary $R_{\mathrm{out}} = 20$ of the computational domain, expressed in the units of the planetary radius. We do not introduce physical resistivity so that the reconnection of the

Table 1. Parameters used in PLUTO setup file `pluto.ini` in our simulations. The pulsar wind (PW) (Speed, MagField, Dens and Temp) are setting the related initial values.

PWSpeed (cm s^{-1})	PWMagField (G)	PWDens (g cm^{-3})	PWTemp (K))
1.0×10^9	3.0	1.0×10^{-17}	2.0×10^5

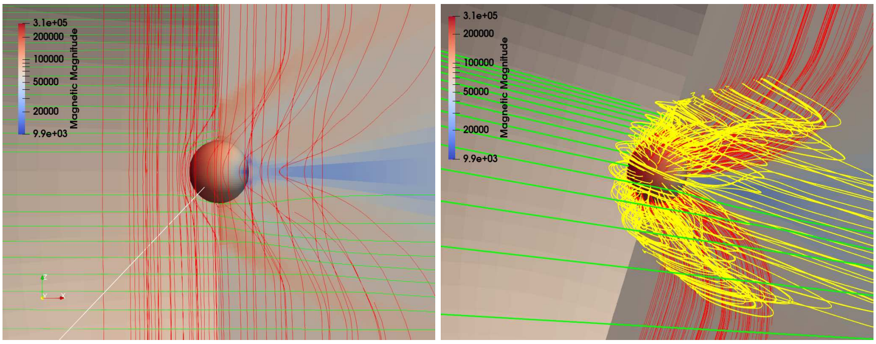

Figure 2. The results with the conductive planetary surface. *Left panel*: magnetic field strength is shown in the color grading, red solid lines represent the magnetic field lines, and green horizontal lines represent the velocity. *Right panel*: Yellow lines show the electric currents, red lines are the magnetic field lines connected to the planet, and green lines show the velocity streamlines of pulsar wind. Magnetic field magnitude is shown in color grading.

magnetic field is driven by the numerical magnetic diffusivity, evaluated from numerical experiments with the same grid resolution in a simpler setup. In Varela et al. (2018) it was estimated to $\eta \sim 10^{12}$ cm^2 s^{-1}. Parameters used in our simulations are given in the Table 1, with $R_{NS} \sim 10$ km. The `PW(Speed, MagField, Dens, Temp)` are our best estimates for the largely unknown millisecond pulsar environment. The minimal density is set to `dens_min`=0.01. The inner boundary of the system R_{inb} is set to unity.

3 RESULTS OF NUMERICAL SIMULATIONS

We present results in our simulations with pulsar planets without intrinsic planetary magnetic field. In Fig. 2, we show the result for the conducting, and in Fig. 3 for the ferromagnetic planetary surface.

In the case of conducting planetary surface, the pulsar magnetic field lines are connected with the planet surface, while in the ferromagnetic case, they envelop the planet, producing a wider spread of the strong field region atop the planet. The results are shown in the left panels of the Figs. 2 and 3.

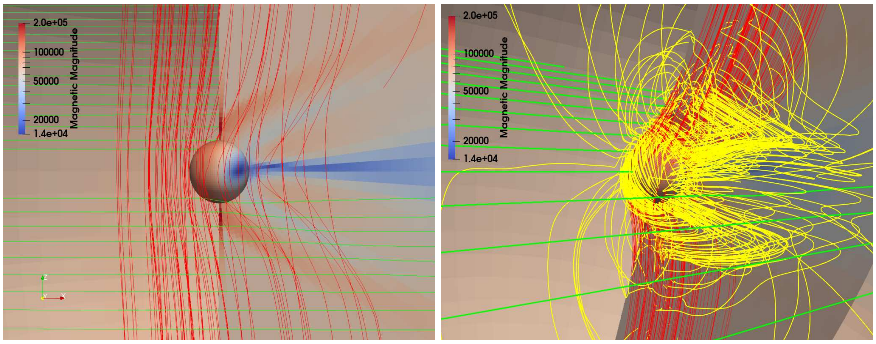

Figure 3. The results with the ferromagnetic planetary surface. The meaning of colors and lines is the same as in Fig. 2.

For the conducting planet's surface, electric current loops remain close to the planet's surface, while for the ferromagnetic planet's surface, the currents show an extended dipolar electric field structure, as shown in the right panels in the corresponding figures.

Anticipating the more violent environment, we set the magnetic field in the wind flow meeting the planet's surface to a much larger value than it would be in the Sun-like stars, and the flow velocity is also much larger.

In the previous work by Varela et al., simulations were conducted with intrinsic planetary magnetic field, so here we present the first attempt into the non-magnetic planets. Nevertheless, the magnetospheric interaction with the planetary surface occurs, as it is the obstacle in the magnetised flow with its induced field. The magnetotail is formed, but more narrow than in the cases with planetary field.

4 CONCLUSIONS

In our numerical simulations, we obtain the first results for the magnetospheric interaction of a millisecond pulsar and non-magnetized planets orbiting it. We find that in the cases of conductive and ferromagnetic planetary surface interacting with the pulsar magnetic field, the resulting flow near the planets shows different geometry of the induced electric field and currents. The strength of the induced magnetic field is different in the two cases, so the resulting radio emission from such objects would be different.

Here, we presented the concept of auroral emission from the vicinity of the millisecond pulsar planets. The plasma outflowing from the vicinity of a millisecond pulsar is expected to be lighter (electron-positron pairs instead of protons) and much faster than in the stellar wind from the Sun-like stars. In future work, we will compute the emerging radio-emission in the special-relativistic regime and assess the needed sensitivity for its observation from Earth. Such measurements would provide a new window to pulsar wind and planets in such extreme environments. It would be the first direct probe into the pulsar wind.

ACKNOWLEDGEMENTS

MČ work in Opava is funded by the Czech Science Foundation (GAČR) grant No. 21-06825X, and his work in Poland by a Polish NCN grant No. 2019/33/B/ST9/01564. JV acknowledges project 2019-T1/AMB-13648 funded by the Comunidad de Madrid. We thank ASIAA, Taipei, Taiwan and CAMK in Warsaw, Poland, for access to their Linux computer clusters (XL and CHUCK, respectively) for high-performance computations.

REFERENCES

Lorimer, D. R. (2008), Binary and Millisecond Pulsars, *Living Reviews in Relativity*, **11**(1), 8, arXiv: `0811.0762`.

Mignone, A., Bodo, G., Massaglia, S., Matsakos, T., Tesileanu, O., Zanni, C. and Ferrari, A. (2007), PLUTO: A Numerical Code for Computational Astrophysics, *The Astrophysical Journal Supplement Series*, **170**(1), pp. 228–242, arXiv: `astro-ph/0701854`.

Varela, J., Réville, V., Brun, A. S., Zarka, P. and Pantellini, F. (2018), Effect of the exoplanet magnetic field topology on its magnetospheric radio emission, *Astronomy & Astrophysics*, **616**, A182, arXiv: `1807.04417`.

Wolszczan, A. (1994), Confirmation of Earth-Mass Planets Orbiting the Millisecond Pulsar PSR B1257+12, *Science*, **264**(5158), pp. 538–542.

Wolszczan, A. and Frail, D. A. (1992), A planetary system around the millisecond pulsar PSR1257 + 12, *Nature*, **355**(6356), pp. 145–147.

Proceedings of *RAGtime 23–25*
Z. Stuchlík, G. Török, V. Karas and D. Lančová, editors, Silesian University in Opava, 2023, pp. 47–53

Energy spectrum of ultra high energy cosmic rays accelerated by rotating supermassive black holes

Martin Kološ[1,a] and Arman Tursunov[2,1,b]

[1]Institute of Physics, Silesian University in Opava,
Bezručovo nám.13, CZ-74601 Opava, Czech Republic
[2]Max Planck Institute for Radio Astronomy,
Auf dem Hügel 69, Bonn D-53121, Germany
[a]`martin.kolos@physics.slu.cz`
[b]`arman.tursunov@physics.slu.cz`

ABSTRACT
We explore the acceleration of charged particles in the combined gravitational and magnetic field around a rotating Kerr black hole. We derive the energy spectrum for ionized particles escaping to infinity, which can serve as injection spectrum for observed ultra-high energy cosmic rays.

Keywords: Black hole – resonances – particle dynamics – magnetic field

1 INTRODUCTION

Rotating black holes (BHs) are likely the largest energy reservoirs in the Universe as predicted by BH thermodynamics, while cosmic rays (CRs) are the most energetic among particles detected on Earth. Magnetic fields surrounding BHs combined with strong gravity effects, thanks to the spacetime symmetries, turn the BHs into powerful accelerators of charged particles (Kardashev, 1995). At the same time, in the age of multi-wavelength and multi-messenger astronomy, BHs and their environments have not yet been probed with CR messengers despite being observed across most of the electromagnetic spectrum, neutrino and gravitational waves.

The production and acceleration mechanisms of ultra-high-energy cosmic rays (UHECRs) of energy $> 10^{20}$eV, beyond the GZK-cutoff limit remain unclear and point to the exotic nature of the phenomena. Recent observations of extragalactic neutrinos may indicate that the source of UHECRs is an extragalactic supermassive black hole (SMBH). Tursunov et al. (2020) have shown that SMBH can efficiently accelerate UHECR protons through the extraction of rotational energy of SMBH in the presence of an external magnetic field. Applying to a larger number of SMBH candidates in the centers of active galactic nuclei (AGN) in the local universe, Tursunov et al. (2022) have found that the mean energy of primary cosmic rays in most AGN sources is roughly of or above the order of

978-80-7510-576-9

the spectral ankle – a flattening of the slope of the cosmic-ray spectrum measured around $10^{18.6}$ eV energy. Therefore, local SMBH can provide a sufficient contribution to the ankle and observed all-particle spectrum, which necessitates further analysis of the model and prediction of the energy spectrum of accelerated particles from SMBH, taking into account the dynamic surroundings of AGN.

2 ELECTROMAGNETIC FIELD AROUND ROTATING BLACK HOLE

When the magnetic field surrounding a black hole is weaker than $B \ll B_{\mathrm{G}} = 10^{19}(M_{\odot}/M)$ Gs, its contribution to background spacetime geometry is negligible, and the geometry of the rotating black hole is given the Kerr metric

$$\mathrm{d}s^2 = g_{tt}\mathrm{d}t^2 + 2g_{t\phi}\mathrm{d}t\mathrm{d}\phi + g_{\phi\phi}\mathrm{d}\phi^2 + g_{rr}\mathrm{d}r^2 + g_{\theta\theta}\mathrm{d}\theta^2, \tag{1}$$

with the nonzero components of the metric tensor taking in the standard Boyer-Lindquist coordinates the form

$$\begin{aligned} g_{tt} &= -\left(1 - \frac{2Mr}{\Sigma}\right), \quad g_{rr} = \frac{\Sigma}{\Delta}, \quad g_{\theta\theta} = \Sigma, \quad g_{t\phi} = -\frac{2Mra\sin^2\theta}{\Sigma}, \\ g_{\phi\phi} &= \left(r^2 + a^2 + \frac{2Mra^2}{\Sigma}\sin^2\theta\right)\sin^2\theta, \end{aligned} \tag{2}$$

where $\Sigma = r^2 + a^2\cos^2\theta, \quad \Delta = r^2 - 2Mr + a^2$. Here, M is the gravitational mass of the black hole, and a is its spin parameter.

Due to the stationarity and axial symmetry of the Kerr black hole spacetime, the four-vector potential of the weak magnetic field introduced by Wald (1974), which is the solution of the vacuum Maxwell equations, takes the form

$$A_t = \frac{B}{2}\left(g_{t\phi} + 2ag_{tt}\right), \quad A_\phi = \frac{B}{2}\left(g_{\phi\phi} + 2ag_{t\phi}\right). \tag{3}$$

The terms proportional to the rotation parameter a contribute to Faraday induction, which generates an electric potential producing an induced electric field (Wald, 1974). The potential difference between the horizon of a black hole and infinity takes the form

$$\Delta\varphi = \varphi_{\mathrm{H}} - \varphi_{\infty} = \frac{Q - 2aMB}{2M}. \tag{4}$$

This causes a selective accretion of charged particles into the rotating black hole. The process is similar to the field generated by the rotating conductor immersed in a magnetic field.

Thus, the expressions (3) for the non-zero covariant components of the four-vector potential have to be rewritten as (Tursunov et al., 2016)

$$A_t = \frac{B}{2}\left(g_{t\phi} + 2ag_{tt}\right) - \frac{Q}{2M}g_{tt}, \quad A_\phi = \frac{B}{2}\left(g_{\phi\phi} + 2ag_{t\phi}\right) - \frac{Q}{2M}g_{t\phi}. \tag{5}$$

The process of selective accretion for astrophysical black holes surrounded by plasma occurs in very short timescales, until the potential difference vanishes, which means that the

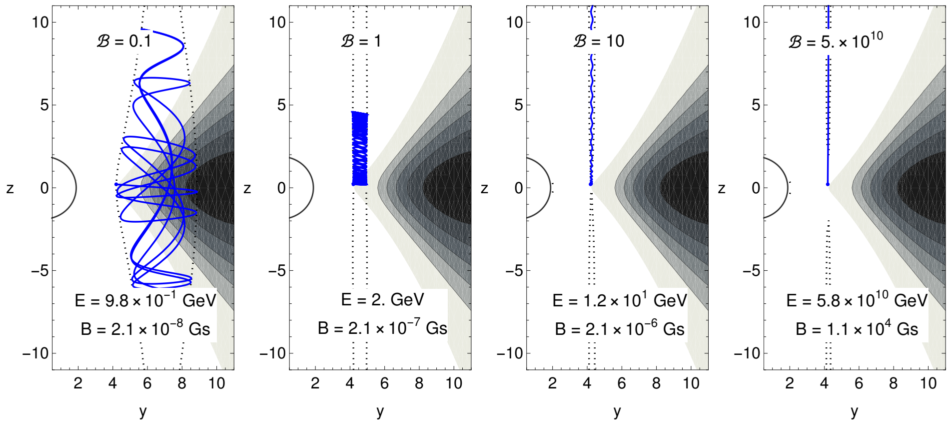

Figure 1. Examples of ionized charged particle trajectories around magnetized rotating Kerr SMBH ($M = 10^8 M_\odot, a = 0.5$). The solid blue curves represent a projection of the particle's trajectory into the x-z plane, and the dotted lines show the boundaries of the motion given by the combined effect of gravity and magnetic field. The black circle represents the BH horizon, and a cross-section of the accretion torus is plotted with different shades of grey. If the electromagnetic field influence (EFI) is small or comparable with gravity ($\mathcal{B} = 0.1$ and $\mathcal{B} = 1$), the charged particle is bounded by the gravitational potential of BH. In this case, we observe a rich, chaotic dynamic; if EFI slightly dominates over gravity ($\mathcal{B} = 10$), the particle predominantly orbits along magnetic field lines; and finally, if EFI is much stronger than gravity ($\mathcal{B} = 5 \cdot 10^{10}$), the charged particle flies away with the γ-factor proportional to the parameter $\mathcal{B}$.

black hole acquires an induced electric charge $Q_\mathrm{W} = 2aMB$. Despite the classical screening effect of plasma, it has been shown by Komissarov (2022) that the induced electric field of a black hole cannot be shielded, at least within the ergosphere. The role of this charge and its possible observational test were discussed by Zajaček et al. (2018) for the Galactic centre SMBH. The value of the Wald charge $Q_\mathrm{W} = 2MaB \leq 2M^2 B$ is

$$Q_\mathrm{W} \leq 10^{14} \left(\frac{M}{M_\odot}\right)^2 \left(\frac{B}{10^4 \mathrm{Gs}}\right) \mathrm{statC}, \tag{6}$$

which is weak in the same sense as the external magnetic field, that is, it cannot modify the background geometry of the black hole.

Despite the weakness of the electromagnetic field for spacetime curvature, in astrophysical conditions, its effect is non-negligible for the motion of charged particles, such as electrons and ions. The relative influence of magnetic and gravitational forces is governed by the specific charge of the particle (ratio of the electric charge to mass of the particle) and is of the order of (Frolov and Shoom, 2010)

$$b \sim 4.7 \times 10^7 \left(\frac{q}{e}\right) \left(\frac{m}{m_\mathrm{p}}\right)^{-1} \left(\frac{B}{10^8 \mathrm{Gs}}\right) \left(\frac{M}{10 M_\odot}\right), \tag{7}$$

where m_p is the proton mass.

3 ENERGY SPECTRUM OF IONIZED ACCELERATED PARTICLES

Black holes can accelerate particles through the Penrose process (Penrose and Floyd, 1971), where an initial particle splits in the ergosphere of the rotating Kerr black hole into two fragments. If one of the secondary particles, after splitting, attains negative energy with respect to an observer at infinity, it will inevitably be captured by the black hole. Thanks to the energy conservation law, the second fragment gets a chance to escape to infinity with energy greater than that of the initial particle. Such an energy gain occurs at the expense of the black hole's rotational energy. For neutral particles, the increase in energy per particle is limited to $\eta = 0.21$. However, the inclusion of an electromagnetic interaction into the Penrose process changes the situation dramatically (Wagh et al., 1985; Stuchlík and Kološ, 2016; Dadhich et al., 2018; Tursunov et al., 2021). In the magnetic Penrose process (MPP) (Wagh et al., 1985), the charged particles can increase their energies by the factor even exceeding $\eta = 10^{12}$ (Tursunov et al., 2020; Tursunov and Dadhich, 2019; Tursunov et al., 2022). Moreover, in contrast to the neutral version, in MPP, the acceleration zone goes far beyond the ergosphere (a region with negative energy orbits of neutral particles) to an effective ergoregion (a region with negative energy orbits of neutral particles).

In the MPP ionization process, a neutral particle 1 splits into two oppositely charged particles – 2 and 3, with charges q_2 and q_3, respectively. The conservation of the electric charge and canonical momentum gives

$$0 = q_2 + q_3 \quad \pi_{\alpha(1)} = \pi_{\alpha(2)} + \pi_{\alpha(3)}, \tag{8}$$

where $\pi_{\alpha(i)}$, $i = \{1, 2, 3\}$ denotes the canonical momentum of 1st, 2nd and 3rd particles, respectively. Due to the charge conservation, the momentum conservation from Eq. (8) takes the form

$$p_{\alpha(1)} = p_{\alpha(2)} + q_2 A_\alpha + p_{\alpha(3)} + q_3 A_\alpha = p_{\alpha(2)} + p_{\alpha(3)}. \tag{9}$$

In physical scenarios, ionized particles are much more massive than electrons, i.e., $m_2/m_3 \gg 1$, as in the case of ionization of neutral atoms. The time component of the canonical momentum gives the energy of the particle with respect to the distant observer $E = -\pi_t$. As we can see from Eq. (8), the accelerated particle is gaining energy mostly through qA_t term, and if the electromagnetic interaction is strong enough, the particle's momentum can be neglected

$$E \sim qA_t(r, \theta). \tag{10}$$

One can estimate the maximal energy of an escaping particle (for example, a proton) from supermassive BH with the realistic magnetic field

$$E_\mathrm{p} = 1.7 \times 10^{11}\,\mathrm{GeV} \left(\frac{q}{e}\right)\left(\frac{m_p}{m}\right)\left(\frac{B}{10^4\mathrm{Gs}}\right)\left(\frac{M}{10^9 M_\odot}\right)\left(\frac{a}{0.8}\right), \tag{11}$$

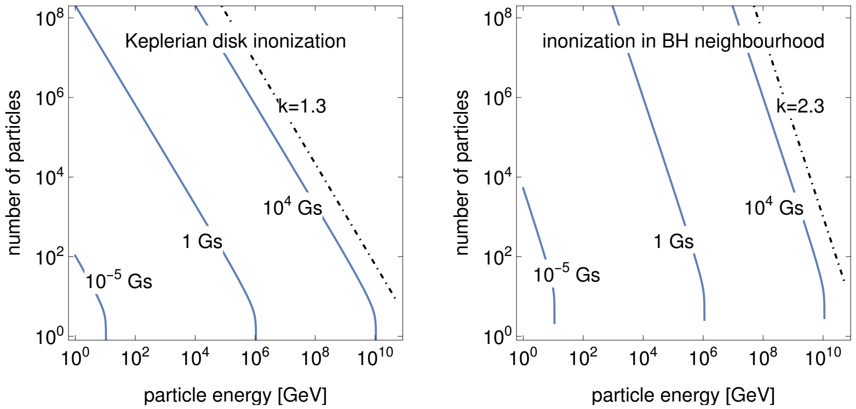

Figure 2. Distribution of accelerated particles as a function of energy for cosmic rays accelerated by SMBHs ($M = 10^8 M_{\rm sun}$) in a magnetic field with various strengths. The BH is rotating with $a = 0.5$ spin parameter, and the ionization probability is $\epsilon = 1$ for the proton. Both models for particle distribution in the Keplerian disk (left) and in the volume of the black hole's environment (right) are presented. The spectral index k is sensitive to the initial distribution of the particle. The sudden drop in the number of particles with higher energies is caused by the truncation of the particle distribution at the innermost edge of the accretion disk.

predicting energy of proton $E_{\rm p}$ exceeding 10^{11} GeV for $M \sim 10^9 M_\odot$ and $B \sim 10^4$Gs (Tursunov et al., 2022). Presented MPP acceleration scenario for BHs, belong to "one-shot" models as classified in Rieger (2022).

An example of charged particle trajectories can be found in Fig. 1, where the trajectory for ultra-high energy particles is plotted. As one can see from Eq. 11, rotating supermassive BHs can accelerate charged particles to the highest observed UHECR, or even higher. To check the validity of UHECR production through MPP, one needs to find the UHECR energy spectrum, giving the number of particles N per energy E, that particle energy spectrum $N = N(E)$ (Rieger, 2022).

The toy model for the particle energy distribution function $N(E)$ can be obtained from the analogy of a black hole as a point charge Q accelerating test particle of charge q. The electrostatic potential energy for such a system from a classical physics viewpoint is proportional to both charges and inversely proportional to the distance $E \sim qQ/r$. We assume that the total number of particles in the volume of a radius r is proportional to the number of accelerated ionized particles, so that $N \sim r^3$. One can write particle energy spectrum

$$N = N_0 E^k, \tag{12}$$

where the spectral index k is $k = 3$. For a rotating black hole in a magnetic field, a more sophisticated model can be constructed, although the spectral index has to remain in the range $k \in (1, 3)$.

Let us assume that the accretion disk of a black hole is located mostly in the equatorial plane and that the probability of neutral particle ionization is proportional to the particle density $\sigma(r)$ and the temperature profile $T(r)$ of the accretion disk. This gives

$$N(r) = \epsilon\, r^2\, \sigma(r)\, T(r), \tag{13}$$

where ϵ is a dimensional constant representing the probability of the ionization process. The energy of a charged particle after the MPP ionization process is

$$E(r) \approx qA_t(r, \pi/2) \approx -\frac{q\, 2aB}{r}, \tag{14}$$

which is an electrostatic energy between the charge q of the particle and that of the Wald charge $2aB$.

In Fig. 3, we plotted the energy spectrum of accelerated particles in the MPP for the constant density profile of the accretion disk, $\sigma(r)$=const, and for the temperature profile

$$T(r) = r^{3/4} \left(1 - \sqrt{\frac{r_{\text{in}}}{r}}\right)^{1/4}, \tag{15}$$

where r_{in} is accretion disk inner edge. As we can see, the spectral index k for particle energy spectrum from Eq. 12 is now $k = 1.33$. A more complex model with both energy profile $E = E(r, \theta)$ and particle ionization profile $N = N(r, \theta)$ as a function of r and θ is given in as preliminary results Fig. 3 (right).

We assume the number density of accelerated high energy particles to be proportional to the total number density of particles in the accretion flow. The flux of high-energy particles escaping the vicinity of a black hole can be assumed to be proportional to the accretion rate of the black hole $\dot{M}$ if the particles are accelerated at the expense of the rotational energy of the black hole.

4 CONCLUSIONS

In this contribution, we have shown that SMBH in AGN can serve as the primary UHECR source. We calculate the distribution of accelerated particles in energy spaces, estimating the initial energetic spectral index k for the MPP one-shot acceleration model in the range $k \in (1, 3)$. Our initial injection spectrum is expected to change during the propagation of particles from the source to the detectors. More specific calculations of the spectrum taking into account energy losses and their effect on the spectral index for different possible CRs sources, including SMBH at the Galactic Center, are now in preparation.

ACKNOWLEDGEMENTS

This work was supported by Czech Science Foundation Grant (GAČR) No. 23-07043S. We also thank the internal grant of Silesian University, SGS/30/2023: Dynamics of structures in strong gravomagnetic fields of compact objects modeled in the framework of Einstein or alternative theories of gravity.

REFERENCES

Dadhich, N., Tursunov, A., Ahmedov, B. and Stuchlík, Z. (2018), The distinguishing signature of magnetic Penrose process, *Monthly Notices of the Royal Astronomical Society* , **478**(1), pp. L89–L94, arXiv: `1804.09679`.

Frolov, V. P. and Shoom, A. A. (2010), Motion of charged particles near a weakly magnetized Schwarzschild black hole, *Phys. Rev. D* , **82**(8), 084034, arXiv: `1008.2985`.

Kardashev, N. S. (1995), Cosmic supercollider, *Monthly Notices of the Royal Astronomical Society* , **276**(2), pp. 515–520.

Komissarov, S. S. (2022), Electrically charged black holes and the Blandford-Znajek mechanism, *Monthly Notices of the Royal Astronomical Society* , **512**(2), pp. 2798–2805, arXiv: `2108.08161`.

Penrose, R. and Floyd, R. M. (1971), Extraction of Rotational Energy from a Black Hole, *Nature Physical Science*, **229**(6), pp. 177–179.

Rieger, F. M. (2022), Active Galactic Nuclei as Potential Sources of Ultra-High Energy Cosmic Rays, *Universe*, **8**(11), p. 607, arXiv: `2211.12202`.

Stuchlík, Z. and Kološ, M. (2016), Acceleration of the charged particles due to chaotic scattering in the combined black hole gravitational field and asymptotically uniform magnetic field, *European Physical Journal C*, **76**, 32, arXiv: `1511.02936`.

Tursunov, A. and Dadhich, N. (2019), Fifty Years of Energy Extraction from Rotating Black Hole: Revisiting Magnetic Penrose Process, *Universe*, **5**(5), p. 125, arXiv: `1905.05321`.

Tursunov, A., Juraev, B., Stuchlík, Z. and Kološ, M. (2021), Electric Penrose process: High-energy acceleration of ionized particles by nonrotating weakly charged black hole, *Phys. Rev. D* , **104**(8), 084099, arXiv: `2109.10288`.

Tursunov, A., Kološ, M. and Stuchlík, Z. (2022), Constraints on Cosmic Ray Acceleration Capabilities of Black Holes in X-ray Binaries and Active Galactic Nuclei, *Symmetry*, **14**(3), p. 482.

Tursunov, A., Stuchlík, Z. and Kološ, M. (2016), Circular orbits and related quasi-harmonic oscillatory motion of charged particles around weakly magnetized rotating black holes, *Phys. Rev. D* , **93**(8), 084012, arXiv: `1603.07264`.

Tursunov, A., Stuchlík, Z., Kološ, M., Dadhich, N. and Ahmedov, B. (2020), Supermassive Black Holes as Possible Sources of Ultrahigh-energy Cosmic Rays, *The Astrophysical Journal* , **895**(1), 14, arXiv: `2004.07907`.

Wagh, S. M., Dhurandhar, S. V. and Dadhich, N. (1985), Revival of the Penrose Process for Astrophysical Applications, *The Astrophysical Journal* , **290**, p. 12.

Wald, R. M. (1974), Black hole in a uniform magnetic field, *Phys. Rev. D* , **10**, pp. 1680–1685.

Zajaček, M., Tursunov, A., Eckart, A. and Britzen, S. (2018), On the charge of the Galactic centre black hole, *Monthly Notices of the Royal Astronomical Society* , **480**(4), pp. 4408–4423, arXiv: `1808.07327`.

Proceedings of *RAGtime 23–25*
Z. Stuchlík, G. Török, V. Karas and D. Lančová, editors, Silesian University in Opava, 2023, pp. 55–65

Signal from neutron star obscured by oscillating accretion torus

Kateřina Klimovičová[1,a] Debora Lančová[1]
and Gabriel Török[1]

[1]Research Center for Computational Physics and Data Processing,
Institute of Physics, Silesian University in Opava, Bezručovo nám. 13,
CZ-746-01 Opava, Czech Republic
[a]`katerina.klimovicova@physics.slu.cz`

ABSTRACT
X-ray fluxes of low-mass neutron star binaries reveal rapid, nearly periodic changes corresponding to frequencies in the order of hundreds of hertz. Two closely related peaks often appear in the power spectral density and are designated as twin-peak Quasi-Periodic Oscillations (QPOs). Some QPO models attribute the observed effects to the torus oscillating in the inner region of the accretion flow. Since the observed variability is very strong, oscillations of a torus can be reflected in the observed light curves either by modulation of an accretion flow and/or by a periodic obscuration of a hot region on the neutron star surface. Applying a self-consistent description of the oscillations and full relativistic ray tracing, we analyse how the obscuration effect can affect the light curve detected by a distant observer. Within the same paradigm, we also investigate a possible product of torus instability and the implied signature of the Keplerian frequency in the light curve.

Keywords: Black hole – neutron star – X–ray binary – rapid variability

1 INTRODUCTION

Low-mass X-ray binaries (LMXBs) are among the most luminous sources in the X-ray universe. X-ray satellite observations on very short timescales showed that their luminosity varies periodically (or quasi-periodically). Some of the variability has already been explained in terms of the spin of the neutron star (NS), while a complex variability posing a broad phenomenology, the so-called quasi-periodic oscillations (QPOs), remains a mystery (e.g., Van der Klis, 2006; Török et al., 2022, and references therein).

The observed flux of LMXBs can change very rapidly, and the fastest variability is attributed to two distinguished frequency peaks in the power spectral density (PSD) of the signal in the range of hundreds of hertz, sometimes reaching kHz frequencies, provided that the binary contains a NS. In this case, in contrast to the black hole (BH) system observations, the two peaks are often clearly present simultaneously, which gave them the name

978-80-7510-576-9

twin-peak QPOs (see, e.g., van der Klis, 1998; McClintock and Remillard, 2006; Motta, 2016).

In our recent paper Török et al. (submitted) (hereafter Paper I), we contribute to solving the mystery of the rapid variability of LMXBs signal manifested by the twin-peak QPOs. We follow the path outlined by the series of previous works of other authors, who suggested that the changes in flux are caused by oscillations of an accretion torus in the innermost regions of the binary, very close to the central compact object (Abramowicz and Kluźniak, 2001; Kluźniak and Abramowicz, 2001; Rezzolla et al., 2003a,b; Abramowicz and Kluźniak, 2004; Bursa et al., 2004; Montero et al., 2004; Bursa, 2005; Horák, 2005; Török et al., 2005; Schnittman and Rezzolla, 2006; Abramowicz et al., 2007; Blaes et al., 2007; Ingram and Done, 2010; Mazur et al., 2016; Parthasarathy et al., 2017; de Avellar et al., 2018; Török et al., 2022, and references therein).

Oscillations of such torus can be reflected in the observed light curves either by the modulation of the accretion flow, giving rise to changes of the source luminosity due to a loss of energy of accreted matter reaching the NS, and/or by a periodic obscuration of the hot region on the central star's surface. The hot region corresponds to the boundary layer (BL) on the surface of a temperature much higher than that of the star. The accreted material, which reaches the star's surface there, slowly spreads towards the poles, and its temperature steadily drops towards the value on the surface. In principle, the amount of the accreted material, thus the temperature and local emissivity, may depend on the distance of the accretion torus to the star. For instance, when the torus is (radially) oscillating, the emissivity should follow those oscillations, resulting in periodic changes of the flux from the BL (Paczyński, 1987; Horák, 2005).

In this work, we follow our Paper I and consider two main scenarios. First, the modulation is caused by obscuring the NS surface with a radially and vertically oscillating torus. Second, the torus oscillates radially, but the other modulation is caused by the torus instability. In addition, we also compare these two scenarios to the consideration of radiating hot spots orbiting in the inner accretion region. Our present Proceedings paper is primarily intended as supplementary material for Paper I. We present here and discuss in more detail the setup of the simulations we have performed, and, furthermore, we introduce and analyse some results that did not fit the limited scope of Paper I.

2 MODELS, SIMULATIONS, AND THEIR SETUP

To validate the modulation model introduced in Paper I and to present its effects on the observable signal, we simulate the propagation of photons in a strong gravitational field. We use an analytical approximation for the inner accretion flow structure following the "Polish doughnut" model of Jaroszyski et al. (1980).

2.1 Models

We consider the following three scenarios. The justification for their selection and related references can be found in Paper I.

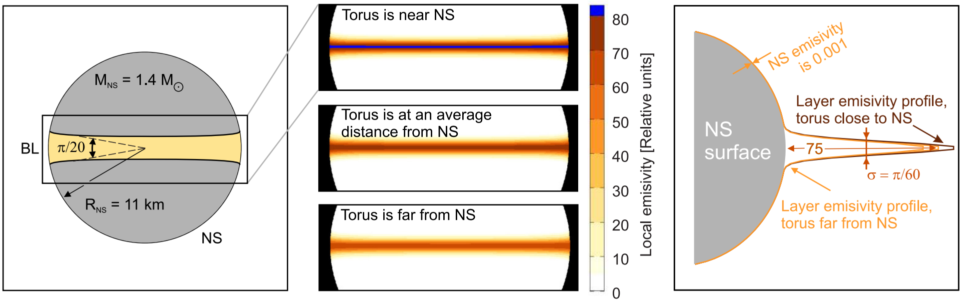

Figure 1. Setup of the BL simulations. The local emissivity of a NS and the hot BL on it. *Left:* Overall setup of our simulations. *Middle:* Maps showing the change in the BL local emissivity as the torus oscillates radially. The figure shows what a distant observer would see if relativistic changes in the photon energy were neglected (for the figure, we assume the g-factor $g = u^t_{\mathrm{observer}}/u^t_{\mathrm{emmitter}} = 1$). *Right:* Schematic profile of local emissivity of the star and BL system.

Model 1: Radially and vertically oscillating torus that periodically obscures the star's surface.

Model 2: Radially oscillating torus that is disrupted due to instabilities leading to the formation of a gap. The torus fragment orbits the NS, periodically uncovering part of its surface.

Model 3: A hot spot orbiting in the inner region of the equatorial accretion disk.

The first model considers a torus that oscillates radially and vertically and conceals the hot region of a BL on the NS's surface. This elaborate concept represents a continuation of ideas introduced in a series of papers by Abramowicz and Kluźniak (2001); Kluźniak and Abramowicz (2001); Abramowicz et al. (2007); Parthasarathy et al. (2017). The second model considers a fragmented torus as a product of instability. A gap forms within it, which orbits with the same (Keplerian) frequency as the original torus, periodically revealing the luminous BL on the surface (Török et al., 2016, 2022).

We expect that such configurations assumed within the first and second models can cause strong flux modulation with both radial and vertical (or orbital) frequencies. The third model considers a standard scenario of a hot spot orbiting within a thin accretion disk (Kluźniak et al., 1990; Karas and Bao, 1992; Stuchlík and Bao, 1992; Karas, 1999; Stella et al., 1999; Stella and Vietri, 1999). Since it is known that this model rather fails to explain the high amplitudes of QPOs, it is included merely for the sake of comparison.

To obtain light curves measured by a distant observer originating in a system with a compact object, one needs to utilise a code that calculates the propagation of light in a strong gravitational field (Cunningham and Bardeen, 1973; Karas et al., 1992; Beckwith and Done, 2005; Schnittman and Rezzolla, 2006; Dexter and Agol, 2009; Vincent et al., 2011; Chan et al., 2013; Bronzwaer et al., 2018; Prather et al., 2023). Within the context of the QPO modeling, ray-tracing was pioneered by Bursa et al. (2004); Schnittman and

Bertschinger (2004); Bursa (2005); Schnittman (2005); Schnittman et al. (2006b,a); Bakala et al. (2014, 2015); Mishra et al. (2017).

Here, we use the `LSD` relativistic ray-tracing code developed by our colleague Pavel (Bakala et al., 2015). In all examples in this contribution, except for those in Section 4, we assume the inclination of the observer, $i = 80°$, close to the equatorial plane.

2.2 Components of the system

The systems described by Models 1 – 3 consist of several components, which we describe in more detail:

Model 1: NS, BL on its surface, and an oscillating torus.

Model 2: NS, BL on its surface, and a product of torus instability.

Model 3: NS and a thin equatorial disk with a hot spot orbiting within it.

Each of the components has specific properties, which are summarised below.

NS: A spherical star with homogeneous local emissivity from the surface; in the relative units we use, the emissivity has a value of 0.001. Here, for simplicity, the NS does not rotate (see Figure 1).

BL: An equatorial region where the hot accreted material would fall on the star's surface. The local emissivity peaks at the value of 75 in relative units and decreases towards the poles to the value of the star's emissivity. Furthermore, it changes with the radial position of the nearby accretion torus centre, which reflects the accretion flow modulation by torus oscillations (see Figure 1). The four-velocity of the material within the BL at the equator corresponds to the Keplerian value of the specific angular momentum on the innermost stable circular orbit. As the material approaches the poles, it converges towards the four-velocity of the star's surface, with the same profile as the emissivity (Suleimanov and Poutanen, 2006; Gilfanov and Sunyaev, 2014). Thus, in our simplified case of a non-rotating star, the material at the pole is completely decelerated (see also the middle panel of Figure 4).

Torus: The torus configuration follows the setup developed by Bursa et al. (2004). The centre of the torus oscillates as

$$r = r_0 + \delta r \sin(\omega_{r,0}\, t)\,, \qquad z = 0 + \delta z \sin(\omega_{z,0}), \tag{1}$$

where δr and δz are the amplitudes in radial and vertical directions (in Model 2, $\delta z = 0$). Here, r_0 is the radial coordinate around which the torus oscillates and the position of the torus centre. Frequencies $\omega_{r,0}$ and $\omega_{z,0}$ correspond to the radial and vertical epicyclic frequencies of free test particles. The torus' local emissivity in our relative units is r_0/r (torus emissivity integrated over the whole surface from a distant observer is constant; see Figure 2). The four-velocity of the surface is given by the condition that the specific angular momentum is constant (see Figure 4). In Model 2, we consider a product of torus instability (e.g., Papaloizou and Pringle, 1984; Goldreich et al., 1986; Goodman

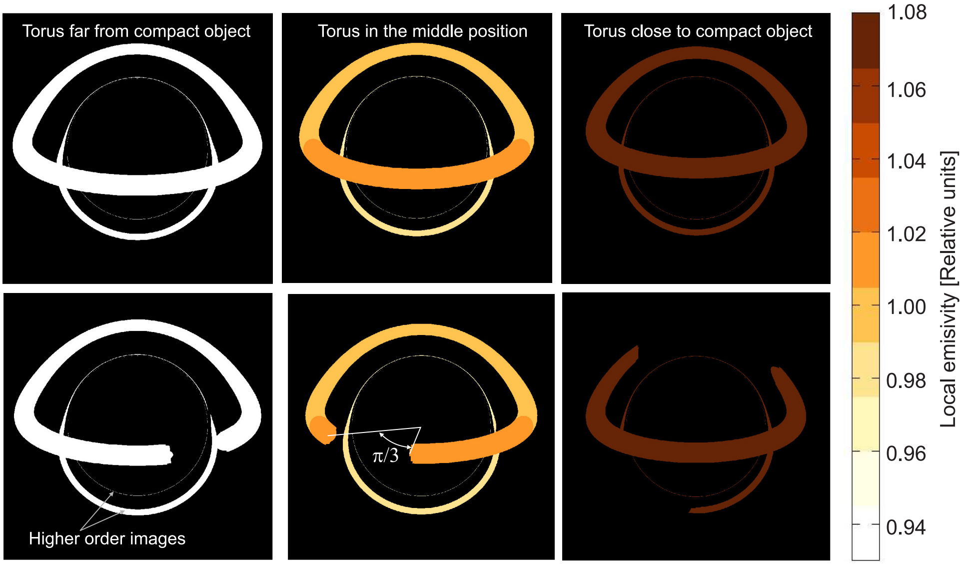

Figure 2. Local emissivity maps of the oscillating torus (without a NS star in the centre). The images show what a distant observer would see if relativistic changes in the photon energy were neglected. However, the relativistic effects on the photon trajectory are taken into account. Therefore, we see the characteristic relativistic shape of the torus with higher-order images. The local emissivity changes that occur with the radial oscillations of the torus are also visible. *Top*: Torus oscillating in the radial and vertical directions (Model 1). *Bottom*: Fragmented torus as a product of torus instability oscillating in the radial direction (Model 2).

et al., 1987), that causes fragmentation of the torus and formation of one or more gaps. We only model the case with one resulting fragment orbiting with the Keplerian frequency (see the bottom line of Figure 2).

Keplerian thin disk: An infinitesimally thin disk on Keplerian orbits in the equatorial plane, its local emissivity in relative units is proportional to $(r_{ms}/r)^3$, where $r_{ms} = 6.0M$ is the innermost stable circular orbit.

Hot spot: A spot with the emissivity of a Gaussian distribution (with $\sigma = 1/3M$) around its centre (see Figure 3). The spot oscillates in the radial direction. It has the same four-velocity as its centre.

3 RESULTS

In each case, we place the torus centre (or the spot) at the same radius, $r_0 = 6.75\,r_g$, which is frequently assumed for processes close to the ISCO. At this radius, the radial and vertical epicyclic frequencies are in a 3:1 frequency ratio (note that for a non-rotating NS,

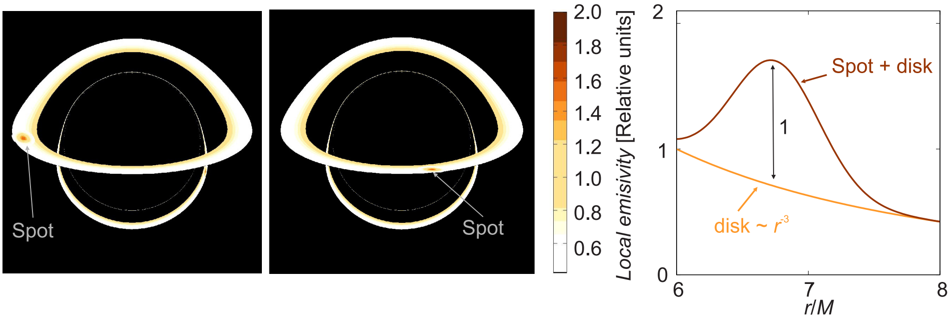

Figure 3. Local emissivity of the equatorial disk and a hot spot orbiting within the disk. *Left and Middle*: Maps of the torus emissivity at different moments during the orbital motion. The meaning is the same as in Figure 2. *Right:* Profile of the local emissivity of the spot and the equatorial disk in relative units.

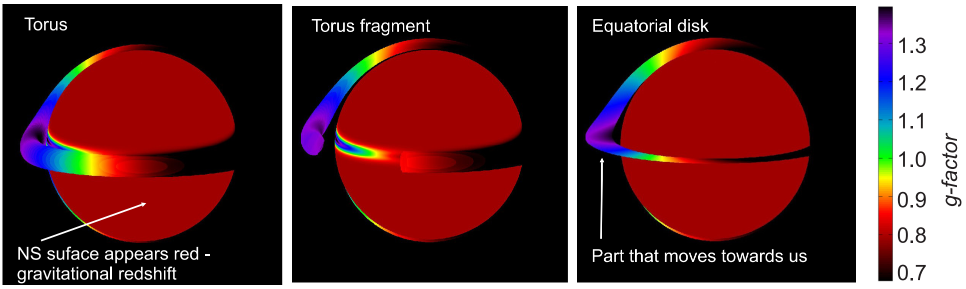

Figure 4. Maps of the g-factor illustrating the four velocities of the objects considered in our simulations. In the local system, the objects are green. The false colour scale corresponds to the human eye perception.

vertical epicyclic frequency equals the Keplerian frequency). This can have importance within the framework of QPO models considering resonances (Abramowicz et al., 2003). Nevertheless, for our simulations, the frequency ratio is not of primary importance.

For the above setup, we present the results of a thorough analysis of the images and light curves for a distant observer obtained from simulations of the previously described systems (four velocities of relevant objects are compared in Figure 4). In Figure 5, we show the synthetic light curves obtained for all models.

Apparently, it is possible to achieve significant amplitudes of variability of the measured flux using the configurations of Models 1 and 2. On the other hand, only small variability can be achieved using Model 3. The comparison of the intensity maps is illustrated in Figure 6.

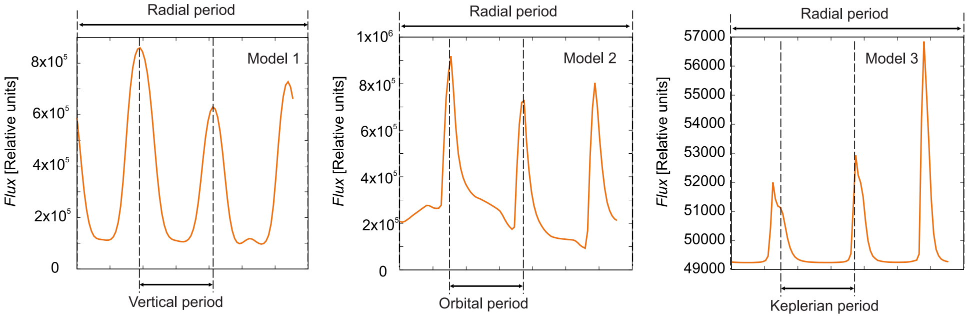

Figure 5. Light curves for all three models compared to each other, showing one period of the radial oscillations. *Left:* Model 1. *Middle:* Model 2. *Right:* Model 3. Note the different scales on the vertical axes - in the right panel, it does not start from 0. In our case, the vertical, orbital, and Keplerian periods have the same values but different physical meanings.

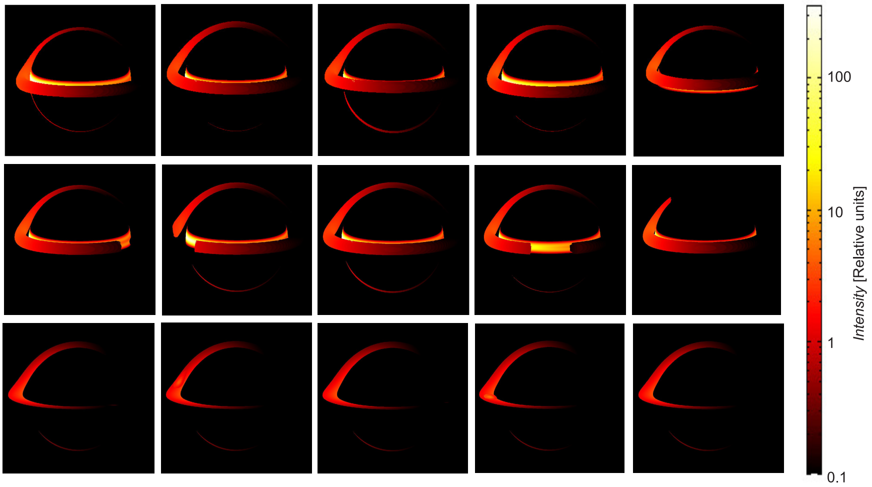

Figure 6. Intensity maps for all three models at different moments during the orbit. The configurations are the same as those corresponding to light curves presented in Figure 5. *Top*: Model 1. *Middle*: Model 2. *Bottom*: Model 3.

4 DISCUSSION AND CONCLUSIONS

This proceeding paper is intended as supplementary material to Paper I, extending the description of the models and presenting additional results that were beyond the scope of Paper I. We demonstrate how the torus, which periodically obscures the hot regions on the star, can modulate the observed light curves, leading to much higher variability amplitudes, usually absent in the other QPO models. The light curves of the two models (and the hot-spot model for comparison) are shown in Figure 5. Clearly, models incorporating the BL

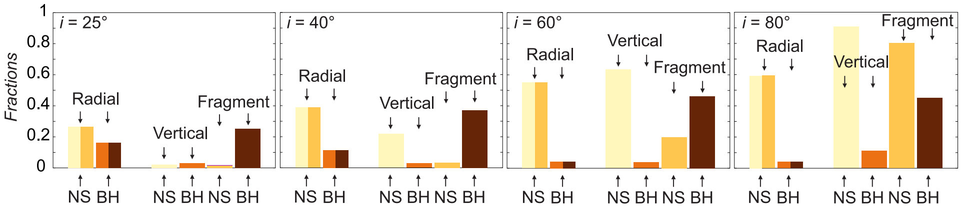

Figure 7. Fraction of fluxes affected by a given oscillatory (or orbital) motion for different observer's inclinations. Fractions correspond to the difference between the highest and lowest flux normalised to the highest flux value. The inclination angle increases from left to right.

obscuration into the modelling mechanism can potentially solve the problem of very high amplitudes of the observed QPOs.

To support our statement further, we quantified the fractions of flux affected by the individual oscillatory motions. For this purpose, we performed simulations for the radial and vertical oscillations separately. We also carried out an extra simulation for the non-oscillating but fragmented torus. The resulting fraction of fluxes affected by the given oscillatory motions for various observer's inclinations are compared in Figure 7. Furthermore, we compared the case of the luminous NS with a BL to that of a BH scenario where no radiation comes from the central object.

It is evident that a significant variability is induced in both Models 1 and 2 and almost all assumed configurations. Figure 7 also shows that the fragmented torus model (Model 2) can generate comparably high amplitudes of both QPOs also in the BH case, which the other models can reproduce only to a limited extent (see, e.g., Bursa et al., 2004).

ACKNOWLEDGEMENTS

We acknowledge the Czech Science Foundation (GAČR) grant No. 21-06825X. We also thank the internal grant of the Silesian University, SGS/31/2023.

REFERENCES

Abramowicz, M. A., Horák, J. and Kluźniak, W. (2007), Modulation of the Neutron Star Boundary Layer Luminosity by Disk Oscillations, Acta Astron., **57**, pp. 1–10.

Abramowicz, M. A., Karas, V., Kluzniak, W., Lee, W. H. and Rebusco, P. (2003), Non-Linear Resonance in Nearly Geodesic Motion in Low-Mass X-Ray Binaries, PASJ, **55**, pp. 467–466, arXiv: `astro-ph/0302183`.

Abramowicz, M. A. and Kluźniak, W. (2001), A precise determination of black hole spin in GRO J1655-40, A&A, **374**, pp. L19–L20, arXiv: `astro-ph/0105077`.

Abramowicz, M. A. and Kluźniak, W. (2004), Interpreting black hole QPOs, in P. Kaaret, F. K. Lamb and J. H. Swank, editors, *X-ray Timing 2003: Rossi and Beyond*, volume 714 of *American Institute of Physics Conference Series*, pp. 21–28, arXiv: `astro-ph/0312396`.

Bakala, P., Goluchová, K., Török, G., Šrámková, E., Abramowicz, M. A., Vincent, F. H. and Mazur, G. P. (2015), Twin peak high-frequency quasi-periodic oscillations as a spectral imprint of dual oscillation modes of accretion tori, *A&A*, **581**, A35, arXiv: `1505.06673`.

Bakala, P., Török, G., Karas, V., Dovčiak, M., Wildner, M., Wzientek, D., Šrámková, E., Abramowicz, M., Goluchová, K., Mazur, G. P. and Vincent, F. H. (2014), Power density spectra of modes of orbital motion in strongly curved space-time: obtaining the observable signal, MNRAS, **439**(2), pp. 1933–1939, arXiv: `1401.4468`.

Beckwith, K. and Done, C. (2005), Extreme gravitational lensing near rotating black holes, MNRAS, **359**(4), pp. 1217–1228, arXiv: `astro-ph/0411339`.

Blaes, O. M., Šrámková, E., Abramowicz, M. A., Kluźniak, W. and Torkelsson, U. (2007), Epicyclic Oscillations of Fluid Bodies: Newtonian Nonslender Torus, ApJ, **665**(1), pp. 642–653, arXiv: `0706.4483`.

Bronzwaer, T., Davelaar, J., Younsi, Z., Mościbrodzka, M., Falcke, H., Kramer, M. and Rezzolla, L. (2018), RAPTOR. I. Time-dependent radiative transfer in arbitrary spacetimes, A&A, **613**, A2, arXiv: `1801.10452`.

Bursa, M. (2005), Global oscillations of a fluid torus as a modulation mechanism for black-hole high-frequency QPOs, *Astronomische Nachrichten*, **326**(9), pp. 849–855, arXiv: `astro-ph/0510460`.

Bursa, M., Abramowicz, M. A., Karas, V. and Kluźniak, W. (2004), The Upper Kilohertz Quasi-periodic Oscillation: A Gravitationally Lensed Vertical Oscillation, ApJ, **617**(1), pp. L45–L48, arXiv: `astro-ph/0406586`.

Chan, C.-k., Psaltis, D. and Özel, F. (2013), GRay: A Massively Parallel GPU-based Code for Ray Tracing in Relativistic Spacetimes, ApJ, **777**(1), 13, arXiv: `1303.5057`.

Cunningham, C. T. and Bardeen, J. M. (1973), The Optical Appearance of a Star Orbiting an Extreme Kerr Black Hole, ApJ, **183**, pp. 237–264.

de Avellar, M. G. B., Porth, O., Younsi, Z. and Rezzolla, L. (2018), Kilohertz QPOs in low-mass X-ray binaries as oscillation modes of tori around neutron stars - I, MNRAS, **474**(3), pp. 3967–3975.

Dexter, J. and Agol, E. (2009), A Fast New Public Code for Computing Photon Orbits in a Kerr Spacetime, ApJ, **696**(2), pp. 1616–1629, arXiv: `0903.0620`.

Gilfanov, M. R. and Sunyaev, R. A. (2014), Radiation-dominated boundary layer between an accretion disc and the surface of a neutron star: theory and observations, *Physics Uspekhi*, **57**(4), 377-388.

Goldreich, P., Goodman, J. and Narayan, R. (1986), The stability of accretion tori. I - Long-wavelength modes of slender tori, MNRAS, **221**, pp. 339–364.

Goodman, J., Narayan, R. and Goldreich, P. (1987), The stability of accretion tori. II - Non-linear evolution to discrete planets, MNRAS, **225**, pp. 695–711.

Horák, J. (2005), A possible mechanism for QPOs modulation in neutron star sources, *Astronomische Nachrichten*, **326**(9), pp. 845–848, arXiv: `astro-ph/0511569`.

Ingram, A. and Done, C. (2010), A physical interpretation of the variability power spectral components in accreting neutron stars, MNRAS, **405**(4), pp. 2447–2452, arXiv: `0907.5485`.

Jaroszyski, M., Abramowicz, M. A. and Paczyski, B. (1980), Supercritical accretion disks around black holes, *Acta Astron.*, **30**(1), p. 134.

Karas, V. (1999), Twin Peak Separation in Sources with Kilohertz Quasi-periodic Oscillations Caused by Orbital Motion, ApJ, **526**(2), pp. 953–956.

Karas, V. and Bao, G. (1992), On the light curve of an orbiting spot., A&A, **257**, pp. 531–533.

Karas, V., Vokrouhlický, D. and Polnarev, A. G. (1992), In the vicinity of a rotating black hole: a fast numerical code for computing observational effects., MNRAS, **259**, pp. 569–575.

Kluźniak, W. and Abramowicz, M. A. (2001), Strong-Field Gravity and Orbital Resonance in Black Holes and Neutron Stars — kHz Quasi-Periodic Oscillations (QPO), *Acta Physica Polonica B*, **32**(11), p. 3605.

Kluźniak, W., Michelson, P. and Wagoner, R. V. (1990), Determining the Properties of Accretion-Gap Neutron Stars, ApJ, **358**, p. 538.

Mazur, G. P., Zanotti, O., Sądowski, A., Mishra, B. and Kluźniak, W. (2016), Oscillations of radiation pressure supported tori near black holes, MNRAS, **456**(3), pp. 3245–3252, arXiv: `1510.08810`.

McClintock, J. E. and Remillard, R. A. (2006), Black hole binaries, in *Compact stellar X-ray sources*, volume 39, pp. 157–213, Cambridge, UK: Cambridge University Press.

Mishra, B., Vincent, F. H., Manousakis, A., Fragile, P. C., Paumard, T. and Kluźniak, W. (2017), Quasi-periodic oscillations from relativistic ray-traced hydrodynamical tori, MNRAS, **467**(4), pp. 4036–4049, arXiv: `1510.07414`.

Montero, P. J., Rezzolla, L. and Yoshida, S. (2004), Oscillations of vertically integrated relativistic tori - II. Axisymmetric modes in a Kerr space-time, MNRAS, **354**(4), pp. 1040–1052, arXiv: `astro-ph/0407642`.

Motta, S. E. (2016), Quasi periodic oscillations in black hole binaries, *Astronomische Nachrichten*, **337**(4-5), p. 398, arXiv: `1603.07885`.

Paczyński, B. (1987), Possible relation between the X-ray QPO phenomenon and general relativity, Nature, **327**(6120), pp. 303–304.

Papaloizou, J. C. B. and Pringle, J. E. (1984), The dynamical stability of differentially rotating discs with constant specific angular momentum, MNRAS, **208**, pp. 721–750.

Parthasarathy, V., Kluźniak, W. and Čemeljić, M. (2017), MHD simulations of oscillating cusp-filling tori around neutron stars - missing upper kHz QPO, MNRAS, **470**(1), pp. L34–L38, arXiv: `1703.05036`.

Prather, B. S., Dexter, J., Moscibrodzka, M. and Event Horizon Telescope Collaboration (2023), Comparison of Polarized Radiative Transfer Codes Used by the EHT Collaboration, ApJ, **950**(1), 35, arXiv: `2303.12004`.

Rezzolla, L., Yoshida, S., Maccarone, T. J. and Zanotti, O. (2003a), A new simple model for high-frequency quasi-periodic oscillations in black hole candidates, MNRAS, **344**(3), pp. L37–L41, arXiv: `astro-ph/0307487`.

Rezzolla, L., Yoshida, S. and Zanotti, O. (2003b), Oscillations of vertically integrated relativistic tori - I. Axisymmetric modes in a Schwarzschild space-time, MNRAS, **344**(3), pp. 978–992, arXiv: `astro-ph/0307488`.

Schnittman, J. D. (2005), Interpreting the High-Frequency Quasi-periodic Oscillation Power Spectra of Accreting Black Holes, ApJ, **621**(2), pp. 940–950, arXiv: `astro-ph/0407179`.

Schnittman, J. D. and Bertschinger, E. (2004), The Harmonic Structure of High-Frequency Quasi-periodic Oscillations in Accreting Black Holes, ApJ, **606**(2), pp. 1098–1111, arXiv: `astro-ph/0309458`.

Schnittman, J. D., Homan, J. and Miller, J. M. (2006a), A Precessing Ring Model for Low-Frequency Quasi-periodic Oscillations, ApJ, **642**(1), pp. 420–426, arXiv: `astro-ph/0512595`.

Schnittman, J. D., Krolik, J. H. and Hawley, J. F. (2006b), Light Curves from an MHD Simulation of a Black Hole Accretion Disk, ApJ, **651**(2), pp. 1031–1048, arXiv: `astro-ph/0606615`.

Schnittman, J. D. and Rezzolla, L. (2006), Quasi-periodic Oscillations in the X-Ray Light Curves from Relativistic Tori, ApJ, **637**(2), pp. L113–L116, arXiv: `astro-ph/0506702`.

Stella, L. and Vietri, M. (1999), kHz Quasiperiodic Oscillations in Low-Mass X-Ray Binaries as Probes of General Relativity in the Strong-Field Regime, Phys. Rev. Lett., **82**(1), pp. 17–20, arXiv: `astro-ph/9812124`.

Stella, L., Vietri, M. and Morsink, S. M. (1999), Correlations in the Quasi-periodic Oscillation Frequencies of Low-Mass X-Ray Binaries and the Relativistic Precession Model, ApJ, **524**(1), pp. L63–L66, arXiv: `astro-ph/9907346`.

Stuchlík, Z. and Bao, G. (1992), Radiation from hot spots orbiting an extreme Reissner-Nordström black hole, *General Relativity and Gravitation*, **24**(9), pp. 945–957.

Suleimanov, V. and Poutanen, J. (2006), Spectra of the spreading layers on the neutron star surface and constraints on the neutron star equation of state, MNRAS, **369**(4), pp. 2036–2048, arXiv: `astro-ph/0601689`.

Török, G., Abramowicz, M. A., Kluźniak, W. and Stuchlík, Z. (2005), The orbital resonance model for twin peak kHz quasi periodic oscillations in microquasars, A&A, **436**(1), pp. 1–8.

Török, G., Goluchová, K., Horák, J., Šrámková, E., Urbanec, M., Pecháček, T. and Bakala, P. (2016), Twin peak quasi-periodic oscillations as signature of oscillating cusp torus, MNRAS, **457**(1), pp. L19–L23, arXiv: `1512.03841`.

Török, G., Klimovičová, K., Lančová, D., Matuszková, M., Šrámková, E., Urbanec, M., Čemeljić, M. and Karas, V. (submitted), Modulation mechanism of twin-peak quasi-periodic oscillations.

Török, G., Kotrlová, A., Matuszková, M., Klimovičová, K., Lančová, D., Urbancová, G. and Šrámková, E. (2022), Simple Analytic Formula Relating the Mass and Spin of Accreting Compact Objects to Their Rapid X-Ray Variability, ApJ, **929**(1), 28, arXiv: `2203.04787`.

van der Klis, M. (1998), Kilohertz quasi-periodic oscillations in low-mass x-ray binaries, *Advances in Space Research*, **22**(7), pp. 925–934, arXiv: `astro-ph/9704272`.

Van der Klis, M. (2006), Rapid x-ray variability, *in Compact stellar X-ray sources*, **39**, pp. 39–112, cambridge University Press.

Vincent, F. H., Paumard, T., Gourgoulhon, E. and Perrin, G. (2011), GYOTO: a new general relativistic ray-tracing code, *Classical and Quantum Gravity*, **28**(22), 225011, arXiv: `1109.4769`.

Proceedings of *RAGtime 23–25*
Z. Stuchlík, G. Török, V. Karas and D. Lančová, editors, Silesian University in Opava, 2023, pp. 67–74

Can extended bodies follow geodesic trajectories?

Georgios Lukes-Gerakopoulos[1,a] and Sajal Mukherjee[1,2,b]

[1] Astronomical Institute of the Czech Academy of Sciences, Boční II 1401/1a, CZ-14100 Prague, Czech Republic
[2] Department of Physics, Birla Institute of Technology and Science - Pilani, Rajasthan 333031, India
[a] `gglukes@gmail.com`
[b] `sajal.mukherjee@pilani.bits-pilani.ac.in`

ABSTRACT
We provide an extension of the analysis on whether an extended test body can follow a geodesic trajectory given by Mukherjee et al. (2022). In particular, we consider a test body in a pole-dipole-quadrupole approximation under the Ohashi-Kyrian-Semerák spin supplementary condition moving in the Schwarzschild and Kerr background. Using orbital setups under which a pole-dipole body can follow geodesic motion, we explore under which conditions this can also take place in the pole-dipole-quadrupole approximation when only the mass quadrupole is taken into account. For our analysis, we employ the assumption that the dipole contribution and the quadrupole contribution vanish independently.

Keywords: MathissonPapapetrouDixon equations – particle dynamics – black holes

1 INTRODUCTION

The framework of an extended test body moving on a curved background, which we employ, dates back to the pioneering works of Mathisson (1937) and Papapetrou (1951). A significant contribution to this framework was provided by Dixon (1970a,b, 1974), which resulted in calling the respective equation of motion the Mathisson-Papapetrou-Dixon (MPD) equations. These equations in the pole-dipole-quadrupole approximation, when only gravitational interactions are considered, read Steinhoff and Puetzfeld (2010, 2012)

$$\dot{P}^{\mu} = -\frac{1}{2}R^{\mu}{}_{\nu\alpha\beta}\mathcal{U}^{\nu}S^{\alpha\beta} - \frac{1}{6}J^{\alpha\beta\gamma\delta}\nabla^{\mu}R_{\alpha\beta\gamma\delta}, \tag{1}$$

$$\dot{S}^{\mu\nu} = 2P^{[\mu}\mathcal{U}^{\nu]} + \frac{4}{3}J^{\alpha\beta\gamma[\mu}R^{\nu]}{}_{\gamma\alpha\beta}, \tag{2}$$

where $R^{\mu}{}_{\nu\alpha\beta}$ is the Riemann tensor, $S^{\alpha\beta}$ is the spin tensor, $J^{\alpha\beta\gamma\delta}$ is the quadrupole tensor, P^{μ} is the four-momentum and $\mathcal{U}^{\mu}$ is the four-velocity, while the 'dot' defines a covariant

978-80-7510-576-9

derivative with respect to the proper time. The MPD equations do not describe the evolution of the quadrupole moment, which has to be determined by the matter structure of the body (see, e.g., Steinhoff and Puetzfeld, 2012).

It is obvious from Eq. (1) that an extended body should, in general, deviate from a geodesic trajectory even if $P^\mu || \mathcal{U}^\mu$. Note that $P^\mu || \mathcal{U}^\mu$ is not in general the case for the MPD equations. The question we tackled in Mukherjee et al. (2022) was whether these rules can have exceptions on a black hole background, i.e. can extended bodies follow geodesic trajectories? We have found some positive answers in the pole-dipole approximation but failed to do so in the pole-dipole-quadrupole in the spin-induced quadrupole case.

In the present work, we restrict our analysis to the contribution of the mass quadrupole moment $Q^{\beta\gamma}$ to the quadrupole term. Then, the quadrupole tensor reads

$$J^{\alpha\beta\gamma\delta} = -3\mathcal{V}^{[\alpha}Q^{\beta][\gamma}\mathcal{V}^{\delta]}, \tag{3}$$

where $\mathcal{V}$ is a future-oriented time-like vector, which is employed to fix the centre of the mass of the body by using the constraint

$$\mathcal{V}_\mu S^{\mu\nu} = 0. \tag{4}$$

This constraint is known in the literature as the spin supplementary condition (SSC). There are several SSCs (see, e.g., Costa et al., 2018), but in Mukherjee et al. (2022) as in this work we focus on the Ohashi-Kyrian-Semerák (OKS) one (Ohashi, 2003; Kyrian and Semerak, 2007). For this SSC, a vector $\mathcal{V}^\mu = w^\mu$ is chosen so that $\dot{w}^\mu = 0$ and $w^\mu w_\mu = -1$.

This OKS choice leads to $\dot{S}^{\mu\nu} w_\mu = 0$, $\ddot{S}^{\mu\nu} w_\mu = 0$ and all the contractions of w^μ with the higher covariant derivatives of the spin tensor are also equal to zero. Hence, by contracting Eq. (2) with w_μ leads to

$$P^\mu = \frac{1}{-w_\nu \mathcal{U}^\nu}\left[\left(-P^\gamma w_\gamma\right)\mathcal{U}^\mu + K^{\mu\delta} w_\delta\right], \tag{5}$$

where we have set $K^{\mu\nu} = 4/3\, J^{\alpha\beta\gamma[\mu} R^{\nu]}{}_{\gamma\alpha\beta}$. It is straightforward that if there is no quadrupole term, then the four-momentum and the four-velocity become parallel, which is a feature of geodesic orbits. Mukherjee et al. (2022) have shown that this feature of OKS SSC can be recovered even with the quadrupole term as long as

$$K^{\mu\gamma} w_\gamma = 0 \tag{6}$$

holds.

In the cases that $P^\mu || \mathcal{U}^\mu$, it is said that the hidden momentum vanishes, since P^μ can be split in a part parallel $P^\mu_{||}$ to $\mathcal{U}^\mu$ and to the hidden momentum part P^μ_{hid} (Filipe Costa and Natário, 2014) leading to

$$P^\mu = P^\mu_{||} + P^\mu_{\text{hid}}. \tag{7}$$

The parallel part reads

$$P^\mu_{||} = m\,\mathcal{U}^\mu, \tag{8}$$

where the mass $m := -P_\mu \mathcal{U}^\mu$. In the MPD formalism, there is also another mass defined as $\mu^2 = -P^\mu P_\mu$. Note that μ and m in general do not coincide.

Our work concerns motion in a Kerr black hole background, for which the metric tensor in the Boyer-Lindquist coordinates $\{t, r, \theta, \phi\}$ reads

$$g_{tt} = -\left(1 - \frac{2Mr}{\Sigma}\right) , \; g_{t\phi} = -\frac{2aMr\sin^2\theta}{\Sigma} , \; g_{\phi\phi} = \frac{\left(\varpi^4 - a^2\Delta\sin^2\theta\right)\sin^2\theta}{\Sigma} ,$$
$$g_{\theta\theta} = \Sigma , \; g_{rr} = \frac{\Sigma}{\Delta} , \tag{9}$$

with

$$\Sigma = r^2 + a^2\cos^2\theta , \; \Delta = \varpi^2 - 2Mr , \; \varpi^2 = r^2 + a^2 , \tag{10}$$

where M is the mass of the black hole and a corresponds to its angular momentum per mass M. By setting $a = 0$ in Kerr's metric tensor, we recover the spherically symmetric Schwarzschild black hole metric tensor. To simplify some computations in Kerr (Carter, 1968) we can employ the following tetrad field

$$e^{(0)}_\mu = \left(\sqrt{\frac{\Delta}{\Sigma}}, 0, 0, -a\sin^2\theta\sqrt{\frac{\Delta}{\Sigma}}\right), \quad e^{(1)}_\mu = \left(0, \sqrt{\frac{\Sigma}{\Delta}}, 0, 0\right),$$
$$e^{(2)}_\mu = \left(0, 0, \sqrt{\Sigma}, 0\right), \quad e^{(3)}_\mu = \left(\frac{-a\sin\theta}{\sqrt{\Sigma}}, 0, 0, \frac{r^2 + a^2}{\sqrt{\Sigma}}\sin\theta\right). \tag{11}$$

Having briefed the basic concepts and notions for our analysis. We will start our investigation with the simpler Schwarzschild case and then move to the more complex Kerr one. In both of these investigations, we make the assumption that the dipole and the quadrupole contribution vanish independently. To address a more realistic scenario, this assumption should be dropped. However, we believe that it allows an interesting insight into the problem. In the framework provided by this assumption, we can use the results of Mukherjee et al. (2022) for the pole-dipole case and then deal with the quadrupole contribution to the MPD equations. For the quadruple contribution, we first tackle the issue of whether the hidden momentum vanishes, and then we explore under which condition a geodesic motion is possible.

2 RADIAL MOTION IN THE SCHWARZSCHILD BACKGROUND

In the pole-dipole approximation, an extended body can move on a geodesic trajectory in the Schwarzschild background if it follows a radial trajectory (Mukherjee et al., 2022). The geodesic motion in this spherically symmetric background can be restricted to the equatorial plane, i.e.,

$$\mathcal{U}_t = -\tilde{E}_\mathrm{g}, \quad \mathcal{U}_r = \pm\sqrt{\tilde{E}_\mathrm{g}^2 - f\left(1 + \frac{\tilde{L}_\mathrm{z}^2}{r^2}\right)}\Big/\left(1 - \frac{2M}{r}\right), \quad \mathcal{U}_\theta = 0, \quad \mathcal{U}_\phi = \tilde{L}_\mathrm{z}, \tag{12}$$

where $\tilde{E}_{\mathrm{g}}$ and $\tilde{L}_{\mathrm{z}}$ denote the conserved specific geodesic energy and orbital angular momentum,respectively. It is obvious that for the radial motion $\tilde{L}_{\mathrm{z}} = 0$. Because of the OKS SSC, i.e. $\dot{w}^{\mu} = 0$, the radial motion implies for the polar component of w^{μ} that

$$\frac{\mathrm{d}w^{\theta}}{\mathrm{d}\tau} + \frac{\mathcal{U}^{r}}{r} w^{\theta} = 0, \tag{13}$$

i.e. $r w^{\theta}$ = constant. By assuming for simplicity that this constant is zero, we get $w^{\theta} = 0$. On a radial trajectory, the azimuthal component of w^{μ} obeys a similar equation to Eq. (13), which allows us also to have $w^{\phi} = 0$ for simplicity.

Let us now discuss whether the hidden momentum vanishes for the radial trajectory, i.e. if the Eq. (6) is satisfied. By applying $w^{\theta} = 0$ on Eq. (3) for the OKS SSC we get

$$\begin{aligned}
K^{tr} =& K^{\theta\phi} = 0, \\
K^{t\theta} =& \frac{9M}{2r^{2}\left(2M - r^{2}\right)} \left\{ w^{r} \left(Q^{\theta r} w^{t} - Q^{\theta t} w^{r} \right) + r\left(2M - r\right) w^{\phi} \left(Q^{\theta\phi} w^{t} - Q^{\theta t} w^{\phi} \right) \right\}, \\
K^{t\phi} =& \frac{9M}{2r^{2}\left(2M - r^{2}\right)} \left\{ w^{r} \left(Q^{\phi r} w^{t} - Q^{\phi t} w^{r} \right) + w^{\phi} \left(Q^{rt} w^{r} - Q^{rr} w^{t} \right) \right. \\
& \left. + r\left(r - 2M\right) Q^{\theta\theta} w^{t} w^{\phi} \right\}, \\
K^{r\theta} =& \frac{9M}{2r^{4}} \left\{ r^{3} w^{\phi} \left(Q^{\theta r} w^{\phi} - Q^{\theta\phi} w^{r} \right) + \left(2M - r\right) w^{t} \left(Q^{\theta r} w^{t} - Q^{\theta t} w^{r} \right) \right\}, \\
K^{r\phi} =& \frac{9M\left(2M - r\right)}{2r^{4}} \left\{ w^{t} \left(Q^{\phi r} w^{t} - Q^{\phi t} w^{r} \right) + w^{\phi} \left(Q^{tt} w^{r} - Q^{tr} w^{t} \right) \right\} - \frac{9Mr^{3} Q^{\theta\theta} w^{r} w^{\phi}}{2r^{4}}.
\end{aligned} \tag{14}$$

Taking the above relations into account when calculating $K^{\mu\nu} w_{\nu}$ does not allow the contraction to vanish identically. Only if we assume $w^{\phi} = 0$ along with $w^{\theta} = 0$ leads to $K^{\mu\nu} w_{\nu} = 0$. Once the latter holds, we have a vanishing hidden momentum, allowing $P^{\mu} \| \mathcal{U}^{\mu}$. Since we want the body to be on a geodesic trajectory, i.e. $\dot{\mathcal{U}}^{\mu} = 0$, then $\dot{P}^{\mu} = \dot{m}\mathcal{U}^{\mu}$. However, as we show below, we can achieve the same result without setting $w^{\phi} = 0$ under our assumption of independently vanishing dipole and quadrupole terms.

The MPD equations in the case of geodesic motion reduce to

$$\dot{m}\, \mathcal{U}^{\mu} = -\frac{1}{2} R^{\mu}{}_{\nu\kappa\lambda} \mathcal{U}^{\nu} S^{\kappa\lambda} + F^{\mu}, \tag{15}$$

$$\dot{S}^{\mu\nu} = K^{\mu\nu}, \tag{16}$$

where $F^{\mu} = -1/6\, J^{\alpha\beta\gamma\delta} \nabla^{\mu} R_{\alpha\beta\gamma\delta}$. Since on the radial trajectory for the pole-dipole the spin curvature coupling vanishes and $\dot{S}^{\mu\nu} = 0$ (Mukherjee et al., 2022), then we have that: a) $\dot{S}^{\mu\nu} = 0$ implies because of Eq. (16) that $K^{\mu\nu} = 0$ and b)

$$\dot{m}\, \mathcal{U}^{\mu} = F^{\mu}. \tag{17}$$

We see that assuming independent vanishing of the dipole and quadrupole contributions, we are led to $K^{\mu\nu} w_{\nu} = 0$ without necessarily setting $w^{\phi} = 0$.

For $K^{\mu\nu} = 0$, under the reasonable assumptions that in general $w^r \neq 0$ and $w^t \neq 0$, Eq. (14) boils down to

$$
\begin{aligned}
Q^{tr} &= \frac{1}{2w^t w^r}\left(Q^{rr}\left[w^t\right]^2 + Q^{tt}\left[w^r\right]^2\right) + \frac{rQ^{\theta\theta}}{2\left(r-2M\right)w^t w^r}\left\{-\left(r-2M\right)^2\left[w^t\right]^2 + r^2\left[w^r\right]^2\right\},\\
Q^{t\theta} &= \frac{Q^{r\theta}w^t}{w^r}, \quad Q^{\theta\phi} = \frac{Q^{r\theta}w^\phi}{w^r}, \qquad (18)\\
Q^{t\phi} &= \frac{Q^{r\phi}w^t}{w^r} + \frac{w^\phi}{2w^t\left[w^r\right]^2}\left\{Q^{tt}\left[w^r\right]^2 - Q^{rr}\left[w^t\right]^2 - \frac{rQ^{\theta\theta}\left[r^2\left(w^r\right)^2 + \left(2M-r\right)^2\left(w^t\right)^2\right]}{2M-r}\right\}.
\end{aligned}
$$

By substituting the above relations Eq. (18) into F^μ, we obtain

$$
\begin{aligned}
F^r =& \frac{3M\left[r^2\left(w^r\right)^2 - \left(r-2M\right)^2\left(w^t\right)^2\right]}{2r^4\left(w^r\right)^2}\left[\left\{Q^{rr} + \left(2M-r\right)Q^{\theta\theta}\right\}\left(w^\phi\right)^2\right.\\
&\left. + \left(Q^{\phi\phi} - Q^{\theta\theta}\right)\left(w^r\right)^2 - 2Q^{r\phi}w^r w^\phi\right], \qquad (19)
\end{aligned}
$$

and $F^t = F^\theta = F^\phi = 0$. The latter implies that $\dot{m} = 0$, which in turn implies that $F^r = 0$ resulting in the additional constraint

$$
Q^{\phi\phi} = \frac{1}{\left[w^r\right]^2}\left[Q^{\theta\theta}\left(\left[w^r\right]^2 + \left(r-2M\right)\left[w^\phi\right]^2\right) + w^\phi\left(2Q^{r\phi}w^r - Q^{rr}w^\phi\right)\right]. \qquad (20)
$$

To sum up, we have imposed geodesic motion in the Schwarzschild spacetime to a pole-dipole-quadrupole body under OKS SSC, assuming that only the mass quadrupole contributes to the quadrupole tensor. Moreover, we have assumed that the dipole and the quadrupole contributions to the MPD vanish independently. This setup led us to the constraints Eq. (18) and Eq. (20), which are coupling components of the mass quadrupole tensor $Q^{\mu\nu}$ and the components of the reference vector w^μ. The MPD equations do not prescribe an evolution equation for the quadrupole tensor and so from this point of view, there is no evolution equation for the mass quadrupole tensor. However, for the reference vector, we have $\dot{w}^\mu = 0$, hence the constraints Eq. (18) and Eq. (20) dictate the way the mass quadrupole tensor evolves under OKS SSC, if the pole-dipole-quadrupole body is set to follow a geodesic trajectory.

2.1 Equatorial motion in the Kerr background

In this section, we discuss under which conditions a pole-dipole-quadrupole body can follow an equatorial geodesic trajectory in the Kerr background. As in Section-(2), we discuss the case for which the mass quadrupole is the only component of the quadrupole moment (Eq. (3)). On the equatorial plane, Eq. (13) holds also for Kerr (Harms et al., 2016). Hence, we can set $w^\theta = 0$ for simplicity, which in turn implies that $w^{(\theta)} = 0$. The $K^{\mu\nu}$ expressed in the tetrad field frame reads

$$\begin{aligned}
K^{(t)(r)} =& K^{(\theta)(\phi)} = 0,\\
K^{(t)(\theta)} =& \frac{9M}{2r^3}\left\{w^{(r)}\left(Q^{(t)(\theta)}w^{(r)} - Q^{(r)(\theta)}w^{(t)}\right) + w^{(\phi)}\left(Q^{(\theta)(\phi)}w^{(t)} - Q^{(\theta)(t)}w^{(t)}\right)\right\},\\
K^{(t)(\phi)} =& -\frac{9M}{2r^3}\left\{w^{(r)}\left(Q^{(r)(\phi)}w^{(t)} - Q^{(t)(\phi)}w^{(r)}\right) + w^{(\phi)}\left(Q^{(t)(r)}w^{(r)} - Q^{(r)(r)}w^{(t)}\right)\right.\\
&\left.+Q^{(\theta)(\theta)}w^{(t)}w^{(\phi)}\right\},\\
K^{(r)(\theta)} =& \frac{9M}{2r^3}\left\{w^{(t)}\left(Q^{(t)(\theta)}w^{(r)} - Q^{(r)(\theta)}w^{(t)}\right) + w^{(\phi)}\left(Q^{(\theta)(\phi)}w^{(r)} - Q^{(r)(\theta)}w^{(\phi)}\right)\right\},\\
K^{(r)(\phi)} =& -\frac{9M}{2r^3}\left\{w^{(t)}\left(Q^{(r)(\phi)}w^{(t)} - Q^{(t)(\phi)}w^{(t)}\right) + w^{(\phi)}\left(Q^{(t)(t)}w^{(r)} - Q^{(t)(r)}w^{(t)}\right)\right.\\
&\left.+Q^{(\theta)(\theta)}w^{(r)}w^{(\phi)}\right\}.
\end{aligned} \tag{21}$$

The above equations imply that on the equatorial plane $K^{(\mu\nu)}w_{(\nu)}$ does not vanish if we just set $w^{(\theta)} = 0$, we need to set also $w^{(\phi)} = 0$ to achieve it. However, since Mukherjee et al. (2022) showed that the spin curvature coupling for a pole-dipole body vanishes for equatorial trajectories satisfying the relation $\tilde{L}_z = a\tilde{E}_g$, by following the same procedure as in Section-(2), i.e. by assuming that the dipole and quadrupole contribution vanishes independently, we end up with $K^{(\mu)(\nu)} = 0$. This results in $K^{(\mu)(\nu)}w_{(\nu)} = 0$ and Eq. (21) provides the following relations between the components of the quadrupole moment tensor:

$$\begin{aligned}
Q^{(t)(r)} =& \frac{Q^{(r)(r)}\left[w^{(t)}\right]^2 + Q^{(t)(t)}\left[w^{(r)}\right]^2 + Q^{(\theta)(\theta)}\left(-\left[w^{(t)}\right]^2 + \left[w^{(r)}\right]^2\right)}{2w^{(t)}w^{(r)}},\\
Q^{(t)(\theta)} =& \frac{Q^{(r)(\theta)}w^{(t)}}{w^{(r)}}, \quad Q^{(\theta)(\phi)} = \frac{Q^{(r)(\theta)}w^{(\phi)}}{w^{(r)}},\\
Q^{(t)(\phi)} =& \frac{Q^{(r)(\phi)}w^{(t)}}{w^{(r)}} + \frac{w^{(\phi)}}{2w^{(t)}[w^{(r)}]^2}\left\{Q^{(t)(t)}\left[w^{(r)}\right]^2 - Q^{(r)(r)}\left[w^{(t)}\right]^2\right.\\
&\left.+Q^{(\theta)(\theta)}\left(\left[w^{(t)}\right]^2 + \left[w^{(r)}\right]^2\right)\right\}.
\end{aligned} \tag{22}$$

If we now substitute the above relations into $F^{(\mu)}$, we find that

$$\begin{aligned}
F^{(r)} =& \frac{9M\sqrt{\Delta}}{r^5\left[w^{(r)}\right]^2}\left(\left[w^{(t)}\right]^2 - \left[w^{(r)}\right]^2\right)\left[Q^{(\theta)(\theta)}\left(\left[w^{(r)}\right]^2 + \left[w^{(\phi)}\right]^2\right)\right.\\
&\left.+w^{(\phi)}\left(2Q^{(r)(\phi)}w^{(r)} - Q^{(r)(r)}w^{(\phi)}\right) - Q^{(\phi)(\phi)}\left[w^{(r)}\right]^2\right]
\end{aligned}$$

and $F^{(t)} = F^{(\theta)} = F^{(\phi)} = 0$. The latter result implies because of Eq. (17) that $\dot{m} = 0$ and hence, from $F(r) = 0$, we obtain the following relation

$$Q^{(\phi)(\phi)} = \frac{1}{\left[w^{(r)}\right]^2}\left[Q^{(\theta)(\theta)}\left(\left[w^{(r)}\right]^2 + \left[w^{(\phi)}\right]^2\right) + w^{(\phi)}\left(2Q^{(r)(\phi)}w^{(r)} - Q^{(r)(r)}w^{(\phi)}\right)\right]. \tag{23}$$

The interpretation we give to the constraints Eq. (22) is the same as in Section-(2). Namely, in order for the pole-dipole-quadrupole body to follow a geodesic trajectory the parallel transported along the geodesic reference vector $w^{(\mu)}$ has to dictate the evolution of the mass quadrupole through these constraints.

3 CONCLUSIONS

Using trajectories of the pole-dipole body that coincide with geodesics on a black hole background, we explored under which condition a pole-dipole-quadrupole body obeying OKS SSC can follow these trajectories as well when the mass quadrupole tensor is the only component of the quadrupole tensor. To achieve these conditions, we have used the not-so-realistic assumption that the dipole and quadrupole contributions to the MPD vanish independently. We showed that there are constraints between the components of the mass quadrupole tensor and the reference vector w^{μ}, which have to be obeyed in order for the body to follow the aforementioned trajectories. Since the reference vector is parallel transported along a geodesic, these constraints, in a sense, substitute the missing evolution equations for the quadrupole moment from the MPD equations.

ACKNOWLEDGEMENTS

G.L.-G. and S.M. have been supported by the fellowship Lumina Quaeruntur No. LQ100032102 of the Czech Academy of Sciences.

REFERENCES

Carter, B. (1968), Hamilton-jacobi and schrodinger separable solutions of einsteins equations, *Communications in Mathematical Physics*, **10**, pp. 280–310.

Costa, L. F. O., Lukes-Gerakopoulos, G. and Semerák, O. (2018), Spinning particles in general relativity: Momentum-velocity relation for the Mathisson-Pirani spin condition, *Phys. Rev.*, **D97**(8), p. 084023, arXiv: `1712.07281`.

Dixon, W. G. (1970a), Dynamics of extended bodies in general relativity-ii. moments of the charge-current vector, *Proceedings of the Royal Society of London. A. Mathematical and Physical Sciences*, **319**(1539), pp. 509–547.

Dixon, W. G. (1970b), Dynamics of extended bodies in general relativity-ii. moments of the charge-current vector, *Proceedings of the Royal Society of London. A. Mathematical and Physical Sciences*, **319**(1539), pp. 509–547.

Dixon, W. G. (1974), Dynamics of extended bodies in general relativity iii. equations of motion, *Philosophical Transactions of the Royal Society of London. Series A, Mathematical and Physical Sciences*, **277**(1264), pp. 59–119.

Filipe Costa, L. and Natário, J. (2014), Center of mass, spin supplementary conditions, and the momentum of spinning particles, *arXiv e-prints*, pp. arXiv–1410.

Harms, E., Lukes-Gerakopoulos, G., Bernuzzi, S. and Nagar, A. (2016), Spinning test body orbiting around a Schwarzschild black hole: Circular dynamics and gravitational-wave fluxes, *Phys. Rev. D*, **94**(10), 104010, arXiv: `1609.00356`.

Kyrian, K. and Semerak, O. (2007), Spinning test particles in a Kerr field, *Mon. Not. Roy. Astron. Soc.*, **382**, p. 1922.

Mathisson, M. (1937), Neue mechanik materieller systemes, *Acta Phys. Polon.*, **6**, pp. 163–2900.

Mukherjee, S., Lukes-Gerakopoulos, G. and Nayak, R. K. (2022), Extended bodies moving on geodesic trajectories, *General Relativity and Gravitation*, **54**(9), 113, arXiv: `1907.05659`.

Ohashi, A. (2003), Multipole particle in relativity, *Phys.Rev. D*, **68**(4), 044009, arXiv: `gr-qc/0306062`.

Papapetrou, A. (1951), Spinning test particles in general relativity. 1., *Proc. Roy. Soc. Lond.*, **A209**, pp. 248–258.

Steinhoff, J. and Puetzfeld, D. (2010), Multipolar equations of motion for extended test bodies in General Relativity, *Phys. Rev.*, **D81**, p. 044019, arXiv: `0909.3756`.

Steinhoff, J. and Puetzfeld, D. (2012), Influence of internal structure on the motion of test bodies in extreme mass ratio situations, *Phys. Rev.*, **D86**, p. 044033, arXiv: `1205.3926`.

Proceedings of *RAGtime 23–25*
Z. Stuchlík, G. Török, V. Karas and D. Lančová, editors, Silesian University in Opava, 2023, pp. 75–81

On Reflection of Torus in the Kerr "Mirror"

Jan Schee,[1,a] Sudipta Hensh[2,b] and Dmitriy Ovchinnikov[1,c]

[1]Research Centre for Theoretical Physics and Astrophysics, Institute of Physics, Silesian University in Opava, Bezručovo nám. 13, CZ-746 01 Opava, Czech Republic
[2]Theoretical Astrophysics, Department of Earth and Space Science, Graduate School of Science, Osaka University, 1-1 Machikaneyama, Toyonaka, Osaka 560-0043, Japan
[a]`jan.schee@physics.slu.cz`
[b]`hensh@astro-osaka.jp,sudiptahensh2009@gmail.com`
[c]`uzdmitriy91@gmail.com`

ABSTRACT

We investigate the effect of a reflective firewall surrounding the Kerr black hole. For a perfect fluid torus model, we construct a specific intensity map and corresponding specific intensity profile for impact parameter $\beta = 0$. We show that the "mirror" creates additional multi-ring structures in the image area below the photon orbit. We quantitatively show this effect in terms of the profile of the specific intensity $I_{\nu_0}(\alpha,\beta = 0)$ and show that the visibility of this multi-ring structure depends on the reflection efficiency of the mirror.

Keywords: Kerr black-hole – perfect fluid torus – raytracing – radiative transfer equation

1 INTRODUCTION

In the late '70s, Stephen Hawking's semi-classical treatment of black hole evaporation (Hawking, 1975) showed that black holes do radiate, which raised the still unresolved issue of so-called black hole information loss problem (Hawking, 1976). It exposes the conflict between quantum theory and general relativity. Gauge/gravity duality gives evidence that all information swallowed by a black hole is carried away by Hawking radiation. Now, it is believed that an external observer sees this information emitted by complex dynamical processes in close vicinity of the horizon, while the in-falling observer sees nothing special there. Almhein, Marolf, Polchinski, and Sully (AMPS) pointed out that the local quantum gravity, unitarity and "no drama" (assumption in-falling observer sees nothing special at the horizon) cannot be consistent with each other (Almheiri et al., 2013). They suggest giving up the "no drama" assumption, replacing it with the assumption that an in-falling observer should be terminated when hitting the so-called firewall. It is usually expected that firewalls lie on the black hole event horizons, however, in quantum mechanics, the boundaries are blurry, and the position of the horizon is uncertain up to fluctuations of the order of Planck length. In fact, a firewall may lie slightly inside the event horizons. In this case, it will fall

978-80-7510-576-9

down to physical singularity faster than the black hole size can shrink. However, it is supposed that a new firewall will be dynamically created on each fast-scrambling timescale. If the firewall lies inside of the horizon, it will be undetectable if one assumes that a firewall's location is determined by the past history of the Hawking evaporating black hole spacetime and is near where the event horizon would be if the evaporation rate were smooth, without quantum fluctuations. One can then show that quantum fluctuations of the evaporation rate in the future can migrate the event horizon to the inside of the firewall location and make the firewall naked and possibly detectable (Chen et al., 2016).

In this short contribution, we discuss the possible effect of reflecting mirror, whose existence is motivated by the firewall hypothesis, on the optical effects associated with the radiation emission of marginally stable torus orbiting central body generating Kerr spacetime with a horizon covered by the firewall (mirror). We start by introducing the mathematical formulation of the model. We present simulation results and make concluding remarks on calculated results.

2 THE MODEL

The gravitational field of a rotating compact object is modeled by Kerr spacetime defined by the dimensionless spin parameter $|a| \leq 1$. The mass of the black hole M is set to unity in what follows unless stated explicitly. In the Boyer-Lindquist coordinates (t, r, θ, ϕ) it takes the usual form (Kerr, 1963; Bardeen et al., 1972)

$$\mathrm{d}s^2 = -\left(1 - \frac{2r}{\Sigma}\right)\mathrm{d}t^2 + \frac{\Sigma}{\Delta}\mathrm{d}r^2 + \Sigma\mathrm{d}\theta^2 + \frac{A\ \sin^2\theta}{\Sigma}\mathrm{d}\phi^2 - \frac{4a\,r\ \sin^2\theta}{\Sigma}\mathrm{d}t\mathrm{d}\phi, \tag{1}$$

where is $\Sigma = r^2 + a^2\cos^2\theta$, $\Delta \equiv r^2 - 2r + a^2$, and $A = (r^2 + a^2)^2 - a^2\Delta\ \sin^2\theta$. The coordinate singularity, following from $\Delta = 0$, reveals the existence of the event horizon located at

$$r_h = 1 + \sqrt{1 - a^2}. \tag{2}$$

We envelope it with a reflective mirror that reflects infalling radiation with efficiency $0 \leq \eta \leq 1$, and we call it a "firewall". The firewall is located at the spacelike surface, orthogonal to $\partial/\partial r$ vector. The radius of that surface is

$$r_f \equiv r_h\,(1 + \epsilon)\,, \tag{3}$$

where is the parameter $\epsilon > 0$.

The source of the radiation is perfect fluid, marginally stable torus. The pressure and density equipotential surface coincides with the potential (Kozłowski et al., 1978)

$$W\,(r, \theta) = \frac{1}{2}\log\left\{\frac{\Delta[a^2\,(1 + \cos 2\theta) + 2r^2]^2\sin^2\theta}{4\Sigma\left[l_d^2\left(\Delta - a^2\sin^2\theta\right) - \sin^2\theta\,(A - 4a\,l_d\,r)\right]}\right\}, \tag{4}$$

where $l_d = const$ is the fluid angular momentum per unit mass. An element of the torus at given coordinates (r, θ) orbits the center with angular velocity (Kozłowski et al., 1978)

$$\Omega\,(r, \theta) = \frac{\left(2ar\ \sin^\theta + a^2 l_d\ \cos^2\theta\right) + l_d\,(r - 2)\,r}{\sin^2\theta\left[(A - a^2\Delta\cos^2\theta)\sin^2\theta - 2al_d\,r\right]}. \tag{5}$$

Now, the outer surface of the torus is determined by $W(r,\theta) = W_0$. We assume that the specific emissivity profiles also coincide with equipotential surfaces of constant W, and we specify it as

$$j_\nu(r,\theta) \equiv j_0 \exp\left[-\frac{1}{\sigma^2}\left(\frac{W - W_c}{W_0 - W_c}\right)\right] \text{ for } W < W_0 \text{ and 0 elsewhere.} \tag{6}$$

We introduced, here, the value of $W = W_c$ corresponding to the highest pressure/density being the local minimum of W.

The radiation follows null geodesics, identified by impact parameters l and q, in the Kerr spacetime. We divide the integration into two parts. First, there is a radial turning, we integrate the system of ordinary differential equations (Schee et al., 2023)

$$\frac{\mathrm{d}^2 u}{\mathrm{d}\lambda^2} = \frac{1}{2\Sigma^2}\left(\frac{\mathrm{d}U}{\mathrm{d}u} - 2\Sigma\frac{\mathrm{d}\Sigma}{\mathrm{d}\lambda}k^u\right), \tag{7}$$

$$\frac{\mathrm{d}^2 m}{\mathrm{d}\lambda^2} = \frac{1}{2\Sigma^2}\left(\frac{\mathrm{d}M}{\mathrm{d}m} - 2\Sigma\frac{\mathrm{d}\Sigma}{\mathrm{d}\lambda}k^m\right), \tag{8}$$

$$\frac{\mathrm{d}I_{\nu o}}{\mathrm{d}\lambda} = g^2\, j_\nu. \tag{9}$$

Second, there is no turning point, a photon heads toward the collision with the “firewall”, and we solve the set of differential equations (Schee et al., 2023)

$$\frac{\mathrm{d}^2 m}{\mathrm{d}u^2} = \frac{1}{2U^2}\left(\frac{\mathrm{d}M}{\mathrm{d}m} - U\frac{\mathrm{d}U}{\mathrm{d}u}\frac{\mathrm{d}m}{\mathrm{d}u}\right), \tag{10}$$

$$\frac{\mathrm{d}I_{\nu o}}{\mathrm{d}u} = \frac{1}{k^u}g^2\, j_\nu. \tag{11}$$

Here we introduced effective potentials $U \equiv 1 + u^2(a^2 - l^2 - q + u(2((a-l)^2 + q) - a^2 q u))$ and $M \equiv q + m^2(a^2 - l^2 - q - a^2 m^2)$ and new coordinates $u \equiv 1/r$ and $m \equiv \cos(\theta)$ and $k^u = \mathrm{d}u/\mathrm{d}\lambda$. The frequency shift, g, of photon emitted at particular fluid element of torus reads (Fanton et al., 1997)

$$g = \frac{\sqrt{1 - 2r(1 - a\Omega\sin^2\theta)^2/\Sigma - (r^2 + a^2)\Omega^2\sin^2\theta}}{1 - l\Omega}. \tag{12}$$

In the no-turning point case, the photon hits the firewall and is reflected. We reflect that photon in locally non-rotating frames (LNRF) in such a way that $k_r^{(0)} = k_i^{(0)}$, $k_r^{(1)} = -k_i^{(1)}$, $k_r^{(2)} = k_i^{(2)}$, and $k_r^{(3)} = k_i^{(3)}$; here the subscripts r and i represents the tetrad before and after reflection respectively. Now, the transformation of photon 4-momentum components from LNRF to coordinate frame reads $k^{(a)} = \Lambda^{(a)}_{\mu} k^{\mu}$, in particular $k^{(1)} = \Lambda^{(1)}_{r}\, k^{r}$ and therefore we obtain the reflection in terms of components relative to coordinate basis in the form $k_r^t = k_i^t$, $k_r^r = -k_i^r$, $k_r^\theta = k_i^\theta$, and $k_r^\phi = k_i^\phi$.

3 SIMULATION PARAMETERS AND RESULTS

We choose to illustrate the effect of the firewall on the specific intensity map of a marginally stable torus with the outer surface $W(r,\theta) = W_0 = -0.05$, angular momentum

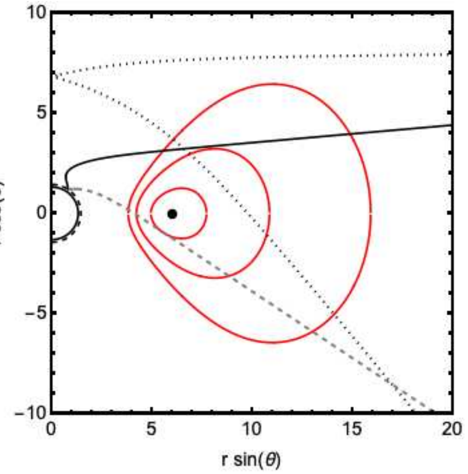

Figure 1. Meridional cross-section of the torus (red equipotential curves), firewall (black thick dashed line), ray with a turning point (black dotted line), and ray with no turning point (impacting segment dashed line and reflected segment black solid line).

$l_d = 3$ orbiting the Kerr black hole with spin parameter $a = 0.95$. The meridional cross-section of this configuration is in Fig. 1. The projection plane coordinates ranges are $(\alpha,\beta) = ([-20M, 20M], [-20M, 20M])$. Observer is located at $(u_o, \theta_o) = (10^{-4}M^{-1}, 15°)$, $(10^{-4}M^{-1}, 45°)$, and $(10^{-4}M^{-1}, 80°)$. For each point (α,β) we determine impact parameters (l, q) from formulas $l = \alpha\sqrt{1-m_o^2}$ and $q = \beta^2 + m_o^2(\alpha^2 - a^2)$, and we integrate null geodesics using (7) -(9) in case there is a radial turning point or (10)-(11) in case there is no radial turning point. In the second case, the geodesics are parametrized with u, and we integrate them down to $u = 1/r_f$. If a firewall is present, the ray is reflected, and we integrate null geodesics outward to $u = 1/(1.5r_{\text{out}})$ where r_{out} is the outermost radius of the torus.

The simulation results in $I_{\nu o}(\alpha,\beta)$ map presented in Fig. 2, where are nine density plots of torus image for three representative values of efficiency parameter $\eta = 0$ (left column), 0.4 (middle column), 1.0 (right column), and three representative values of observer inclination $\theta_o = 15°$ (top row), 45° (middle row) and 80° (bottom row). In each row, the observed specific intensity is normalised by the maximum of the observed specific intensity in case $\eta = 0$ (black hole). In this set of figures, we clearly see that the additional image structure in the region inside of the photon sphere is present, and its intensity relative to maximal intensity decreases with the observer inclination due to the strong enhancement of the Doppler effect becoming stronger for higher inclinations.

This effect is quantitatively illustrated in the $\beta = 0$ profiles of $I_{\nu o}(\alpha,\beta)$ plotted in Figs 3. In each figure there are three plots designated A (for $\eta = 0$), B (for $\eta = 0.4$), and C (for $\eta = 1.0$). The presence of the firewall (mirror) is revealed in the form of additional peaks in the region between the main peaks, which is also present in the black hole case. The amplitude is proportional to the reflection efficiency parameter η as expected.

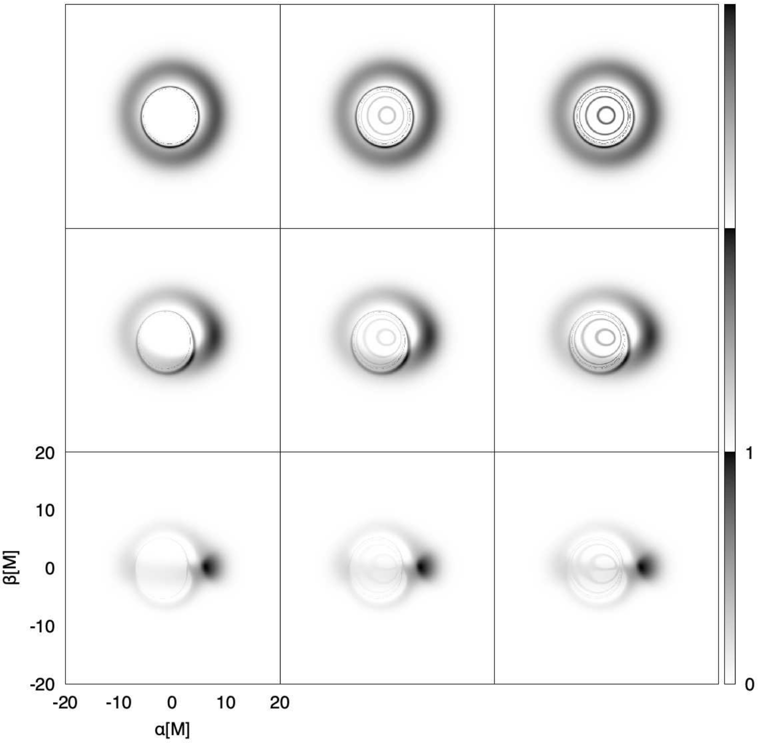

Figure 2. Illustrative examples of $I_{\nu 0}$ maps of disk image around a black hole (left) and firewall (right) with spin 0.95. The observer inclination is $\theta_o = 15°$ (top), 45° (middle), and 80° (bottom).

The intensity of reflected images does not depend on the firewall radius in the case of a stationary structure.

However, in the case of a system of temporal variability of emissivity, the deeper the radius of the firewall, the longer the time it takes a photon to reach the firewall, reflect, and climb out of the potential well. The effect of radiation echo takes place here, and the changes in the direct image of the disk intensity are observed before the changes in reflected images with a time delay corresponding to the depth of potential well (Hensh et al., 2022).

4 CONCLUSIONS

We presented a toy model of firewall a mirror with reflection efficiency η and radius $r_f = r_h(1 + \epsilon)$ and simulated the specific intensity image maps and their α profiles, $I_{\nu o}(\alpha,\beta = 0)$. We showed that additional images of the torus appear in the region below the photon spherical orbit and that their intensity is proportional to the mirror reflection

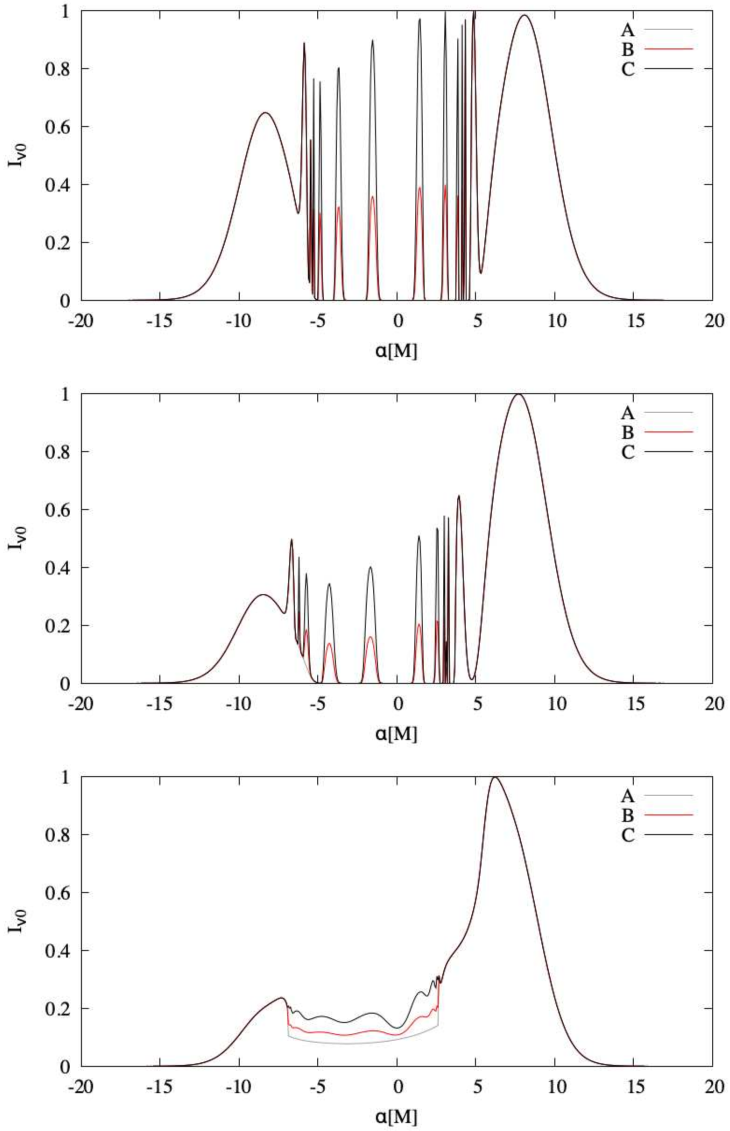

Figure 3. Profiles of $I_{\nu 0}(\alpha,\beta = 0)$ in case of spin parameter $a = 0.95$ and observer inclination $\theta_o = 15°,45°$, and $80°$.

efficiency. We find that the observed specific intensity does not depend on the radius of the mirror. The visibility of the firewall depends strongly on the mirror reflection efficiency.

ACKNOWLEDGEMENT

The authors would like to acknowledge the technical and institutional support of the Institute of Physics, Silesian University in Opava. We also thank the internal grant of Silesian University, SGS/30/2023: Dynamics of structures in strong gravomagnetic fields of compact objects modeled in the framework of Einstein or alternative theories of gravity.

REFERENCES

Almheiri, A., Marolf, D., Polchinski, J. and Sully, J. (2013), Black holes: complementarity or firewalls?, *Jour. of High En. Phys.*, **2013**(62).

Bardeen, J. M., Press, W. H. and Teukolsky, S. A. (1972), Rotating black holes: Locally nonrotating frames, energy extraction, and scalar synchrotron radiation, *Astrophys. J.*, **178**, pp. 347 – 370.

Chen, P., Ong, Y. C., Sasaki, D. N. P. M. and Yeom, D. (2016), Naked black hole firewalls, *Phys. Rev. Lett.*, **116**(161304).

Fanton, C., Calvani, M., de Felice, F. and Cadez, A. (1997), Detecting accretion disks in active galactic nuclei, *Pubs. of the Astron. Soc. of Jap.*, **49**, pp. 159–169.

Hawking, S. W. (1975), Particle Creation by Black Holes, *Commun. Math. Phys.*, **43**, pp. 199–220, [Erratum: Commun.Math.Phys. 46, 206 (1976)].

Hawking, S. W. (1976), Breakdown of predictability in gravitational collapse, *Phys. Rev. D*, **14**(10), pp. 2460–2473.

Hensh, S., Schee, J. and Stuchlík, Z. (2022), Light curve of a hotspot on equatorial orbit around kerr black hole surrounded by reflective firewall, *ArXiv(to be published)*, (2202.13897).

Kerr, R. P. (1963), Gravitational field of a spinning mass as an example of algebraically special metrics, *Phys. Rev. D*, **11**(5), pp. 237–238.

Kozłowski, M., M. Jaroszński, M. and Abramowicz, M. A. (1978), The analytic theory of fluid disks orbiting the kerr black hole, *Astron. & Astrophys.*, **63**, pp. 209 – 220.

Schee, J., Hensh, S. and Barrause, E. (2023), The shadow of rotating horizonless black hole mimickers, *in preparation*.

Proceedings of *RAGtime 23–25*
Z. Stuchlík, G. Török, V. Karas and D. Lančová, editors, Silesian University in Opava, 2023, pp. 83–91

Collapsing massive stars with self-gravity and their electromagnetic transients

Agnieszka Janiuk[1,a] Narjes Shahamat[2] and Dominika Król[3]

[1]Center for Theoretical Physics, Polish Academy of Sciences
Al. Lotników 32/46, 02-668, Warsaw, Poland
[2]Department of Physics, School of Science
Ferdowsi University, Mashhad, Iran
[3]Astronomical Observatory, Jagiellonian University
Kraków, Poland
[a]`agnes@cft.edu.pl`

ABSTRACT
We investigate the fate of a collapsing stellar core, which is the final state of evolution of a massive, rotating star of a Wolf-Rayet type. Such stars explode as type I b/c supernovae, which have been observed in association with long gamma-ray bursts (GRBs). The core of the star is potentially forming a black hole, which is embedded in a dense, rotating, and possibly highly magnetized envelope. We study the process of collapse using General Relativistic MHD simulations, and we account for the growth of the black hole mass and its spin, as well as the related evolution of the spacetime metric. We find that some particular configurations of the initial black hole spin, the content of angular momentum in the stellar core, and the magnetic field configuration and its strength are favoured for producing a bright electromagnetic transient (i.e., a gamma-ray burst). On the other hand, most of the typical configurations studied in our models do not lead to a transient electromagnetic explosion and will end up in a direct collapse, accompanied by some residual variability induced by changing accretion rate. We also study the role of self-gravity in the stellar core and quantify the relative strength of the interfacial instabilities, such as Self-Gravity Interfacial (SGI) instability and Rayleigh-Taylor (RT), which may account for the production of an inhomogeneous structure, including spikes and bubbles, through the inner radii of the collapsing core (inside $\sim 200\ r_\mathrm{g}$). We find that in self-gravitating collapsars, the RT modes cannot grow efficiently. We also conclude that transonic shocks are formed in the collapsing envelope, but they are weaker in magnetized stars.

Keywords: Accretion–black hole physics – gravitation – magnetohydrodynamics – massive stars – gamma-ray bursts

1 INTRODUCTION

Long gamma-ray bursts (GRBs) originate from the collapse of massive, rotating stars. Some of the GRBs exhibit much stronger variability patterns in the prompt GRB emis-

978-80-7510-576-9

sion than the usual stochastic variations. We discuss the mechanisms of these variations in the frame of the self-gravitating collapsar model.

Our computations confirm that gravitational instability can account for flaring activity in GRBs and the variations in their prompt emission. Rapid variability detected in the brightest GRBs, most likely powered by spinning black holes, is consistent with the self-gravitating collapsar model, where the density inhomogeneities are formed. The transonic shocks may also appear, but their effect should be weakened by the magnetic field.

We calculate the time evolution of the collapsing massive star using the General Relativistic Magneto-Hydrodynamic (GR MHD) scheme. We have developed a new version of the code HARM-METRIC, upgraded from that presented in Janiuk et al. (2018). The evolution of the space-time Kerr metric is accounted for by the increasing mass and changing spin of the black hole. We also added new terms that describe the self-gravity of the star and are changing at every time step during dynamical simulation.

In our formulation, the black hole has already been formed in the centre of the collapsing stellar core and its initial mass in of $3M_{\odot}$. Our computational grid size is 1000 $r_{\rm g}$, which makes it smaller than a compact C-O core of a Wolf-Rayet star or a presupernova. Therefore, our model is compact enough to address the problem of self-gravitating gas close to the horizon of a newly formed black hole, but we do not address any prior or ongoing supernova explosion.

Depending on the rotation of the star, the ultimate outcome might be either a direct collapse or the formation of a mini-disc inside the core, that is, a collapsar which may lead to an electromagnetic transient. At the onset of the GRB, the collapsar consists of a black hole, a stellar envelope composed of accreting shells with decreasing density, and a rotationally supported disc formed at the equatorial region. At any chosen radius above the horizon, the gas is subject to gravity force induced by the Kerr black hole, the centrifugal force due to envelope rotation, and in addition, it feels the perturbative force due to the self-gravity of the matter enclosed within a given radius.

2 NUMERICAL CODE AND SETUP

We use the general relativistic MHD code called high-accuracy relativistic magnetohydrodynamics (HARM), originally published by Gammie et al. (2003) and further developed by various groups. Our code version, HARM-METRIC, includes the Kerr metric evolution, as first described in Janiuk et al. (2018).

The code introduces a conservative, shock-capturing scheme with low numerical viscosity to solve the hyperbolic system of partial differential equations of GR MHD. The numerical scheme uses the plasma energy-momentum tensor, with contributions from matter (gas) and electromagnetic field. For the GR MHD evolution, two fundamental equations are solved for the mass and energy-momentum conservation

$$(\rho u^{\mu})_{;\mu} = 0, \qquad T^{\mu}_{\nu;\mu} = 0, \tag{1}$$

$$T^{\mu\nu}_{(m)} = \rho h u^{\mu} u^{\nu} + p g^{\mu\nu}, \tag{2}$$

Physical quantity	Geometrical units	cgs units
Length	$r_g = \frac{GM}{c^2}$	4.44×10^5 cm
Time	$T_{unit} = \frac{r_g}{c}$	1.38×10^{-5} s

Table 1. Conversion units between numerical code and physical scale of the collapsar.

$$T^{\mu\nu}_{(em)} = b^k b_k h u^\mu u^\nu + \frac{1}{2} b^k b_k g^{\mu\nu} - b^\mu b^\nu, \tag{3}$$

$$T^{\mu\nu} = T^{\mu\nu}_{(m)} + T^{\mu\nu}_{(em)}. \tag{4}$$

An additional constraint is given by the Equation of State (EOS). In the current project, we used an analytic form of adiabatic EOS that relates gas pressure with density. This scale, with a power of 4/3, is adequate for a relativistic gas of degenerate particles

$$p = K\rho^\gamma, \qquad \gamma = \frac{4}{3}. \tag{5}$$

The HARM code works in dimensionless units of G = c = 1. Conversion coefficients can be found in 1, where the black hole of 3 Solar masses is assumed. Notice that in the plots below, we use geometric units to express distance, while physical units are used to express time.

2.1 Initial conditions

Initial conditions for our collapsing stellar core are given by the quasi-spherical distribution of gas endowed with small angular momentum, concentrated at the equatorial plane (Król and Janiuk, 2021). The distributions of density and radial velocity are obtained from the Bondi solution, integrated numerically below and above the sonic point. The sonic point is a parameter of our model, and here it is assumed at $80 r_g$. Below this point, matter flows into a black hole supersonically and reaches the speed of light at the horizon.

We illustrate the initial condition in Figure 1, left panel. The density of the gas is normalised to physical units (given in cgs on the plot), assuming that the collapsing star has the initial mass of 25 Solar masses. This mass is enclosed within our computational domain with an outer radius of a $R_{\rm out} = 1000 r_g$. The plot shows only the innermost region of 100 r_g. Most mass of the core is located very near to the center, as it represents the evolved state of stellar evolution with a compact (iron) core formed.

In the initial conditions, we also introduce a small angular momentum imposed on the spherically distributed gas. The specific angular momentum is normalised by the parameter S, with respect to that at the innermost stable circular orbit (ISCO). In addition, the rotation velocity scales with the polar angle to be maximal at the equator, $\theta = \pi/2$.

$$l = S\, l_{\rm isco} r^2 \sin^2\theta, \tag{6}$$

with

$$l_{\mathrm{isco}} = u_{\phi,\mathrm{isco}} = \frac{r_{\mathrm{isco}}^{1/2} - 2a/r_{\mathrm{isco}} + a^2/r_{\mathrm{isco}}^{3/2}}{\sqrt{1 - 3/r_{\mathrm{isco}} + 2a/r_{\mathrm{isco}}^{3/2}}}. \tag{7}$$

Notice that the radius r_{ISCO} in Kerr geometry depends on the black hole spin. In this proceeding, we show results obtained for the value of initial black hole spin $a_0 = 0.5$. We use several values of rotation parameter, as denoted on the plots in the next sections.

After the onset of collapse, the rotation of gas induces the formation of a mini-disk, i.e. toroidal structure, located at the equatorial plane. The density distribution becomes no longer spherical. Also, the radial velocity is decreased as the gas is subject to a centrifugal barrier. Flow is falling into the black hole with supersonic speed from the poles, while at the equator, the speed is subsonic.

The map on Figure 1, right panel, shows the flow distribution at time t=0.089 s for the model normalized with rotation parameter S=1.4. This means that the specific angular momentum is above a critical value (S=1), which allows for the formation of a rotationally supported torus. The sonic surface, Mach=1, is plotted with a solid line and marks the location of a transonic shock at the equatorial region.

3 IMPACT OF SELF-GRAVITY ON THE COLLAPSE

In our new simulations, both the mass and angular momentum accreted onto the event horizon – and used to update the Kerr metric coefficients – are now modified by the perturbation acting on the metric in the region above the horizon due to the self-gravity force that the gas feels at a given distance from the horizon. These perturbative terms are calculated from the stress-energy tensor. Therefore, in addition to the two equations governing the growth of black hole mass and spin via the mass and angular momentum transfer through the horizon, as given below, (Król and Janiuk, 2021), we now add perturbative terms to mass and angular momentum, computed at every radius above the event horizon.

$$\dot{M}_{\mathrm{BH}} = \int \mathrm{d}\theta \mathrm{d}\phi \, \sqrt{-g}\, T^r{}_t, \tag{8}$$

$$\dot{J} = \int \mathrm{d}\theta \mathrm{d}\phi \, \sqrt{-g}\, T^r{}_\phi, \tag{9}$$

$$\delta M_{\mathrm{BH}}(t,r) = 2\pi \int_{r_{\mathrm{hor}}}^{r} T^r_t \sqrt{-g} \mathrm{d}\theta, \tag{10}$$

$$\delta J(t,r) = 2\pi \int_{r_{\mathrm{hor}}}^{r} T^r_\phi \sqrt{-g} \mathrm{d}\theta, \tag{11}$$

$$\delta a = \frac{J + \delta J(r)}{M_{\rm BH} + \delta M_{\rm BH}(r)} - a^i, \tag{12}$$

$$a^i = a^{i-1} + \Delta a. \tag{13}$$

The terms computed in addition to mass and angular momentum changes (Janiuk et al., 2018) as these self-gravity perturbations are integrated at each grid point in the radial direction and at each time. They affect the change of Kerr metric coefficients, which are sensitive to the mass and spin updates. The dimensionless black hole spin, a, evolves as a result of black hole mass and angular momentum changes due to the accretion of mass under the horizon and is additionally changed due to the self-gravity of the collapsing core. The numerical method has been described in detail in Janiuk et al. (2023). Below, we compare the results of self-gravitating collapsar models to the runs without self-gravity in order to emphasize the difference and to investigate the role of self-gravity in collapsar physics.

As shown in Figure 2, the results are strongly sensitive to the adopted self-gravity effects and also weakly sensitive to the rotation of the collapsing envelope. The latter is normalized with respect to the critical angular momentum, for which the flow is circularized at the innermost stable orbit, ISCO (Król and Janiuk, 2021). In addition, the rotation velocity scales with the polar angle so that at the equator, the rotation of the star is maximal. We notice that the larger the initial rotation magnitude, the longer it takes for the black hole mass to evolve. The non-SG simulations end with very different final black hole mass, depending on the rotation parameter.

In contrast, the self-gravity of the envelope can speed up the evolution of the collapsing stellar core significantly. Also, the accretion rate and its fluctuations are of much higher amplitude when self-gravity effects are taken into account. Without self-gravity, there are longer time intervals where there is considerably less fluctuation of the accretion rate; in this case, there exist only some small oscillations in the accretion rate during some time intervals (around 0.2 s for S=1.4, and 0.4-0.5 s for S=2).

3.1 Instabilities on the collapsing core

As an effect of self-gravity, we observe density inhomogeneities and formation of the accretion shocks in all our models, regardless of the initial black hole spin or rotation parameter of the collapsar. First, there appears an equatorial outflow of matter, which reaches radii of up to about 80 $r_{\rm g}$ and is then stalled in the transonic shock. The small inhomogeneities in the pressure and density at the chosen time intervals are visible in more detail in the plots below, in Figure 3 and in Figure 4, respectively.

We quantify the inhomogeneities in the collapsar by computing the radial derivatives of density and pressure at specific times and locations. We identify the mechanism for their creation as the SGI instability (Self-Gravity Interfacial instability), and we compare its strength with another well-known hydrodynamical instability, the Rayleigh-Taylor (RT) instability. Their growth rates are given as below (Kifonidis et al., 2003; Hunter Jr et al., 1997)

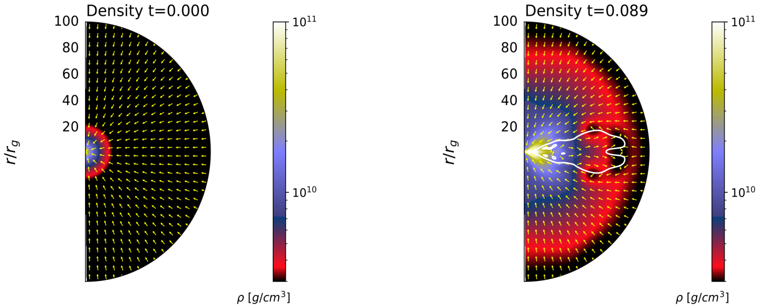

Figure 1. Left: Density distribution at the onset of core collapse. Arrows represent the velocity field (normalised length). Density distribution and velocity field after the onset of collapse. The model is parameterized with rotation parameter S=1.4. The thick white line represents the sonic surface, Mach=1. **Right:** Density distribution at the onset of core collapse. Arrows represent the velocity field.

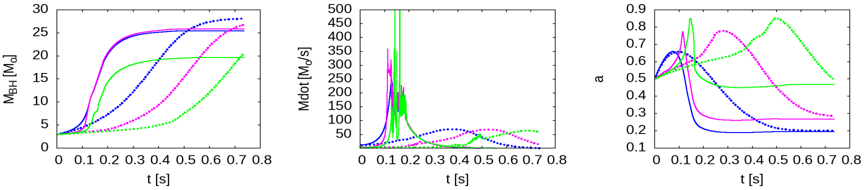

Figure 2. Left: Black hole mass changing as a function of time during the collapse. We start from 3 Solar mass black hole. Models including and excluding self-gravity are plotted by the thick and thin curves, respectively. Three colors refer to different amounts of angular momentum in the collapsing star: S=1.0 (blue), S=1.4 (red) and S=2.0 (green). **Middle:** Evolution of accretion rate through the horizon for self-gravitating and non-self-gravitating collapsars, shown with thick and thin lines, respectively. The different colors refer to various amounts of angular momentum in the collapsar, the same as in the left plot. **Right:** Evolution of the black hole dimensionless spin parameter during the collapse. We start from an oderately spinning black hole with a=0.5. Models including and excluding self-gravity are plotted by the thick and thin curves, respectively. Three color refer to different amounts of angular momentum in the collapsing star, the same as in the left and middle plots.

$$\sigma_{\mathrm{RT}} = \sqrt{-\frac{p}{\rho}\frac{\partial ln\rho}{\partial r}\frac{\partial lnp}{\partial r}}, \tag{14}$$

$$\sigma_{\mathrm{SGI}} = \sqrt{\frac{2\pi G(\rho_2 - \rho_1)^2}{(\rho_2 + \rho_1)}}. \tag{15}$$

The RT and SGI instabilities result in very similar configurations at density snapshots. However, they have their own characteristics, which allows us to differentiate between them. As self-gravity has no 'preferred' direction, it is destabilizing across all density interfaces, while an interface is RT-unstable only if the heavy fluid is on top of the light fluid. It has also been confirmed that RT instability is characterized by dense spikes penetrating the tenuous fluid, whereas the SGI develops with tenuous spikes streaming into the denser fluid.

We find that SGI instability seems to dominate over RT instability and produces the inhomogeneities. In particular, we checked that the growth rates of RT are having imaginary values, as computed at radii between 20 and 25 r_{g}, around the mixing boundary.

Finally, we investigated the formation of transonic shocks in the collapsars. In Figure 5, we present radial profiles of Mach number at some specific time snapshots for models with $S = 2$ and $a_0 = 0.5$. The left panel shows the profiles in the self-gravitating case, while the plot in the right panel shows those of the self-gravitating magnetized case (we introduced a weak vertical magnetic field in the initial condition). For the sake of more visibility, we provide zoomed-in inset panels representing the inner regions. We observe the sonic front expansion and also some transient shock formation during the collapse. At early times, the small transonic shocks appear around 100 r_{g}, and they present a moderate density contrast (pre-shock to post-shock density ratio $R = \rho_1/\rho_2 \sim 10$). Such shocks also appear at later times. Their formation is enhanced by the self-gravity effects. We find that the magnetic field does not make any significant difference in the shock expansion timescales, but it affects the strength of the shock, consistently with previous studies (Komissarov, 1999).

4 CONCLUSIONS

In this work, we show numerical models of the collapsing stellar core where we account for the dynamical evolution of central black hole mass and its spin. The related coefficients of the Kerr space-time metric are evolved accordingly, at every time step. In addition, we calculate the self-gravity of the stellar envelope, and we add the relevant perturbative terms to the dynamical evolution of the black hole spin parameter.

The last modification of the model turned out to have an impact on the global evolution of the collapsing star and produce dramatic fluctuations in the accretion rate at the initial phase of collapse. More importantly, it also plays a crucial role in the development of the SGI interfacial instability in its specific regions. We identified inhomogeneities in density and pressure distributions which arise due to self-gravity, and we concluded that the SGI

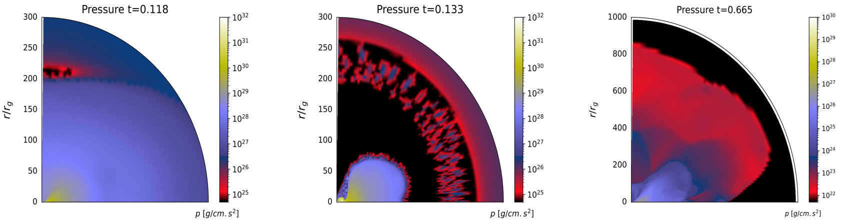

Figure 3. Left: Pressure profile for the model with rotation parameter S=2 and initial black hole spin $A_0 = 0.5$, taken at time t=0.118 s., at which largest accretion rate fluctuations appear. **Middle:** Pressure profile at time t=0.133, for the same model as in the left plot. Strong inhomogeneity regions are visible. **Right:** Pressure profile at a later time of the simulation for the same model as in the left and middle plots. Inhomogeneities are the same, and at this time, accretion rate fluctuations are smoothed as well. The map is zoomed out to a larger radius.

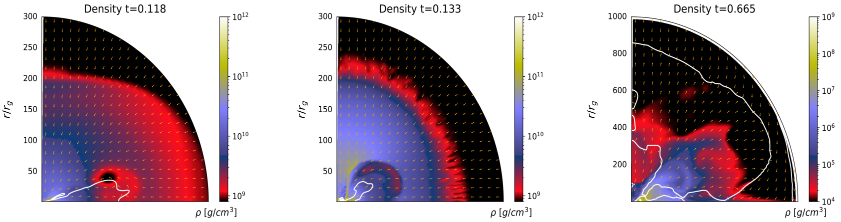

Figure 4. Left: Density profile at t=0.118, for the same model as above. **Middle:** Density profile at t=0.133, for the same model as above. **Right:** Density profile at late time, t=0.665, for the same model as above.

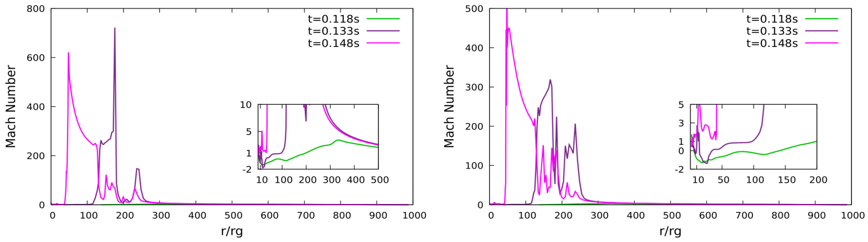

Figure 5. Left: Mach number profile at three different times, t=0.118, t=0.133, and t=0.148 s, for the model with $S = 2.0$. **Right:** Mach number profile at three different times for the same model with a magnetic field.

instability dominates over the RT, as its growth rate is positive in the regions of mixing boundaries.

ACKNOWLEDGEMENTS

The present work was supported by the grant DEC-2019/35/B/ST9/04000 from Polish National Science Center. We made use of computational resources of the PL-Grid infrastructure under grant pglgrb6 and Warsaw University ICM. D. . K. was supported by the Polish National Science Center Dec-2019/35/O/ST9/04054, and N. Sh. D. was supported by Iran National Science Foundation (INSF) under project number No.4013178 and also acknowledges the Ferdowsi University of Mashhad (FUM), Iran, and the FUM Sci-HPC center. Prof. Shahram Abbassi also deserves gratitude for his accompaniment to N.Sh.D. in this project. A.J. acknowledges the Czech-Polish mobility program (MŠMT 8J20PL037 and PPN/BCZ/2019/1/00069).

REFERENCES

Gammie, C. F., McKinney, J. C. and Tóth, G. (2003), HARM: A Numerical Scheme for General Relativistic Magnetohydrodynamics, *Astrophysical Journal*, **589**(1), pp. 444–457, arXiv: `astro-ph/0301509`.

Hunter Jr, J. H., Whitaker, R. W. and Lovelace, R. V. (1997), Kelvin-helmholtz and thermal-dynamic instabilities with self-gravity: a new gravitational interface instability, *The Astrophysical Journal*, **482**(2), p. 852.

Janiuk, A., Shahamat Dehsorkh, N. and Król, D. Ł. (2023), Self-gravitating collapsing star and black hole spin-up in long gamma ray bursts, *Astronomy & Astrophysics*, **677**, A19, arXiv: `2304.01342`.

Janiuk, A., Sukova, P. and Palit, I. (2018), Accretion in a Dynamical Spacetime and the Spinning Up of the Black Hole in the Gamma-Ray Burst Central Engine, *Astrophysical Journal*, **868**(1), 68, arXiv: `1810.05261`.

Kifonidis, K., Plewa, T., Janka, H.-T. and Müller, E. (2003), Non-spherical core collapse supernovae-i. neutrino-driven convection, rayleigh-taylor instabilities, and the formation and propagation of metal clumps, *Astronomy & Astrophysics*, **408**(2), pp. 621–649.

Komissarov, S. S. (1999), Numerical simulations of relativistic magnetized jets, *MNRAS*, **308**(4), pp. 1069–1076.

Król, D. Ł. and Janiuk, A. (2021), Accretion-induced Black Hole Spin-up Revised by Numerical General Relativistic MHD, *Astrophysical Journal*, **912**(2), 132, arXiv: `2104.00741`.

Proceedings of *RAGtime 23–25*
Z. Stuchlík, G. Török, V. Karas and D. Lančová, editors, Silesian University in Opava, 2023, pp. 93–107

Non-conducting tori around black hole immersed in parabolic magnetic field

Martin Blaschke[1,a] Zdeněk Stuchlík[1] Jiří Kovář[1]
and Petr Slaný[1]

[1]Research Centre for Theoretical Physics and Astrophysics,
Institute of Physics, Silesian University in Opava.
Bezručovo náměstí 13, CZ-746 01 Opava, Czech Republic
[a]`martin.blaschke@physics.slu.cz`

ABSTRACT

We study charged fluid tori with vanishing conduction current orbiting in the background given by a Schwarzschild black hole immersed in a parabolic magnetic field introduced in the context of the Blandford-Znajek process. In our study, we focus on the off-equatorial charged tori that could be related to the creation of jets due to the Blandford-Znajek process.

Keywords: Black holes – parabolic magnetic field – general relativity

1 INTRODUCTION

Accretion disks orbiting a central black hole are assumed as engines of active galactic nuclei with central supermassive black holes, or microquasars in binary systems containing a stellar-mass black hole (Abramowicz and Fragile, 2013a). The extraordinary energy outputs observed in such objects are related to the radiation of the disks and the related jets. Basically, accretion disks are modeled as geometrically thin Keplerian accretion disks governed mainly by the spacetime circular geodesics (Novikov and Thorne, 1973), or as geometrically thick accretion disks governed by the Euler equation and the related effective potential reflecting the interplay of the gravitational and inertial forces with the pressure gradients (Kozlowski et al., 1978; Stuchlík et al., 2000). Closed equipotential surfaces of the effective potential govern equilibrium tori, accretion (excretion) tori are governed by self-crossing equipotential surfaces; open equipotential surfaces govern jets. Complex equatorial toroidal structures, named ringed accretion disks, orbiting Kerr black holes and describing simultaneously relatively counter-rotating tori were introduced in Pugliese and Stuchlík (2015, 2016, 2017, 2018); Pugliese and Stuchlik (2019). The jets are usually modeled in the framework of the Blanford-Znajek process that involves electromagnetic fields external to the black hole and generated by electric currents in the accretion disks (Blandford and Znajek, 1977).

978-80-7510-576-9

The electromagnetic fields external to the central black hole are generally very important both for the behavior of the accretion disks and the creation of related jets. Recently, it has been demonstrated that the external magnetic field strongly influences ionized Keplerian disks, causing their transformation to thick disks or leading, in extreme cases, to their destruction Kološ et al. (2015); Stuchlík and Kološ (2016); Tursunov et al. (2016); Pánis et al. (2019); Stuchlík et al. (2019). In complex general-relativistic magneto-hydrodynamic approach Gammie et al. (2003); Komissarov (2004); Tchekhovskoy et al. (2008) describing simultaneously the disks and the jets, fluid plasma structures are usually studied in the force-free approximation corresponding to infinite conductivity – for recent comments on the relation of the Blandford–Znajek process and the magnetic Penrose process (see Dadhich et al. (2018); Stuchlík et al. (2020)).

Existence of non-equatorial charged-particle circular orbits in the external magnetic fields around black holes (Kovář et al., 2008; Kovář et al., 2010; Kopáček et al., 2010) inspired idea of charged "non-conducting (more precisely: with vanishing conduction current)" fluid structures treated in an approximation of zero conductivity, representing a direct of usually used approximation of infinite conductivity. The model of charged non-conducting tori was introduced in Kovář et al. (2011) and further developed in Slaný et al. (2013); Cremaschini et al. (2013); Kovář et al. (2014); Kovář et al. (2016); Trova et al. (2018); Schroven et al. (2018). Such tori can be equatorial, but also can be off-equatorial, levitating outside the equatorial plane due to the electromagnetic interaction of the fluid charge with the magnetic field.

The magnetic field external to the black hole can be an external galactic magnetic fields amplified in the black hole's strong gravity, or a black hole can be immersed in the extremely strong magnetic field of a magnetar (Kovář et al., 2014). Of course, the accretion disk itself is constituted of conducting plasma that can create electric flows that can generate a magnetic field external to the black hole, as assumed in the Blandford-Znajek process.

The basic and simplest approximation of the magnetic fields is the uniform magnetic field introduced by Wald (Wald, 1974). The charged non-conducting tori were studied in the Kerr (Schwarzschild) black hole spacetimes and the uniform or dipole external magnetic fields (Slaný et al., 2013; Kovář et al., 2014), moreover, the off-equatorial tori having sufficiently low density can be considered as collision-less plasma (Cremaschini et al., 2013).

However, of special interest is the possibility of the existence of the off-equatorial non-conducting charged tori in the magnetic fields generated in the accretion disks, creating jets due to the Blandford-Znajek process that are thus also of direct astrophysical relevance. The split-monopole magnetic field generated by currents in thin accretion disks introduced in the first treatment of the Blandford-Znajek process (Blandford and Znajek, 1977), and confirmed as physically relevant by magneto-hydro-dynamic models (Komissarov, 2004), has been studied for the off-equatorial charged tori in Stuchlík et al. (2022).

Here, we focus attention on the possible existence of the off-equatorial charged tori in the parabolic magnetic field treated as a second possibility for the generation of jets in Blandford and Znajek (1977). The relevance of the parabolic field in the vicinity of the black holes is supported by recent numerical general relativistic magneto-hydrodynamic models of thick accretion disks, indicating that the evolution of the tori immersed initially in any magnetic field results in a final state with a parabolic field located outside the torus near the rotation axis of the system (Tchekhovskoy et al., 2008).

We first present basic ideas of the model of the charged non-conducting fluid structures and then investigate the existence and properties of the charged tori around Schwarzschild black holes surrounded by the parabolic magnetic field that can be considered as a simple but realistic approximation of the electromagnetic fields. We use the geometric unit with $c = G = 1$.

2 MODEL OF CHARGED FLUID TORI

We assume a stationary and axisymmetric background field composed of gravitational, $g_{\alpha\beta}$, and electromagnetic, $F_{\alpha\beta} = \nabla_\alpha A_\beta - \nabla_\beta A_\alpha$, parts. Test configurations of a perfect fluid with charge density q_ρ, energy density ϵ and pressure p allowing their orbiting in the fixed background. The considered background fields and the charged configurations have a common axis. Under the presented assumptions, the equilibrium charged fluid configurations are determined by the general energy-momentum conservation law

$$\nabla_\beta \mathcal{T}^{\alpha\beta} = 0, \tag{1}$$

where the energy-momentum tensor $\mathcal{T}^{\alpha\beta} = T^{\alpha\beta} + T^{\alpha\beta}_{\text{em}}$ with its parts

$$T^{\alpha\beta} =(\epsilon + p)U^\alpha U^\beta + p g^{\alpha\beta}, \tag{2}$$

$$T^{\alpha\beta}_{\text{em}} =\frac{1}{4\pi}\left(\mathcal{F}^{\alpha}{}_{\gamma}\mathcal{F}^{\beta\gamma} - \frac{1}{4}\mathcal{F}_{\gamma\delta}\mathcal{F}^{\gamma\delta}g^{\alpha\beta}\right), \tag{3}$$

describes charged fluid with negligible viscosity and heat conduction. The general electromagnetic part of this tensor is related to the Faraday tensor having two parts, $\mathcal{F}^{\alpha\beta} = F^{\alpha\beta} + F^{\alpha\beta}_{\text{self}}$, where the background and the self electromagnetic components satisfy the Maxwell equations

$$\nabla_\beta F^{\alpha\beta} = 0, \quad \nabla_\beta F^{\alpha\beta}_{\text{self}} = 4\pi J^\alpha, \tag{4}$$

with the four-current density field of the charged fluid J^α satisfying the general Ohm law

$$J^\alpha = q_\rho U^\alpha + \sigma F^{\alpha\beta} U_\beta. \tag{5}$$

Usually, the so-called force-free model assumes that the conductivity $\sigma \to \infty$ is applied for the description of the phenomena around the black holes (see, e.g., Blandford and Znajek, 1977). The dynamics of the charged matter is then governed by the force-free relation $F^{\alpha\beta}U_\beta = 0$, and the inertia of the matter is fully abandoned. Then, the first term of the right-hand side of the Ohm law is not considered. In the model of non-conducting charged fluids, assuming $\sigma \to 0$, the situation is inverse, and the second term in the Ohm law is abandoned – in this approach, it is thus supposed that the electric charges are fixed to the rotating matter. The assumption of vanishing conductivity is necessary for the self-consistency of the axial symmetry of the model of charged fluid tori, as a non-zero conductivity implies due to the Ohm law existence of radial electric flows – for details see Kovář et al. (2016) (of course, the inclusion of both the terms in the right-hand side of the Ohm law implies complex configurations including the conducting electric flows and possible strong self-electromagnetic fields). The charged non-conducting fluid tori are then governed by the so-called "master equation" (Kovář et al., 2011)

$$\nabla_\beta T^{\alpha\beta}_{\text{fluid}} = F^{\alpha\beta}_{\text{ext}} J_\beta, \tag{6}$$

where $F^{\alpha\beta}_{\text{ext}}$ denotes the background electromagnetic field that can be of internal origin being related directly to the black hole as in the case of the Kerr-Newman (Reissner–Nordström) backgrounds, or can be of external origin being related to the Kerr (Schwarzschild) gravitational backgrounds as is the case of our study; the basic differences between the internal and external fields are discussed in Stuchlík et al. (2019). The master equation determines the balance equations of the orbiting charged non-conducting fluid. In the following we simplify notation to $F^{\alpha\beta}_{\text{ext}} = F^{\alpha\beta}$.

2.1 Balance equations of the equilibrium fluid configurations

The basic features of the charged fluid model can be summarized as follows. The elementary charges in the fluid are adherent to the fluid elements, i.e. we assume $\sigma = 0$; the charged elements are uniformly rotating in the azimuthal direction with the four-velocity field $U^\alpha = (U^t, 0, 0, U^\phi)$ and $U^\alpha \neq U^\alpha(t, \phi)$. Moreover, presuming the electromagnetically test fluid, $F^{\alpha\beta}_{\text{self}} \ll F^{\alpha\beta}$, the general energy-momentum conservation law (1) reduces to the final form (Kovář et al., 2011)

$$\nabla_\beta T^{\alpha\beta} = F^{\alpha\beta} J_\beta, \tag{7}$$

governing the orbiting charged non-conducting fluid. The related fluid-flow pressure balance equations take the form

$$\begin{aligned} \partial_r p &= -\,(p+\epsilon)\mathbb{R}^\circ + q_\rho \mathbb{R}^* \equiv \mathbb{R}, \\ \partial_\theta p &= -\,(p+\epsilon)\mathbb{T}^\circ + q_\rho \mathbb{T}^* \equiv \mathbb{T}. \end{aligned} \tag{8}$$

The right-hand sides of the equations governing the pressure gradients guaranteeing the fluid balance are denoted as $\mathbb{R} = \mathbb{R}(r, \theta)$ and $\mathbb{T} = \mathbb{T}(r, \theta)$, and are separated them into two parts – the hydrodynamical, and the additional electro-magneto-hydrodynamical that are given by the relations

$$\begin{aligned} \mathbb{R}^\circ &= \partial_r \, \ln|U_t| - \frac{\Omega \partial_r \ell}{1 - \Omega \ell}, \quad \mathbb{R}^* = U^t \partial_r A_t + U^\phi \partial_r A_\phi, \\ \mathbb{T}^\circ &= \partial_\theta \, \ln|U_t| - \frac{\Omega \partial_\theta \ell}{1 - \Omega \ell}, \quad \mathbb{T}^* = U^t \partial_\theta A_t + U^\phi \partial_\theta A_\phi. \end{aligned}$$

The standard fluid models of toroidal configurations (Kozlowski et al., 1978; Stuchlík et al., 2000) are governed by the pure hydrodynamical parts $\mathbb{R}^\circ$ and $\mathbb{T}^\circ$.

The specific angular momentum profile of the rotating fluid, $\ell = -U_\phi/U_t$, and the angular velocity related to the static distant observers, $\Omega = U^\phi/U^t$, are related by the formula

$$\Omega = -\frac{\ell g_{tt} + g_{t\phi}}{\ell g_{t\phi} + g_{\phi\phi}}. \tag{9}$$

The profile of the time component of the four-velocity U_t can be expressed as

$$(U_t)^2 = \frac{g_{t\phi}^2 - g_{tt}g_{\phi\phi}}{\ell^2 g_{tt} + 2\ell g_{t\phi} + g_{\phi\phi}} = \frac{g_{t\phi}^2 - g_{tt}g_{\phi\phi}}{g_{tt} + 2\Omega g_{t\phi} + \Omega^2 g_{\phi\phi}}\,. \tag{10}$$

The axial component of the four-velocity field is then given by the relation $U_\phi = -\ell U_t$. Derivation of the pressure equations (8) can be found in Kovář et al. (2011); Kovář et al. (2014); Kovář et al. (2016); their uncharged limit $q_\rho = 0$ corresponds to the Euler equation describing a rotating electrically neutral perfect fluid (Kozlowski et al., 1978; Abramowicz et al., 1978a; Stuchlík, 2005; Stuchlík et al., 2009).

The specific angular momentum ℓ profile, the angular velocity Ω profile, and the charge density profile are linked due to the relation

$$\partial_\theta \mathbb{R} + \mathbb{T}\partial_p \mathbb{R} = \partial_r \mathbb{T} + \mathbb{R}\partial_p \mathbb{T}, \tag{11}$$

i.e., the integrability condition of the pressure balance equations (8); the profiles $q_\rho = q_\rho(r,\theta)$ and $\ell = \ell(r,\theta)$ ($\Omega = \Omega(r,\theta)$) have to be adjusted to each other in accord with this condition. To close the system of equations, we assume perfect fluid governed by the polytropic equation of state, with the polytropic energy density, rest energy density and pressure related by equations

$$p = \kappa\rho^\Gamma, \quad \epsilon = \rho + \frac{1}{\Gamma - 1}p, \tag{12}$$

where κ and Γ denote the polytropic coefficient and exponent.

2.1.1 Intergal analytical solution of the pressure balance equations

For the charged non-conducting fluids, we can make a significant simplification, enabling even analytic integration of the balance pressure equations. By introducing the charge density transformation

$$\mathcal{K} = \frac{q_\rho}{\epsilon + p}U^\phi, \tag{13}$$

and the pressure transformations

$$\partial_r w = \frac{\partial_r p}{(p + \epsilon)}, \quad \partial_\theta w = \frac{\partial_\theta p}{(p + \epsilon)}, \tag{14}$$

and the electromagnetic vector time component transformation relations

$$\partial_r a_t = \Omega^{-1}\partial_r A_t, \quad \partial_\theta a_t = \Omega^{-1}\partial_\theta A_t\,, \tag{15}$$

we arrive to the transformed pressure balance equations

$$\partial_r w = -\partial_r \ \ln |U_t| + \frac{\Omega \partial_r \ell}{1 - \Omega \ell} + \mathcal{K} \partial_r A,$$
$$\partial_\theta w = -\partial_\theta \ \ln |U_t| + \frac{\Omega \partial_\theta \ell}{1 - \Omega \ell} + \mathcal{K} \partial_\theta A, \tag{16}$$

where $\partial_r A = \partial_r a_t + \partial_r A_\phi$ and $\partial_\theta A = \partial_\theta a_t + \partial_\theta A_\phi$, enabling a unification. That is, if the barotropic fluid is considered, having $\epsilon = \epsilon(p)$ guaranteed by the chosen polytropic equation of state (12), the fluid rotation regime and charged density chosen so that $\Omega = \Omega_1(\ell)$, $\Omega = \Omega_2(A_t)$ and $\mathcal{K} = \mathcal{K}(A)$, we can join the system of equations (16) into the unified integral form

$$\int_0^w \mathrm{d}w = -\ln \left| \frac{U_t}{U_{t_\mathrm{in}}} \right| + \int_{\ell_\mathrm{in}}^{\ell} \frac{\Omega \mathrm{d}\ell}{1 - \Omega \ell} + \int_{A_\mathrm{in}}^{A} \mathcal{K} \mathrm{d}A \,, \tag{17}$$

with the solution written in the form

$$w = \int_0^w \mathrm{d}w = -W + W_\mathrm{in} \,. \tag{18}$$

The function $W(r, \theta)$ is the effective potential (variable part of the right-hand side of equation (17)), and the subscript 'in' represents the inner edge of the orbiting fluid structure at $r = r_\mathrm{in}$ for $\theta = \theta_\mathrm{in}$, whereas for a function $X = X(r, \theta)$, we denote $X_\mathrm{in} = X(r_\mathrm{in}, \theta_\mathrm{in})$ governing the constant of integration W_in .

Due to pressure transformation relations (14) integrated to give

$$\int_0^w \mathrm{d}w = \int_0^p \frac{\mathrm{d}p}{p + \epsilon}, \tag{19}$$

the equipressure surfaces, p = const, determining the topology of the orbiting fluid structure coincide with the equipotential surfaces, W = const. It is well known that the effective potential governs all relevant aspects of the behavior of the stationary and axisymmetric fluid configurations both for uncharged fluids (Abramowicz et al., 1978b; Stuchlík et al., 2009) and for charged non-conducting fluids (Kovář et al., 2014; Kovář et al., 2016).

3 BLACK HOLES SURROUNDED BY PARABOLIC MAGNETIC FIELD

We focus here on the charged, non-conducting fluid circling in the background given by the static Schwarzschild black hole immersed in the parabolic magnetic field considered as a test field that is not influencing the spacetime. The Schwarzschild black holes are represented by the vacuum geometry with the line element taking the form (in the geometric units $c = G = 1$)

$$\mathrm{d}s^2 = g_{tt} \mathrm{d}t^2 + g_{rr} \mathrm{d}r^2 + g_{\theta\theta} \mathrm{d}\theta^2 + g_{\phi\phi} \mathrm{d}\phi^2, \tag{20}$$

where

$$g_{\theta\theta} = r^2 \,, \quad g_{\phi\phi} = r^2 \sin^2 \theta \,, \quad g_{tt} = -f(r) \,, \quad g_{rr} = \frac{1}{f(r)} \,, \tag{21}$$

and the lapse function

$$f(r) = 1 - \frac{2M}{r} \,. \tag{22}$$

M denotes the black hole mass. For simplicity, we will use, in the following, the dimensionless coordinates ($r = r/M, t = t/M, s = s/M$) that are equivalent to using $M = 1$.

The parabolic magnetic field was introduced in Blandford and Znajek (1977) for modeling the creation of jets in the magnetosphere of the rotating black holes in the regions close to their horizon. The physical relevance of such a special kind of magnetic field was confirmed by numerical, fully general relativistic models of magneto-hydrodynamic processes around black holes, where it has been demonstrated that evolution of a thick accretion disk (toroid) under influence of various external magnetic fields (uniform, dipole, parabolic) always results in a final configuration having the magnetic field exterior to the toroidal configuration and close to the rotation axis of the black hole and torus system of the parabolic character (Tchekhovskoy et al., 2008).

For completeness, we also add the case of parabolic magnetic field as magneto-hydrodynamic fluid models of thick accretion disks orbiting a black hole demonstrate the final creation of a parabolic magnetic field near the rotation axis of the orbiting matter independently of the original configuration of the external magnetic field (Nakamura et al., 2018). The parabolic magnetic field predicted by some magnetohydrodynamic simulations is determined by the four-vector electromagnetic potential (Nakamura et al., 2018).

In the static Schwarzschild vacuum spacetimes, the parabolic magnetic field is static and axially symmetric, it thus has not the spherical symmetry of the Schwarzschild spacetime as is the case of the split monopole magnetic field; its $four-vector$ electromagnetic potential has thus the only non-zero component

$$A_\mu = (0, 0, 0, A_\phi), \tag{23}$$

and the axial component reads

$$A_\phi = \frac{g}{2} r\,(1 - \cos\theta) + 2M\,(1 + \cos\theta)\,[1 - \ln\,(1 + \cos\theta)]\,, \tag{24}$$

where the parameter g governs the intensity of the magnetic field and is directly related to the intensity of the electric current generating the magnetic field – for details as the asymptotic behaviour at the horizon and weak-field limit see Blandford and Znajek (1977).

Commonly used approximation to Eq. (24) is given by Crinquand et al. (2020); McKinney and Narayan (2007a,b)

$$A_\phi = \frac{g}{2} r^k\,(1 - |\cos\theta|)\ , \tag{25}$$

where $k \in [0; 1.25]$ is declination of magnetic field lines. The split monopole solution (Blandford and Znajek, 1977; Stuchlík et al., 2022) corresponds to $k = 0$ and Blandford-Znajeck paraboloidal model to $k = 1$. Mostly used value for the black hole magnetosphere in the jet funnel is $k = 3/4$ (Nakamura et al., 2018; Stuchlík et al., 2019).

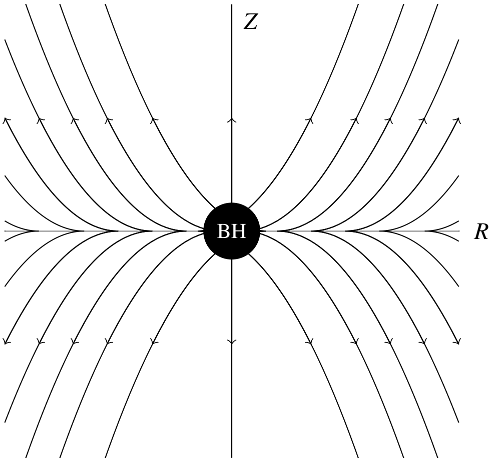

Figure 1. Scheme of a parabolic magnetic field in cylindrical coordinates given by Eq. (37).

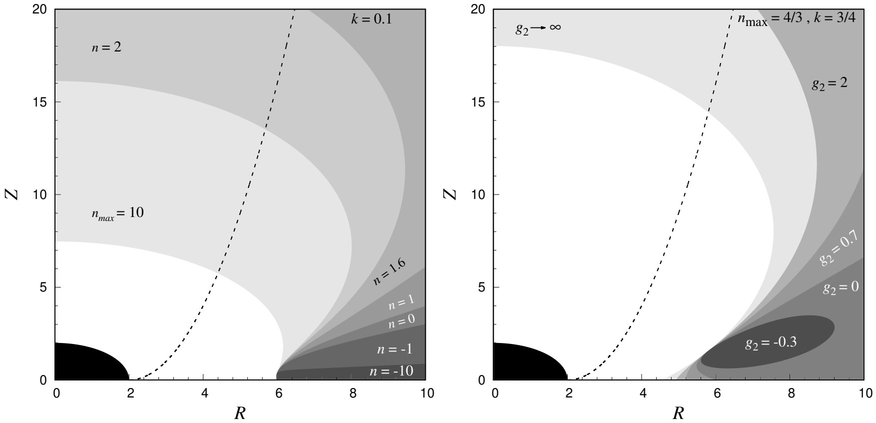

Figure 2. Left: Regions supporting minima of potential W under monomial ℓ =const. model. Parameter n spans from -10 to $n_{\rm max} \equiv 1/k$, i.e. the maximal value of this parameter consistent with physical potential ($\partial W/\partial r \to 0$ as $r \to \infty$). **Right:** Regions supporting minima of polynomial potential W under polynomial ℓ =const. model. In the figures, we have depicted the behaviour of parameter $n_{\rm max} \equiv 1/k$. We see that regions supporting the existence of minima are generally enlarged due to the non-zero g_2 constant. Also, that minima can now go under $R = 6$. We also see strange effects. For negative values of g_2, equatorial structures are suppressed. For thick discs, the model is relevant only above the dashed line, but for thin disks, it is relevant everywhere.

4 CHARGE TORI AROUND BLACK HOLES IN PARABOLIC MAGNETOSPHERE

In the Schwarzschild spacetimes, the four-velocity components satisfy the relations $U^t = g^{tt} U_t$, $U^\phi = g^{\phi\phi} U_\phi$ and the relation for the energy of the orbiting element simplifies to

$$(U_t)^2 = \frac{-g_{tt} g_{\phi\phi}}{\ell^2 g_{tt} + g_{\phi\phi}} = -\frac{f(r) r^2 \sin^2\theta}{\ell^2 f(r) - r^2 \sin^2\theta}. \tag{26}$$

The condition $(U_t)^2 > 0$ requires $\ell^2 g_{tt} + g_{\phi\phi} > 0$, implying the restriction on the acceptable values of the specific angular momentum in the form

$$\ell^2 < \frac{r^3 \sin^2\theta}{r-2} \equiv l^2_{\mathrm{ph}}(r, \theta). \tag{27}$$

The function $l^2_{\mathrm{ph}}(r; \theta = \pi/2)$ governs the motion of photons in the equatorial plane, and for $l^2 = 27$ we obtain the circular photon orbit at $r = 3$ that represents the innermost limit on the position of circular geodesics.

Due to the simple form of the vector potential (23), the transformed pressure balance equations (16) reduce to the form

$$\begin{aligned} \partial_r w &= -\,\partial_r \,\ln|U_t| + \frac{\Omega \partial_r \ell}{1 - \Omega\ell} + \mathcal{K} \partial_r A_\phi, \\ \partial_\theta w &= -\,\partial_\theta \,\ln|U_t| + \frac{\Omega \partial_\theta \ell}{1 - \Omega\ell} + \mathcal{K} \partial_\theta A_\phi, \end{aligned} \tag{28}$$

whereas we require $\Omega = \Omega(\ell)$ and $\mathcal{K} = \mathcal{K}(A_\phi)$ for the integrability. Thus, the solution can be written in the form

$$w = -\ln\left|\frac{U_t}{U_{t_{\mathrm{in}}}}\right| + \int_{\ell_{\mathrm{in}}}^{\ell} \frac{\Omega \mathrm{d}\ell}{1 - \Omega\ell} + g \int_{A_{\phi_{\mathrm{in}}}}^{A_\phi} \mathcal{K}\, \mathrm{d}A_\phi = -W + W_{\mathrm{in}}. \tag{29}$$

Below we demonstrate the existence of the off-equatorial tori, with their centers, possibly located at $(r_{\mathrm{c}}, \theta_{\mathrm{c}})$, corresponding to local minima of the effective potential W (maxima of the pressure p). Thus, these locations must satisfy the necessary conditions

$$\partial_r W|_{\substack{r = r_{\mathrm{c}} \\ \theta = \theta_{\mathrm{c}}}} = 0, \quad \partial_\theta W|_{\substack{r = r_{\mathrm{c}} \\ \theta = \theta_{\mathrm{c}}}} = 0, \tag{30}$$

and, moreover, the sufficient conditions

$$\partial^2_{\theta\theta} W|_{\substack{r = r_{\mathrm{c}} \\ \theta = \theta_{\mathrm{c}}}} > 0, \quad \det \mathcal{H}|_{\substack{r = r_{\mathrm{c}} \\ \theta = \theta_{\mathrm{c}}}} > 0, \tag{31}$$

where

$$\mathcal{H} = \begin{pmatrix} \partial^2_{rr} W & \partial^2_{r\theta} W \\ \partial^2_{\theta r} W & \partial^2_{\theta\theta} W \end{pmatrix}, \tag{32}$$

[t]

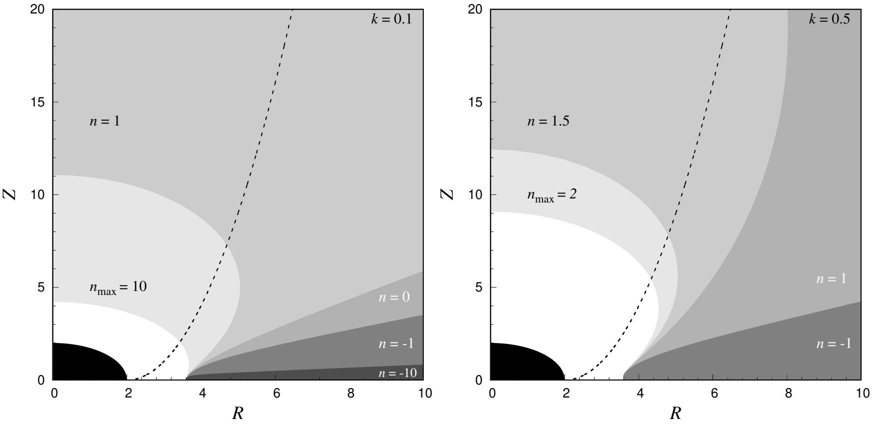

Figure 3. Regions supporting minima of potential W under monomial $\Omega = \ell^2/K$ model. Parameter n spans from -10 to $n_{\max} \equiv 1/k$, i.e. maximal value of this parameter consistent with physical potential ($\partial W/\partial r \to 0$ as $r \to \infty$). For thick discs, the model is relevant only above the dashed line, but for thin disks, it is relevant everywhere.

is the Hessian matrix. We survey a couple of rotation regimes of the fluid, particularly the case $\ell = \text{const.}$ and two cases $\ell \neq \text{const.}$ satisfying the condition $\Omega = \Omega(\ell)$, and the distribution of the charge density given by the monomial profile of the function $\mathcal{K} = \mathcal{K}(A_\phi)$, integrated as

$$\int \mathcal{K} \, \mathrm{d}A_\phi = g r^{kn} \left(1 - \cos\theta\right)^n , \tag{33}$$

for $n \neq 0$, relaxing the integration constants. For simplicity's sake, we consider cases $n = 0$ as a limiting case to avoid explicit logarithmic functions.

We also survey Polynomial regimes in the form

$$\int \mathcal{K} \, \mathrm{d}A_\phi = g r^{kn} \left(1 - \cos\theta\right)^n + g_2 r^{k(n-1)} \left(1 - \cos\theta\right)^{n-1} , \tag{34}$$

for $n \neq 0$ and $n \neq 1$ to again avoid explicit logarithmic functions.

4.1 Rotation regime $\ell = \text{const.}$

The rotation regime $\ell = \text{const}$ is a unique one, representing the marginally stable distribution of ℓ that is able to govern the basic properties of general acceptable equilibrium tori (Abramowicz and Fragile, 2013b). The potential given by Eg. (29), governing the toroidal configurations, takes under our assumptions form

$$W = \ln|U_t| - g r^{kn} \left(1 - \cos\theta\right)^n , \tag{35}$$

where we neglect the integration constant and consider the upper plane only, i.e. $\theta \in [0, \pi/2]$.
The necessary conditions (30) implying the set of equations (for any n)

$$\begin{aligned}
g =& \frac{\cos\theta_c \left(r_c^k \sin^2 \frac{\theta_c}{2}\right)^{-n}}{3 - r_c + (3 - r_c + k(r_c - 2))\cos\theta_c}\,, \\
\ell^2 =& \frac{r_c^3 \sin^2\theta_c}{(r_c - 2)^2 \left(1 - k\cot\theta_c \tan\frac{\theta_c}{2}\right)}\,.
\end{aligned} \tag{36}$$

These equations determine regions where a minimum of W exists. For picturing these regions and corresponding potentials W, it is more convenient to use cylindrical coordinates

$$R = r\sin\theta\,, \quad Z = r\cos\theta\,. \tag{37}$$

Regions are depicted in the left part of Fig. 2 where we have depicted the regions supporting minima of potential W under monomial ℓ =const. model. Here the parameter n spans from -10 to $n_{\max} \equiv 1/k$, i.e. the maximal value of this parameter consistent with physical potential ($\partial W/\partial r \to 0$ as $r \to \infty$). The model is only relevant for thick discs above the dashed line but for thin disks everywhere.

4.2 Polynomial potential

In the last section, we have seen that monomial potential might be too simple to support the effect on broad ranges of parameter k. Since we are interested in the minima of the potential W, let us introduce the polynomial character to it in the hope that a more complicated function would bring more minima points in the potential.

Therefore, let us explore the potential W in the polynomial form:

$$W = \ln|U_t| - g r^{kn}(1 - \cos\theta)^n - g_2 r^{k(n-1)}(1 - \cos\theta)^{(n-1)}\,, \tag{38}$$

where g_2 is another constant.

The example behaviour of this potential can be seen in the right part of Fig. (2). Here, we can see that the constant g_2 generally enlarges the areas where the potential W admit the existence of minima.

4.3 Rotation regime Ω = const.

Let us consider another very elemental regime with constant Ω. The potential is given by the relation

$$W = \ln|U_t| + \ln|1 - \Omega\ell| - g r^{kn}(1 - \cos\theta)^n\,. \tag{39}$$

Here ℓ is given by Eq. (10) and it is equal to

$$\ell = \Omega\frac{r^2\sin^2\theta}{f(r)}\,. \tag{40}$$

Due to the necessary conditions (30), in the centers of the toroidal structures, the constant Ω takes value

$$\Omega_{\mathrm{c}}^2 = \frac{1}{r_{\mathrm{c}}^3 \sin\theta_{\mathrm{c}} \left(\sin\theta - k\cos\theta \tan\frac{\theta}{2}\right)} \tag{41}$$

and the constant g takes the same form as was given in the previous case by Eq. (36).

However, putting all these conditions into effective potential, we can see that for any profile of the function $\mathcal{K}$, there are no possible centres of the toroidal structures. This result is consistent with findings in Stuchlík et al. (2022).

4.4 Rotation regime $\Omega \sim \ell^2$.

The integrability condition $\Omega(\ell)$ restricts possible choices of angular velocity. The choice

$$\Omega = \frac{\ell^2}{K}, \tag{42}$$

where K is an arbitrary non-zero constant, is equivalent via eq. (10) to

$$\ell = K\frac{f(r)}{r^2\sin^2\theta}, \tag{43}$$

usually supports the existence of an off-equatorial minimum in potential W. The potential is given by the relation

$$W = \ln|U_t| + \ln\left|1 - \frac{K^2 f^3(r)}{r^6\sin^6\theta}\right| - g r^{kn}\left(1-\cos\theta\right)^n . \tag{44}$$

The center is given by the same g as in eq. (36) and by

$$K = \frac{r_{\mathrm{c}}^{\frac{5}{2}}\sin^3\theta_{\mathrm{c}}}{f^2(r_{\mathrm{c}})\sqrt{1 - k\cot(\theta)\tan\left(\frac{\theta}{2}\right)}} . \tag{45}$$

The example behaviour of this potential can be seen in Fig. (3), where we have depicted the regions supporting minima of potential W under the monomial $\Omega = \ell^2/K$ model. Here, the parameter n spans from -10 to $n_{\mathrm{max}} \equiv 1/k$, i.e. the maximal value of this parameter consistent with physical potential ($\partial W/\partial r \to 0$ as $r \to \infty$). For thick discs, the model is relevant only above the dashed line, but for thin disks, it is relevant everywhere.

5 CONCLUSIONS

In modeling jets created by the Blandford-Znajek process, the one of assumed magnetic field has the character of the parabolic field.

We have demonstrated the existence of nonconducting charged tori located off the equatorial plane for properly chosen parameters governing their location and structure; namely, the distribution of the specific angular momentum, and the electric charge density.

We conclude that we were able to demonstrate clearly existence of nonconducting charged tori created by heavy particles located off the equatorial plane that could be, under the properly chosen condition on the charged matter, its distribution, and distribution of the specific angular momentum governing their equilibrium configurations, allowed to occur near the symmetry axis of the magnetized black hole. The charged tori is located near the symmetry axis could represent a possible obstacle for the matter of the jets that should probably interact with such configurations–the accelerated electrons should collide with heavy particles constituting the charged tori. Interactions of extremely accelerated electrons of the jet with the equilibrium tori created by heavy particles should lead to specific effects that could be observed and maybe to some modifications of the Blandford–Znajek process. Clearly, the phenomenon of charged nonconducting tori located near the symmetry axis would be a serious challenge for future research in the field of accretion disks and related jets.

ACKNOWLEDGEMENTS

The authors thanks the referee for careful reading of the original version of the manuscript. The work was supported by Institute of Physics in Opava. We also thank the internal grant of Silesian University, SGS/30/2023: Dynamics of structures in strong gravomagnetic fields of compact objects modeled in the framework of Einstein or alternative theories of gravity.

REFERENCES

Abramowicz, M., Jaroszynski, M. and Sikora, M. (1978a), Relativistic, accreting disks., *A&A*, **63**, pp. 221–224.

Abramowicz, M., Jaroszynski, M. and Sikora, M. (1978b), Relativistic, accreting disks, *A&A*, **63**, pp. 221–224.

Abramowicz, M. A. and Fragile, P. C. (2013a), Foundations of Black Hole Accretion Disk Theory, *Living Reviews in Relativity*, **16**(1), 1, arXiv: `1104.5499`.

Abramowicz, M. A. and Fragile, P. C. (2013b), Foundations of Black Hole Accretion Disk Theory, *Living Reviews in Relativity*, **16**(1), 1, arXiv: `1104.5499`.

Blandford, R. D. and Znajek, R. L. (1977), Electromagnetic extraction of energy from Kerr black holes, *Monthly Notices of the RAS*, **179**, pp. 433–456.

Cremaschini, C., Kovář, J., Slaný, P., Stuchlík, Z. and Karas, V. (2013), Kinetic Theory of Equilibrium Axisymmetric Collisionless Plasmas in Off-equatorial Tori around Compact Objects, *Astrophysical Journal, Supplement*, **209**, 15, arXiv: `1309.3979`.

Crinquand, B., Cerutti, B., Dubus, G., Parfrey, K. and Philippov, A. (2020), Synthetic gamma-ray lightcurves of Kerr black-hole magnetospheric activity from particle-in-cell simulations, *arXiv e-prints*, arXiv:2012.09733, arXiv: `2012.09733`.

Dadhich, N., Tursunov, A., Ahmedov, B. and Stuchlík, Z. (2018), The distinguishing signature of magnetic Penrose process, *Monthly Notices of the RAS*, **478**(1), pp. L89–L94, arXiv: `1804.09679`.

Gammie, C. F., McKinney, J. C. and Tóth, G. (2003), HARM: A Numerical Scheme for General Relativistic Magnetohydrodynamics, *ApJ*, **589**, pp. 444–457, arXiv: `astro-ph/0301509`.

Kološ, M., Stuchlík, Z. and Tursunov, A. (2015), Quasi-harmonic oscillatory motion of charged particles around a Schwarzschild black hole immersed in a uniform magnetic field, *Classical and Quantum Gravity*, **32**(16), 165009, arXiv: `1506.06799`.

Komissarov, S. S. (2004), Electrodynamics of black hole magnetospheres, *Monthly Notices of the RAS*, **350**(2), pp. 427–448.

Kopáček, O., Karas, V., Kovář, J. and Stuchlík, Z. (2010), Transition from Regular to Chaotic Circulation in Magnetized Coronae near Compact Objects, *ApJ*, **722**(2), pp. 1240–1259, arXiv: `1008.4650`.

Kovář, J., Slaný, P., Cremaschini, C., Stuchlík, Z., Karas, V. and Trova, A. (2014), Electrically charged matter in rigid rotation around magnetized black hole, *Phys. Rev. D*, **90**(4), 044029, arXiv: `1409.0418`.

Kovář, J., Stuchlík, Z. and Karas, V. (2008), Off-equatorial orbits in strong gravitational fields near compact objects, *Classical and Quantum Gravity*, **25**(9), 095011, arXiv: `0803.3155`.

Kovář, J., Kopáček, O., Karas, V. and Stuchlík, Z. (2010), Off-equatorial orbits in strong gravitational fields near compact objects—II: halo motion around magnetic compact stars and magnetized black holes, *Classical and Quantum Gravity*, **27**(13), 135006, arXiv: `1005.3270`.

Kovář, J., Slaný, P., Cremaschini, C., Stuchlík, Z., Karas, V. and Trova, A. (2016), Charged perfect fluid tori in strong central gravitational and dipolar magnetic fields, *Physical Review D*, **93**, p. 124055.

Kovář, J., Slaný, P., Stuchlík, Z., Karas, V., Cremaschini, C. and Miller, J. C. (2011), Role of electric charge in shaping equilibrium configurations of fluid tori encircling black holes, *Phys. Rev. D*, **84**(8), 084002, arXiv: `1110.4843`.

Kozlowski, M., Jaroszynski, M. and Abramowicz, M. A. (1978), The analytic theory of fluid disks orbiting the Kerr black hole., *A&A*, **63**(1-2), pp. 209–220.

McKinney, J. C. and Narayan, R. (2007a), Disc-jet coupling in black hole accretion systems - I. General relativistic magnetohydrodynamical models, *Monthly Notices of the RAS*, **375**(2), pp. 513–530, arXiv: `astro-ph/0607575`.

McKinney, J. C. and Narayan, R. (2007b), Disc-jet coupling in black hole accretion systems - II. Force-free electrodynamical models, *Monthly Notices of the RAS*, **375**(2), pp. 531–547, arXiv: `astro-ph/0607576`.

Nakamura, M., Asada, K., Hada, K., Pu, H.-Y., Noble, S., Tseng, C., Toma, K., Kino, M., Nagai, H., Takahashi, K., Algaba, J.-C., Orienti, M., Akiyama, K., Doi, A., Giovannini, G., Giroletti, M., Honma, M., Koyama, S., Lico, R., Niinuma, K. and Tazaki, F. (2018), Parabolic Jets from the Spinning Black Hole in M87, *ApJ*, **868**(2), 146, arXiv: `1810.09963`.

Novikov, I. D. and Thorne, K. S. (1973), Astrophysics of black holes., in C. Dewitt and B. S. Dewitt, editors, *Black Holes (Les Astres Occlus)*, pp. 343–450.

Pánis, R., Kološ, M. and Stuchlík, Z. (2019), Determination of chaotic behaviour in time series generated by charged particle motion around magnetized Schwarzschild black holes, *arXiv e-prints*, arXiv:1905.01186, arXiv: `1905.01186`.

Pugliese, D. and Stuchlík, Z. (2015), Ringed accretion disks: Equilibrium configurations, *The Astrophysical Journal Supplement Series*, **221**, p. 25.

Pugliese, D. and Stuchlík, Z. (2016), Ringed accretion disks: Instabilities, *The Astrophysical Journal Supplement Series*, **223**, p. 27.

Pugliese, D. and Stuchlík, Z. (2017), Ringed accretion disks: Evolution of double toroidal configurations, *The Astrophysical Journal Supplement Series*, **229**, p. 40.

Pugliese, D. and Stuchlík, Z. (2018), Relating kerr smbhs in active galactic nuclei to rads configurations, *Classical and Quantum Gravity*, **35**, p. 185008.

Pugliese, D. and Stuchlik, Z. (2019), Multi-accretion events from corotating and counterrotating SMBHs tori, *arXiv e-prints*, arXiv:1910.03925, arXiv: `1910.03925`.

Schroven, K., Trova, A., Hackmann, E. and Lämmerzahl, C. (2018), Charged fluid structures around a rotating compact object with a magnetic dipole field, *Phys. Rev. D*, **98**(2), 023017, arXiv: `1804.11286`.

Slaný, P., Kovář, J., Stuchlík, Z. and Karas, V. (2013), Charged Tori in Spherical Gravitational and Dipolar Magnetic Fields, *Astrophysical Journal, Supplement*, **205**, 3, arXiv: `1302.2356`.

Stuchlík, Z. (2005), Influence of the RELICT Cosmological Constant on Accretion Discs, *Modern Physics Letters A*, **20**, pp. 561–575, arXiv: `0804.2266`.

Stuchlík, Z., Blaschke, M., Kovář, J. and Slaný, P. (2022), Charged fluid nonconducting toroidal structures orbiting a schwarzschild black hole immersed in a split-monopole magnetic field, *Phys. Rev. D*, **105**, p. 103012, URL `https://link.aps.org/doi/10.1103/PhysRevD.105.103012`.

Stuchlík, Z., Kološ, M. and Tursunov, A. (2019), Magnetized black holes: Ionized keplerian disks and acceleration of ultra-high energy particles, in *Recent Progress in Relativistic Astrophysics*, MDPI, URL `https://doi.org/10.3390/proceedings2019017013`.

Stuchlík, Z. and Kološ, M. (2016), Acceleration of the charged particles due to chaotic scattering in the combined black hole gravitational field and asymptotically uniform magnetic field, *European Physical Journal C*, **76**, 32, arXiv: `1511.02936`.

Stuchlík, Z., Kološ, M., Kovář, J., Slaný, P. and Tursunov, A. (2020), Influence of Cosmic Repulsion and Magnetic Fields on Accretion Disks Rotating around Kerr Black Holes, *Universe*, **6**(2), p. 26.

Stuchlík, Z., Kološ, M. and Tursunov, A. A. (2019), Magnetized black holes: Ionized keplerian disks and acceleration of ultra-high energy particles, *Proceedings*, **17**(1), ISSN 2504-3900, URL `https://www.mdpi.com/2504-3900/17/1/13`.

Stuchlík, Z., Slaný, P. and Hledík, S. (2000), Equilibrium configurations of perfect fluid orbiting Schwarzschild-de Sitter black holes, *A&A*, **363**, pp. 425–439.

Stuchlík, Z., Slaný, P. and Kovář, J. (2009), Pseudo-Newtonian and general relativistic barotropic tori in Schwarzschild-de Sitter spacetimes, *Classical and Quantum Gravity*, **26**(21), 215013, arXiv: `0910.3184`.

Tchekhovskoy, A., McKinney, J. C. and Narayan, R. (2008), Simulations of ultrarelativistic magnetodynamic jets from gamma-ray burst engines, *Monthly Notices of the RAS*, **388**(2), pp. 551–572, arXiv: `0803.3807`.

Trova, A., Schroven, K., Hackmann, E., Karas, V., Kovář, J. and Slaný, P. (2018), Equilibrium configurations of a charged fluid around a Kerr black hole, *Phys. Rev. D*, **97**(10), 104019, arXiv: `1803.02262`.

Tursunov, A., Stuchlík, Z. and Kološ, M. (2016), Circular orbits and related quasi-harmonic oscillatory motion of charged particles around weakly magnetized rotating black holes, *Phys. Rev. D*, **93**(8), 084012, arXiv: `1603.07264`.

Wald, R. M. (1974), Black hole in a uniform magnetic field, *Phys. Rev. D*, **10**, pp. 1680–1685.

Proceedings of *RAGtime 23–25*
Z. Stuchlík, G. Török, V. Karas and D. Lančová, editors, Silesian University in Opava, 2023, pp. 109–117

MAD UFOs: Magnetically Arrested Discs with persistent Ultra-Fast Outflows

Petra Suková[1,a] Michal Zajaček[2] and Vladimír Karas[1]

[1]Astronomical Institute of the Czech Academy of Sciences, Boční II 1401,
CZ-180 00 Prague, Czech Republic
[2]Department of Theoretical Physics and Astrophysics, Faculty of Science,
Masaryk University, Kotlářská 2, CZ-611 37 Brno, Czech Republic
[a]`petra.sukova@asu.cas.cz`

ABSTRACT
General-relativistic magneto-hydrodynamical (GRMHD) simulations of accreting black holes suggest that the accretion flows form toroidal structures embedded in a large scale component of magnetic field, which becomes organized on length-scales exceeding the gravitational radius of the central black hole. Magnetic field grows gradually until a Magnetically Arrested Disc (MAD) develops that diminishes or inhibits further accretion. We study an outflow that develops in the MAD state in 3D GRMHD simulations. We show that the outflow can be accelerated to relativistic velocities and persist over the course of our simulation. We compare the properties of the outflow from MAD discs with those launched by orbiting secondary at close orbit. The main difference is that the orbiting body launches a more coherent, quasiperiodic ultrafast outflow at lower velocities ($v < 0.5c$) while the outflow launched in the MAD state (without the body) has a stochastic behaviour and has an approximately flat velocity distribution between lower anf higher outflow velocities, $0.2c < v < 0.3c$ and $v > 0.5c$.

Keywords: Accretion discs – black holes – Active Galactic Nuclei – MHD simulations – outflows

1 INTRODUCTION

In the course of the recent decade, high-resolution data brought compelling evidence that the electromagnetic variability of accreting black holes has its origin in the hot plasma orbiting on event-horizon scales (Gravity Collaboration et al., 2018; Event Horizon Telescope Collab. et al., 2019). Despite these observational breakthroughs, the precise factors that determine the accretion rate as well as the origin of the outflows, flares, and oscillations seen in these systems remain largely unknown. With the upcoming missions aiming to observe black hole systems at ever-increasing sensitivity and resolution (e.g. LSST, Athena, ESO Extremely Large Telescope), an improvement in understanding of these dynamical processes is of prime importance.

978-80-7510-576-9

In a recent study (Suková et al., 2021), we focused on the observable effects that can be caused by repetitive transits of perturbers through accretion flows near supermassive black holes (SMBHs). We have modified the GRMHD `HARMPI` code (Ressler et al., 2015) to assume a rigid body moving along geodesics in a hot accretion flow. An important outcome of this study is the existence of quasiperiodic ultrafast outflows from the central region launched by the transit of the perturber through the accretion disc. The body penetrates through the disc and kicks off blobs of magnetized plasma into the empty, but strongly magnetized funnel region. This material moves at a mildly relativistic speed $\sim (0.1\text{–}0.5)c$ along the boundary between the funnel and the accretion torus. One of the possible observational effects could be quasiperiodic absorption events if the blobs cross our line of sight and the partially ionized gas can absorb a fraction of the X-ray emission of the underlying accretion flow. Moreover, when the body is large enough and sufficiently close to the SMBH, the accretion rate can be significantly influenced by the close fly-by, yielding periodic changes to the luminosity and the spectral shape of the source.

Recently, a previously quiescent galactic nucleus in a nearby galaxy ($z = 0.056$) went into outburst and regular monitoring of the source revealed absorption events with quasiperiodically changing column density (Pasham et al., 2023). These absorption events can be interpreted as an outflow with the velocity of $\sim 0.3c$, whose column density varies by approximately one order of magnitude with a period of 8.5 days. Due to the fact, that the achieved velocity is about one order of magnitude larger than the usual stellar wind, such highly ionized absorbers are called an ultra-fast outflow (UFO; Pounds et al., 2003; Tombesi et al., 2010). Under an assumption of one absorption event per orbit and in combination with the mass estimate of the central SMBH, $\log(M/M_\odot) = 7.5 \pm 0.5$, this gives us the characteristic orbital distance of the perturber $r_{\rm per} \sim 90M$ [1]. Several possible scenarios explaining these observations are discussed in detail in Pasham et al. (2023), showing that the perturber-induced outflow is a viable mechanism to produce such an outcome. If such an observational pattern could be unambiguously classified as a large mass-ratio binary system, high-cadence, large field-of-view X-ray surveys will help to identify more candidates for close binaries in active galactic nuclei (AGN).

Binaries, in which at least one of the components is an SMBH are the main extragalactic targets for the upcoming European space-based GW observatory LISA (Klein et al., 2016; Babak et al., 2017). The targeted binaries can have various objects as the other component, ranging from stellar-origin black holes or neutron stars (SOBHs/NSs) through intermediate-mass black holes (IMBH), to other SMBHs. In all cases, the GW emission causes a gradual degradation of the orbit up to the merger. If and when such events are seen by LISA, it will be of the utmost scientific interest to localize the host galaxy, which would make it a multi-messenger standard siren for cosmology (Holz and Hughes, 2005; Tamanini et al., 2016).

In this paper, we will focus on the competing possible mechanism causing the quasiperiodic UFOs, in which the UFOs originate in the magnetic reconnection events in the innermost region of the so-called magnetically arrested accretion disc (MAD disc). By means

---

[1] We work in the geometrized unit system with $G = c = 1$, hence velocities become dimensionless and times and lengths can be measured in terms of M (using standard SI or cgs units, gravitational radii are defined as $r_g = GM/c^2$ and gravitational times as GM/c^3).

of GRMHD simulations, we will compare the properties of the outflow launched by the motion of the perturber and that emanating from the temporal variability of the MAD disc stemming from the interchange instability of the plasma near the horizon. We will show that even though the 2D simulations of MAD discs yield strong periodic flares with larger amplitudes in the accretion and outflow rates, relaxing the axial symmetry assumption in 3D simulations leads to much less fierce evolution with rather stochastic variability. Moreover, the velocity of the outflow originating in the inner $\sim$ 10–20 gravitational radii achieves higher values than observed in the above-mentioned system.

In summary, the accretion in the MAD disc state does not seem to explain the observed features of the UFO better than the perturber-induced-outflow scenario.

This contribution is structured as follows. In Section 2, we introduce the numerical setup of the GRMHD simulations. The results are presented in Section 3 and we conclude with Section 4.

2 NUMERICAL SETUP

We study the behavior of the plasma numerically using the general relativistic magnetohydrodynamical code HARMPI (Ressler et al., 2015; Tchekhovskoy et al., 2007), which is based on the HARM code (Gammie et al., 2003). The code, which we have equipped with our own modifications, is 3D and parallelized. The perturber is moving along a geodesic trajectory in Kerr spacetime, assuming the accreting gas has a negligible gravitational field with respect to the central SMBH. The effect of the gravitational wave losses or the hydrodynamical drag on the secondary body can be omitted because they are negligible in such a setup during the time span of our simulation (covering tens to hundreds of orbits). Its dynamical effect on the gas is simulated assuming that all gas within the sphere of influence of the orbiting body characterized by the radius $\mathcal{R}$ is comoving with the body. The details of the numerical procedure are given in Suková et al. (2021).

The simulations proceed in two steps. In the first step, we spontaneously evolve the initial accretion torus, which is obtained as the exact solution of a magnetized torus with a non-constant angular momentum profile in equilibrium (Witzany and Jefremov, 2018). We omit the equilibrium toroidal magnetic field, instead, we equip the torus with poloidal magnetic loops, so that the MRI starts working shortly after the beginning of the simulation and the torus starts to accrete. After an initial transient time, a quasi-stationary accretion state is achieved.

We use two different configurations of the initial magnetic field. First, the magnetic field lines follow the isocontours of the density of the torus, forming one big magnetic loop over the whole torus. Such initial conditions are known to be prone to quick formation of the MAD state, in which the magnetic pressure close to the horizon balances the gas pressure, the accretion is shut down and proceeds only via the interchange instability when small blobs of matter accrete onto the black hole during the reconnection of the magnetic field lines (Bisnovatyi-Kogan and Ruzmaikin, 1974, 1976; Narayan et al., 2003). The other initial condition consists of several smaller loops with alternating polarity, which leads to a so-called SANE (standard-and-normal evolution) state.

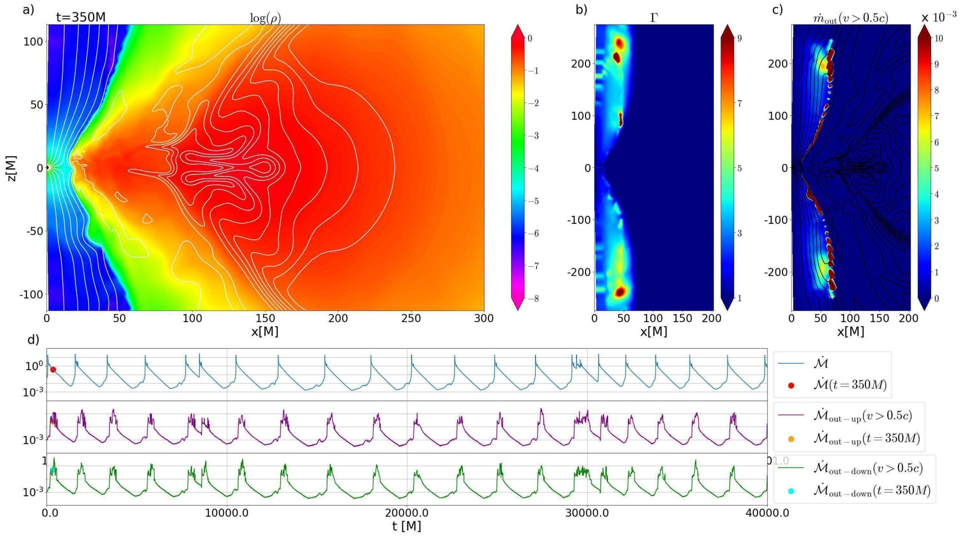

Figure 1. An instant from the 2D GRMHD numerical simulation of the accretion flow in the MAD state. The density, the Lorentz factor, and the outflowing rate density is shown in the first row, the time dependence of the accretion rate (blue), and the outflowing rate directed upward (purple) and downward (green) are shown in the bottom panel. In the two-dimensional simulation, the pressure of the accumulated organized large-scale vertical magnetic field balances the gas pressure, the accretion is halted and proceeds only intermittently via the interchange instability close to the horizon, which results in the simultaneous accretion event and ejection of relativistic outflow to both directions.

After achieving the quasi-stationary accretion state (see Fig. 1), we restart the simulation. At that point, we can regrid our simulation domain from 2D to 3D in such a way, that we copy the 2D slice into all ϕ directions, introducing a $\sim 1\%$ random perturbation in density to relax the axial symmetry and enable the evolution in the ϕ-direction (axial symmetry is preserved by the numerical scheme). At this point, we can also turn on the motion of the perturber.

With two 3D GRMHD simulations, we aim to show the distinctive nature of the outflow launched by the magnetic reconnection yielding the magnetic flux eruptions in the MAD accretion state (run 3D-MAD) and the outflow driven by the transiting body through the accretion flow (run 3D-star). We also provide long-term evolution of the 2D-MAD simulation for comparison (see Table 1 for the overview of the runs).

3 RESULTS

For our study of the MAD state, we have chosen one slice from a 2D simulation of a MAD accretion torus. At first, we continue this 2D simulation for $40\,000M$ (run-2D-MAD). In the first row of Fig. 1, we show panels with the density in logarithmic scale, the Lorentz factor, and the outflow with $v > 0.5c$. In the bottom, the three panels show the time

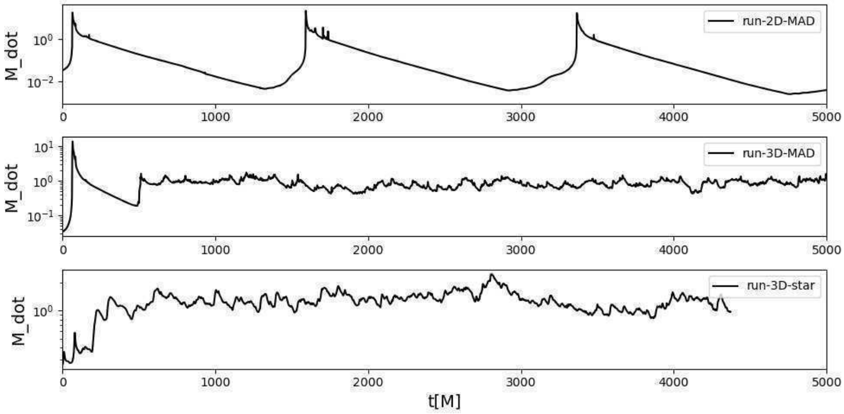

Figure 2. Time dependence of the accretion rate for all three runs shown in the time interval $[0, 5\,000]M$.

profile of accretion rate $\dot{\mathcal{M}}$ and outflowing rate $\dot{\mathcal{M}}_{\rm out}(v > 0.5c)$ directed into the upper or lower part of the funnel. We can see the time-correlated large-amplitude quasi-periodic flares in accretion rate and outflows upwards and downwards persisting during the whole simulation.

Starting with the same initial conditions as run-2D-MAD we initialize a 3D run (run-3D-MAD) with a total duration of $5\,000M$. In Fig. 2, we show the comparison of the accretion rate for all the runs. We can notice that in the 3D simulation, the disc still completes one cycle similar to the ones seen in the 2D simulation (due to our regrid procedure), but after the axisymmetry is completely lost, the accretion proceeds in a much more steady regime, the large peaks and dips are smoothed. This is due to the fact that in 3D, the individual gaseous blobs are accreting from different directions, following the magnetic reconnection events, therefore, the averaged accretion rate is more steady and does not show large-amplitude flares. Instead, smaller blobs are expelled during the accretion, which are getting stretched in the azimuthal direction, forming long dense filaments on a helical

run	a	resolution	$t_{\rm max}$	$\mathcal{R}[M]$	i	e
run-2D-MAD	0.9	384 x 192	$40\,000M$	—	—	
run-3D-MAD	0.9	384 x 192 x 96	$5\,000M$	—	—	
run-3D-star	0.5	384 x 256 x 96	$4\,370M$	2	65.5°	0.19

Table 1. Table of the performed GRMHD runs. In the columns, we list the name of the run, the SMBH spin a, the resolution of the grid, the total duration of the run, and in case of binary simulation, the influence radius $\mathcal{R}$ of the secondary and the inclination and eccentricity of the orbit.

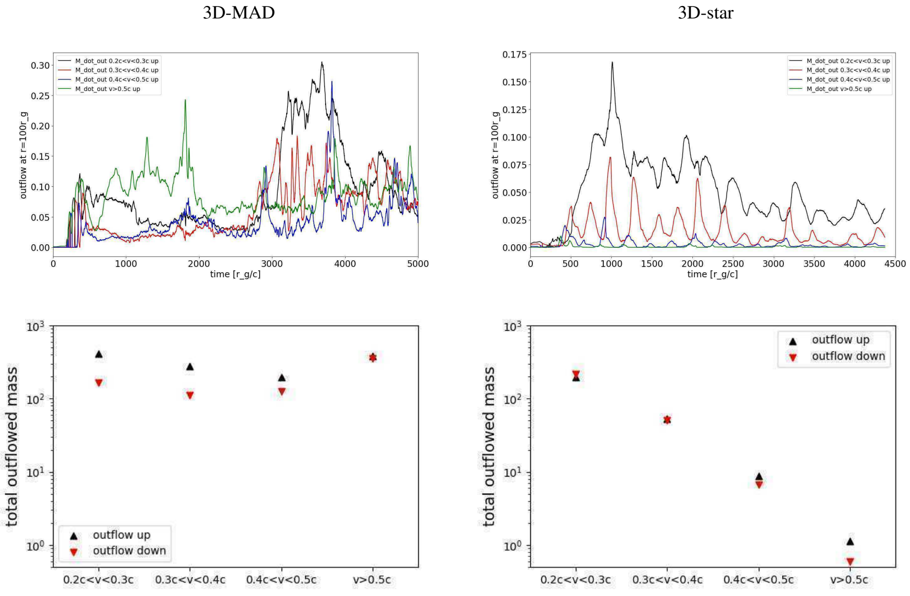
3D-MAD

3D-star

Figure 3. In the first row, we show the time profiles of the ultrafast nuclear outflow measured at $r = 100M$. On the left, we show the case corresponding to run-3D-MAD, while on the right, we show run-3D-star. With different colors, the outflow rates in 4 different velocity bins are depicted. The second row shows the total outflow in the upward (black) and downward (red) directions during the simulation in the four bins.

trajectory (see the left panel in Fig. 4). This finding is in agreement with a recent particle-in-cell simulation of reconnection-driven flares by El Mellah, I. et al. (2023). During the duration of run-3D-MAD, the accretion rate or the outflowing rates do not show prominent quasi-periodicity. However, to probe the periodicity on the time scales of about $2\,000M$ (reported e.g. in Curd and Narayan, 2022) up to about $6\,000M$, which corresponds to the observed variability, a longer 3D run is needed, which is currently beyond the scope of this contribution.

In run-3D-star, due to the computational cost of 3D simulations, we need to put the orbiting perturber on a tighter orbit than the derived characteristic distance $r_{\mathrm{pert}} = 90M$ for the above-mentioned source so that we are able to cover several consecutive revolutions of the body. The orbit is inclined with $i = 65.5°$ from the equatorial plane and slightly eccentric ($e = 0.19$), with pericenter $r_p = 10M$ and apocenter $r_a = 14.68M$. The fundamental periods in r, θ, ϕ directions (Fujita and Hikida, 2009) are $P_r = 370M, P_\theta = 273M, P_\phi = 270M$ (i.e. about 20x shorter than the measured period). Hence, the total duration of the simulation ($4370M$) covers about 16 orbits of the body, which is in line with the observed 13 peaks during the outburst of the aforementioned galactic nucleus (Pasham et al., 2023).

While the accretion rate, shown in Fig. 2, does not show strong periodicity correlated with the motion of the perturber, when looking at the corresponding time profiles of the

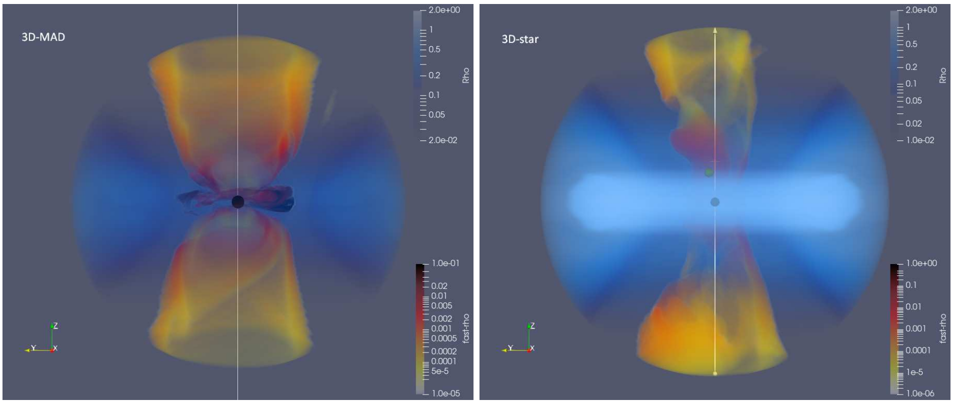

Figure 4. Snapshots from 3D simulations showing the slowly moving gas (with $\gamma < \gamma_{\rm thr}$ in the blue color scale) and fast outflowing gas (with $\gamma > \gamma_{\rm thr}$ and positive radial velocity) in the yellow-red-black color scale. On the left, we show run-3D-MAD with $\gamma_{\rm thr} = 1.05$, while on the right, we show run-3D-star with $\gamma_{\rm thr} = 1.02$.

outflowing rates, we do notice a qualitative difference. In Fig. 3 we show the outflow rates evaluated at $r = 100M$ in 4 different velocity bins, i.e. $0.2c < v < 0.3c$, $0.3c < v < 0.4c$, $0.4c < v < 0.5c$, $v > 0.5c$. We can see prominent quasiperiodicity corresponding to the motion of the perturber for the outflow velocity in the range of $0.2c < v < 0.5c$. Furthermore, while the total outflowing mass in each velocity bin is rapidly decreasing for the run-3D-star, in the case of the MAD accretion flow, the outflow with $v > 0.5c$ is larger than the outflow in three lower-velocity bins (see Fig. 3, second row). As a result, a much higher amount of mass with $v > 0.3c$ is expelled than in the perturber-induced outflow model, which can serve as a distinguishing factor between the MAD-driven nuclear outflows and the perturber-driven outflows.

4 CONCLUSIONS

We have performed two 3D GRMHD simulations, which correspond to the advection-dominated, hot accretion flow in the MAD state and the one perturbed by an orbiting body. The simulations have shown the different nature of the outflow induced by the magnetic reconnection events near the horizon in the MAD state and the outflow expelled by the transits of the secondary body through the accretion flow. The main difference lies in the more coherent periodicity of the outflows caused by the orbiting perturber on the one hand and the higher speed reached by the outflow launched by the MAD disc on the other hand.

ACKNOWLEDGEMENTS

PS has been supported by the fellowship Lumina Quaeruntur No. LQ100032102 of the Czech Academy of Sciences. This work was supported by the Ministry of Education, Youth and Sports of the Czech Republic through the e-INFRA CZ (ID:90140). VK and MZ acknowledge the Czech Science Foundation project (ref. GF23-04053L).

REFERENCES

Babak, S., Gair, J., Sesana, A., Barausse, E., Sopuerta, C. F., Berry, C. P. L., Berti, E., Amaro-Seoane, P., Petiteau, A. and Klein, A. (2017), Science with the space-based interferometer LISA. V. Extreme mass-ratio inspirals, *Phys. Rev. D*, **95**(10), 103012, arXiv: `1703.09722`.

Bisnovatyi-Kogan, G. S. and Ruzmaikin, A. A. (1974), The Accretion of Matter by a Collapsing Star in the Presence of a Magnetic Field, *Astrophys. Space Sci.*, **28**(1), pp. 45–59.

Bisnovatyi-Kogan, G. S. and Ruzmaikin, A. A. (1976), The Accretion of Matter by a Collapsing Star in the Presence of a Magnetic Field. II: Self-consistent Stationary Picture, *Astrophys. Space Sci.*, **42**(2), pp. 401–424.

Curd, B. and Narayan, R. (2022), GRRMHD simulations of MAD accretion discs declining from super-Eddington to sub-Eddington accretion rates, *Monthly Notices of the Royal Astronomical Society*, **518**(3), pp. 3441–3461, ISSN 0035-8711, arXiv: `https://academic.oup.com/mnras/article-pdf/518/3/3441/47466433/stac3330.pdf`, URL `https://doi.org/10.1093/mnras/stac3330`.

El Mellah, I., Cerutti, B. and Crinquand, B. (2023), Reconnection-driven flares in 3d black hole magnetospheres - a scenario for hot spots around sagittarius a*, *A&A*, **677**, p. A67, URL `https://doi.org/10.1051/0004-6361/202346781`.

Event Horizon Telescope Collab., Akiyama, K., Alberdi, A. et al. (2019), First M87 Event Horizon Telescope Results. I. The Shadow of the Supermassive Black Hole, *Astrophys. J. Lett.*, **875**(1), L1, arXiv: `1906.11238`.

Fujita, R. and Hikida, W. (2009), Analytical solutions of bound timelike geodesic orbits in kerr spacetime, *Classical and Quantum Gravity*, **26**(13), p. 135002, URL `https://dx.doi.org/10.1088/0264-9381/26/13/135002`.

Gammie, C. F., McKinney, J. C. and Tóth, G. (2003), Harm: A numerical scheme for general relativistic magnetohydrodynamics, *ApJ*, **589**(1), p. 444, URL `http://stacks.iop.org/0004-637X/589/i=1/a=444`.

Gravity Collaboration, Abuter, R., Amorim, A., Bauböck, M. et al. (2018), Detection of orbital motions near the last stable circular orbit of the massive black hole SgrA*, *Astron. Astrophys.*, **618**, L10, arXiv: `1810.12641`.

Holz, D. E. and Hughes, S. A. (2005), Using gravitational-wave standard sirens, *Apj*, **629**(1), p. 15.

Klein, A., Barausse, E., Sesana, A., Petiteau, A., Berti, E., Babak, S., Gair, J., Aoudia, S., Hinder, I., Ohme, F. and Wardell, B. (2016), Science with the space-based interferometer eLISA: Supermassive black hole binaries, *Phys. Rev. D*, **93**(2), 024003, arXiv: `1511.05581`.

Narayan, R., Igumenshchev, I. V. and Abramowicz, M. A. (2003), Magnetically Arrested Disk: an Energetically Efficient Accretion Flow, *Publ. Astron. Soc. Jpn*, **55**, pp. L69–L72, arXiv: `astro-ph/0305029`.

Pasham, D. R., Tombesi, F., Suková, P., Zajacek, M., Rakshit, S., Coughlin, E., Kosec, P. and Karas, V. (2023), A Case for a Binary Black Hole System Revealed via Quasi-Periodic Outflows, *submitted to Nature*.

Pounds, K. A., Reeves, J. N., King, A. R., Page, K. L., O'Brien, P. T. and Turner, M. J. L. (2003), A high-velocity ionized outflow and XUV photosphere in the narrow emission line quasar PG1211+143, *Mon. Not. R. Astron. Soc.*, **345**(3), pp. 705–713, arXiv: `astro-ph/0303603`.

Ressler, S. M., Tchekhovskoy, A., Quataert, E., Chandra, M. and Gammie, C. F. (2015), Electron thermodynamics in GRMHD simulations of low-luminosity black hole accretion, *Mon. Not. R. Astron. Soc.*, **454**, pp. 1848–1870, arXiv: `1509.04717`.

Suková, P., Zajaček, M., Witzany, V. and Karas, V. (2021), Stellar transits across a magnetized accretion torus as a mechanism for plasmoid ejection, *ApJ*, **917**(1), p. 43, URL `https://doi.org/10.3847/1538-4357/ac05c6`.

Tamanini, N., Caprini, C., Barausse, E., Sesana, A., Klein, A. and Petiteau, A. (2016), Science with the space-based interferometer eLISA. III: probing the expansion of the universe using gravitational wave standard sirens, *J. Cosmol. Astropart. Phys.*, **2016**(4), 002, arXiv: `1601.07112`.

Tchekhovskoy, A., McKinney, J. C. and Narayan, R. (2007), WHAM: a WENO-based general relativistic numerical scheme - I. Hydrodynamics, *Mon. Not. R. Astron. Soc.*, **379**, pp. 469–497, arXiv: `0704.2608`.

Tombesi, F., Cappi, M., Reeves, J. N., Palumbo, G. G. C., Yaqoob, T., Braito, V. and Dadina, M. (2010), Evidence for ultra-fast outflows in radio-quiet AGNs. I. Detection and statistical incidence of Fe K-shell absorption lines, *Astron. Astrophys.*, **521**, A57, arXiv: `1006.2858`.

Witzany, V. and Jefremov, P. (2018), New closed analytical solutions for geometrically thick fluid tori around black holes. Numerical evolution and the onset of the magneto-rotational instability, *Astron. Astrophys.*, **614**, A75, arXiv: `1711.09241`.

Proceedings of *RAGtime 23–25*
Z. Stuchlík, G. Török, V. Karas and D. Lančová, editors, Silesian University in Opava, 2023, pp. 119–134

Theory-agnostic parametrization of wormhole spacetimes

Thomas D. Pappas

Research Centre for Theoretical Physics and Astrophysics, Institute of Physics,
Silesian University in Opava, Bezručovo náměstí 13, CZ-746 01 Opava, Czech Republic
`thomas.pappas@physics.slu.cz`

ABSTRACT
We present[1] a generalization of the Rezzolla-Zhidenko theory-agnostic parametrization of black-hole spacetimes to accommodate spherically-symmetric Lorentzian, traversable wormholes (WHs) in an arbitrary metric theory of gravity. By applying our parametrization to various known WH metrics and performing calculations involving shadows and quasinormal modes, we show that only a few parameters are important for finding potentially observable quantities in a WH spacetime.

Keywords: Wormholes – theory-agnostic parametrization – wormhole shadows – quasinormal modes

1 INTRODUCTION

Wormholes (WHs) are hypothetical tunnel-like spacetime structures that connect two different regions of our Universe and can even be envisaged as bridges between different universes (Visser, 1995). The concept of a WH emerged as early as 1916 in the work by Flamm (1916), and also in the works of Einstein and Rosen (1935) and Wheeler (1955), however, these WHs were non-traversable. The first examples of exact solutions in GR corresponding to traversable WHs sourced by a phantom scalar field have been obtained in Bronnikov (1973); Ellis (1973). A significant rekindling of interest in the subject came about with the work of Morris and Thorne (1988).

As the work of Morris and Thorne and subsequent studies have revealed, traversable WHs typically come with a number of problems, such as the requirement of exotic forms of matter to support the throat from collapsing (Morris and Thorne, 1988), and/or dynamical instabilities (Bronnikov and Grinyok, 2001; Gonzalez et al., 2009; Bronnikov et al., 2011, 2012; Bronnikov, 2018; Cuyubamba et al., 2018). To date, *there is no known fully satisfactory model for a traversable, Lorentzian WH that has been proven to be both free of the necessity for exotic mater for its existence and at the same time corresponding to a dynamically stable configuration.* As a consequence, a general theory-agnostic approach

---

[1] Talk given by the author at RAGtime 23, Opava, Czech Republic, based on Bronnikov et al. (2021).

978-80-7510-576-9

to parametrizing a WH geometry in such a way that can be constrained by current and upcoming observations could provide a solution. For a recent review on the search for astrophysical WHs in our Universe, the reader is directed to Bambi and Stojkovic (2021).

In the case of black hole (BH) geometries, a general theory-agnostic parametrization that can be constrained from observations has been proposed by Rezzolla and Zhidenko (2014) (RZ). This method is similar in spirit to the parametrized post-Newtonian formalism, albeit with validity that is not limited to the weak-field regime but rather covers the whole spacetime outside the event horizon of the BH. The RZ BH metric is defined in terms of a compact radial coordinate and a continued fraction expansion involving an infinite tower of dimensionless parameters. Due to the rapid convergence properties of the continued fractions, however, in practice, only the first few of the expansion parameters are dominant and important for describing observable quantities in a BH background. Inspired by the above, in Bronnikov et al. (2021), we proposed a modification of the RZ BH metric that allows for the parametrization of WH geometries in a theory-agnostic way.

This article is structured as follows. In Sec. 2, we discuss in general terms some features of asymptotically flat WH spacetimes. In Sec. 3, we provide a brief overview of the RZ BH parametrization and then introduce our extended parametrization for WH. In Sec. 4 we obtain parmetrizations for examples of known WH metrics. Section 5 is dedicated to the study of shadows and quasinormal modes on the parametrized WH backgrounds as tests for the accuracy of our method. We conclude in Sec. 6.

2 WORMHOLE SPACETIMES: GENERAL CONSIDERATIONS

2.1 Asymptotically flat, traversable Lorentzian wormholes

The line element for an arbitrary four-dimensional static, spherically symmetric geometry can be written as

$$\mathrm{d}s^2 = -f(r)\mathrm{d}t^2 + \frac{1}{h(r)}\mathrm{d}r^2 + K^2(r)\left(\mathrm{d}\theta^2 + \sin^2\theta\,\mathrm{d}\phi^2\right). \tag{1}$$

Out of the three metric functions $f(r)$, $h(r)$, $K(r)$ in the above ansatz, only two are independent, and upon appropriately transforming the radial coordinate, any metric can be cast in the form where $K(r) = r$, however, this might not always be feasible analytically. In general, the area of the sphere at radial coordinate r is $A(r) = 4\pi K^2(r)$. A WH structure is characterized by a minimum radius r_0 called the *throat* (the narrowest part of the tunnel) for which the surface area is minimized, namely

$$A'(r_0) = 0 \rightarrow K'(r_0) = 0\,. \tag{2}$$

The metric functions $f(r)$ and $h(r)$ are regular and positive in a range of r containing the throat and values of r on both sides from the throat such that $K(r) \gg K(r_0)$. It is then said that the metric (1) describes a *traversable, Lorentzian WH*. Furthermore, a WH is classified as being asymptotically flat if, for r tending to some $r = r_\infty$, the following conditions are satisfied

$$f(r) \rightarrow 1\,, \qquad h(r)\left(\frac{\mathrm{d}K(r)}{\mathrm{d}r}\right)^2 \rightarrow 1\,. \tag{3}$$

2.2 The Morris-Thorne frame

A very commonly used frame in the literature where WH metrics are written is the one introduced by Morris and Thorne (1988) (MT)

$$ds^2 = -e^{2\Phi(r)}dt^2 + \left(1 - \frac{b(r)}{r}\right)^{-1} dr^2 + r^2 d\Omega^2. \tag{4}$$

There are two arbitrary metric functions in the above line element. The first, $\Phi(r)$, is often called the *redshift function*, and the absence of event horizons (WH traversability) requires that it should be finite everywhere. The second, $b(r)$, is called *shape function*, and indirectly determines the spatial shape of the WH in its embedding diagram representation. In the MT frame, r_0 is determined by the condition

$$h(r) = \left(1 - \frac{b(r)}{r}\right) = 0, \tag{5}$$

while $e^{\Phi(r_0)} > 0$ is required, and the radial coordinate is defined for $r \in [r_0, \infty)$. The shape function should satisfy the so-called flair-out conditions on the throat, $b(r_0) = r_0$ and $b'(r_0) < 1$ while $b(r) < r$ for $r \neq r_0$. In the framework of GR, Morris and Thorne (1988) showed that WHs require the presence of some sort of exotic matter that violates the null energy condition. For recent developments regarding traversable WHs without exotic matter in Einstein-Dirac-Maxwell theory see Blázquez-Salcedo et al. (2021); Bolokhov et al. (2021); Konoplya and Zhidenko (2022b).

2.3 Wormhole shadows

In this section, we outline the method for the computation of shadows in an arbitrary static spherically symmetric and asymptotically flat spacetime Synge (1966); Perlick et al. (2015). Starting with the general metric ansatz (1), it is convenient to introduce the function

$$w^2(r) \equiv \frac{K^2(r)}{f(r)}. \tag{6}$$

The photon-sphere radius $r_{\rm ph}$, corresponds to the minimum of $w^2(r)$ and is thus determined as a solution to

$$\frac{dw^2(r_{\rm ph})}{dr} = 0. \tag{7}$$

The angular radius of the shadow (associated with the outermost photon sphere), as seen by a distant static observer located at $r_{\rm O}$, is then obtained by means of (6) as

$$\sin^2 \alpha_{\rm sh} = \frac{w^2(r_{\rm ph})}{w^2(r_{\rm O})}. \tag{8}$$

Under the assumption $r_{\rm O} \gg r_0$, where r_0 is a characteristic length scale that can be identified with the radius of the WH throat or the BH event horizon depending on the nature of the compact object under consideration, we have that

$$f(r_{\rm O}) \simeq 1, \quad K^2(r_{\rm O}) \simeq r_O^2, \tag{9}$$

and thus, one finds that the radius of the shadow is given by

$$R_{\rm sh} \simeq r_{\rm O} \sin a_{\rm sh} \simeq w(r_{\rm ph}) = \frac{K(r_{\rm ph})}{\sqrt{f(r_{\rm ph})}} \,. \tag{10}$$

3 CONTINUED-FRACTION PARAMETRIZATION FOR WORMHOLES

3.1 The Rezzolla-Zhidenko parametrized black-hole metric

Let us begin this section by briefly reviewing the parametrization of spherically symmetric BHs suggested in Rezzolla and Zhidenko (2014) (RZ), and subsequently, we will see which modifications of this approach are required when going over to WH geometries. The RZ parametrization is based on a dimensionless compact coordinate (DCC) that maps $[r_0, \infty) \to [0, 1]$ according to

$$x(r) \equiv 1 - \frac{r_0}{r} \,, \tag{11}$$

where r_0 is the location of the outer event horizon of the BH determined via the condition $f(r_0) = 0$. If $K^2(r) = r^2$, then r_0 is also the radius of the outer event horizon. In terms of (11), the following parametrization equations are introduced:

$$f(r) = \widetilde{A}\,(x) \,, \tag{12}$$

$$\frac{1}{h(r)} = \frac{\widetilde{B}\,(x)}{\widetilde{A}\,(x)} \,, \tag{13}$$

where the parametrization functions $\widetilde{A}(x)$ and $\widetilde{B}(x)$ are defined as

$$\widetilde{A}\,(x) \equiv x \left[1 - \epsilon\,(1-x) + (a_0 - \epsilon)\,(1-x)^2 + \cfrac{a_1}{1 + \cfrac{a_2 x}{1 + \cfrac{a_3 x}{\cdots}}}\,(1-x)^3 \right], \tag{14}$$

$$\widetilde{B}\,(x) \equiv \left[1 + b_0\,(1-x) + \cfrac{b_1}{1 + \cfrac{b_2 x}{1 + \cfrac{b_3 x}{\cdots}}}\,(1-x)^2 \right]^2 \,. \tag{15}$$

The above parametrization involves two families of parameters. The first family consists of three "asymptotic" parameters (ϵ, a_0, b_0), which are determined via the expansions of the parametrization equations at spatial infinity ($x = 1$), while the second family consists of the remaining parameters $(a_1, a_2, \ldots, b_1, b_2, \ldots)$ i.e. the "near-field" parameters which are determined at the location of the event horizon ($x = 0$). For the axially-symmetric generalization of the RZ metric see Konoplya et al. (2016), while for its higher-dimensional extension see Konoplya et al. (2020b). More recently, an extension of the parametrization to non-asymptotically flat cases has been proposed in Konoplya and Zhidenko (2022a, 2023).

3.2 The parametrized wormhole metric

To construct our WH parametrization, we consider the radial coordinate compactification according to (11), with r_0 interpreted in this context as the location of the WH radius[2]. Then, we may parametrize the metric functions according to Bronnikov et al. (2021)

$$f(r) = f_0 + x\left[(1-f_0) - (\epsilon + f_0)(1-x) + (a_0 - \epsilon - f_0)(1-x)^2 + \frac{a_1(1-x)^3}{1 + \frac{a_2 x}{1+\frac{a_3 x}{\dots}}}\right], \tag{16}$$

$$h(r) = h_0 + x\left[(1-h_0) - (b_0 + h_0)(1-x) + \frac{b_1(1-x)^2}{1 + \frac{b_2 x}{1+\frac{b_3 x}{\dots}}}\right]. \tag{17}$$

Being an extension of the RZ parametrization, it is no surprise that our parametrized WH metric shares several appealing properties with its BH predecessor, to which it reduces in the limit $(f_0, h_0) \to (0, 0)$. Quite importantly, it is valid for all space ($x \in [0, 1]$), not only near $x = 0$ or $x = 1$, and the continued-fraction expansions, endow the parametrization with quick converge properties[3]. The $n-$th order approximation of a given metric can be easily obtained by setting the $(n+1) - th$ near-field parameters (a_{n+1}, b_{n+1}) equal to zero, thus removing all the higher-order parameters from the expressions of the metric functions. The metric (16)-(17) involves once again two families of parameters, the asymptotic (ϵ, a_0, b_0), which are determined at $(x = 1)$ and the set (f_0, h_0, a_i, b_i) which are determined near the throat of the WH ($x = 0$), in analogy to the BH case discussed in the previous section.

3.3 Observational constraints on the asymptotic parameters

Given that the parametrization is developed in a theory-agnostic way, i.e. independently of the underlying theory of gravity, there are no precise constraints to be imposed on the metric functions $f(r)$ and $h(r)$. However, general constraints on the asymptotic parameters can be imposed via the parameterized post-Newtonian (PPN) expansions (Will, 2006, 2014). To this end, consider the expansions of our parametrized metric (16)-(17) at $x = 1$

$$f(r) = 1 - (1+\epsilon)(1-x) + a_0(1-x)^2 + O\Big((1-x)^3\Big), \tag{18}$$

$$\frac{1}{h(r)} = 1 + (1+b_0)(1-x) + O\Big((1-x)^2\Big). \tag{19}$$

It is then straightforward, by comparison with the PPN expansions, to associate the asymptotic parameters (ϵ, a_0, b_0) with the PPN parameters β and γ in the following way

$$\epsilon = \frac{2M}{r_0} - 1\,, \quad a_0 = \frac{2M^2}{r_0^2}(\beta - \gamma)\,, \tag{20}$$

---

[2] For alternative definitions of the DCC and its optimization see Bronnikov et al. (2021).

[3] These properties, allow for the parametrization to also be utilized for the analytic representation of numerical WH solutions along the lines of the analyses performed for BH spacetimes, see e.g. Younsi et al. (2016); Kokkotas et al. (2017); Hennigar et al. (2018); Konoplya and Zhidenko (2019); Konoplya et al. (2020a).

and

$$b_0 = \gamma \frac{2M}{r_0} - 1 \quad \Rightarrow \quad b_0 = \gamma\,(\epsilon + 1) - 1\,. \tag{21}$$

Since β and γ are constrained as $|\beta - 1| \lesssim 2.3 \times 10^{-4}$, and $|\gamma - 1| \lesssim 2.3 \times 10^{-5}$, it follows that in our parametrization, astrophysically viable WHs must be characterized by $a_0 \simeq 0$ and $b_0 \simeq \epsilon$. This is to be contrasted with the PPN constraints on the BH parametrization for which one finds $a_0 \simeq 0$ and $b_0 \simeq 0$ (Rezzolla and Zhidenko, 2014; Bronnikov et al., 2021).

4 EXAMPLES OF PARAMETRIZATION

In this section, we consider various exact WH geometries and obtain the parametrizations for the first few orders in the continued-fraction expansion. This will provide a means to test the adequacy of the proposed method in providing accurate approximations for WH geometries in terms of only a few coefficients of the expansion. For more details and examples of WH parametrizations the interested reader is referred to Bronnikov et al. (2021).

4.1 The Bronnikov-Kim II braneworld wormhole solution

In the context of the so-called Randall-Sundrum II braneworld model (Randall and Sundrum, 1999), by solving the Shiromizu-Maeda-Sasaki modified Einstein equations on the brane (Shiromizu et al., 2000), Bronnikov and Kim in Bronnikov and Kim (2003) have obtained a large class of static, spherically symmetric Lorentzian wormhole solutions. Here, we consider one of those solutions corresponding to a two-parametric family of spacetimes, with a line element given by

$$\begin{aligned} \mathrm{d}s^2 &= -\left(1 - \frac{\alpha^2}{r^2}\right)\mathrm{d}t^2 + \left(1 - \frac{\alpha^2}{r^2}\right)^{-1}\left(1 + \frac{C - \alpha}{\sqrt{2r^2 - \alpha^2}}\right)^{-1}\mathrm{d}r^2 + r^2\mathrm{d}\Omega^2, \\ &= -\left(1 - \frac{\alpha^2}{r^2}\right)\mathrm{d}t^2 + \left(1 - \frac{\alpha^2}{r^2}\right)^{-1}\left(1 - \sqrt{\frac{2r_0^2 - \alpha^2}{2r^2 - \alpha^2}}\right)^{-1}\mathrm{d}r^2 + r^2\mathrm{d}\Omega^2\,, \end{aligned} \tag{22}$$

where in the second line we have used the condition (5) for the determination of the location of the WH throat r_0, in order to write $C = \alpha - \left(2r_0^2 - \alpha^2\right)^{1/2}$. The above line element is one with a zero Schwarzschild mass and exhibits black-hole and wormhole branches. For the WH branch, the absence of horizons implies $f(r) \equiv -g_{tt}(r) > 0\,\forall\, r \in [r_0, \infty)$ and so the following condition between the parameters is established

$$f(r_0) = \left(1 - \frac{\alpha^2}{r_0^2}\right) \geqslant 0 \Rightarrow r_0 \geqslant \alpha\,. \tag{23}$$

The threshold between the WH and BH branches of the solution corresponds to $\alpha = r_0$, where in this case, r_0 is identified with the location of the (double) BH event horizon. The WH/BH threshold is of special importance for testing the accuracy of the parametrization in the case of WHs that deviate only slightly from a BH geometry, thus corresponding to BH mimickers, see e.g. Damour and Solodukhin (2007); Churilova and Stuchlik (2020); Bronnikov and Konoplya (2020). For the metric function $f(r)$ the parametrization is exact[4] with the values of the expansion parameters (EPs) being

$$\epsilon = -1\,, \quad a_0 = -\frac{\alpha^2}{r_0^2}\,, \quad f_0 = 1 - \frac{\alpha^2}{r_0^2}\,, \quad a_i = 0 \quad \forall i \geqslant 1\,. \tag{24}$$

On the other hand, the parametrization of $h(r)$ is not exact, the first few EPs are

$$b_0 = \sqrt{1 - \frac{\alpha^2}{2r_0^2}} - 1\,, \quad h_0 = 0\,, \quad b_1 = b_0 + \frac{\alpha^2}{\alpha^2 + 2r_0^2}\,, \tag{25}$$

$$b_2 = \frac{2\alpha^4\,(1 + b_0) - \alpha^2\,(7 + 8b_0)\,r_0^2 + 8b_0 r_0^4}{b_1\left(\alpha^2 - 2\,r_0^2\right)^2} - 3\,. \tag{26}$$

According to results presented in Table 1, the first-order approximation, provides a very accurate description of the metric (22) with an absolute relative error (ARE) less than 1% for the majority of the parametric space, i.e. for $p \lesssim 0.6$, but becomes less accurate as the WH/BH threshold is approached ($p \to 1$). However, it is also evident that the parametrization converges very quickly and as a consequence, the error is significantly reduced once the second-order correction is taken into account even at the WH/BH threshold (Bronnikov et al., 2021).

Table 1. The maximum ARE in percents between the exact metric $h(r)$ and its approximation at various orders in terms of the dimensionless parameter $p \equiv \alpha/r_0 \leqslant 1$. The WH/BH threshold corresponds to $p = 1$.

order	$p = 0.1$	$p = 0.3$	$p = 0.5$	$p = 0.7$	$p = 0.8$	$p = 0.99$
1	0.00063	0.05460	0.49509	2.53408	5.39226	31.12707
2	0.00010	0.00840	0.07270	0.34042	0.67203	2.49612
3	0.00001	0.00118	0.00829	0.02370	0.02622	0.13332
4	$O(10^{-8})$	0.00004	0.00093	0.00883	0.02312	0.12947

4.2 The Simpson-Visser geometry

In Simpson and Visser (2019) (SV), an interesting geometry has been introduced as a toy-model via a one-parameter deformation of the Schwarzschild metric. Written in terms of the quasiglobal coordinate, the SV line element reads

$$\mathrm{d}s^2 = -\left(1 - \frac{2\,m}{\sqrt{r^2 + \alpha^2}}\right)\mathrm{d}t^2 + \frac{\mathrm{d}r^2}{\left(1 - \frac{2\,m}{\sqrt{r^2+\alpha^2}}\right)} + \left(r^2 + \alpha^2\right)\mathrm{d}\Omega^2\,. \tag{27}$$

---

[4] Note that, whenever a metric function has a polynomial form, the parametrization is, by construction, always exact at a finite order. This holds true for both the original RZ (14)-(15) and our (16)-(17) parametrized metrics.

The above line-element has been generalized to axial symmetry by Mazza et al. (2021), while the field sources for the SV metric have been obtained recently by Bronnikov and Walia (2022). Depending on the value of the dimensionless parameter $p \equiv \alpha/m$, the SV metric describes a traversable WH for $p > 2$, an extremal regular BH for $p = 2$ (thus this value of p defines also the WH/BH threshold), for $p < 2$ a black-bounce state is obtained (see Simpson and Visser, 2019)[5], while for $p = 0$ the Schwarzschild geometry is recovered, see also Fig. 1.

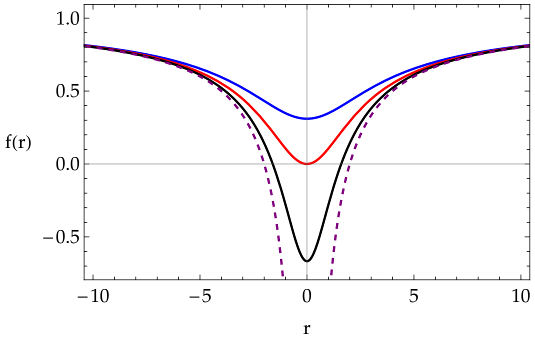

Figure 1. The $f(r)$ metric function of the Simpson-Visser geometry (27) corresponding to a traversable wormhole (blue curve, for $p \equiv \alpha/m = 2.9$), an extremal regular BH (red curve, for $p = 2$), a black bounce (black curve, for $p = 1.2$), the Schwarzschild BH limit (dashed curve, for $p \to 0$).

Notice that the metric (27) is not in the Morris-Thorne frame (4) since $K^2(r) \neq r^2$. To this end, one may perform the coordinate transformation $r \to \tilde{r} : \tilde{r}^2 = r^2 + \alpha^2$, in order to recast the metric to the MT frame where it is written as

$$ds^2 = -\left(1 - \frac{2m}{\tilde{r}}\right)dt^2 + \left(1 - \frac{2m}{\tilde{r}}\right)^{-1}\left(1 - \frac{\alpha^2}{\tilde{r}^2}\right)^{-1} d\tilde{r}^2 + \tilde{r}^2 d\Omega^2. \tag{28}$$

Then, one may proceed with the parametrization in terms of (11) and (17). The condition (5), which determines the location of the WH throat r_0 in the MT frame, yields the following equation in the case of the SV wormhole

$$h(r) \equiv \left(1 - \frac{2m}{\tilde{r}}\right)\left(1 - \frac{\alpha^2}{\tilde{r}^2}\right) = 0. \tag{29}$$

There are two roots to the above equation, which are located at $\tilde{r} = 2m$ and $\tilde{r} = \alpha$. The former root, is not a suitable choice for a WH throat because, in this case, $f(\tilde{r}_0) = 0$, and an event horizon emerges. Thus, the WH branch corresponds to the region in the parametric

---

[5] See also Bronnikov and Fabris (2006); Bronnikov et al. (2007); Bolokhov et al. (2012).

space defined by $\alpha > 2m$. Since the metric functions in (28) are of polynomial form, the parametrization is exact with the EPs given by

$$\begin{aligned}
&\epsilon = \frac{2m}{\alpha} - 1\,, \quad a_0 = 0\,, \quad f_0 = 1 - \frac{2m}{\alpha}\,, \quad a_i = 0 \quad \forall i \geqslant 1,\\
&b_0 = \frac{2m}{\alpha} - 1\,, \quad h_0 = 0\,, \quad b_1 = -\frac{2m}{\alpha}\,, \quad b_i = 0 \quad \forall i \geqslant 2.
\end{aligned} \tag{30}$$

A general parametrization for WH metrics in non-MT frames by means of (16) and (17) is also possible upon appropriate modification of the DCC. In particular, for the line-element (27), the optimized version of the DCC[6]

$$x(r) = 1 - \sqrt{\frac{R_0^2}{R_0^2 + r^2}}\,, \qquad R_0 = \alpha\sqrt{\frac{3}{2}}\,, \tag{31}$$

yields a parametrization for the SV metric with the first few EPs given by

$$\begin{aligned}
&\epsilon = \frac{2m}{R_0} - 1\,, \quad a_0 = 0\,, \quad f_0 = 1 - \frac{2m}{\alpha}\,, \quad a_1 = 2\epsilon + 3f_0 - 1 + \frac{2mR_0^2}{\alpha^3},\\
&a_2 = \frac{3}{2a_1}\left(4\epsilon + 5f_0 - 3a_1 - 1 + \frac{2mR_0^4}{\alpha^5}\right).
\end{aligned} \tag{32}$$

5 SHADOWS AND PERTURBATIONS OF TEST FIELDS

In this section, as gauge-invariant tests for the accuracy of the parametrization, we consider shadows and perturbations of test fields in the background of the approximate WH metrics obtained by considering various orders in the continued-fraction expansion and compare them with the corresponding values obtained when the exact metric expressions are used.

5.1 Shadows of the anti-Fisher wormhole

In the context of GR with a massless minimally-coupled scalar field, a solution containing a naked singularity has been found (Fisher, 1948). When the kinetic term of the scalar field has the opposite sign, a solution emerges which has a WH branch and has been called anti-Fisher solution (Bronnikov, 1973). The metric functions for the latter solution assume the following form

$$f(r) = h(r) = e^{2u(r)}, \quad K^2(r) = e^{-2u(r)}\left(r^2 + \alpha^2\right), \quad u(r) \equiv \frac{m}{\alpha}\left(\arctan\frac{r}{\alpha} - \frac{\pi}{2}\right). \tag{33}$$

Substitution of (33) in the general expression (10), yields the shadow radius for the anti-Fisher WH

$$R_{\rm sh} = e^{-2\,u(r_{\rm ph})}\sqrt{4m^2 + \alpha^2}, \tag{34}$$

---

[6] For more details on the DCC optimization see Bronnikov et al. (2021).

where $r_{\rm ph} = 2m$ is the photon sphere radius which has been determined via (7). The first few EPs for the parametrization of $f(r)$ in this case are given by

$$\epsilon = 1, \quad a_0 = 2, \quad f_0 = e^{2u(m)}, \quad a_1 = f_0\left(3 + \frac{2m^2}{\alpha^2 + m^2}\right) - 1,$$
$$a_2 = \frac{6f_0 - 4a_1 - 2}{a_1}, \quad a_3 = -\frac{f_0\left[\frac{2m^4}{3(\alpha^2+m^2)^2} - 10\right] + a_1\left[10 + a_2\left(5 + a_2\right)\right] + 4}{a_1 a_2}. \tag{35}$$

By considering various orders in the approximation of $f(r)$ via (16) and (35), we once again compute the shadow radius by means of (10) and compare the result order-by-order with the exact value given in Eq. (34). Our findings (Bronnikov et al., 2021) are presented in terms of the dimensionless parameter $p \equiv \alpha/m$ in Table 2. The high accuracy of the approximation already at the first order and the quick convergence are evident.

Table 2. The percentage of absolute relative error between the exact value of the shadow radius (34) and its value as obtained via Eq. (10) for various approximation orders of the metric function $f(r)$.

order	$p = 0.01$	$p = 0.2$	$p = 0.3$	$p = 0.4$	$p = 0.5$	$p = 0.6$
1	1.04775	0.95530	0.83863	0.67406	0.46096	0.19918
2	0.02753	0.03339	0.04295	0.06093	0.09281	0.14633
3	0.00304	0.00387	0.00570	0.01061	0.02367	0.05883
4	0.00011	0.00019	0.00034	0.00063	0.00112	0.00186

5.2 Shadows of the Simpson-Visser wormhole

As a second example for shadows in a wormhole background, we consider the SV metric in the non-Morris-Thorne frame i.e. (27), for which we obtain the exact expression for the shadow radius

$$R_{\rm sh} = 3\sqrt{3}m. \tag{36}$$

Notice that the value of $R_{\rm sh}$ is independent of the parameter α and it is identified with the shadow radius of the Schwarzschild BH, for detailed discussions see Tsukamoto (2021); Lima et al. (2021). Subsequently, by considering various orders for the approximate metric according to (32), we compute once again $R_{\rm sh}$ and compare it with the exact result (36). The range of values for the dimensionless parameter $p \equiv \alpha/m$ that is relevant for the analysis here is $p \in [2, 3]$ where the lower bound corresponds to the WH/BH threshold and the upper bound corresponds to the maximum value of p for which the spacetime under consideration exhibits a photon sphere. Our findings (Bronnikov et al., 2021) are displayed in Table 3.

Table 3. The percentage of absolute relative error between the analytic value of the shadow and its value for various approximation orders of the metric.

order	$p = 2.01$	$p = 2.1$	$p = 2.4$	$p = 2.5$	$p = 2.7$	$p = 2.99$
1	0.54727	0.47968	0.25291	0.18463	0.07285	0.00009
2	0.01973	0.01568	0.00544	0.00329	0.00076	$\mathcal{O}(10^{-8})$
3	0.00278	0.00200	0.00046	0.00023	0.00003	$\mathcal{O}(10^{-11})$
4	0.00060	0.00039	0.00005	0.00002	$\mathcal{O}(10^{-6})$	$\mathcal{O}(10^{-13})$

We observe that already with the first-order approximation of the metric, the error is less than 1% for all values of p, and it is monotonically decreasing from the WH/BH threshold all the way to the no-photon sphere limit. Furthermore, one can see the quick convergence of the series where the error is reduced by approximately one order of magnitude with each additional term in the expansion that is taken into account.

5.3 Quasinormal modes

Let us now consider the fundamental quasinormal modes (QNMs) of the electromagnetic field propagating in a WH background. QNMs are characteristic frequencies of a compact object which are independent of the initial conditions of perturbations and are completely determined by the parameters of the compact object under consideration (Kokkotas and Schmidt, 1999; Berti et al., 2009; Konoplya and Zhidenko, 2011). The real part of a QNM represents a real oscillation frequency, while the imaginary part is proportional to the damping rate. For a non exhaustive list of works where QNMs in WHs backgrounds have been studied, see Konoplya and Zhidenko (2010); Bronnikov et al. (2012); Taylor (2014); Cuyubamba et al. (2018); Völkel and Kokkotas (2018); Aneesh et al. (2018); Konoplya (2018); Kim et al. (2018); Dutta Roy et al. (2020); Churilova et al. (2020); Jusufi (2021); Biswas et al. (2022). An electromagnetic field obeys the general covariant Maxwell equations

$$\frac{1}{\sqrt{-g}}\partial_\mu\left(F_{\rho\sigma}g^{\rho\nu}g^{\sigma\mu}\sqrt{-g}\right) = 0. \tag{37}$$

Here $F_{\rho\sigma} = \partial_\rho A_\sigma - \partial_\sigma A_\rho$ and A_μ is a vector potential. For the spherically-symmetric spacetime (1), one may introduce the "tortoise coordinate" r_*, in terms of the metric functions $f(r)$ and $h(r)$ as

$$\mathrm{d}r_* = \frac{\mathrm{d}r}{\sqrt{f(r)h(r)}}. \tag{38}$$

Then, after separation of variables, Eq. (37) assumes the following wave-like form

$$\frac{\mathrm{d}^2\Psi}{\mathrm{d}r_*^2} + \left(\omega^2 - V(r)\right)\Psi = 0, \tag{39}$$

and the effective potential reads as

$$V_{\mathrm{em}}(r) = f(r)\frac{\ell(\ell+1)}{r^2}. \tag{40}$$

Even though the effective potential depends on the gravitational background only via the metric function $f(r)$, the QNMs will depend on both $f(r)$ and $h(r)$ implicitly via the tortoise coordinate (38). The boundary conditions for finding QNMs in a WH background correspond to purely outgoing waves at both infinities $r_* \to \pm\infty$ (Konoplya and Molina, 2005). The values of QNMs obtained for the Bronnikov-Kim II and Simpson-Viser WHs both of which have been discussed in the previous sections, are displayed in Tables 4 and 5 respectively (Bronnikov et al., 2021).

Table 4. Fundamental quasinormal modes ($\ell = 1$, $n = 0$) of the electromagnetic field for the Bronnikov-Kim II wormhole.

order	$C = -0.01$	$C = -0.3$	$C = -0.7$
exact	$0.64306 - 0.20529i$	$0.70322 - 0.03991i$	$0.73338 - 0.09961i$
1st	$0.65899 - 0.19306i$	$0.70232 - 0.03741i$	$0.73304 - 0.09836i$
2nd	$0.64093 - 0.20593i$	$0.70332 - 0.04009i$	$0.73345 - 0.09969i$

Table 5. Fundamental quasinormal modes ($\ell = 1, n = 0$) of the electromagnetic field for the Simpson-Visser wormhole ($m = 1/2$).

order	$\alpha = 1.01$	$\alpha = 1.25$	$\alpha = 1.4$
exact	$0.51125 - 0.13311i$	$0.55491 - 0.03299i$	$0.56858 - 0.05986i$
1st	$0.50899 - 0.13211i$	$0.55394 - 0.03297i$	$0.56770 - 0.05982i$
2nd	$0.51241 - 0.13405i$	$0.55520 - 0.03286i$	$0.56885 - 0.05969i$

As it can be seen, the QNMs obtained with the first two orders in the continued-fraction expansion of the background metric approximate very accurately the values obtained in terms of the exact metric.

6 CONCLUSIONS

Building upon the Rezzolla and Zhidenko (2014) theory-agnostic parametrization of BH spacetimes, we have introduced an extension that allows for general Lorentzian, traversable, static and asymptotically-flat WH metrics to be accommodated in this parameterized framework (Bronnikov et al., 2021). The parametrization is based on a continued-fraction expansion in terms of a compactified radial coordinate, exhibits rapid convergence properties, and is valid in all of spacetime.

We have obtained the parametrizations for various examples of known wormhole geometries and studied the shadows and perturbations of test fields in these gravitational backgrounds for different orders in the expansion. Quite importantly, by considering geometries that interpolate continuously between a BH and a WH, we have demonstrated that the parametrization is very accurate, (already at the first and in some cases second-order in the expansion), even at the WH/BH threshold and this is relevant for WHs that act as BH mimickers.

Our analysis demonstrates that when a WH metric changes relatively slowly in the radiation zone, the observable effects in the wormhole background depend only on a few parameters and the following approximation for the line-element is sufficient (Bronnikov et al., 2021)[7]

$$\mathrm{d}s^2 = -f(r)\mathrm{d}t^2 + \frac{1}{h(r)}\mathrm{d}r^2 + r^2\mathrm{d}\Omega^2\,, \tag{41}$$

$$f(r) = 1 - \frac{r_0\,(1+\epsilon)}{r} + \frac{r_0^3\,(a_1 + f_0 + \epsilon)}{r^3} - \frac{r_0^4\,a_1}{r^4}\,, \tag{42}$$

$$h(r) = 1 - \frac{r_0\,(1+\epsilon)}{r} + \frac{r_0^2\,(b_1 + h_0 + \epsilon)}{r^2} - \frac{r_0^3\,b_1}{r^3}\,. \tag{43}$$

ACKNOWLEDGMENTS

The author would like to thank the organizers of RAGtime 23 for giving him the opportunity to present this work, and acknowledges the support of the Research Centre for Theoretical Physics and Astrophysics of the Institute of Physics at the Silesian University in Opava.

REFERENCES

Aneesh, S., Bose, S. and Kar, S. (2018), Gravitational waves from quasinormal modes of a class of Lorentzian wormholes, *Phys. Rev.*, **D97**(12), p. 124004, arXiv: `1803.10204`.

Bambi, C. and Stojkovic, D. (2021), Astrophysical Wormholes, *Universe*, **7**(5), p. 136, arXiv: `2105.00881`.

Berti, E., Cardoso, V. and Starinets, A. O. (2009), Quasinormal modes of black holes and black branes, *Class. Quant. Grav.*, **26**, p. 163001, arXiv: `0905.2975`.

Biswas, S., Rahman, M. and Chakraborty, S. (2022), Echoes from braneworld wormholes, *Phys. Rev. D*, **106**(12), p. 124003, arXiv: `2205.14743`.

Blázquez-Salcedo, J. L., Knoll, C. and Radu, E. (2021), Traversable wormholes in Einstein-Dirac-Maxwell theory, *Phys. Rev. Lett.*, **126**(10), p. 101102, arXiv: `2010.07317`.

Bolokhov, S., Bronnikov, K., Krasnikov, S. and Skvortsova, M. (2021), A Note on “Traversable Wormholes in Einstein–Dirac–Maxwell Theory”, *Grav. Cosmol.*, **27**(4), pp. 401–402, arXiv: `2104.10933`.

Bolokhov, S. V., Bronnikov, K. A. and Skvortsova, M. V. (2012), Magnetic black universes and wormholes with a phantom scalar, *Class. Quant. Grav.*, **29**, p. 245006, arXiv: `1208.4619`.

Bronnikov, K. and Kim, S.-W. (2003), Possible wormholes in a brane world, *Phys. Rev. D*, **67**, p. 064027, arXiv: `gr-qc/0212112`.

Bronnikov, K. A. (1973), Scalar-tensor theory and scalar charge, *Acta Phys. Polon. B*, **4**, pp. 251–266.

Bronnikov, K. A. (2018), Scalar fields as sources for wormholes and regular black holes, *Particles*, **1**(1), pp. 56–81, arXiv: `1802.00098`.

Bronnikov, K. A. and Fabris, J. C. (2006), Regular phantom black holes, *Phys. Rev. Lett.*, **96**, p. 251101, arXiv: `gr-qc/0511109`.

---

[7] We have also extended the general parametrized metric (41)-(43) to accommodate slowly-rotating WHs Bronnikov et al. (2021).

Bronnikov, K. A., Fabris, J. C. and Zhidenko, A. (2011), On the stability of scalar-vacuum spacetimes, *Eur. Phys. J. C*, **71**, p. 1791, arXiv: `1109.6576`.

Bronnikov, K. A. and Grinyok, S. (2001), Instability of wormholes with a nonminimally coupled scalar field, *Grav. Cosmol.*, **7**, pp. 297–300, arXiv: `gr-qc/0201083`.

Bronnikov, K. A. and Konoplya, R. A. (2020), Echoes in brane worlds: ringing at a black hole–wormhole transition, *Phys. Rev. D*, **101**(6), p. 064004, arXiv: `1912.05315`.

Bronnikov, K. A., Konoplya, R. A. and Pappas, T. D. (2021), General parametrization of wormhole spacetimes and its application to shadows and quasinormal modes, *Phys. Rev. D*, **103**(12), p. 124062, arXiv: `2102.10679`.

Bronnikov, K. A., Konoplya, R. A. and Zhidenko, A. (2012), Instabilities of wormholes and regular black holes supported by a phantom scalar field, *Phys. Rev.*, **D86**, p. 024028, arXiv: `1205.2224`.

Bronnikov, K. A., Melnikov, V. N. and Dehnen, H. (2007), Regular black holes and black universes, *Gen. Rel. Grav.*, **39**, pp. 973–987, arXiv: `gr-qc/0611022`.

Bronnikov, K. A. and Walia, R. K. (2022), Field sources for Simpson-Visser spacetimes, *Phys. Rev. D*, **105**(4), p. 044039, arXiv: `2112.13198`.

Churilova, M. S., Konoplya, R. A. and Zhidenko, A. (2020), Arbitrarily long-lived quasinormal modes in a wormhole background, *Phys. Lett.*, **B802**, p. 135207, arXiv: `1911.05246`.

Churilova, M. S. and Stuchlik, Z. (2020), Ringing of the regular black-hole/wormhole transition, *Class. Quant. Grav.*, **37**(7), p. 075014, arXiv: `1911.11823`.

Cuyubamba, M. A., Konoplya, R. A. and Zhidenko, A. (2018), No stable wormholes in Einstein-dilaton-Gauss-Bonnet theory, *Phys. Rev.*, **D98**(4), p. 044040, arXiv: `1804.11170`.

Damour, T. and Solodukhin, S. N. (2007), Wormholes as black hole foils, *Phys. Rev.*, **D76**, p. 024016, arXiv: `0704.2667`.

Dutta Roy, P., Aneesh, S. and Kar, S. (2020), Revisiting a family of wormholes: geometry, matter, scalar quasinormal modes and echoes, *Eur. Phys. J.*, **C80**(9), p. 850, arXiv: `1910.08746`.

Einstein, A. and Rosen, N. (1935), The Particle Problem in the General Theory of Relativity, *Phys. Rev.*, **48**, pp. 73–77.

Ellis, H. G. (1973), Ether flow through a drainhole - a particle model in general relativity, *J. Math. Phys.*, **14**, pp. 104–118.

Fisher, I. Z. (1948), Scalar mesostatic field with regard for gravitational effects, *Zh. Eksp. Teor. Fiz.*, **18**, pp. 636–640, arXiv: `gr-qc/9911008`.

Flamm, L. (1916), Beiträge zur Einsteinschen Gravitationstheorie, *Phys. Z.*, **17**, p. 448.

Gonzalez, J. A., Guzman, F. S. and Sarbach, O. (2009), Instability of wormholes supported by a ghost scalar field. I. Linear stability analysis, *Class. Quant. Grav.*, **26**, p. 015010, arXiv: `0806.0608`.

Hennigar, R. A., Poshteh, M. B. J. and Mann, R. B. (2018), Shadows, Signals, and Stability in Einsteinian Cubic Gravity, *Phys. Rev. D*, **97**(6), p. 064041, arXiv: `1801.03223`.

Jusufi, K. (2021), Correspondence between quasinormal modes and the shadow radius in a wormhole spacetime, *Gen. Rel. Grav.*, **53**(9), p. 87, arXiv: `2007.16019`.

Kim, J. Y., Lee, C. O. and Park, M.-I. (2018), Quasi-Normal Modes of a Natural AdS Wormhole in Einstein-Born-Infeld Gravity, *Eur. Phys. J.*, **C78**(12), p. 990, arXiv: `1808.03748`.

Kokkotas, K., Konoplya, R. A. and Zhidenko, A. (2017), Non-Schwarzschild black-hole metric in four dimensional higher derivative gravity: analytical approximation, *Phys. Rev. D*, **96**, p. 064007, arXiv: `1705.09875`.

Kokkotas, K. D. and Schmidt, B. G. (1999), Quasinormal modes of stars and black holes, *Living Rev. Rel.*, **2**, p. 2, arXiv: `gr-qc/9909058`.

Konoplya, R., Rezzolla, L. and Zhidenko, A. (2016), General parametrization of axisymmetric black holes in metric theories of gravity, *Phys. Rev.*, **D93**(6), p. 064015, arXiv: `1602.02378`.

Konoplya, R. and Zhidenko, A. (2010), Passage of radiation through wormholes of arbitrary shape, *Phys. Rev. D*, **81**, p. 124036, arXiv: `1004.1284`.

Konoplya, R. A. (2018), How to tell the shape of a wormhole by its quasinormal modes, *Phys. Lett.*, **B784**, pp. 43–49, arXiv: `1805.04718`.

Konoplya, R. A. and Molina, C. (2005), The Ringing wormholes, *Phys. Rev.*, **D71**, p. 124009, arXiv: `gr-qc/0504139`.

Konoplya, R. A., Pappas, T. and Zhidenko, A. (2020a), Einstein-scalar–Gauss-Bonnet black holes: Analytical approximation for the metric and applications to calculations of shadows, *Phys. Rev. D*, **101**(4), p. 044054, arXiv: `1907.10112`.

Konoplya, R. A., Pappas, T. D. and Stuchlík, Z. (2020b), General parametrization of higher-dimensional black holes and its application to Einstein-Lovelock theory, *Phys. Rev. D*, **102**(8), p. 084043, arXiv: `2007.14860`.

Konoplya, R. A. and Zhidenko, A. (2011), Quasinormal modes of black holes: From astrophysics to string theory, *Rev. Mod. Phys.*, **83**, pp. 793–836, arXiv: `1102.4014`.

Konoplya, R. A. and Zhidenko, A. (2019), Analytical representation for metrics of scalarized Einstein-Maxwell black holes and their shadows, *Phys. Rev. D*, **100**(4), p. 044015, arXiv: `1907.05551`.

Konoplya, R. A. and Zhidenko, A. (2022a), How general is the strong cosmic censorship bound for quasinormal modes?, *JCAP*, **11**, p. 028, arXiv: `2210.04314`.

Konoplya, R. A. and Zhidenko, A. (2022b), Traversable Wormholes in General Relativity, *Phys. Rev. Lett.*, **128**(9), p. 091104, arXiv: `2106.05034`.

Konoplya, R. A. and Zhidenko, A. (2023), Overtones' outburst of asymptotically AdS black holes, arXiv: `2310.19205`.

Lima, H. C. D., Junior., Crispino, L. C. B., Cunha, P. V. P. and Herdeiro, C. A. R. (2021), Can different black holes cast the same shadow?, *Phys. Rev. D*, **103**(8), p. 084040, arXiv: `2102.07034`.

Mazza, J., Franzin, E. and Liberati, S. (2021), A novel family of rotating black hole mimickers, *JCAP*, **04**, p. 082, arXiv: `2102.01105`.

Morris, M. S. and Thorne, K. S. (1988), Wormholes in space-time and their use for interstellar travel: A tool for teaching general relativity, *Am. J. Phys.*, **56**, pp. 395–412.

Perlick, V., Tsupko, O. Y. and Bisnovatyi-Kogan, G. S. (2015), Influence of a plasma on the shadow of a spherically symmetric black hole, *Phys. Rev. D*, **92**(10), p. 104031, arXiv: `1507.04217`.

Randall, L. and Sundrum, R. (1999), An Alternative to compactification, *Phys. Rev. Lett.*, **83**, pp. 4690–4693, arXiv: `hep-th/9906064`.

Rezzolla, L. and Zhidenko, A. (2014), New parametrization for spherically symmetric black holes in metric theories of gravity, *Phys. Rev. D*, **90**(8), p. 084009, arXiv: `1407.3086`.

Shiromizu, T., Maeda, K.-i. and Sasaki, M. (2000), The Einstein equation on the 3-brane world, *Phys. Rev.*, **D62**, p. 024012, arXiv: `gr-qc/9910076`.

Simpson, A. and Visser, M. (2019), Black-bounce to traversable wormhole, *JCAP*, **02**, p. 042, arXiv: `1812.07114`.

Synge, J. L. (1966), The Escape of Photons from Gravitationally Intense Stars, *Mon. Not. Roy. Astron. Soc.*, **131**(3), pp. 463–466.

Taylor, P. (2014), Propagation of Test Particles and Scalar Fields on a Class of Wormhole Space-Times, *Phys. Rev.*, **D90**(2), p. 024057, [Erratum: Phys. Rev.D95,no.10,109904(2017)], arXiv: `1404.7210`.

Tsukamoto, N. (2021), Gravitational lensing in the Simpson-Visser black-bounce spacetime in a strong deflection limit, *Phys. Rev. D*, **103**(2), p. 024033, arXiv: `2011.03932`.

Visser, M. (1995), *Lorentzian wormholes: From Einstein to Hawking*, ISBN 978-1-56396-653-8.

Völkel, S. H. and Kokkotas, K. D. (2018), Wormhole Potentials and Throats from Quasi-Normal Modes, *Class. Quant. Grav.*, **35**(10), p. 105018, arXiv: `1802.08525`.

Wheeler, J. A. (1955), Geons, *Phys. Rev.*, **97**, pp. 511–536.

Will, C. M. (2006), The Confrontation between general relativity and experiment, *Living Rev. Rel.*, **9**, p. 3, arXiv: `gr-qc/0510072`.

Will, C. M. (2014), The Confrontation between General Relativity and Experiment, *Living Rev. Rel.*, **17**, p. 4, arXiv: `1403.7377`.

Younsi, Z., Zhidenko, A., Rezzolla, L., Konoplya, R. and Mizuno, Y. (2016), New method for shadow calculations: Application to parametrized axisymmetric black holes, *Phys. Rev. D*, **94**(8), p. 084025, arXiv: `1607.05767`.

Proceedings of *RAGtime 23–25*
Z. Stuchlík, G. Török, V. Karas and D. Lančová, editors, Silesian University in Opava, 2023, pp. 135–142

Energy dissipation in astrophysical simulations: results of the Orszag-Tang test problem

Fatemeh Kayanikhoo,[1,a] Miljenko Čemeljić,[1,2,3]
Maciek Wielgus[4] and Wodek Kluźniak[1]

[1]Nicolaus Copernicus Astronomical Center,
Bartycka 18, 00-716, Warszaw, Poland,
[2]Research Centre for Computational Physics and Data Processing,
Institute of Physics, Silesian University in Opava,
Bezručovo nám. 13, CZ-746 01 Opava, Czech Republic,
[3]Academia Sinica, Institute of Astronomy and Astrophysics,
P.O. Box 23-141, Taipei 106, Taiwan
[4]Max-Planck-Institut für Radioastronomie,
Auf dem Hügel 69, D-53121 Bonn, Germany
[a]`fatima@camk.edu.pl`

ABSTRACT
The magnetic field through the magnetic reconnection process affects the dynamics and structure of astrophysical systems. Numerical simulations are the tools to study the evolution of these systems. However, the resolution, dimensions, resistivity, and turbulence of the system are some important parameters to take into account in the simulations. In this paper, we investigate the evolution of magnetic energy in astrophysical simulations by performing a standard test problem for MHD codes, Orszag-Tang. We estimate the numerical dissipation in the simulations using state-of-the-art numerical simulation code in astrophysics, PLUTO. The estimated numerical resistivity in 2D simulations corresponds to the Lundquist number $\approx 10^4$ in the resolution of 512×512 grid cells. It is also shown that the plasmoid unstable reconnection layer can be resolved with sufficient resolutions. Our analysis demonstrates that in non-relativistic magnetohydrodynamics simulations, magnetic and kinetic energies undergo conversion into internal energy, resulting in plasma heating.

Keywords: Magnetohydrodynamics – magnetic energy dissipation – resistivity – numerical simulations – PLUTO

1 INTRODUCTION

The evolution of magnetic fields has a significant impact on the dynamics and structure of astrophysical systems, ranging from stars and planets to galaxies and even the large-scale structure of the universe. Magnetic reconnection is believed to be a responsible mechanism of magnetic field evolution. Magnetic reconnection can explain the heating and acceleration of particles or plasmoids which are observed in high energy ejections like solar

978-80-7510-576-9

flares (Giovanelli, 1946; Jiang et al., 2021), magnetic substorms in the Earth magnetosphere (McPherron, 1979; Akasofu, 1968), jets, and relativistic ejections from the accretion discs of compact objects (Ripperda et al., 2020, 2022).

In this study, we conduct the Orszag-Tang (OT; Orszag and Tang, 1979), a well-known test problem in numerical magnetohydrodynamics (MHD) simulation codes, used to examine the dissipation of magnetic energy and substructure formation in magnetized plasma. We estimate the numerical resistivity by employing a resistive MHD (Res-MHD) module in the PLUTO code (Mignone et al., 2007), and we find a resolution sufficient for investigating the system's properties. Subsequently, we investigate the energy conversion in MHD simulations.

This paper is structured into the following sections: In Section 2, we present the MHD equations, describe the initial and boundary conditions of the OT test problem, and detail the numerical setups. Section 3 is dedicated to the discussion of simulation results, including the estimation of numerical resistivity and analysis of energy conversion. The final section provides the conclusions.

2 NUMERICAL APPROACH AND PROBLEM CONDITIONS

2.1 Magnetohydrodynamics (MHD) method

The MHD method is based on the equations of conservation of mass, momentum, and energy, and Maxwell's equations as follows

$$\frac{\partial\rho}{\partial t} + \boldsymbol{\nabla}\cdot(\rho\boldsymbol{v}) = 0, \tag{1}$$

$$\frac{\partial\rho\boldsymbol{v}}{\partial t} + \boldsymbol{\nabla}\cdot(\rho\boldsymbol{v}\boldsymbol{v} + p\boldsymbol{I} + \boldsymbol{T}_{\mathrm{EM}}) = 0, \tag{2}$$

$$\frac{\partial\varepsilon}{\partial t} + \boldsymbol{\nabla}\cdot\left[\left(\omega + \rho\frac{v^2}{2}\right)\boldsymbol{v} + c\boldsymbol{E}\times\boldsymbol{B}\right] = 0, \tag{3}$$

where ρ and $\boldsymbol{v}$ are density and velocity, respectively. $\boldsymbol{I}$ represents the identity tensor, T_{EM} is the electromagnetic stress tensor, ϵ is the total energy density and $\omega = p + U_{\mathrm{int}}$ is enthalpy density, where U_{int} is the internal energy. Magnetic and electric fields are denoted with $\boldsymbol{B}$ and $\boldsymbol{E}$, respectively,

$$\frac{1}{c}\frac{\partial\boldsymbol{B}}{\partial t} + \boldsymbol{\nabla}\times\boldsymbol{E} = 0, \tag{4}$$

$$\frac{1}{c}\frac{\partial\boldsymbol{E}}{\partial t} - \boldsymbol{\nabla}\times\boldsymbol{B} = -\frac{\boldsymbol{J}}{c}. \tag{5}$$

In the equations above, $\boldsymbol{J}$ is the current density that comes from Ohms law,

$$\boldsymbol{J} = \frac{c^2}{\eta}\left(\boldsymbol{E} + \frac{\boldsymbol{v}}{c}\times\boldsymbol{B}\right) = c\boldsymbol{\nabla}\times\boldsymbol{B}, \tag{6}$$

where, in the cgs system of units we use, η represents the physical resistivity.

2.2 Initial and boundary conditions

We solve the OT test problem using the MHD approximation method. This problem is a standard test problem in MHD codes to examine the power of the code to capture the MHD shocks and shock-shock interactions.

We set up the simulations of the OT test problem in a 2D box $0 < x, y < 2\pi$ with periodic boundary conditions (Orszag and Tang, 1979) with the polytropic equation of stat with adiabatic index $\gamma = 4/3$.

The initial velocity and magnetic fields of the OT test problem are

$$v = v_0 \, (-\sin y, \sin x, 0) \, , \tag{7}$$

$$B = B_0 \, (-\sin y, \sin 2x, 0) \, , \tag{8}$$

where we define $v_0 = 0.99c/\sqrt{2}$ and $B_0 = c\sqrt{4\pi\rho_0}$ where ρ_0 is the scaling factor of density in code unit. The simulation results are presented in the code unit where the factor $1/\sqrt{4\pi}$ and speed of light c are absorbed in the magnetic field and velocity, respectively. The initial density and pressure are constant ($\rho = 1$ and $P = 10$ in the code unit).

2.3 Numerical setup

We perform the OT test problem in Minkowski coordinate in the Newtonian code `PLUTO` v. 4.4. The equations are solved using the `HLLC` Riemann solver and the Monotonized Central difference limiter `MC`. The equations are evolved in time using the second-order Runge-Kutta method (`RK2`). To ensure $\boldsymbol{\nabla} \cdot \boldsymbol{B} = 0$, we use the flux-constrained transport `CT` method.

3 SIMULATION RESULTS AND DISCUSSION

The simulations are performed in the resolutions in the range of 64×64 to 4096×4096 grid cells, with the step of multiplying by 2 in each direction. All simulations run to the final time $t = 10\, t_c$ ($t_c = L/c$ is the light-crossing time with $L = 1$ as the typical length of the system).

We study the energy evolution of the system by exploring the averaged energy densities $\overline{Q}$ defined by

$$\overline{Q} = \frac{\iint_S Q \, \mathrm{d}x \, \mathrm{d}y}{\iint_S \mathrm{d}x \, \mathrm{d}y} . \tag{9}$$

3.1 Numerical resistivity

To investigate the system evolution, we determine the required resolution at which the numerical error has the least effect on the physics of the system.

In this section, we assess the numerical resistivity in simulations at different resolutions using the resistive MHD (Res-MHD) module in `PLUTO`. The sufficient resolution is the resolution in which the numerical resistivity is less than the physical resistivity, and the substructures (plasmoids) are captured. Plasmoids are regions of higher density and lower magnetization relative to their surroundings that may exist in the magnetic reconnection layers. Plasmoids evolve along the reconnection layers by growth, bulk acceleration, and mergers. Theoretical studies show that the plasmoid unstable reconnection layers exist when the Lundquist number ($S = L/\eta$) is larger than 10^4 (Ripperda et al., 2020; Loureiro et al., 2007). We search for the resolution that the numerical resistivity in the code unit is less than 10^{-4}.

In the left panel of Fig. 1, we present the time evolution of $\overline{B^2}$ in the non-resistive, ideal MHD simulations at various resolutions. The value of $\overline{B^2}$ shows an increase as the resolution is enhanced (numerical resistivity decreases). This indicates that as the resolution increases, the curves exhibit greater convergence.

To determine the numerical resistivity at each resolution, we compare the time evolution of $\overline{B^2}$ in ideal MHD simulations ($\eta = 0$) and Res-MHD simulations at different physical resistivity values (e.g. $\eta = 10^{-4}$, 10^{-3}, and 5×10^{-3}). When the Res-MHD curve converges to the MHD curve, it indicates that the numerical resistivity is less than/equal to the physical resistivity.

For example, in the right panel of Fig. 1, we present the results of simulations at a resolution of 512×512 grid cells. It is evident that the curve corresponding to $\eta = 10^{-4}$ converges to the MHD curve ($\eta = 0$). This convergence implies that the numerical dissipation at the resolution of 512×512 grid cells is $\geq 10^{-4}$. Therefore, the resolutions $\geq 512 \times 512$ grid cells can be suitable for studying the evolution and properties of the system.

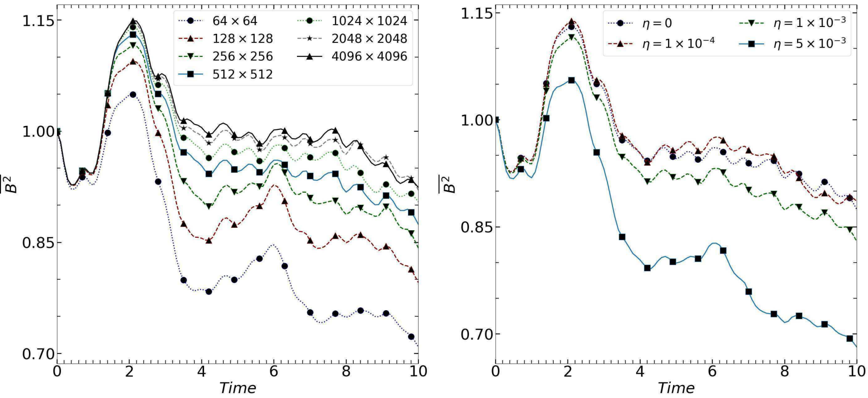

Figure 1. Time evolution of $\overline{B^2}$ in MHD simulations in different resolutions (*Left*) and in Res-MHD simulations in the resolution of 512×512 grid cells and different physical resistivities (*Right*) using PLUTO code.

In Fig. 2 are shown the current densities in ideal MHD simulations in two resolutions at $t = 2.5\,t_c$. The zoomed frames at the bottom show the reconnection layer in the middle of the simulation boxes. The left panel shows the results with the resolution of 1024×1024 grid cells, where the numerical resistivity is less than 10^{-4}, so the current layer is thin enough to become plasmoid unstable. The right panel shows the results in lower resolution

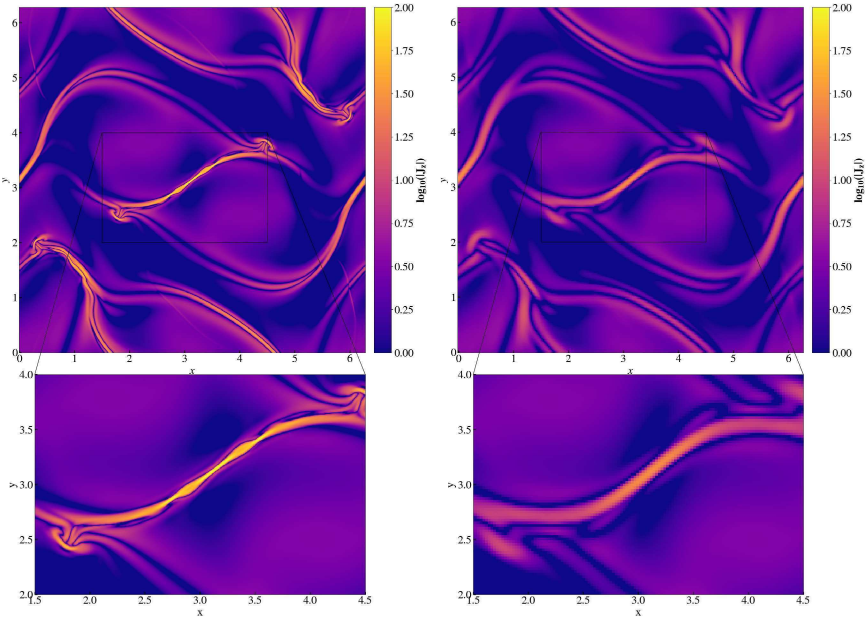

Figure 2. Current density J_z at $t = 2.5\,t_c$ of MHD simulation in the resolution of 1024×1024 (*left*) and 256×256 grid cells (*right*). The bottom frames show the zoomed-out of the reconnection layer in the middle of the simulation box.

256×256 grid cells that give higher numerical resistivity ($> 10^{-4}$), the layer is thick, and plasmoids do not emerge. We studied the magnetic reconnection and plasmoid formation in different models of resistive MHD, relativistic MHD, and 3D simulations in Kayanikhoo et al. (2023). In addition, Puzzoni et al. (2021) studied the particle acceleration in the reconnection layer using `PLUTO` concerning the impact of Riemann solvers and reconstruction methods, grid resolutions, and numerical resistivity on particle acceleration in magnetic reconnection simulations. Their findings demonstrate that particle acceleration undergoes variations based on the choice of numerical solvers and Lundquist numbers ($S \geq 10^3$).

3.2 Energy conversion in MHD simulations

In this section, we study the magnetic energy dissipation in MHD and Res-MHD simulations. The conserved total energy density contains magnetic energy density $E_B = B^2/2$, kinetic energy density $E_k = \rho v^2/2$, internal energy $U_{\text{int}} = p/(\gamma - 1)$, and electric energy density $E_E = E^2/2$. We present the energy components that are computed at the resolution of 512×512 grid cells in Fig. 3. The left column displays ideal MHD simulations ($\eta = 0$), while the right column represents Res-MHD simulations ($\eta = 5 \times 10^{-3}$).

In the top row of panels, we show the time evolution of magnetic energy. The magnetic energy increases to ≈ 1.15 times its initial value at $t \simeq 2\,t_c$, coinciding with the presence of a current layer. Shortly after, at $2.5\,t_c$, plasmoids emerge within the current layer in the ideal

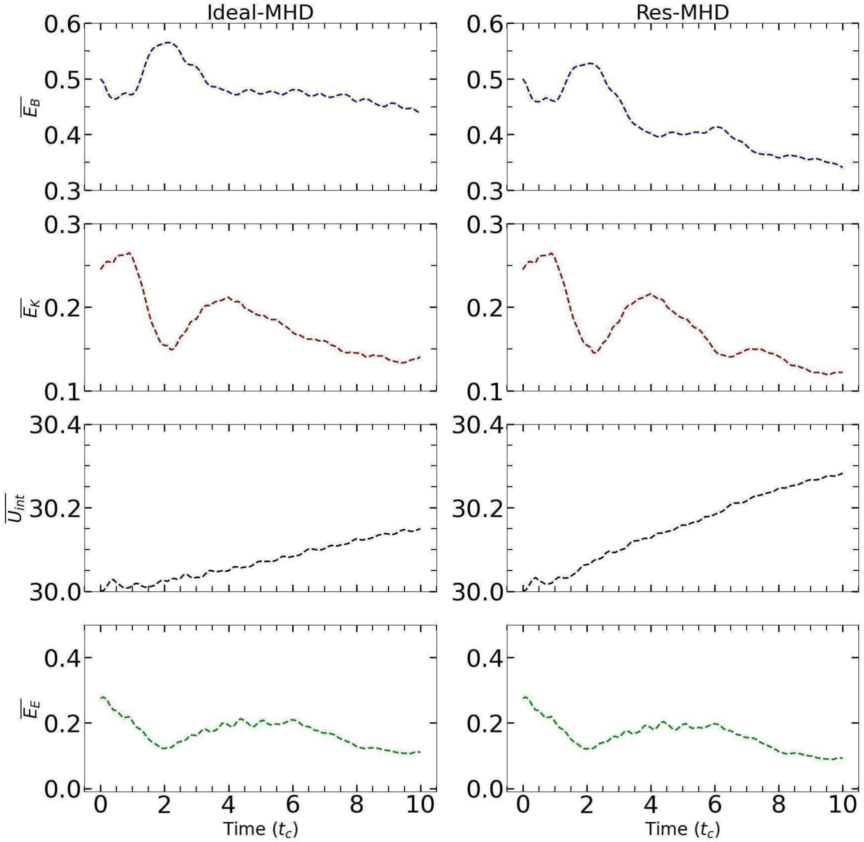

Figure 3. The time evolution of the averaged density of energy components in the simulations MHD and Res-MHD ($\eta = 5 \times 10^{-3}$) at the resolution of 512×512 grid cells.

MHD simulation (shown in Fig. 2). Subsequently, magnetic energy gradually dissipates as the simulation progresses. In the Res-MHD simulation, we note that the magnetic energy dissipates at a faster rate compared to the ideal MHD simulation.

In the second row of Fig. 3, we show the average density of kinetic energy. The evolution of kinetic and magnetic energies illustrates that kinetic energy leads to the amplification of the magnetic field at approximately $2\,t_c$. Magnetic energy converts to kinetic energy through the magnetic reconnection to the time step $t \simeq 4\,t_c$.

Both kinetic and magnetic energies dissipate into internal energy by the end of the simulation time, heating the plasma, as shown in the third-row panels. It is evident that resistivity results in increased dissipation, causing internal energy to rise by approximately 0.5% more than in the ideal MHD simulation. The last row of panels represents electric energy, which evolves similarly to magnetic and kinetic energy, as expected.

4 CONCLUSIONS

In this paper, we investigated the magnetic energy evolution in the magnetized plasma by performing the Orszag-Tang (OT) test problem, in astrophysical magnetohydrodynamic (MHD) code `PLUTO` v. 4.4. OT is a standard test problem to test the power of MHD codes to capture shocks and resolve the substructures.

Using the resistive MHD module in `PLUTO`, we estimate the numerical dissipation in each resolution. The numerical resistivity in the resolution of 512×512 grid cells is estimated to be $\geq 10^{-4}$ which represents the lowest limit for the existence of the plasmoid-unstable current layer. In the ideal MHD simulation in the resolution of 1024×1024 grid cells, the plasmoid-unstable current layer is observed while in the lower resolution, 256×256 grid cells the plasmoids do not appear. Furthermore, our results confirm that in the Res-MHD simulation with a physical resistivity of 10^{-4}, plasmoids do not emerge within the layer.

We studied the energy evolution in MHD and Res-MHD simulations. Our findings show that kinetic energy drives the amplification of the magnetic field, resulting in magnetic energy reaching approximately 1.15 times its initial value. In MHD simulation, shortly after this increase, the plasmoids are observed within the current layer. Subsequently, both magnetic and kinetic energies gradually dissipate over the course of the simulation, with the dissipated energy converting into internal energy and heating the plasma. The results indicate that in resistive MHD simulation with resistivity $\eta = 5 \times 10^{-3}$, the dissipation is 0.5% higher than in MHD simulation.

In Kayanikhoo et al. (2023), we further examined 3D simulations, compared relativistic and non-relativistic MHD simulations through energy conversion and magnetic reconnection rates, and the impact of resolution on reconnection rates in the models. Additionally, we compared two MHD codes widely used in astrophysics `PLUTO` and `KORAL`.

ACKNOWLEDGEMENTS

This project was funded by the Polish NCN grant No.2019/33/B/ST9/01564. MČ acknowledges the Czech Science Foundation (GAČR) grant No. 21-06825X. MW was supported by the European Research Council advanced grant “M2FINDERS - Mapping Magnetic Fields with INterferometry Down to Event hoRizon Scales” (Grant No. 101018682). High-resolution computations in this work were performed on the Prometheus and Ares machines, part of the PLGrid infrastructure.

REFERENCES

Akasofu, S. (1968), *Magnetospheric Substorm*, pp. 212–253, Springer Netherlands, Dordrecht, ISBN 978-94-010-3461-6.

Giovanelli, R. G. (1946), A theory of chromospheric flares, *Nature Astronomy*, **158**(4003), pp. 81–82.

Jiang, X., Chaowei Feng, Liu, R., Yan, X., Hu, Q., Moore, R. L., Duan, A., Cui, J., Zuo, P., Wang, Y. and Wei, F. (2021), A fundamental mechanism of solar eruption initiation, *Nature Astronomy*, **5**, pp. 1126–1138, arXiv: `2107.08204`.

Kayanikhoo, F., Cemeljic, M., Wielgus, M. and Kluzniak, W. (2023), Energy distribution and substructure formation in astrophysical mhd simulations, arXiv: `2308.16062`.

Loureiro, N. F., Schekochihin, A. A. and Cowley, S. C. (2007), Instability of current sheets and formation of plasmoid chains, *Physics of Plasmas*, **14**(10), p. 100703, URL `https://doi.org/10.10632F1.2783986`.

McPherron, R. L. (1979), Magnetospheric substorms, *Reviews of Geophysics*, **17**(4), pp. 657–681.

Mignone, A., Bodo, G., Massaglia, S., Matsakos, T., Tesileanu, O., Zanni, C. and Ferrari, A. (2007), Pluto: A numerical code for computational astrophysics, *APJS*, **170**(1), pp. 228–242, arXiv: `astro-ph/0701854`.

Orszag, S. A. and Tang, C. M. (1979), Small-scale structure of two-dimensional magnetohydrodynamic turbulence, *Journal of Fluid Mechanics*, **90**, pp. 129–143.

Puzzoni, E., Mignone, A. and Bodo, G. (2021), On the impact of the numerical method on magnetic reconnection and particle acceleration–i. the mhd case, *Monthly Notices of the Royal Astronomical Society*, **508**(2), pp. 2771–2783.

Ripperda, B., Bacchini, F. and Philippov, A. A. (2020), Magnetic reconnection and hot spot formation in black hole accretion disks, *The Astrophysical Journal*, **900**(2), p. 100, ISSN 1538-4357.

Ripperda, B., Liska, M., Chatterjee, K., Musoke, G., Philippov, A. A., Markoff, S. B., Tchekhovskoy, A. and Younsi, Z. (2022), Black Hole Flares: Ejection of Accreted Magnetic Flux through 3D Plasmoid-mediated Reconnection, *APJL*, **924**(2), L32, arXiv: `2109.15115`.

Proceedings of *RAGtime 23–25*
Z. Stuchlík, G. Török, V. Karas and D. Lančová, editors, Silesian University in Opava, 2023, pp. 143–149

Quasinormal ringing of Bardeen spacetime

Dmitriy Ovchinnikov

Institute of Physics, Silesian University in Opava,
Bezručovo nám. 13, CZ-746 01 Opava, Czech Republic
`dmitriy.ovchinnikov@physics.slu.cz`

ABSTRACT

We review recent calculations of quasinormal modes and asymptotic tails of the Bardeen spacetime interpreted as a quantum corrected Schwarzschild-like black holes. Massless electromagnetic and Dirac fields and massive scalar fields are considered. The first few overtones are much more sensitive to the change of the quantum correction parameter than the fundamental mode because such correction deforms the black hole geometry near the event horizon. While the asymptotic tails of massless fields are identical to those for the Schwarzschild case, the tails for a massive field differ from the Schwarzschild limit at both intermediate and asymptotic times.

Keywords: Regular spacetimes – quasinormal modes – outburst of overtones – quantum corrected black holes

1 INTRODUCTION

Quasinormal modes of black holes (Kokkotas and Schmidt, 1999; Nollert, 1999; Konoplya and Zhidenko, 2011) are a fundamental aspect of black hole physics and gravitational wave astronomy. These modes represent the characteristic oscillations and decay of perturbations around a black hole after an external perturbation, such as a merger or accretion event. These modes are characterized by complex frequencies, which have direct implications for the detection and interpretation of gravitational wave signals from black hole mergers by observatories like LIGO and Virgo (Abbott et al., 2016).

Quasinormal modes of the historically first model of the regular black holes given by the Bardeen spacetime (Bardeen, 1968) have been extensively studied in a great number of papers (see for instance Flachi and Lemos (2013); Toshmatov et al. (2015, 2019); Mahdavian Yekta et al. (2021); Rincón and Santos (2020); López and Ramírez (2022); Saleh et al. (2018) and reference therein). However, the Bardeen spacetime was considered there mainly as a solution of specific non-linear electrodynamics (Ayon-Beato and Garcia, 2000) which describes a black hole as a gigantic magnetic monopole with zero electric charge (Bronnikov, 2001).

Recently, the quasinormal spectrum of the Bardeen spacetime as a quantum corrected neutral black hole metric (Nicolini et al., 2019) has been considered in (Konoplya et al., 2023; Bolokhov, 2023b) with the emphasis to overtones behavior and asymptotic tails.

978-80-7510-576-9

Here, we review these results and discuss three interesting phenomena related to the Bardeen black hole spectrum: a) outburst of overtones, b) arbitrarily long-lived modes of massive fields, and c) asymptotic tails.

2 BARDEEN SPACETIME AND THE WAVELIKE EQUATIONS

The spherically symmetric line element has the form

$$\mathrm{d}s^2 = -f(r)\mathrm{d}t^2 + f^{-1}(r)\mathrm{d}r^2 + r^2\left(\mathrm{d}\theta^2 + \sin^2\theta\mathrm{d}\varphi^2\right), \tag{1}$$

where for the Bardeen spacetime, the metric function is

$$f(r) = 1 - \frac{2Mr^2}{\left(r^2 + l_0^2\right)^{3/2}}, \tag{2}$$

with M the Komar mass, and parameter l_0 is related to the ultraviolet cutoff (Nicolini et al., 2019). For $l_0 \neq 0$, the space-time in eq.(5) has horizons for $|l_0| \leq 4M/(3\sqrt{3})$.

The general relativistic equations for the scalar (Φ), electromagnetic (A_μ), and Dirac (Υ) fields in a curved spacetime can be written as follows:

$$\frac{1}{\sqrt{-g}}\partial_\mu\left(\sqrt{-g}g^{\mu\nu}\partial_\nu\Phi\right) = 0, \tag{3a}$$

$$\frac{1}{\sqrt{-g}}\partial_\mu\left(F_{\rho\sigma}g^{\rho\nu}g^{\sigma\mu}\sqrt{-g}\right) = 0, \tag{3b}$$

$$\gamma^\alpha\left(\frac{\partial}{\partial x^\alpha} - \Gamma_\alpha\right)\Upsilon = 0. \tag{3c}$$

Here $F_{\mu\nu} = \partial_\mu A_\nu - \partial_\nu A_\mu$ is the electromagnetic tensor, γ^α are gamma matrices and Γ_α are spin connections in the tetrad formalism. Using separation of variables (for example, in case of the scalar field, employing the spherical symmetry and stationarity of the spacetime, we assume $\Phi \sim e^{-i\omega t}Y_\ell^m(\theta,\phi)\Psi(r)/r$, where Y_ℓ^m spherical harmonic function), after some algebra the above dynamical equations (3) take the wave-like form:

$$\frac{\mathrm{d}^2\Psi}{\mathrm{d}r_*^2} + (\omega^2 - V(r))\Psi = 0, \tag{4}$$

where the "tortoise coordinate" r_* is:

$$\mathrm{d}r_* \equiv \frac{\mathrm{d}r}{f(r)}. \tag{5}$$

The effective potentials for the scalar ($s = 0$) and electromagnetic ($s = 1$) fields can be written in a unified form:

$$V(r) = f(r)\frac{\ell(\ell+1)}{r^2} + (1-s)\frac{f(r)}{r}\frac{\mathrm{d}f(r)}{\mathrm{d}r}, \tag{6}$$

where $\ell = s, s+1, s+2, \ldots$ are the multipole numbers. For the Dirac field ($s = 1/2$) the problem is reduced to two iso-spectral effective potentials

$$V_{\pm}(r) = W^2 \pm \frac{\mathrm{d}W}{\mathrm{d}r_*}, \quad W \equiv \left(\ell + \frac{1}{2}\right)\frac{\sqrt{f(r)}}{r}. \tag{7}$$

The iso-spectral wave functions can be transformed one into another by the Darboux transformation

$$\Psi_+ = q\left(W + \frac{\mathrm{d}}{\mathrm{d}r_*}\right)\Psi_-, \quad q = const, \tag{8}$$

so that it is sufficient to analyze the spectrum of only one of the potentials.

3 LONG LIVED QUASINORMAL MODES AND THE OUTBURST OF OVERTONES

The boundary conditions for quasinormal modes are purely outgoing wave at infinity and purely incoming wave at the event horizon so that

$$\Psi = \begin{cases} e^{i\omega r_*}, & \text{for } r_* \to +\infty \quad \text{(purely outgoing)}, \\ e^{-i\omega r_*}, & \text{for } r_* \to -\infty \quad \text{(purely ingoing)}. \end{cases} \tag{9}$$

In order to find low-lying quasinormal frequencies, the quick and relatively accurate method which was used in Konoplya et al. (2023); Bolokhov (2023b) is the 6th order WKB method (Konoplya, 2003; Konoplya et al., 2019a) with the Pade approximants (Matyjasek and Opala, 2017). The WKB method was effectively used in a great number of works (see, for example Kodama et al., 2010; Onozawa et al., 1996; Konoplya et al., 2019a, and references therein). In order to find accurate values of overtones with $n > \ell$, the convergent Leaver method was used (Leaver, 1985), while for the asymptotic tails, the time-domain integration (Gundlach et al., 1994) has been applied. The latter was used in various works as well (for instance, Konoplya and Fontana, 2008; Churilova and Stuchlik, 2020; Bolokhov, 2023a; Bronnikov and Konoplya, 2020) with a good concordance for the dominant frequencies. As all of these methods are broadly discussed in the literature, we will not discuss them here in detail.

Using the first order WKB approach and expanding in terms of $1/L$ and l_0, where $L = \ell + \frac{1}{2}$ we find the position of the maximum of the effective potential:

$$r_{\max} = 3M - \frac{5l_0^2}{6M} - \frac{65l_0^4}{216M^3} + O\left(l_0^6\right), \tag{10}$$

and the frequency

$$\begin{aligned} \omega =& \frac{L}{3\sqrt{3}M} - \frac{i(2n+1)}{6\sqrt{3}M} + l_0^2\left(\frac{L}{18\sqrt{3}M^3} + \frac{i(2n+1)}{54\sqrt{3}M^3}\right) \\ &+ l_0^4\left(\frac{17L}{648\sqrt{3}M^5} + \frac{7i(2n+1)}{324\sqrt{3}M^5}\right) + O\left(\frac{1}{L}, l_0^6\right). \end{aligned} \tag{11}$$

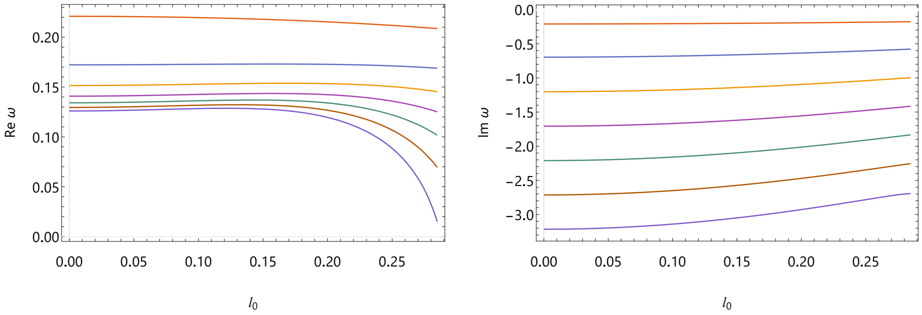

Figure 1. Quasinormal frequencies for the scalar perturbations ($\ell = 0$) and n from 0 to 6 (Konoplya et al., 2023).

Notice that in the eikonal limit, the WKB formula is exact, and the above formula satisfies the eikonal QNMs/null geodesics correspondence (Cardoso et al., 2009), though in general, the latter should be treated carefully since there are a number of exceptions from it (Konoplya and Stuchlík, 2017; Konoplya, 2023; Konoplya et al., 2019b).

From fig. 1, we notice that the overtones deviate from their Schwarzschild limits at an increasing with n rate, which reflects the fact that the Schwarzschild metric is deformed by the l_0 quantum correction mainly near the event horizon (Konoplya and Zhidenko, 2022).

When the scalar field has non-zero mass μ, the spectrum of the Schwarzschild and Reissner-Nordstrom black holes contains arbitrarily long-lived quasinormal modes at some values of μ (Ohashi and Sakagami, 2004). When μ is increased, the damping rate decreases, approaching zero as a kind of threshold at which the mode disappears from the spectrum, and the first overtone becomes the fundamental mode. This way, at particular values of the mass of the field, there exist the modes, called *quasi-resonances*, which are similar to standing waves. In Bolokhov (2023b), it was shown that this phenomenon also takes place for the massive scalar field in the Bardeen background and that the outburst of overtones takes place for such modes as well.

4 TELLING OSCILLATORY TAILS OF THE BARDEEN SPACETIME

At asymptotically late times, the massless scalar and gravitational fields for the Schwarzschild spacetime decay according to the following law (Price, 1972):

$$|\Psi| \sim t^{-(2\ell+3)}, \quad t \to \infty. \tag{12}$$

In fig. 2, we can see that the same law is fulfilled for the Bardeen spacetime.

When the massive term μ is turned on, the late-time behavior of the Reissner-Nordstrom black hole has two regimes (Koyama and Tomimatsu, 2002). At *asymptotic* times

$$\frac{t}{M} > (\mu M)^{-3}, \tag{13}$$

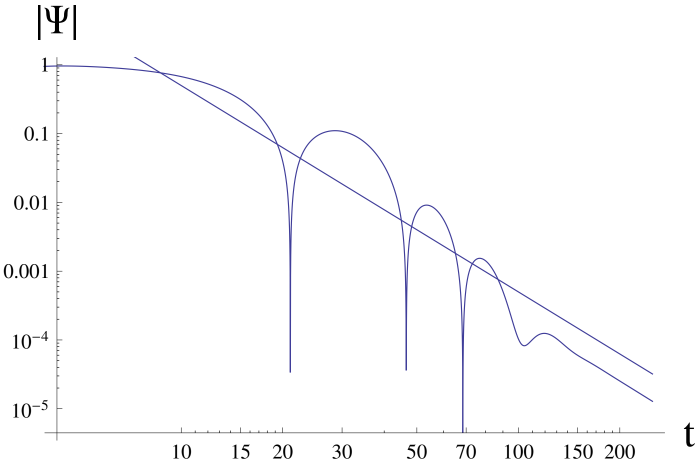

Figure 2. Time-domain profile according to (Konoplya et al., 2023) for scalar field perturbations $\ell = 0$ in the background of the quasi-extremal Bardeen black hole $l_0 = 0.707107$; $r_0 = 1$. Logarithmic plot with the line $\sim t^{-3}$.

the following decay law dominates

$$|\Psi| \sim t^{-5/6} \sin(\mu t), \quad t \to \infty. \tag{14}$$

For the Bardeen spacetime, as was shown in (Bolokhov, 2023b), the decay law is different:

$$|\Psi| \sim t^{-1} \sin(A(\mu)t), \quad t \to \infty, \tag{15}$$

where $A(\mu)$ is some function which could be approximately found by fitting the data for various values of μ. At the *intermediate late* times, corresponding to relatively small value of μM, the decay law for the Bardeen spacetime is (Bolokhov, 2023b),

$$|\Psi| \sim t^{-(\frac{8}{6}+\ell)} \sin(A(\mu)t), \tag{16}$$

which is also different from the Schwarzschild or Reissner-Nordstrom case (Koyama and Tomimatsu, 2002; Konoplya and Zhidenko, 2011).

5 CONCLUSIONS

We have reviewed recent studies (Konoplya et al., 2023; Bolokhov, 2023b) of quasinormal modes and evolution of perturbations of a test scalar, electromagnetic and Dirac fields in the vicinity of the Bardeen spacetime treated as a quantum corrected neutral black hole (Nicolini et al., 2019). The spectrum has a number of interesting and distinctive properties, such as outburst of overtones, long-lived quasinormal modes and different tail the behavior at asymptotic and intermediate times.

ACKNOWLEDGEMENTS

The authors would like to acknowledge useful discussions with A. Zhidenko and S. Bolokhov. This work was supported by the internal grant of the Silesian University in Opava SGS/30/2023.

REFERENCES

Abbott, B. P. et al. (LIGO Scientific, Virgo) (2016), Observation of Gravitational Waves from a Binary Black Hole Merger, *Phys. Rev. Lett.*, **116**(6), p. 061102, arXiv: `1602.03837`.

Ayon-Beato, E. and Garcia, A. (2000), The Bardeen model as a nonlinear magnetic monopole, *Phys. Lett. B*, **493**, pp. 149–152, arXiv: `gr-qc/0009077`.

Bardeen, J. M. (1968), in Abstracts of the 5th international conference on gravitation and the theory of relativity (GR5), Tbilisi, USSR, Sept. 9-13, 1968, edited by V. A. Fock et al. (Tbilisi University Press, 1968) p. 174.

Bolokhov, S. V. (2023a), Black holes in Starobinsky-Bel-Robinson Gravity and the breakdown of quasinormal modes/null geodesics correspondence, arXiv: `2310.12326`.

Bolokhov, S. V. (2023b), Long lived quasinormal modes and telling oscillatory tails of the Bardeen spacetime, 10.20944/preprints202310.0517.v1.

Bronnikov, K. A. (2001), Regular magnetic black holes and monopoles from nonlinear electrodynamics, *Phys. Rev. D*, **63**, p. 044005, arXiv: `gr-qc/0006014`.

Bronnikov, K. A. and Konoplya, R. A. (2020), Echoes in brane worlds: ringing at a black hole–wormhole transition, *Phys. Rev. D*, **101**(6), p. 064004, arXiv: `1912.05315`.

Cardoso, V., Miranda, A. S., Berti, E., Witek, H. and Zanchin, V. T. (2009), Geodesic stability, Lyapunov exponents and quasinormal modes, *Phys. Rev. D*, **79**(6), p. 064016, arXiv: `0812.1806`.

Churilova, M. S. and Stuchlik, Z. (2020), Ringing of the regular black-hole/wormhole transition, *Class. Quant. Grav.*, **37**(7), p. 075014, arXiv: `1911.11823`.

Flachi, A. and Lemos, J. P. S. (2013), Quasinormal modes of regular black holes, *Phys. Rev. D*, **87**(2), p. 024034, arXiv: `1211.6212`.

Gundlach, C., Price, R. H. and Pullin, J. (1994), Late time behavior of stellar collapse and explosions: 1. Linearized perturbations, *Phys. Rev. D*, **49**, pp. 883–889, arXiv: `gr-qc/9307009`.

Kodama, H., Konoplya, R. A. and Zhidenko, A. (2010), Gravitational stability of simply rotating Myers-Perry black holes: Tensorial perturbations, *Phys. Rev. D*, **81**, p. 044007, arXiv: `0904.2154`.

Kokkotas, K. D. and Schmidt, B. G. (1999), Quasinormal modes of stars and black holes, *Living Rev. Rel.*, **2**, p. 2, arXiv: `gr-qc/9909058`.

Konoplya, R. A. (2003), Quasinormal behavior of the d-dimensional Schwarzschild black hole and higher order WKB approach, *Phys. Rev. D*, **68**, p. 024018, arXiv: `gr-qc/0303052`.

Konoplya, R. A. (2023), Further clarification on quasinormal modes/circular null geodesics correspondence, *Phys. Lett. B*, **838**, p. 137674, arXiv: `2210.08373`.

Konoplya, R. A. and Fontana, R. D. B. (2008), Quasinormal modes of black holes immersed in a strong magnetic field, *Phys. Lett. B*, **659**, pp. 375–379, arXiv: `0707.1156`.

Konoplya, R. A., Ovchinnikov, D. and Ahmedov, B. (2023), Bardeen spacetime as a quantum corrected Schwarzschild black hole: Quasinormal modes and Hawking radiation, arXiv: `2307.10801`.

Konoplya, R. A. and Stuchlík, Z. (2017), Are eikonal quasinormal modes linked to the unstable circular null geodesics?, *Phys. Lett. B*, **771**, pp. 597–602, arXiv: `1705.05928`.

Konoplya, R. A. and Zhidenko, A. (2011), Quasinormal modes of black holes: From astrophysics to string theory, *Rev. Mod. Phys.*, **83**, pp. 793–836, arXiv: `1102.4014`.

Konoplya, R. A. and Zhidenko, A. (2022), First few overtones probe the event horizon geometry, arXiv: `2209.00679`.

Konoplya, R. A., Zhidenko, A. and Zinhailo, A. F. (2019a), Higher order WKB formula for quasinormal modes and grey-body factors: recipes for quick and accurate calculations, *Class. Quant. Grav.*, **36**, p. 155002, arXiv: `1904.10333`.

Konoplya, R. A., Zinhailo, A. F. and Stuchlík, Z. (2019b), Quasinormal modes, scattering, and Hawking radiation in the vicinity of an Einstein-dilaton-Gauss-Bonnet black hole, *Phys. Rev. D*, **99**(12), p. 124042, arXiv: `1903.03483`.

Koyama, H. and Tomimatsu, A. (2002), Slowly decaying tails of massive scalar fields in spherically symmetric space-times, *Phys. Rev. D*, **65**, p. 084031, arXiv: `gr-qc/0112075`.

Leaver, E. W. (1985), An Analytic representation for the quasi normal modes of Kerr black holes, *Proc. Roy. Soc. Lond. A*, **402**, pp. 285–298.

López, L. A. and Ramírez, V. (2022), Quasinormal modes of a Generic-class of magnetically charged regular black hole: scalar and electromagnetic perturbations, arXiv: `2205.10166`.

Mahdavian Yekta, D., Karimabadi, M. and Alavi, S. A. (2021), Quasinormal modes for non-minimally coupled scalar fields in regular black hole spacetimes: Grey-body factors, area spectrum and shadow radius, *Annals Phys.*, **434**, p. 168603, arXiv: `1912.12017`.

Matyjasek, J. and Opala, M. (2017), Quasinormal modes of black holes. The improved semianalytic approach, *Phys. Rev. D*, **96**(2), p. 024011, arXiv: `1704.00361`.

Nicolini, P., Spallucci, E. and Wondrak, M. F. (2019), Quantum Corrected Black Holes from String T-Duality, *Phys. Lett. B*, **797**, p. 134888, arXiv: `1902.11242`.

Nollert, H.-P. (1999), TOPICAL REVIEW: Quasinormal modes: the characteristic ‘sound’ of black holes and neutron stars, *Class. Quant. Grav.*, **16**, pp. R159–R216.

Ohashi, A. and Sakagami, M.-a. (2004), Massive quasi-normal mode, *Class. Quant. Grav.*, **21**, pp. 3973–3984, arXiv: `gr-qc/0407009`.

Onozawa, H., Mishima, T., Okamura, T. and Ishihara, H. (1996), Quasinormal modes of maximally charged black holes, *Phys. Rev. D*, **53**, pp. 7033–7040, arXiv: `gr-qc/9603021`.

Price, R. H. (1972), Nonspherical Perturbations of Relativistic Gravitational Collapse. II. Integer-Spin, Zero-Rest-Mass Fields, *Phys. Rev. D*, **5**, pp. 2439–2454.

Rincón, A. and Santos, V. (2020), Greybody factor and quasinormal modes of Regular Black Holes, *Eur. Phys. J. C*, **80**(10), p. 910, arXiv: `2009.04386`.

Saleh, M., Thomas, B. B. and Kofane, T. C. (2018), Quasinormal modes of gravitational perturbation around regular Bardeen black hole surrounded by quintessence, *Eur. Phys. J. C*, **78**(4), p. 325.

Toshmatov, B., Abdujabbarov, A., Stuchlík, Z. and Ahmedov, B. (2015), Quasinormal modes of test fields around regular black holes, *Phys. Rev. D*, **91**(8), p. 083008, arXiv: `1503.05737`.

Toshmatov, B., Stuchlík, Z., Ahmedov, B. and Malafarina, D. (2019), Relaxations of perturbations of spacetimes in general relativity coupled to nonlinear electrodynamics, *Phys. Rev. D*, **99**(6), p. 064043, arXiv: `1903.03778`.

Proceedings of *RAGtime 23–25*
Z. Stuchlík, G. Török, V. Karas and D. Lančová, editors, Silesian University in Opava, 2023, pp. 151–166

Equilibrium tori orbiting Reissner-Nordström naked singularities

Ruchi Mishra[1,a] and Włodek Kluźniak[1]

[1]Nicolaus Copernicus Astronomical Center, Polish Academy of Sciences,
ul. Bartycka 18, 00-716 Warsaw, Poland
[a]`rmishra@camk.edu.pl`

ABSTRACT
In general relativity, the asymptotically flat space-time of a charged, spherically symmetric (non-rotating) body is described by the Reissner-Nordström metric. This metric corresponds to a naked singularity when the absolute value of charge, Q, exceeds the mass, M. For all Reissner-Nordström naked singularities, there exists a zero gravity sphere where a test particle can remain at rest. Outside that sphere, gravity is attractive, inside it, gravity is repulsive. For values of $Q/M > \sqrt{9/8}$, the angular frequency of circular test-particle orbits has a maximum at radius $r = (4/3)\,Q^2/M$. We construct polytropic tori with uniform values of specific angular momentum in the naked singularity regime of the Reissner-Nordström metric ($Q/M > 1$).

Keywords: Stars: gravity – naked singularities – accretion, accretion disks

INTRODUCTION

The gravity of a spherically symmetric, electrically charged body is described by the ReissnerNordström (RN) space-time metric. For values of charge $Q > M$, the metric describes a naked singularity. One of the key features of many spherically symmetric naked singularities is the existence of a “zero-gravity” spherical surface, inside of which gravity is repulsive, whereas outside of it, gravity is attractive as usual (Pugliese et al., 2011; Vieira et al., 2014; Vieira and Kluniak, 2023). This surface marks the innermost boundary for the existence of circular geodesics, representing orbits with zero angular momentum, a test particle remaining stably at rest there. In the RN case, no circular photon orbits exist for $Q/M > \sqrt{9/8}$. For a somewhat larger value still of Q/M, no marginally stable orbits exist, so test-particle circular orbits are stable all the way down to the zero-gravity sphere (Figure 1).

In a standard thin accretion disk, accretion is enabled by (effective) viscous torques transferring angular momentum outwards. This is possible as long as angular frequency decreases monotonically with the radius. In the case of RN space-time, the torque is reversed close to the zero-gravity radius, r_0, as $\mathrm{d}\Omega/\mathrm{d}r > 0$ there, for test particles. It is not yet clear whether a thin disk may exist all the way to the zero-gravity sphere. For this reason, we consider, instead, toroidal orbiting configurations of a perfect fluid.

978-80-7510-576-9

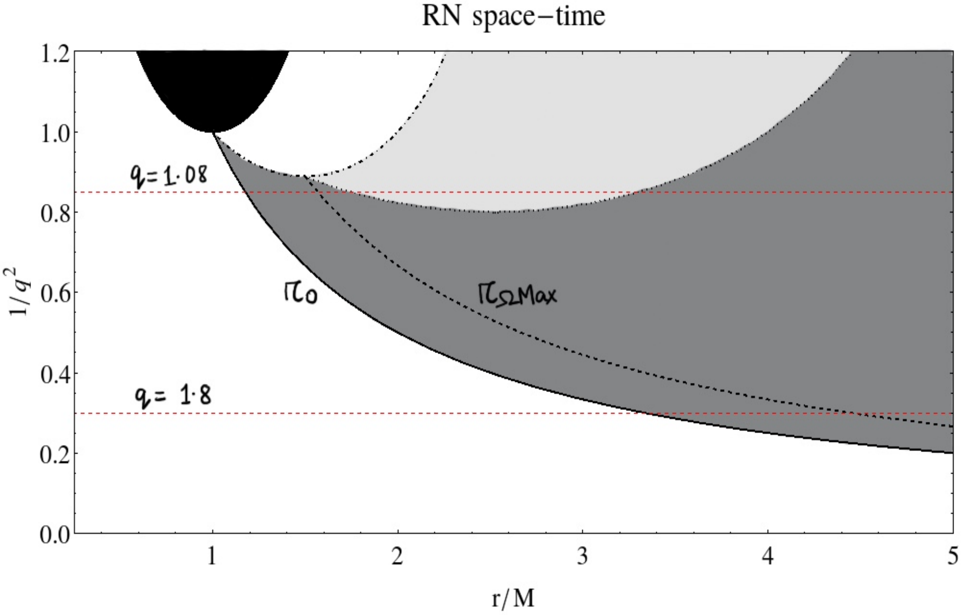

Figure 1. Orbital stability diagram for the RN spacetime ($q \equiv Q/M$). The *black* region corresponds to the hypervolume between the event horizons. The *solid black* line represents the zero gravity sphere (radius r_0). The *black dashed* lines represent the radius, $r_{\Omega\max}$, at which angular frequency is maximum. The black *dotted* line corresponds to the marginally stable orbit, whereas the *dot-dashed* line corresponds to the photon orbit. *Dark grey* region corresponds to the stability region for time-like circular geodesics. *Light grey* region corresponds to the instability region for time-like circular geodesics. No circular geodesics exist in the *white* regions. The horizontal *red dashed* lines correspond to the two choices of Q/M ratio discussed in this contribution.

Here, we focus on the structure and shape[1] of equilibrium tori in which a perfect fluid is orbiting the RN naked singularity. As a first step, we consider uniform angular momentum distributions. Earlier work by Stuchlík et al. (2015); Kucáková et al. (2011); Prada-Méndez et al. (2023) presented the equilibrium toroidal structures in the case of KehagiasSfetsos naked singularities, Reissner-Nordström-(anti-)de Sitter space-times, and q-metric space-time respectively. Our results are qualitatively similar to Stuchlík et al. (2015). We use units with $G = 1, c = 1$. For convenience, since our results depend only on $(Q/M)^2$, we take $Q > 0$ to be the absolute magnitude of charge, the actual charge being $\pm Q$.

---

[1] While the configurations have the topology of a torus, their cross-section is not circular, not even ellipsoidal.

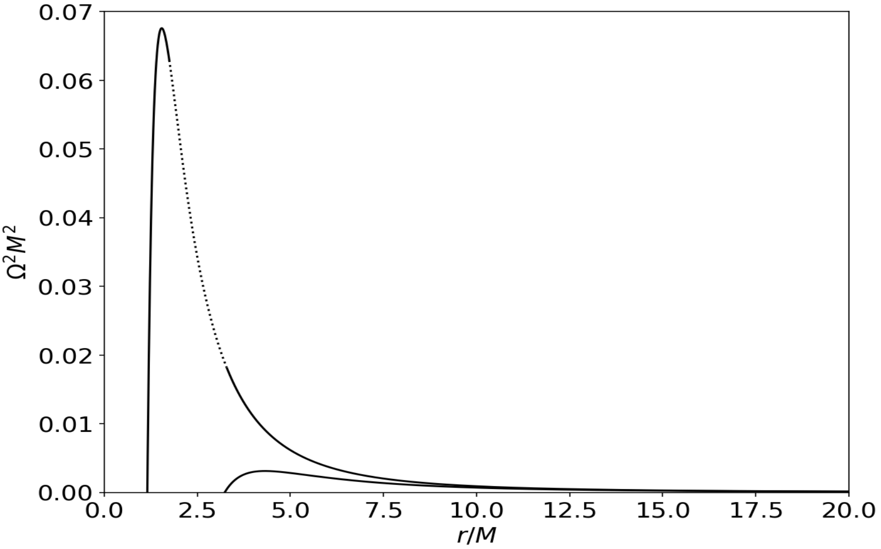

Figure 2. Square of orbital frequency as a function of r/M for charge value $Q/M = 1.08$ *(top)* and $Q/M = 1.8$ *(bottom)*. The dotted line represents the unstable region.

GEODESIC MOTION IN RN SPACE TIME

The RN metric can be expressed in standard spherical coordinates as

$$\mathrm{d}s^2 = -f(r)\,\mathrm{d}t^2 + f^{-1}(r)\,\mathrm{d}r^2 + r^2\left(\mathrm{d}\theta^2 + \sin^2\theta\,\mathrm{d}\phi^2\right), \tag{1}$$

where $f(r)$ is the metric function given by

$$f(r) = 1 - \frac{2M}{r} + \frac{Q^2}{r^2}. \tag{2}$$

For a perfect fluid, the energy-momentum tensor is given by

$$T_{\mu\nu} = (p+\rho)\,u_\mu u_\nu - p g_{\mu\nu}, \tag{3}$$

where ρ is the fluid energy density and p its pressure. The four-velocity of the fluid in a circular orbit is $u^\mu = (u^t, 0, 0, u^\phi)$. The conserved energy and angular momentum of a test particle in this orbit are given by

$$E \equiv -g_{tt}\dot{t} = -u_t, \quad L \equiv g_{\phi\phi}\dot{\phi} = u_\phi. \tag{4}$$

The conserved specific angular momentum l is defined by

$$l \equiv \frac{L}{E} = -\frac{u_\phi}{u_t}. \tag{5}$$

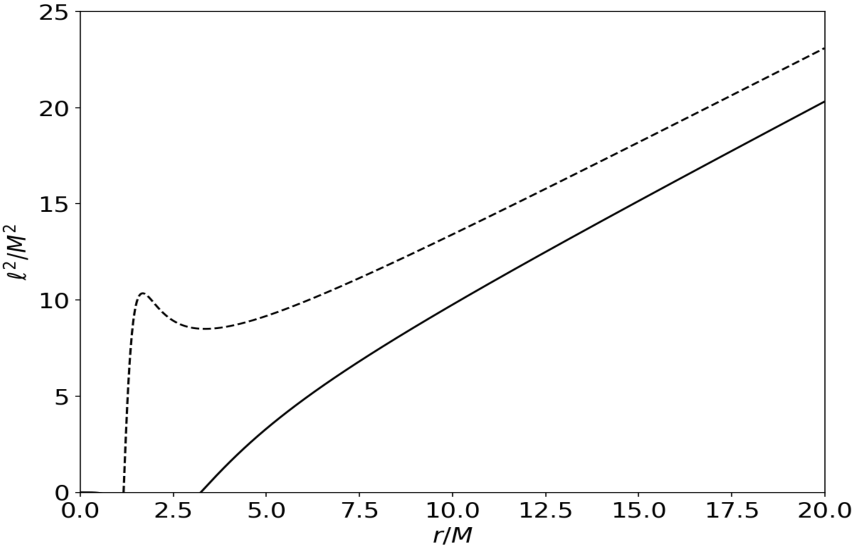

Figure 3. Square of specific angular momentum as a function of r/M for charge value $Q/M = 1.08$ (dashed) and $Q/M = 1.8$ (solid).

We begin with a discussion of test particle circular motion. The effective potential can be conveniently taken to be E^2, in the equatorial plane ($\sin\theta = 1$) it reduces to

$$V_{\text{eff}}(r) = f(r)\left(1 + \frac{L^2}{r^2}\right), \tag{6}$$

where we've used $u_\mu u^\mu = -1$. The condition $\partial V_{\text{eff}}/\partial r = 0$ then gives the angular momentum of circular geodesics, i.e.

$$L^2(r) = \frac{r^3 f'(r)}{2f - rf'(r)}, \tag{7}$$

or

$$l^2(r) = \frac{r^3}{2f^2} f'(r). \tag{8}$$

The orbital angular frequency, $\Omega = u^\phi/u^t$, so

$$\Omega^2(r) = \frac{f'(r)}{2r}. \tag{9}$$

The angular velocity for two values of Q/M is illustrated in Figure 2.

For the RN space-time, the maximum angular velocity is given by the condition

$$\frac{\mathrm{d}\Omega^2}{\mathrm{d}r^2} = \frac{\mathrm{d}}{\mathrm{d}r}\left(\frac{f'(r)}{2r}\right) = 0, \tag{10}$$

so the maximum of angular velocity occurs at

$$r_{\Omega\mathrm{max}} = \frac{4}{3}\frac{Q^2}{M}. \tag{11}$$

In Figure 2 we present this radius, $r_{\Omega\mathrm{max}}$ as a function of Q/M. As circular geodesics are not possible within the photon orbit, $r_{\Omega\mathrm{max}}$ is only defined as long as $Q/M > \sqrt{9/8}$. Note that the marginally orbits, when they exist, are always at a larger radius – the maximum of Ω is always attained in a stable orbit. The specific angular momentum at this orbit (of maximum Ω) is given by,

$$l_{\Omega\mathrm{max}} \equiv l(r_{\Omega\mathrm{max}}). \tag{12}$$

It is interesting to note that the specific angular momentum and its radial derivative in circular orbits are not necessarily monotonic as a function of the radius r. The extrema of the $l\,(r)$ curve (if present) corresponds to the marginally stable orbits. The region between the maximum and minimum of the $Q/M = 1.08$ specific angular momentum curve in Figure 3 correspond to unstable circular orbits (c.f. Figure 2) by Rayleigh's criterion, as $\mathrm{d}l/\mathrm{d}r < 0$ there.

In the case of barotropic fluid, the surfaces of constant pressure (isobars) corresponding to equipotential surfaces $W(r,\theta)$ are given by Boyers condition (e.g., Abramowicz et al., 1978; Kozlowski et al., 1978)

$$-\int_0^p \frac{\mathrm{d}p}{p+\rho} = W - W_{\mathrm{in}} = \ln\frac{u_t}{(u_t)_{\mathrm{in}}} - \int_{l_{\mathrm{in}}}^{l} \frac{\Omega \mathrm{d}l}{1-\Omega l}\,. \tag{13}$$

In the Newtonian limit, W is the usual effective potential. Here, the subscript in refers to the inner edge of the torus. The equipotential surfaces are determined by the condition

$$W(r,\theta) = \text{constant}. \tag{14}$$

For the simplest case of tori with uniform distribution of specific angular momentum, $l_0(r,\theta) = \text{constant}$, W is given by the following equation (Rezzolla and Zanotti, 2013):

$$W(r,\theta) = \ln|u_t| = \frac{1}{2}\ln\left[\frac{f\,(r)\,r^2\sin^2\theta}{r^2\sin^2\theta - f\,(r)\,l_0^2}\right].$$

At a given point in the (r,θ) plane, the potential W can be positive or negative, indicating open and closed equipotential surfaces. In principle, the fluid can fill any of the closed surfaces. Thus, a closed equipotential surface can be taken to represent the surface of

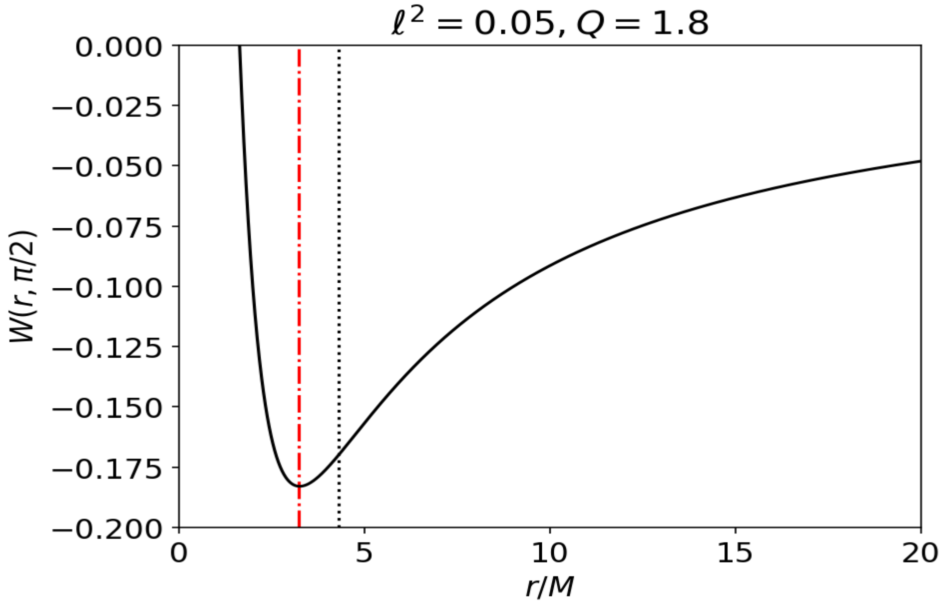

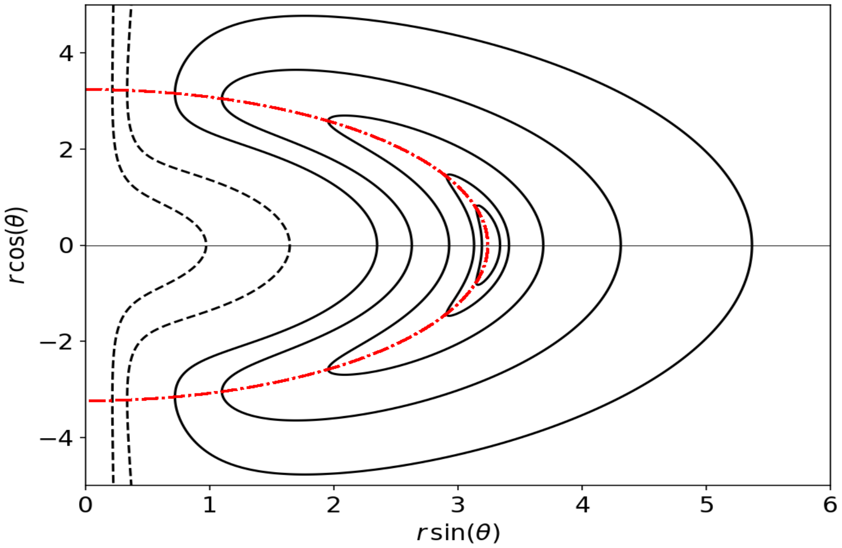

Figure 4. Equilibrium tori around RN naked singularity with Q/M=1.8 with $l_0 < l_{\Omega\max}$. Location of the zero-gravity sphere is indicated by red dotted-dashed line. *Top:* W as a function of r/M in equatorial plane. The radius of maximum angular frequency, $r_{\Omega\max}$, is indicated by the black dotted line. *Bottom:* Meridional cross-section of the equipotential surfaces. Solid closed lines represent toroidal surfaces with negative W value. The black dashed lines represent positive values of W.

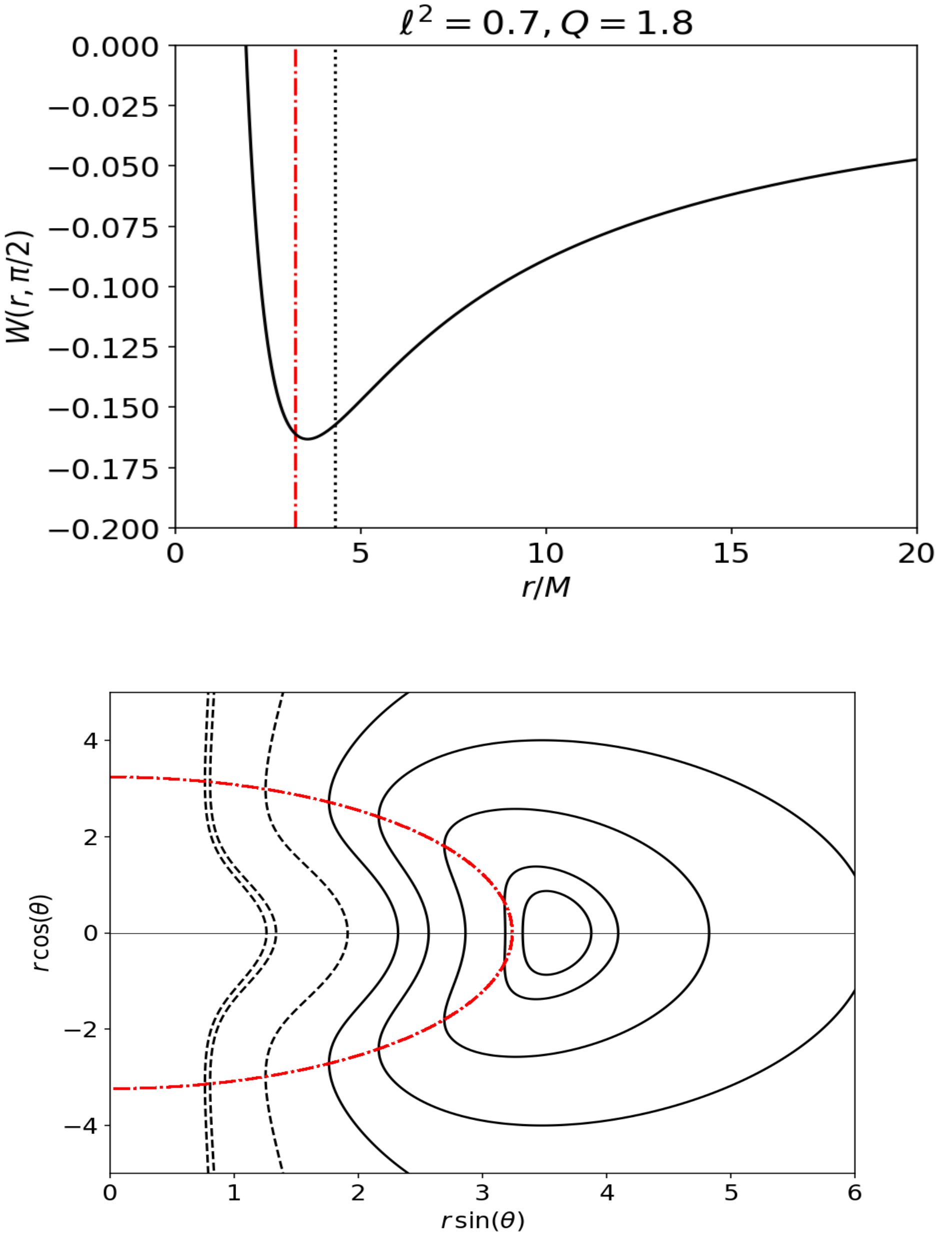

Figure 5. Equilibrium tori around RN naked singularity with Q/M=1.8 with $l_0 < l_{\Omega\max}$. Location of the zero-gravity sphere is indicated by red dotted-dashed line. *Top:* W as a function of r/M in equatorial plane. The radius of maximum angular frequency, $r_{\Omega\max}$, is indicated by the black dotted line. *Bottom:* Meridional cross-section of the equipotential surfaces. Solid closed lines represent toroidal surfaces with negative W value. The black dashed lines represent positive values of W.

a stationary configuration of orbiting fluid. The pressure of the toroidal barytrope is zero at the surface, with a non-zero gradient.

For RN naked singularity for constant specific angular momentum l_0, the potential W takes the following form:

$$W(r,\theta) = \ln|u_t| = \frac{1}{2}\ln\left[\frac{(r^2 - 2Mr + Q^2)\sin^2\theta}{r^2\sin^2\theta - (r^2 - 2Mr + Q^2)l_0^2/r^2}\right]. \tag{15}$$

TOROIDAL PERFECT FLUID CONFIGURATIONS

We construct equilibrium toroidal configurations for four representative values of the angular momentum parameter, l_0, for each of two values of the charge-to-mass ratio (Table 1). These are shown with solid lines in Figs. 4–11. The dashed lines correspond to the surfaces with positive values of W in Eq. (15), so any fluid in their vicinity would be unbound.

The barotropic fluid was assumed to have a uniform distribution of angular momentum. Let us start by discussing the case of $Q/M = 1.8$, representative of singularities with no marginally stable orbits. For low values of specific angular momentum, the circular locus of maximum pressure in the torus (the torus “center") lies very close to the zero-gravity sphere. While the torus can penetrate the zero-gravity sphere, its gradient of pressure balancing the repulsive gravity, a large part of the fluid must necessarily orbit outside of the zero-gravity sphere. The gravitational repulsion of the naked singularity leads to a very distorted shape of the “torus," which by analogy to, and in contrast with, the well-known black hole “cusp" solution[2] (known informally as “Sikora’s beak”) could best be described as open “jaws” ready to snatch the singularity (Figure 4). For solutions with larger values of angular momentum, these jaws become less prominent and finally disappear as the center of the torus shifts outwards with increasing angular momentum parameters (Figures 4–7).

For low values of the charge-to-mass ratio, the presence of marginally stable orbits complicates the solutions. Here, we discuss $Q/M = 1.08$ as an example. For low values of angular momentum, the jaws are again apparent inside the zero-gravity sphere (Figure 8). However, for larger values of angular momentum, the torus ends close to the zero-gravity sphere, as though it hit a wall (Figure 9). For larger values of l_0 still, two separate toroidal solutions appear (Figure 10). This is related to the two stable orbital solutions for a test particle for a certain range of specific angular momenta (e.g., values of l_0 near the maximum of the dashed line in Figure 3). Once angular momentum exceeds the maximum of the $l(r)$ curve, only one stable orbital solution exists at large radii, and the fluid configuration adopts the shape familiar from studies of compact object gravity in the quasi-Newtonian regime, i.e., far from the source of gravity (Figure 11).

---

[2] Introduced for the first time in Abramowicz, Jaroszyski & Sikora 1978.

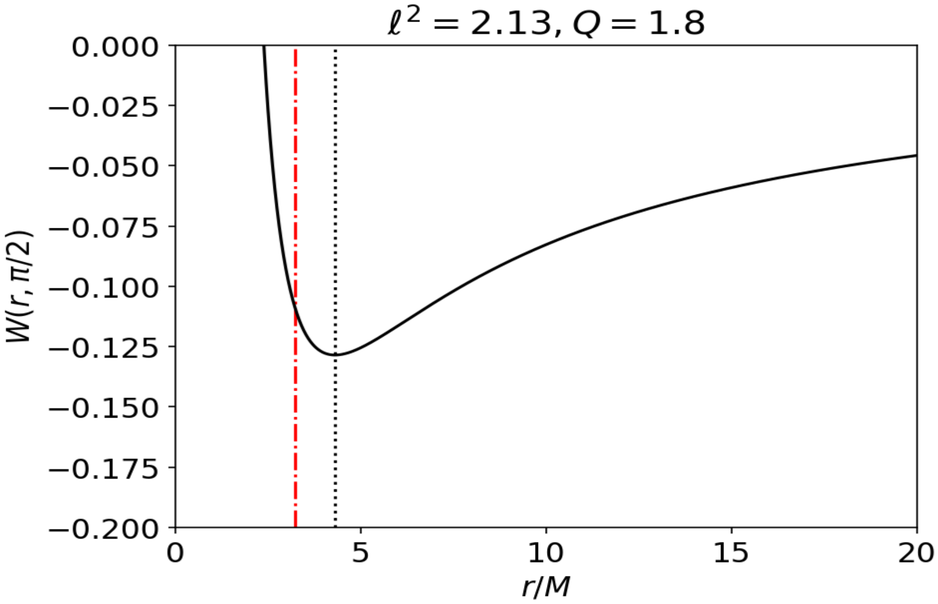

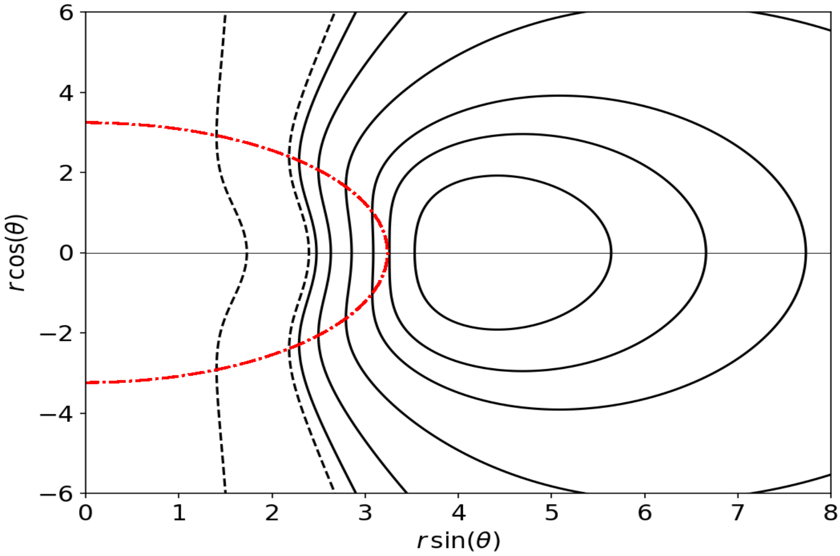

Figure 6. Equilibrium tori around RN naked singularity with Q/M=1.8 with $l_0 = l_{\Omega\max}$. Location of the zero-gravity sphere is indicated by red dotted-dashed line. *Top:* W as a function of r/M in equatorial plane. The radius of maximum angular frequency, $r_{\Omega\max}$, is indicated by the black dotted line. *Bottom:* Meridional cross-section of the equipotential surfaces. Solid closed lines represent toroidal surfaces with negative W value. The black dashed lines represent positive values of W.

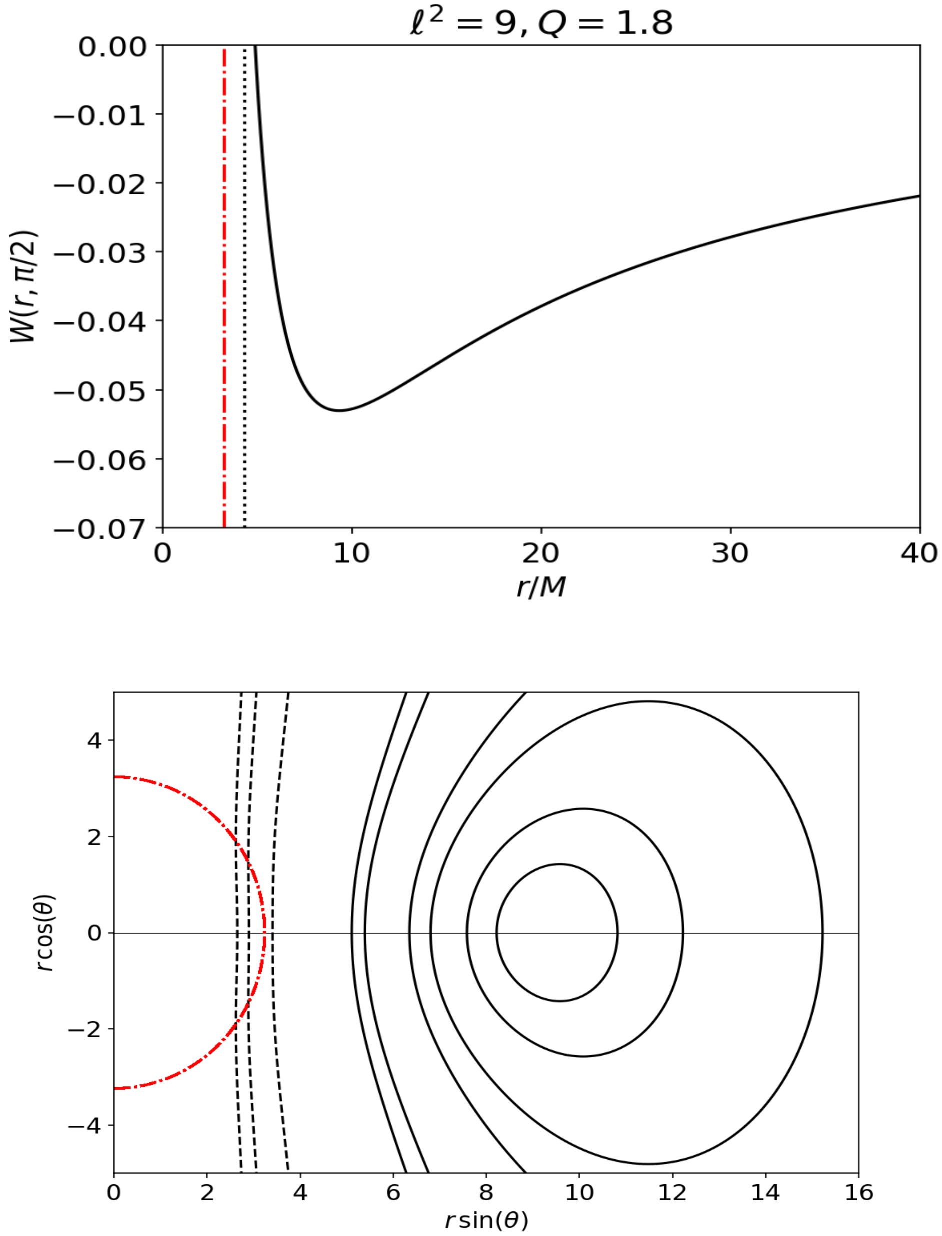

Figure 7. Equilibrium tori around RN naked singularity with Q/M=1.8 with $l_0 > l_{\Omega\max}$. Location of the zero-gravity sphere is indicated by red dotted-dashed line. *Top:* W as a function of r/M in equatorial plane. The radius of maximum angular frequency, $r_{\Omega\max}$, is indicated by the black dotted line. *Bottom:* Meridional cross-section of the equipotential surfaces. Solid closed lines represent toroidal surfaces with negative W value. The black dashed lines represent positive values of W.

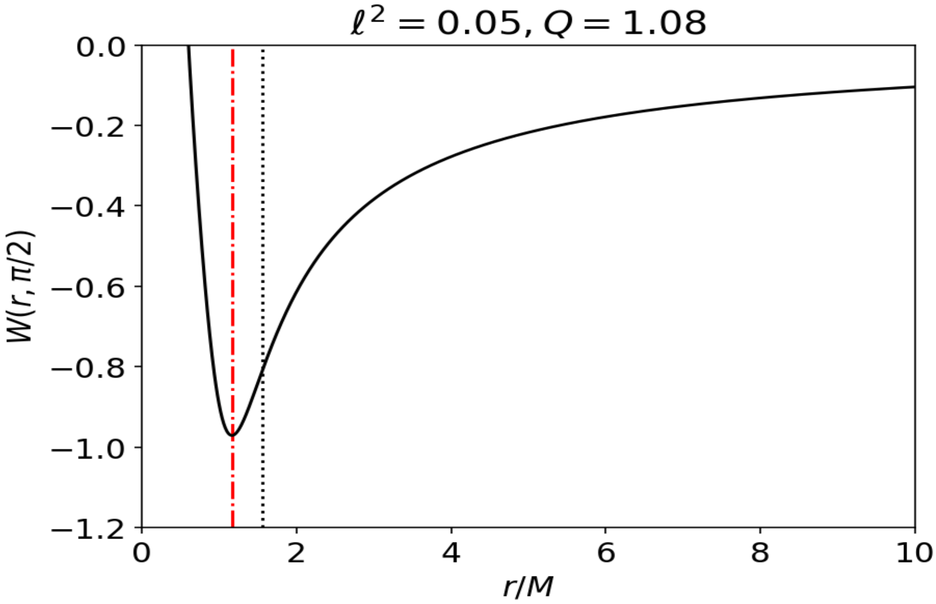

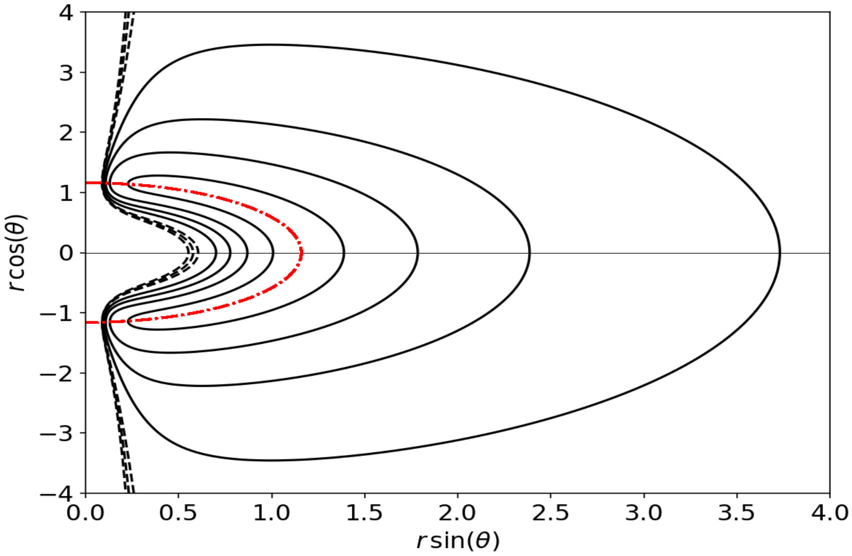

Figure 8. Equilibrium tori around RN naked singularity with Q/M=1.8 with $l_0 < l_{\Omega\max}$. Location of the zero-gravity sphere is indicated by red dotted-dashed line. *Top:* W as a function of r/M in equatorial plane. The radius of maximum angular frequency, $r_{\Omega\max}$, is indicated by the black dotted line. *Bottom:* Meridional cross-section of the equipotential surfaces. Solid closed lines represent toroidal surfaces with negative W value. The black dashed lines represent positive values of W.

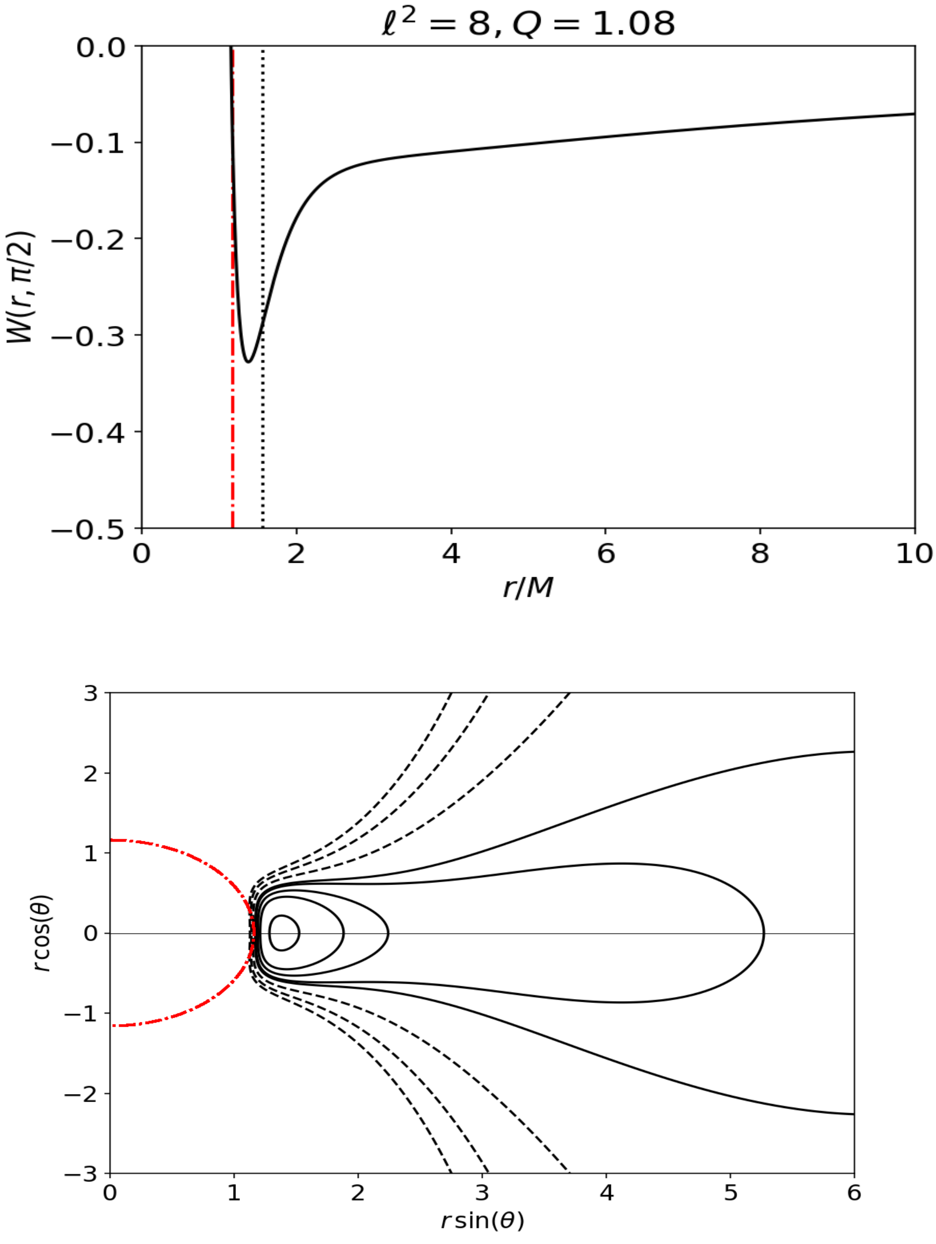

Figure 9. Equilibrium tori around RN naked singularity with Q/M=1.8 with $l_0 < l_{\Omega\max}$. Location of the zero-gravity sphere is indicated by red dotted-dashed line. *Top:* W as a function of r/M in equatorial plane. The radius of maximum angular frequency, $r_{\Omega\max}$, is indicated by the black dotted line. *Bottom:* Meridional cross-section of the equipotential surfaces. Solid closed lines represent toroidal surfaces with negative W value. The black dashed lines represent positive values of W.

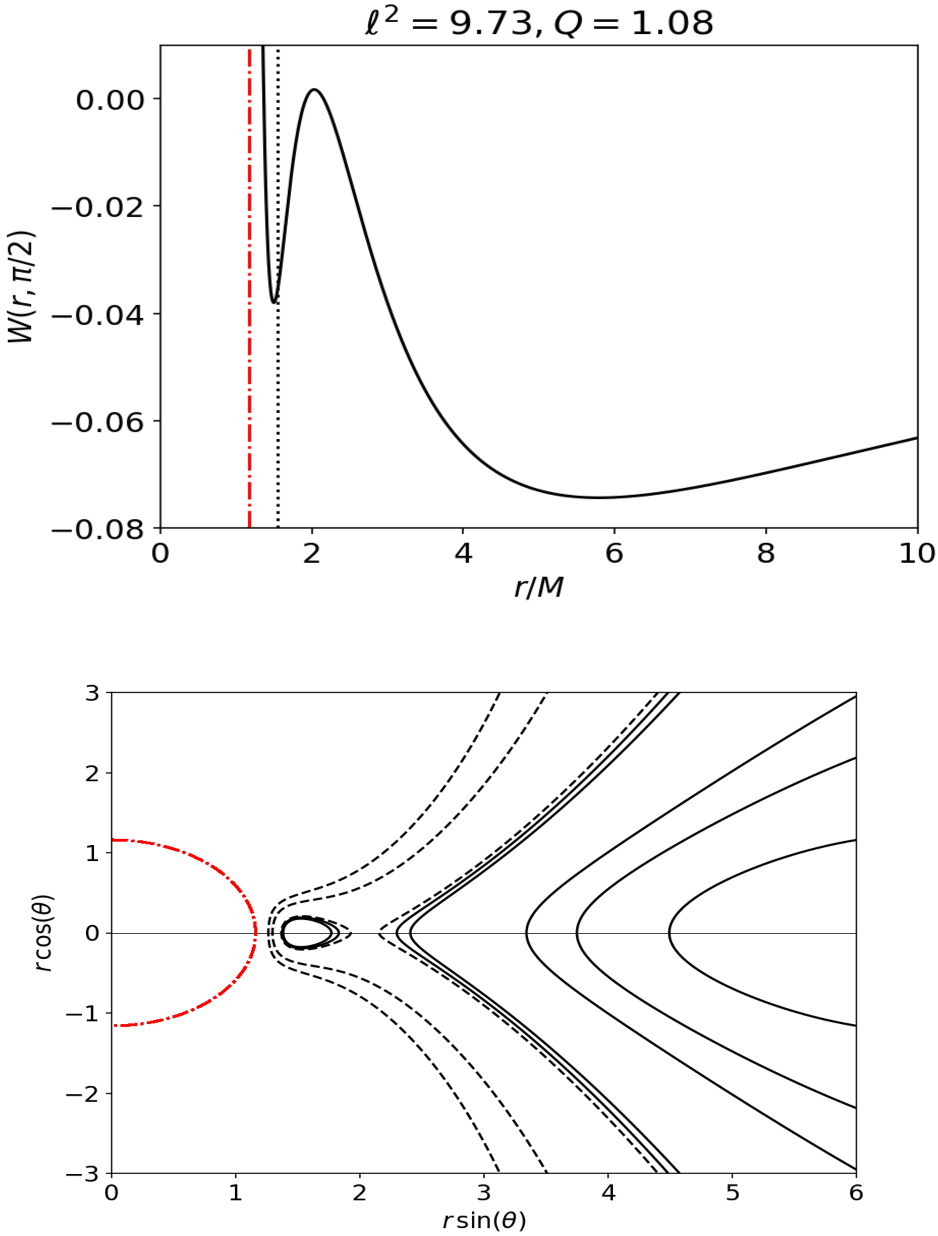

Figure 10. Equilibrium tori around RN naked singularity with Q/M=1.8 with $l_0 = l_{\Omega\max}$. Location of the zero-gravity sphere is indicated by red dotted-dashed line. *Top:* W as a function of r/M in equatorial plane. The radius of maximum angular frequency, $r_{\Omega\max}$, is indicated by the black dotted line. *Bottom:* Meridional cross-section of the equipotential surfaces. Solid closed lines represent toroidal surfaces with negative W value. The black dashed lines represent positive values of W.

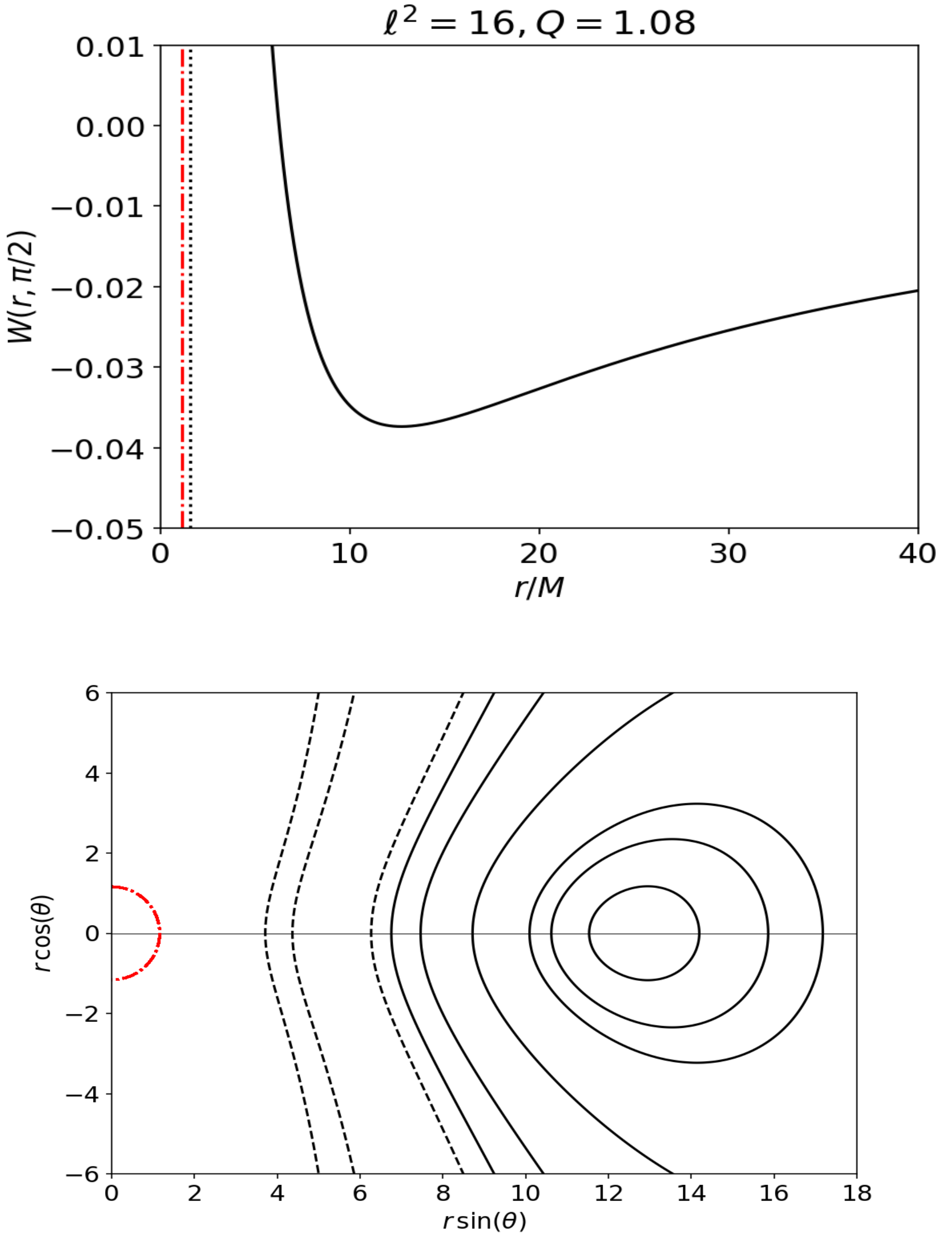

Figure 11. Equilibrium tori around RN naked singularity with Q/M=1.8 with $l_0 > l_{\Omega\max}$. Location of the zero-gravity sphere is indicated by red dotted-dashed line. *Top:* W as a function of r/M in equatorial plane. The radius of maximum angular frequency, $r_{\Omega\max}$, is indicated by the black dotted line. *Bottom:* Meridional cross-section of the equipotential surfaces. Solid closed lines represent toroidal surfaces with negative W value. The black dashed lines represent positive values of W.

Q/M	$l_0^2 << (l_{\Omega\mathrm{max}})^2$	$l_0^2 < (l_{\Omega\mathrm{max}})^2$	$l_0^2 = (l_{\Omega\mathrm{max}})^2$	$l_0^2 > (l_{\Omega\mathrm{max}})^2$
1.08	0.05	8	9.73	16
1.8	0.05	0.7	2.13	9

Table 1. List of specific angular momentum values used in our calculations for two different charge to mass ratios.

CONCLUSIONS

We have studied the shape of fluid tori orbiting the RN naked singularities. Historically, such studies were performed for black holes to gather insight into accretion disks in an era before numerical simulations were feasible. This is the first step of a program aiming to retrace this historical development for the case of naked singularities.

We consider perfect fluid configurations in hydrostatic equilibrium with non-zero[3] uniform angular momentum orbiting Reissner-Nordström singularities. We find that typically, no cusp is formed at the inner edge of toroidal figures of equilibrium around RN singularities. A toroidal solution with a cusp (on the inside of the outer torus or on the outside of the inner torus) can at most be found in that narrow charge-to-mass ratio parameter when marginally stable orbits exist (Figure 10). Unlike in black holes, the equipotential surfaces in RN singularities never self-intersect. Thus, unlike in black holes, where accretion from a toroidal “disk" may proceed onto the compact object through “Roche-lobe-like" overflow with no angular momentum loss, the RN singularity can only be approached if the accreting fluid loses its excess angular momentum—the zero-gravity sphere is engulfed by the fluid only at low values of specific angular momentum (e.g., Figures 4-6). At higher values of specific angular momentum, only unbound matter may approach the singularity (or even the zero-gravity sphere), but it is likely to outflow to infinity (e.g., Figure 7).

The positions and shapes of the constant specific angular momentum equilibrium tori may also be taken to illustrate the general conclusion that for the Reissner-Nordström naked singularity (and similar space-times), a part of any figure of equilibrium of an orbiting fluid must always lie outside of the zero gravity sphere. This may have applications in interpreting the Event Horizon Telescope (EHT) observations of the center of our Galaxy (Mishra and Vieira, 2023).

ACKNOWLEDGEMENTS

This work was supported in part by the Polish NCN grant 2019/33/B/ST9/01564.

---

[3] The zero-angular momentum configurations (levitating atmospheres) are discussed in Vieira and Kluniak (2023)

REFERENCES

Abramowicz, M., Jaroszynski, M. and Sikora, M. (1978), Relativistic, accreting disks., *Astron. Astrophys*, **63**, pp. 221–224.

Kozlowski, M., Jaroszynski, M. and Abramowicz, M. A. (1978), The analytic theory of fluid disks orbiting the Kerr black hole., *Astron. Astrophys*, **63**(1-2), pp. 209–220.

Kucáková, H., Slaný, P. and Stuchlík, Z. (2011), Toroidal configurations of perfect fluid in the Reissner-Nordström-(anti-)de Sitter spacetimes, *J. Cosmol. Astropart. Phys.*, **2011**(1), 033.

Mishra, R. and Vieira, R. S. S. (2023), Conservative limits on the electric charge of Sgr A* in the Reissner-Nordstrom metric, *arXiv e-prints*, arXiv:2304.04313, arXiv: `2304.04313`.

Prada-Méndez, G. D., Lora-Clavijo, F. D. and Velásquez-Cadavid, J. M. (2023), Synchrotron emitting Komissarov torus around naked singularities, *Classical and Quantum Gravity*, **40**(19), 195011, arXiv: `2308.09174`.

Pugliese, D., Quevedo, H. and Ruffini, R. (2011), Circular motion of neutral test particles in Reissner-Nordström spacetime, *Phys. Rev.D*, **83**(2), 024021, arXiv: `1012.5411`.

Rezzolla, L. and Zanotti, O. (2013), *Relativistic Hydrodynamics*.

Stuchlík, Z., Pugliese, D., Schee, J. and Kučáková, H. (2015), Perfect fluid tori orbiting Kehagias-Sfetsos naked singularities, *European Physical Journal C*, **75**, 451, arXiv: `1412.4149`.

Vieira, R. S. S. and Kluniak, W. (2023), Astrophysical cloaking of a naked singularity, *Monthly Notices of the Royal Astronomical Society*, **523**(3), pp. 4615–4623, ISSN 0035-8711, URL `https://doi.org/10.1093/mnras/stad1718`.

Vieira, R. S. S., Schee, J., Kluźniak, W., Stuchlík, Z. c. v. and Abramowicz, M. (2014), Circular geodesics of naked singularities in the kehagias-sfetsos metric of hořava's gravity, *Phys. Rev. D*, **90**, p. 024035.

Proceedings of *RAGtime 23–25*
Z. Stuchlík, G. Török, V. Karas and D. Lančová, editors, Silesian University in Opava, 2023, pp. 167–172

Stability of asymptotically flat (2+1)-dimensional black holes with Gauss-Bonnet corrections

Milena Skvortsova

Peoples' Friendship University of Russia (RUDN University), 6 Miklukho-Maklaya Street,
Moscow, 117198, Russia
`milenas577@mail.ru`

ABSTRACT
Using the integration of wave equation in the time-domain we show that scalar field perturbations around the (2 + 1)-dimensional asymptotically flat black hole with Gauss-Bonnet corrections are dynamically stable even for the near extreme values of the coupling constant.

Keywords: Scalar field perturbations – (2 + 1)-dimensional asymptotically flat black hole – Gauss-Bonnet corrections – quasinormal modes

1 INTRODUCTION

Black holes have been observed in the gravitational (Abbott et al., 2016) and electromagnetic (Akiyama et al., 2019; Goddi et al., 2016) spectra, while ongoing projects promise a great extension of the range of observations (Auclair et al., 2023). Quasinormal modes (Berti et al., 2009; Nollert, 1999; Kokkotas and Schmidt, 1999; Konoplya and Zhidenko, 2011) represent the characteristic oscillations that black holes undergo when perturbed, and they serve as a valuable tool for probing the black holes' fundamental properties. Our study explores the intricate interplay between black hole's quasinormal modes and their (in)stability. Usually, the strict mathematical proof of stability is a very difficult problem (see, for instance, Beyer, 2011). A clear evidence of the linear stability or instability is provided by the analysis of the quasinormal spectrum. If all the quasinormal modes are damped, the black hole is stable, while if there exists at least one unboundedly growing mode, it signifies the onset of instability. Therefore, the instability was extensively studied with the help of quasinormal modes spectra (Takahashi and Soda, 2010; Ishihara et al., 2008; Kodama et al., 2010; Dyatlov, 2011).

The particular black hole metric we will study here is the (2 + 1)-dimensional black hole obtained as a regularization (Glavan and Lin, 2020) of the Einstein-Gauss-Bonnet equations of motion in Konoplya and Zhidenko (2020) and further studied and generalized in Hennigar et al. (2020, 2021). Although the straightforward regularization in Glavan and Lin (2020) did not form a consistent theory in four dimensions, the black hole solution

978-80-7510-576-9

obtained within such a naive approach was also a solution of the well-defined theory formulated in Aoki et al. (2020).

Quasinormal modes of three-dimensional asymptotically AdS (BTZ) spacetimes were extensively studied (Cardoso and Lemos, 2001; Konoplya, 2004; Fontana, 2023), because of their importance in the AdS/CFT correspondence (Birmingham et al., 2002). However, no such analysis has been done so far for the $(2+1)$-dimensional asymptotically flat spacetimes, to the best of our knowledge. Here, we will show that the scalar field perturbations around the $(2+1)$-dimensional asymptotically flat black holes decay with time, even at the near-extreme values of the Gauss-Bonnet coupling.

2 BLACK HOLE METRICS AND WAVELIKE EQUATIONS

The metric of the (2+1)-dimensional black hole has the following form

$$\mathrm{d}s^2 = -f(r)\mathrm{d}t^2 + f(r)^{-1}\mathrm{d}r^2 + r^2\mathrm{d}x^2, \tag{1}$$

where the metric function is

$$f(r) = 1 - \frac{r^2}{2\alpha}\left(-1 + \sqrt{\frac{4\alpha\left(\Lambda\left(r^2 - r_{\mathrm{H}}^2\right) + \frac{\alpha}{r_{\mathrm{H}}^2} + 1\right)}{r^2} + 1}\right). \tag{2}$$

Here, r_{H} is the radius of the event horizon, Λ is the cosmological constant, α is the Gauss-Bonnet coupling constant. When $1 + 2\alpha/r_{\mathrm{H}}^2 > 0$ and the coupling constant $\alpha < 0$ at $\Lambda = 0$ the metric is asymptotically flat and perturbative in α. When the cosmological constant is negative, the metric is reduced to the BTZ one (Banados et al., 1992) up to the redefinition of constants. The general-covariant Klein-Gordon equation

$$\frac{1}{\sqrt{-g}}\partial_\mu\left(\sqrt{-g}g^{\mu\nu}\partial_\nu\Phi\right) = 0, \tag{3}$$

can be reduced to the wave-like form

$$\frac{\mathrm{d}^2\Psi}{\mathrm{d}r_*^2} + (\omega^2 - V(r))\Psi = 0, \tag{4}$$

where the “tortoise coordinate” r_* has the form:

$$\mathrm{d}r_* \equiv \frac{\mathrm{d}r}{f(r)}, \tag{5}$$

and the effective potential is

$$V(r) = f(r)\left(\frac{k^2}{r^2} + \frac{f'(r)}{2r} - \frac{f(r)}{4r^2}\right). \tag{6}$$

Here k is the multipole number.

3 EVOLUTION OF PERTURBATIONS

Quasinormal modes of asymptotically flat black holes are eigenvalues of the above wave-like equation satisfying particular boundary conditions: the waves must be purely outgoing at infinity and purely incoming at the event horizon. For analysis of the evolution of perturbations in time and consideration of the contribution of all the overtones so that the instability, if any, could be detected, we use the time-domain integration method (Gundlach et al., 1994), which was used in numerous works (for instance, Konoplya and Fontana, 2008; Churilova and Stuchlik, 2020; Bronnikov and Konoplya, 2020). It shows a good concordance with more accurate methods. The essence of this method is the integration of the wave equation in the framework of the null-cone coordinates $u = t - r_*$, $v = t + r_*$, using the following discretization (Gundlach et al., 1994),

$$\Psi(N) = \Psi(W) + \Psi(E) - \Psi(S) - \Delta^2 V(S)\,\frac{\Psi(W) + \Psi(E)}{4} + O\left(\Delta^4\right). \tag{7}$$

Here, the points are: $N \equiv (u + \Delta, v + \Delta)$, $W \equiv (u + \Delta, v)$, $E \equiv (u, v + \Delta)$, $S \equiv (u, v)$, and the Gaussian impinging wave package are given on the null surfaces $u = u_0$ and $v = v_0$.

For checking the results obtained by the time-domain integration at $k > 0$ we used the 6th order WKB method with Padé approximants (Konoplya et al., 2019; Matyjasek and Opala, 2017; Konoplya, 2003).

Time-domain profiles show decaying profiles not only for small α (see Fig. 2) but also for the extreme α, as in Fig. 1. If the instability appeared, it would be governed by the non-oscillatory, i.e. purely imaginary, growing mode, as was proved in Konoplya et al. (2008) for generic static backgrounds.

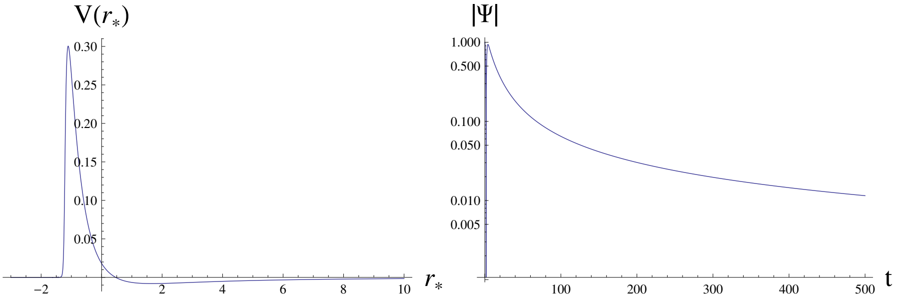

Figure 1. Left: Effective potential as a function of r_*. Right: Time-domain profile of perturbations. Here we have $k = 0$, $\Lambda = 0$, $\alpha = -0.49$. The Prony method suggests that the dominant modes are non-oscillatory $\omega = -0.001899i$

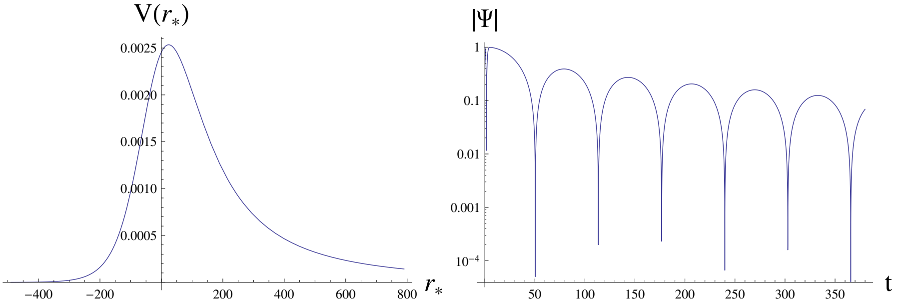

Figure 2. Left: Effective potential as a function of r_*. Right: Time-domain profile of perturbations. Here we have $k = 1$, $\Lambda = 0$, $\alpha = -0.01$. The Prony method gives $\omega = 0.050145 - 0.003598i$, while the 6th order WKB method with Pade approximants gives $\omega = 0.050155 - 0.003579i$

4 CONCLUSIONS

Here, we have shown that asymptotically flat (2 + 1)-dimensional black holes with Gauss-Bonnet corrections are stable even at the near-extreme values of the Gauss-Bonnet coupling. The full parametric range of stability and the other types of asymptotics could be studied in further research. Thus, allowing for a non-zero cosmological constant may bring instabilities to the system (Zhu et al., 2014; Konoplya and Zhidenko, 2014).

ACKNOWLEDGEMENTS

The author acknowledges Dr. R. A. Konoplya for fruitful discussions and for careful reading of the manuscript. This work was supported by RUDN University research project FSSF-2023-0003.

REFERENCES

Abbott, B. P. et al. (LIGO Scientific, Virgo) (2016), Observation of Gravitational Waves from a Binary Black Hole Merger, *Phys. Rev. Lett.*, **116**(6), p. 061102, arXiv: `1602.03837`.

Akiyama, K. et al. (Event Horizon Telescope) (2019), First M87 Event Horizon Telescope Results. I. The Shadow of the Supermassive Black Hole, *Astrophys. J. Lett.*, **875**, p. L1, arXiv: `1906.11238`.

Aoki, K., Gorji, M. A. and Mukohyama, S. (2020), A consistent theory of $D \to 4$ Einstein-Gauss-Bonnet gravity, *Phys. Lett. B*, **810**, p. 135843, arXiv: `2005.03859`.

Auclair, P. et al. (LISA Cosmology Working Group) (2023), Cosmology with the Laser Interferometer Space Antenna, *Living Rev. Rel.*, **26**(1), p. 5, arXiv: `2204.05434`.

Banados, M., Teitelboim, C. and Zanelli, J. (1992), The Black hole in three-dimensional space-time, *Phys. Rev. Lett.*, **69**, pp. 1849–1851, arXiv: `hep-th/9204099`.

Berti, E., Cardoso, V. and Starinets, A. O. (2009), Quasinormal modes of black holes and black branes, *Class. Quant. Grav.*, **26**, p. 163001, arXiv: `0905.2975`.

Beyer, H. R. (2011), On the stability of the massive scalar field in Kerr space-time, *J. Math. Phys.*, **52**, p. 102502, arXiv: `1105.4956`.

Birmingham, D., Sachs, I. and Solodukhin, S. N. (2002), Conformal field theory interpretation of black hole quasinormal modes, *Phys. Rev. Lett.*, **88**, p. 151301, arXiv: `hep-th/0112055`.

Bronnikov, K. A. and Konoplya, R. A. (2020), Echoes in brane worlds: ringing at a black hole–wormhole transition, *Phys. Rev. D*, **101**(6), p. 064004, arXiv: `1912.05315`.

Cardoso, V. and Lemos, J. P. S. (2001), Scalar, electromagnetic and Weyl perturbations of BTZ black holes: Quasinormal modes, *Phys. Rev. D*, **63**, p. 124015, arXiv: `gr-qc/0101052`.

Churilova, M. S. and Stuchlik, Z. (2020), Ringing of the regular black-hole/wormhole transition, *Class. Quant. Grav.*, **37**(7), p. 075014, arXiv: `1911.11823`.

Dyatlov, S. (2011), Quasi-normal modes and exponential energy decay for the Kerr-de Sitter black hole, *Commun. Math. Phys.*, **306**, pp. 119–163, arXiv: `1003.6128`.

Fontana, R. D. B. (2023), Scalar field instabilities in charged BTZ black holes, arXiv: `2306.02504`.

Glavan, D. and Lin, C. (2020), Einstein-Gauss-Bonnet Gravity in Four-Dimensional Spacetime, *Phys. Rev. Lett.*, **124**(8), p. 081301, arXiv: `1905.03601`.

Goddi, C. et al. (2016), BlackHoleCam: Fundamental physics of the galactic center, *Int. J. Mod. Phys. D*, **26**(02), p. 1730001, arXiv: `1606.08879`.

Gundlach, C., Price, R. H. and Pullin, J. (1994), Late time behavior of stellar collapse and explosions: 1. Linearized perturbations, *Phys. Rev. D*, **49**, pp. 883–889, arXiv: `gr-qc/9307009`.

Hennigar, R. A., Kubiznak, D. and Mann, R. B. (2021), Rotating Gauss-Bonnet BTZ Black Holes, *Class. Quant. Grav.*, **38**(3), p. 03LT01, arXiv: `2005.13732`.

Hennigar, R. A., Kubiznak, D., Mann, R. B. and Pollack, C. (2020), Lower-dimensional Gauss–Bonnet gravity and BTZ black holes, *Phys. Lett. B*, **808**, p. 135657, arXiv: `2004.12995`.

Ishihara, H., Kimura, M., Konoplya, R. A., Murata, K., Soda, J. and Zhidenko, A. (2008), Evolution of perturbations of squashed Kaluza-Klein black holes: escape from instability, *Phys. Rev. D*, **77**, p. 084019, arXiv: `0802.0655`.

Kodama, H., Konoplya, R. A. and Zhidenko, A. (2010), Gravitational stability of simply rotating Myers-Perry black holes: Tensorial perturbations, *Phys. Rev. D*, **81**, p. 044007, arXiv: `0904.2154`.

Kokkotas, K. D. and Schmidt, B. G. (1999), Quasinormal modes of stars and black holes, *Living Rev. Rel.*, **2**, p. 2, arXiv: `gr-qc/9909058`.

Konoplya, R. A. (2003), Quasinormal behavior of the d-dimensional Schwarzschild black hole and higher order WKB approach, *Phys. Rev. D*, **68**, p. 024018, arXiv: `gr-qc/0303052`.

Konoplya, R. A. (2004), Influence of the back reaction of the Hawking radiation upon black hole quasinormal modes, *Phys. Rev. D*, **70**, p. 047503, arXiv: `hep-th/0406100`.

Konoplya, R. A. and Fontana, R. D. B. (2008), Quasinormal modes of black holes immersed in a strong magnetic field, *Phys. Lett. B*, **659**, pp. 375–379, arXiv: `0707.1156`.

Konoplya, R. A., Murata, K., Soda, J. and Zhidenko, A. (2008), Looking at the Gregory-Laflamme instability through quasi-normal modes, *Phys. Rev. D*, **78**, p. 084012, arXiv: `0807.1897`.

Konoplya, R. A. and Zhidenko, A. (2011), Quasinormal modes of black holes: From astrophysics to string theory, *Rev. Mod. Phys.*, **83**, pp. 793–836, arXiv: `1102.4014`.

Konoplya, R. A. and Zhidenko, A. (2014), Charged scalar field instability between the event and cosmological horizons, *Phys. Rev. D*, **90**(6), p. 064048, arXiv: `1406.0019`.

Konoplya, R. A. and Zhidenko, A. (2020), BTZ black holes with higher curvature corrections in the 3D Einstein-Lovelock gravity, *Phys. Rev. D*, **102**(6), p. 064004, arXiv: `2003.12171`.

Konoplya, R. A., Zhidenko, A. and Zinhailo, A. F. (2019), Higher order WKB formula for quasinormal modes and grey-body factors: recipes for quick and accurate calculations, *Class. Quant.*

Grav., **36**, p. 155002, arXiv: `1904.10333`.

Matyjasek, J. and Opala, M. (2017), Quasinormal modes of black holes. The improved semianalytic approach, *Phys. Rev. D*, **96**(2), p. 024011, arXiv: `1704.00361`.

Nollert, H.-P. (1999), TOPICAL REVIEW: Quasinormal modes: the characteristic 'sound' of black holes and neutron stars, *Class. Quant. Grav.*, **16**, pp. R159–R216.

Takahashi, T. and Soda, J. (2010), Catastrophic Instability of Small Lovelock Black Holes, *Prog. Theor. Phys.*, **124**, pp. 711–729, arXiv: `1008.1618`.

Zhu, Z., Zhang, S.-J., Pellicer, C. E., Wang, B. and Abdalla, E. (2014), Stability of Reissner-Nordström black hole in de Sitter background under charged scalar perturbation, *Phys. Rev. D*, **90**(4), p. 044042, [Addendum: Phys.Rev.D 90, 049904 (2014)], arXiv: `1405.4931`.

Proceedings of *RAGtime 23–25*
Z. Stuchlík, G. Török, V. Karas and D. Lančová, editors, Silesian University in Opava, 2023, pp. 173–185

General Relativistic Magnetohydrodynamic Simulations of Accreting Tori: Resolution Study

Angelos Karakonstantakis[1,a] Debora Lančová[2,b] and
Miljenko Čemeljić[2,1,3]

[1]Nicolaus Copernicus Astronomical Centre, Polish Academy of Sciences,
ul. Bartycka 18, 00-716 Warsaw, Poland
[2]Research Centre for Computational Physics and Data Processing,
Institute of Physics, Silesian University in Opava,
Bezručovo nám. 13, CZ-746 01 Opava, Czech Republic
[3]Academia Sinica, Institute of Astronomy and Astrophysics,
P.O. Box 23-141, Taipei 106, Taiwan
[a]`karakonang@camk.edu.pl`
[b]`debora.lancova@physics.slu.cz`

ABSTRACT
We present two-dimensional general relativistic radiative magnetohydrodynamical simulations of accretion disks around non-rotating stellar-mass black hole. We study the evolution of an equilibrium accreting torus in different grid resolutions to determine an adequate resolution to produce a stable turbulent disk driven by magneto-rotational instability. We evaluate the quality parameter, Q_θ, from the ratio of MRI wavelength to the grid zone size and examine the effect of resolution in various quantitative values such as the accretion rate, magnetisation, fluxes of physical quantities and disk scale-height. We also analyse how the resolution affects the formation of plasmoids produced in the magnetic reconnection events.

Keywords: Accretion, accretion disks – black hole physics – radiation GRMHD

1 INTRODUCTION

Global General Relativistic (GR) Radiative (R) Magnetohydrodynamical (MHD) simulations are an excellent tool to model the violent and turbulent environment in the vicinity of an accreting compact object. Even though this method can capture the interplay of many different physical processes governing the behaviour of magnetised plasma, it also has many limitations.

One significant limitation is that the GRRMHD solves the flux of quantities on a fixed discrete grid, neglecting the structure inside the grid cells and approximating them as homogeneous. The solution to the related Riemann problem is always only approximate; thus,

978-80-7510-576-9

some information on the low-scale fluctuations is lost. At the same time, accretion in magnetised disks is known to be driven by low-scale turbulences caused by magneto-rotational instability (MRI, Balbus and Hawley, 1991, 1998).

The smaller cell size leads to a smaller time step. The issue becomes even more complex in the case of the GR due to singularities in the commonly used coordinate systems and limitation by the speed of light in the case of radiative MHD. A suitable choice of computational grid parameters is fundamental in GRMHD simulations, as it must have a sufficient resolution to resolve the low-scale turbulences while considering computational demands.

The challenge of the GRMHD method is the scalability of turbulences present in the accretion flow. This makes it difficult to achieve a fully converged solution. Convergence in an accretion disk simulation is often determined by the stability of the flow parameters (e.g., mass accretion rate, density scale height, radiative luminosity). Recently, White et al. (2019) studied numerical convergence in simulations of magnetically arrested disks (MAD) and its effects in the lunch Jets. They studied the effect of 4 different resolutions. They found that turbulent structure does not appear in their lowest resolution, and MRI is suppressed. Also, Ripperda et al. (2022) conducted extreme-resolution 10^4 grid shell resolution 3D simulations of MAD flows and analyzed the appearance of blob structures. They showed that magnetic flux bundles can escape from the event horizon through reconnection and complete a full orbit as low-density hot spots consistent with interferometric observations.

Quality parameters were derived to assess simulation convergence in studies by Hawley et al. (2011, 2013). They are based on the assumption that the characteristic wavelength of the MRI must be well resolved in order to maintain the MRI-induced turbulences. Although satisfying these conditions is important for obtaining reliable and physical results, other limitations and approximations of the GRMHD must still be considered.

Here, we investigate the influence of increasing resolution on simulation results. The structure of this Proceeding is as follows: in Section 2, we describe the employed code `KORAL` and the numerical setup of our simulation. In Section 3, we describe the diagnostic tools we considered; in Section 4, we present the analysis of the simulation results, and in Section 5, we comment on our finding and draw conclusions.

2 NUMERICAL SETUP AND INITIAL CONDITION

2.1 `KORAL` implementation

We use the GRRMHD code `KORAL` to perform global two-dimensional (2D) axisymmetric simulations of accretion onto a $M = 10\,\mathrm{M}_{\odot}$ non-rotating black hole (BH)[1]. The grid resolution is logarithmic in radius and stretches up to $r_{\mathrm{out}} = 1000\,r_{\mathrm{g}}$, where $r_{\mathrm{g}} \equiv GM/c^2$ is the gravitational radius. We considered four increasing-resolution simulation grids described in Table 1.

`KORAL` solves the conservation equations for a fluid with rest-mass density ρ, 4-velocity u^{μ}, and stress-energy tensor $T^{\mu}{}_{\nu}$, coupled with the radiation tensor ($R^{\mu}{}_{\nu}$) via the radiation

---

[1] $\mathrm{M}_{\odot}$ denoting the solar mass

4-force density G_ν. The equations are

$$\nabla_\mu (\rho u^\mu) = 0, \quad \nabla_\mu T^\mu{}_\nu = G_\nu, \quad \nabla_\mu R^\mu{}_\nu = -G_\nu. \tag{1}$$

The MHD stress-energy tensor $T_{\mu\nu}$ is given by

$$T^\mu{}_\nu = \left(\rho + u_{\rm int} + p_{\rm gas} + b^2\right) u^\mu u_\nu + \left(p_{\rm gas} + \frac{1}{2} b^2\right) \delta^\mu_\nu - b^\mu b_\nu, \tag{2}$$

where b^μ is the magnetic field four-vector, $u_{\rm int}$ and $p_{\rm gas} = (\gamma - 1) u_{\rm int}$ are the internal energy and pressure of the gas in the comoving frame, with γ being the adiabatic index.

The implementation of the various processes in the `KORAL` code was described in an extensive collection of published papers, including Sądowski et al. (2013, 2014); Sądowski and Narayan (2015); Sądowski et al. (2015, 2017); Chael et al. (2017), and recently also summarised in Lančová (2023).

2.1.1 Mean-field dynamo

MRI-driven turbulences are responsible for angular momentum transport in BH accretion disks. A physical mechanism is required to sustain the magnetic fields in time against dissipation. Local and global simulations of accretion disks have shown that shearing due to differential rotation induces a turbulent dynamo capable of amplifying and sustaining magnetic fields against dissipation (see Del Zanna et al., 2022 and references therein).

MHD dynamo cannot operate in axisymmetric plasma configurations, as follows from Cowling's anti-dynamo theorem (Brandenburg et al., 1995). Therefore, capturing the growth of MRI self-consistently requires a three-dimensional (3D) simulation, which is computationally expensive given the long evolution times and requirements for high resolution. However, the `KORAL` code implementation allows for replenishment of the magnetic field with an artificial mean-field dynamo term in the case of a 2D axisymmetric configuration, as introduced in Sądowski et al. (2015). The dynamo efficiently counterbalances the magnetic field dissipation.

2.2 Initial state

All simulations presented in this work are initialised by a torus in hydrodynamical equilibrium following Penna et al. (2013). Fig. 1 shows the initial distribution of matter and magnetic field topology in the meridional plane. The inner edge of the initial torus is located at $R_{\rm in} = 22\, r_{\rm g}$. It is initially threaded with a poloidal magnetic field, such that the magnetization in the torus centre is $\beta = p_{\rm mag}/p_{\rm gas} = 20$, where $p_{\rm mag}$ is the magnetic pressure.

The initial angular momentum on the equatorial plane is set up as a fraction of the Keplerian Ω multiplied by a factor $\xi = 0.975$ for $R > R_1 = 30\, r_{\rm g}$. Inside R_1, the angular momentum is constant. The initial state corresponds to simulation `r300a0` (but with single loop magnetic field loop as shown in Fig. 1) in Sądowski et al. (2015), where the results were compared to a 3D simulation with the same parameters but without the dynamo term,

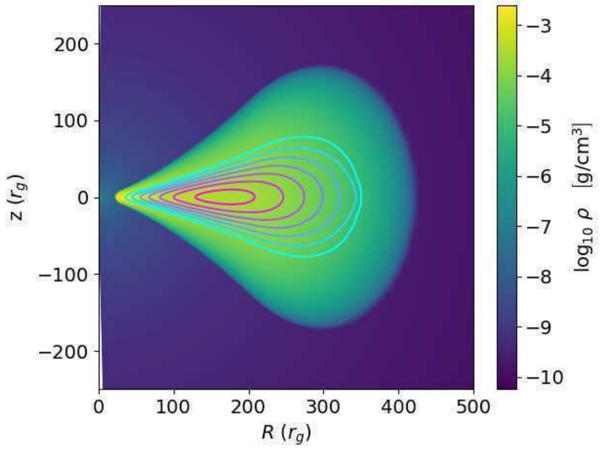

Figure 1. Snapshot of the initial state in our simulations, showing logarithm of gas density. Contours show the initial poloidal magnetic field lines.

leading to comparable time-averaged results. The effects of different magnetic field configurations, including a similar looped configuration, have been studied by Kolo and Janiuk (2020).

The simulations were run for 20 000 $t_{\rm g}$ in total[2]. After $t \sim 10\,000\,t_{\rm g}$ from the beginning, the simulations become more stable as the accretion rate stabilises to a value close to $\dot{M} = \int_0^\pi \rho u^r \sqrt{g} {\rm d}\theta \simeq 10\,\dot{M}_{\rm Edd}$[3]. From this point to the end of the simulation, we averaged the data to study the mean properties of the accretion disk.

3 DIAGNOSTIC TOOLS FOR TESTING RESOLUTION

Inadequate resolution can lead to a number of numerical artefacts, crashing of the simulations, or even wrong results. For example, it may suppress the growth of MRI when the wavelength (of at least) the fastest-growing instability mode is longer than the grid shell size. The MRI produces turbulences, but when the resolution is low, only a small range of wave numbers can be captured, distorting the properties of those turbulences. If the simulation fails to capture the turbulent structure initiated and sustained by MRI fluctuations, angular momentum is not transported outwards, which prevents mass accretion. However, high-resolution simulations are computationally very expensive. Thus, it is useful to determine whether a given simulation has adequate resolution to produce accurate quantitative results.

One would presume that numerical results converge to an exact solution as the grid size decreases. An approach to determine the accuracy of a given simulation is to run

---

[2] $t_{\rm g} = r_{\rm g}/c$

[3] $\dot{M}_{\rm Edd} = L_{\rm Edd}/\eta c^2$, where, $\eta = -L_{\rm tot}/\int_0^\pi \rho u^r {\rm d}\theta c^2$ is the radiative efficiency with $L_{\rm tot}$ defined in eq. (6).

again for a higher (e.g. doubled) resolution and check for convergence in the results. As part of this investigation, we ran a series of simulations with increasing resolution to test the convergence. However, different quantities have different convergence rates and are subject to the limitations of the numerical algorithm used. Still, additional effects beyond resolution, such as resistivity or viscosity terms, significantly impact magnetic stress for the same resolution. Moreover, the chaotic nature of the turbulent processes introduces an additional layer of complexity in interpreting the convergence. These intricacies make it challenging to reach a definitive conclusion regarding the effect of resolution alone.

3.1 MRI quality parameter

The first diagnostic tool considered for resolution is derived from the MRI characteristic wavelength, $\lambda^{\mathrm{MRI}} \propto |u_{\mathrm{A}}|/\Omega$, where u_{A} is the Alfvén velocity and Ω is the angular velocity. Sano et al. (2004) studied the linear evolution of MRI in local shearing box simulation and found that at least 6 resolution grid zones should resolve MRI wavelength ($\lambda_i^{\mathrm{MRI}}/\Delta x_i \geq 6$).

Common indicators for the proper resolution to resolve the MRI turbulences are the quality parameters $Q_i \equiv \lambda_i^{\mathrm{MRI}}/\Delta x_i$ (first introduced in Noble et al., 2010; Hawley et al., 2011), where Δx_i denotes the grid size in the i-th direction. Noble et al. (2010) studied the properties of the turbulence through global GRMHD simulations and suggested that $Q_\theta \gtrsim 20$ is adequate for resolving MRI.

Furthermore, Hawley et al. (2011), who performed global MHD simulations using a pseudo-Newtonian potential and examined previous results of shearing box simulations, emphasise the importance of considering a resolution parameter in the toroidal direction (i.e. $Q_\phi \gtrsim 20$ and $Q_\theta \gtrsim 10$). The authors noted that the two parameters (Q_ϕ, Q_θ) are not independent of each other: higher values in one direction can compensate for lower values in the other. For example $Q_\theta \gtrsim 10-15$ can compensate for a lower value of $Q_\phi \approx 20$ (Sorathia et al., 2012). Hence, the product of $Q_\theta Q_\phi \gtrsim 200$ has also been suggested as a criterion for convergence (Narayan et al., 2012).

In our case of 2D axisymmetric simulations, only Q_θ can be defined. Therefore, we consider $Q_\theta > 20$ as adequate for resolving MRI. We define Q_θ as:

$$Q_\theta = \frac{2\pi}{\Omega \mathrm{d}\hat{x}^\theta} \frac{\left|\hat{b}^\theta\right|}{\sqrt{\rho}}, \tag{3}$$

where the magnetic field component $\hat{b}^\theta$ and the grid cell size $\mathrm{d}\hat{x}^\theta$ are evaluated in the fluid frame (denoted with hats). In addition, we consider the theta average of the quality parameter as a function of radius. For this reason, we compute the density-weighted quality parameter as a function of the cylindrical radius R:

$$\langle Q_\theta \rangle (R) = \frac{\int Q_\theta \rho \mathrm{d}\theta}{\int \rho \mathrm{d}\theta}. \tag{4}$$

4 RESULTS

In this section, we describe selected properties of the accretion flow in the simulations and their dependency on resolution. The quantities are shown either as a function of time or their spatial or radial profile from time-averaged data.

Fig. 2 shows the color-maps of the gas density and the radiation energy density in the fluid frame ($\hat{E}$) from averaged data. The white solid line shows the surface of the last scattering (photosphere) and the dashed lines show the surface corresponds to density scale-height (h_τ). h_τ, calculated in the z direction. It is apparent that for a low resolution, the funnel region is not formed properly, and the disk photosphere is much higher than in the case of the high resolution. In the $(N_r \times N_\theta) = 64^2$ grid shells simulation, the photosphere position cannot be properly established at all, leading to the jump in the bottom half of the domain. We also examined the scale-height h_ρ of the simulated accretion disk, calculated as

$$h_\rho = \sqrt{\frac{\int \rho z^2 \mathrm{d}z}{\int \rho \mathrm{d}z}}, \tag{5}$$

as shown with the dashed lines in Fig. 2 and as a function of radius in the right panel of Fig. 5 with the various solid lines corresponding to different resolutions. The time average scale-height is roughly stable for $R > 20\, r_g$, and a typical value is between 0.25–0.30.

Before discussing other results, we examine if the resolution is adequate for capturing MRI following the discussion in Section 3. Fig. 3 shows the values of Q_θ for each resolution. For higher resolutions, i.e. $(N_r \times N_\theta) = 256^2,\ 512^2$, the values are higher than 20 for the vast majority of the cells, which indicate adequate resolution (see Section 3.1).

For the highest resolution, $Q_\theta > 1000$, while for the lower resolution, the values are < 10. We can conclude that the resolution of 64^2 is inadequate to capture MRI. In the case of $(N_r \times N_\theta) = 128^2$, $Q_\theta \sim 10$ for most cells. However, in the equatorial plane, the values reach $Q_\theta \geq 20$. MRI may be properly resolved in that case, especially if the resolution in the toroidal direction is high enough (i.e. $Q_\phi \gtrsim 20$), which can compensate for lower values in Q_θ. We conclude that the resolution requirement is $(N_r \times N_\theta) = 256^2$ or greater.

In Fig. 4 (left panel), we show the time evolution of the Q parameter measured at $R = 20\, r_g$ and theta as defined from eq. 4. We observe that the values are initially very low and fluctuate until the disk is formed and reaches inflow equilibrium for the measured radius, coinciding with the time when the accretion rate becomes stable.

4.1 Accretion Rate

The time evolution of the accretion rate measured close to the BH event horizon is shown in Fig. 4 (right panel). The mean value and variance of the accretion rate after $10\,000\, t_\mathrm{g}$ (indicated by the vertical line) until the end of each simulation is given in the second column of Table 1 while the third column shows the time average value of the resolution parameter. The variance of the accretion rate fluctuations is decreasing with increasing resolution. The very high variance of the resolution parameter in the highest resolutions is because a vary high value at $t \sim 18\,000\, t_\mathrm{g}$. However, the variability of 2D simulations using the artificial

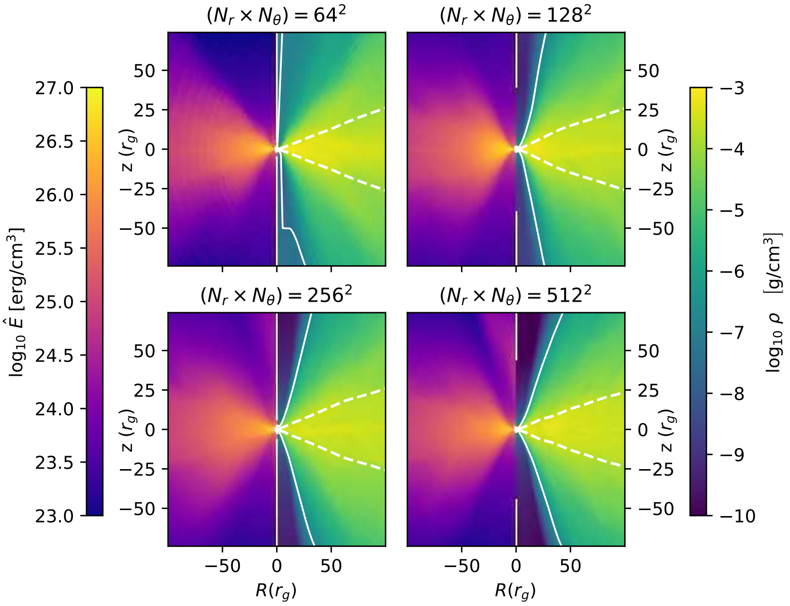

Figure 2. The logarithm of radiation energy density in the fluid frame (*left panels*) and time average density (*right panels*). The solid line surface shows the position of the photosphere and the dashed line correspond to the density scale-height.

Table 1. The $10-20\times10^3\ t_{\rm g}$ average and standard variance of the accretion rate at event horizon and resolution parameter at $R = 20\,r_{\rm g}$.

$(N_r \times N_\theta)$	$\langle \dot{M} \rangle$ $(\dot{M}_{\rm Edd})$	$\langle Q_\theta \rangle$ $(R = 20\,r_{\rm g})$
64^2	11.3 ± 7.2	1.5 ± 1.1
128^2	12.6 ± 5.2	06 ± 38
256^2	11.2 ± 4.4	25 ± 32
512^2	09.4 ± 3.8	100 ± 100

dynamo term is shown to be higher than in the 3D simulations (Sądowski et al., 2015), so these results should be interpreted with caution.

4.2 Magnetization

We calculated the magnetization, $\sigma = b^2/\rho$, across the resolutions. The results are plotted in Fig. 5 (left panel). The magnetization as a function of radial coordinate decreases with increasing radius for all resolutions and the values converge as the resolution is increased with 256^2 and 512^2 grid shells resolution being almost identical. Thus, we can conclude

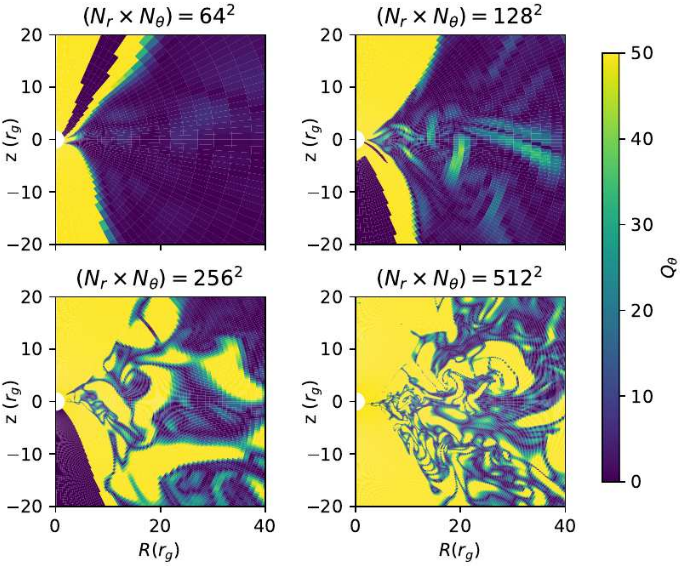

Figure 3. The values of resolution quality parameter Q_θ measured at $t = 15 \times 10^3\, t_\mathrm{g}$.

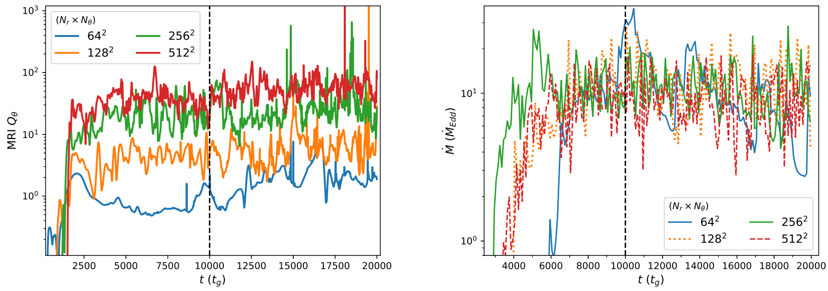

Figure 4. The time evolution of the quality parameter $\langle Q_\theta \rangle (R = 20\, r_\mathrm{g})$ (*left panel*) and of the accretion rate measured close to the black hole event horizon (*right panel*). The vertical line indicates $t \geq 10\,000\, t_\mathrm{g}$ for which we average the results. Dashed lines were chosen for better clarity between overlapping lines.

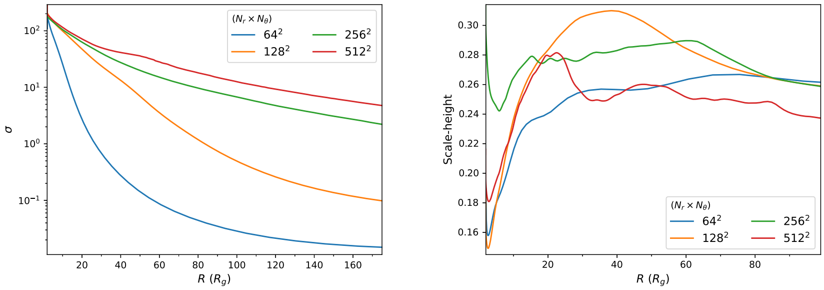

Figure 5. The magnetization (*left panel*) and the disk scale-height (*right panel*) as a function of radius from the time-averaged data.

that magnetization values are affected by resolution and tend to converge at the same value as the resolution increases.

4.3 Luminosities

An interesting application of numerical simulations is to compare the luminosity or spectra with observations. Therefore, in this section we examine if these results converge. The total luminosity in all forms of energy may be defined by integrating the flux carried by gas and radiation:

$$L_{\rm tot}\ (R) = -\int_0^\pi \left(T^r{}_t + R^r{}_t + \rho u^r\right) \sqrt{-g}\,{\rm d}\theta. \tag{6}$$

We define the radiative luminosity:

$$L_{\rm rad}\ (R) = -\int_0^\pi R^r{}_t \sqrt{-g}\,{\rm d}\theta. \tag{7}$$

Fig. 6 shows the values of $L_{\rm tot}$ (left panel) and $L_{\rm rad}$ (right panel) for each resolution. While these values are affected by resolution, they remain within the same order of magnitude. In the left panel of Fig. 7, the radiation energy density measured in the fluid frame, $(\hat{E})$, is identical for all simulations. Interestingly, the resolution does not affect the radiative quantities as much as those related to MHD fluid.

4.4 Formation of Plasmoids

Plasmoids, which in 2D show as magnetic islands, are bubbles of magnetised gas formed in elongated magnetic sheets, and their formation is connected with magnetic reconnection. Current sheets subject to turbulence induced in accretion disks may become thin enough to break apart into plasmoids. Because the thickness of the sheet is limited by numerical resolution, in low resolutions, plasmoids are not formed. In our results, only the highest resolution of 512^2 grid cells allows the current sheet to become thin enough for plasmoids

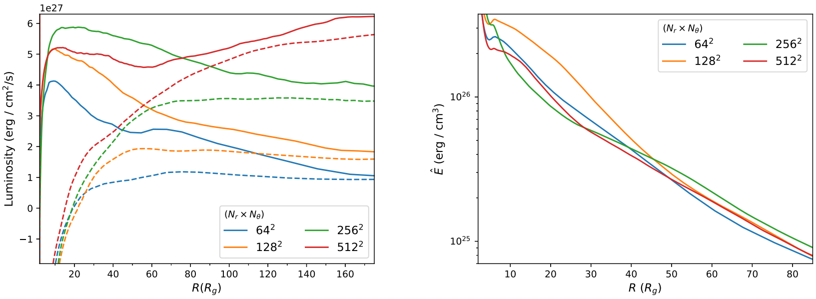

Figure 6. *Left panel:* The value of total (solid lines) and radiative luminosity (dashed lines) from eqs. 6, 7 respectively. *Right panel:* The radiation energy density in the fluid frame.

to form, as shown in the right panel of Fig. 7. This observation underscores the critical role of resolution in capturing intricate magnetic reconnection processes.

5 DISCUSSION AND CONCLUSIONS

In this study, we conducted a series of radiative General Relativistic Magnetohydrodynamics (GRMHD) simulations, systematically varying the resolution to assess convergence. The selected resolutions were tested using quality parameters as resolution diagnostics, analyzed to examine the key properties of the accretion flow and determine the optimal

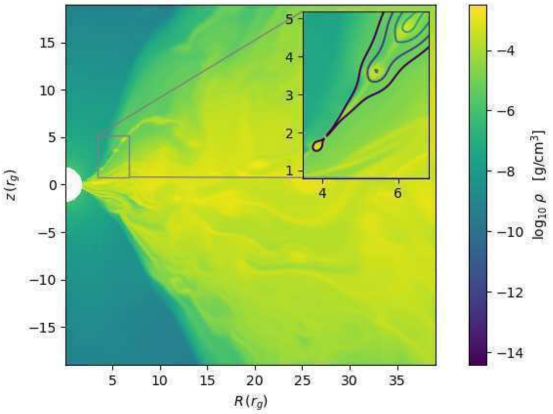

Figure 7. Snapshot at $t \sim 10\,000\,t_g$ showing the logarithm of density and the formation of plasmoids (*inserted panel*) in the simulation with resolution $N_r \times N_\theta = 512^2$ grid cells. Contours show the magnetic field lines.

resolution for magnetohydrodynamic simulations of the accretion disk and assessing result convergence. We summarize our main results below:

(1) We observed that the accretion rate stabilizes when the Magnetorotational Instability (MRI) is properly resolved at $t > 3 \times 10^3\, t_g$ as indicated by the value of quality parameters ($Q_\theta > 20$). The variance of the average value of accretion rate is decreasing with increasing resolution.

(2) Resolutions lower than $(N_R \times N_\theta) < 128^2$ are inadequate to capture MRI suggesting this resolution being a potential threshold. We observed higher resolutions (i.e. 256^2, 512^2) not to have a significant quantitative difference.

(3) The calculation of magnetization showed convergence as resolution increased while radiation energy density remain unaffected by resolution changes, luminosity and scale-height remained relatively stable across resolutions.

(4) Low resolution cannot resolve the fine structure of blobs, plasmoids are only appear in the highest resolution.

This comprehensive analysis demonstrates the critical importance of resolution in accurately simulating and interpreting the dynamics of accretion flows. Adequate resolution is essential for capturing phenomena such as MRI or fine structural details such as the formation of plasmoids, ensuring the reliability of simulation results in understanding the intricate processes governing accretion disks.

ACKNOWLEDGEMENTS

This work was supported in part by the Polish NCN grants 2019/33/B/ST9/01564 and 2019/35/O/ST9/03965. MČ acknowledges the Czech Science Foundation (GAČR) grant No. 21-06825X. DL acknowledge the internal grant of Silesian University, SGS/31/2023. A.K. thanks Włodek Kluźniak and Jiří Horák for the suggestions, and useful conversations. We gratefully acknowledge Polands high-performance computing infrastructure PLGrid (HPC Centers: ACK Cyfronet AGH), for providing computer facilities and support within computational grant no. PLG/2023/016168. Part of the computations for this article have been performed using computer cluster at CAMK PAN.

REFERENCES

Balbus, S. A. and Hawley, J. F. (1991), A Powerful Local Shear Instability in Weakly Magnetized Disks. I. Linear Analysis, *The Astrophysical Journal* , **376**, p. 214.

Balbus, S. A. and Hawley, J. F. (1998), Instability, turbulence, and enhanced transport in accretion disks, *Reviews of Modern Physics*, **70**(1), pp. 1–53.

Brandenburg, A., Nordlund, A., Stein, R. F. and Torkelsson, U. (1995), Dynamo-generated Turbulence and Large-Scale Magnetic Fields in a Keplerian Shear Flow, *The Astrophysical Journal* , **446**, p. 741.

Chael, A. A., Narayan, R. and Sądowski, A. (2017), Evolving non-thermal electrons in simulations of black hole accretion, *Monthly Notices of the Royal Astronomical Society* , **470**(2), pp. 2367–2386, arXiv: `1704.05092`.

Del Zanna, L., Tomei, N., Franceschetti, K., Bugli, M. and Bucciantini, N. (2022), General relativistic magnetohydrodynamics mean-field dynamos, *Fluids*, **7**(2), p. 87, ISSN 2311-5521, URL `http://dx.doi.org/10.3390/fluids7020087`.

Hawley, J. F., Guan, X. and Krolik, J. H. (2011), Assessing Quantitative Results in Accretion Simulations: From Local to Global, *The Astrophysical Journal* , **738**(1), 84, arXiv: `1103.5987`.

Hawley, J. F., Richers, S. A., Guan, X. and Krolik, J. H. (2013), Testing Convergence for Global Accretion Disks, *The Astrophysical Journal* , **772**(2), 102, arXiv: `1306.0243`.

Kolo, M. and Janiuk, A. (2020), Simulations of black hole accretion torus in various magnetic field configurations, arXiv: `2004.07535`.

Lančová, D. (2023), Computer modelling of accretion processes in binary systems with black holes and neutron stars, *arXiv e-prints*, arXiv: `2310.13152`.

Narayan, R., Sądowski, A., Penna, R. F. and Kulkarni, A. K. (2012), GRMHD simulations of magnetized advection-dominated accretion on a non-spinning black hole: role of outflows, *Monthly Notices of the Royal Astronomical Society* , **426**(4), pp. 3241–3259, arXiv: `1206.1213`.

Noble, S. C., Krolik, J. H. and Hawley, J. F. (2010), Dependence of Inner Accretion Disk Stress on Parameters: The Schwarzschild Case, *The Astrophysical Journal* , **711**(2), pp. 959–973, arXiv: `1001.4809`.

Penna, R. F., Kulkarni, A. and Narayan, R. (2013), A new equilibrium torus solution and GRMHD initial conditions, *A&A*, **559**, A116, arXiv: `1309.3680`.

Ripperda, B., Liska, M., Chatterjee, K., Musoke, G., Philippov, A. A., Markoff, S. B., Tchekhovskoy, A. and Younsi, Z. (2022), Black hole flares: Ejection of accreted magnetic flux through 3d plasmoid-mediated reconnection, *The Astrophysical Journal Letters*, **924**(2), p. L32, URL `https://dx.doi.org/10.3847/2041-8213/ac46a1`.

Sano, T., Inutsuka, S.-i., Turner, N. J. and Stone, J. M. (2004), Angular Momentum Transport by Magnetohydrodynamic Turbulence in Accretion Disks: Gas Pressure Dependence of the Saturation Level of the Magnetorotational Instability, *The Astrophysical Journal* , **605**(1), pp. 321–339, arXiv: `astro-ph/0312480`.

Sądowski, A. and Narayan, R. (2015), Photon-conserving Comptonization in simulations of accretion discs around black holes, *Monthly Notices of the Royal Astronomical Society* , **454**(3), pp. 2372–2380, arXiv: `1508.04980`.

Sądowski, A., Narayan, R., McKinney, J. C. and Tchekhovskoy, A. (2014), Numerical simulations of super-critical black hole accretion flows in general relativity, *Monthly Notices of the Royal Astronomical Society* , **439**(1), pp. 503–520, arXiv: `1311.5900`.

Sądowski, A., Narayan, R., Tchekhovskoy, A., Abarca, D., Zhu, Y. and McKinney, J. C. (2015), Global simulations of axisymmetric radiative black hole accretion discs in general relativity with a mean-field magnetic dynamo, *Monthly Notices of the Royal Astronomical Society* , **447**(1), pp. 49–71, arXiv: `1407.4421`.

Sądowski, A., Narayan, R., Tchekhovskoy, A. and Zhu, Y. (2013), Semi-implicit scheme for treating radiation under M1 closure in general relativistic conservative fluid dynamics codes, *Monthly Notices of the Royal Astronomical Society* , **429**(4), pp. 3533–3550, arXiv: `1212.5050`.

Sądowski, A., Wielgus, M., Narayan, R., Abarca, D., McKinney, J. C. and Chael, A. (2017), Radiative, two-temperature simulations of low-luminosity black hole accretion flows in general relativity, *Monthly Notices of the Royal Astronomical Society* , **466**(1), pp. 705–725, arXiv: `1605.03184`.

Sorathia, K. A., Reynolds, C. S., Stone, J. M. and Beckwith, K. (2012), Global Simulations of Accretion Disks. I. Convergence and Comparisons with Local Models, *The Astrophysical Journal* , **749**(2), 189, arXiv: `1106.4019`.

White, C. J., Stone, J. M. and Quataert, E. (2019), A resolution study of magnetically arrested disks, *The Astrophysical Journal*, **874**(2), p. 168, URL `https://dx.doi.org/10.3847/1538-4357/ab0c0c`.

Proceedings of *RAGtime 23–25*
Z. Stuchlík, G. Török, V. Karas and D. Lančová, editors, Silesian University in Opava, 2023, pp. 187–198

Nodal precession model applied for twin HF QPOs observed around magnetized neutron stars

Zdeněk Stuchlík[1] and Jaroslav Vrba[1,a]

[1]Research Centre for Theoretical Physics and Astrophysics,
Institute of Physics, Silesian University in Opava,
Bezručovo nám. 13, 746 01 Opava, CZ
[a]`Jaroslav.Vrba@physics.slu.cz`

ABSTRACT
The nodal oscillations of matter orbiting compact objects such as black holes and neutron stars are usually applied for the explanation of the observed low-frequency quasiperiodic oscillations. In the present paper, we test the applicability of the nodal precession variants of the magnetically modified geodesic model based on the epicyclic motion of slightly charged matter in the magnetosphere of a neutron star represented by the Schwarzschild geometry combined with the dipole magnetic field for fitting of the twin high-frequency quasiperiodic oscillations observed around magnetized neutron stars. We demonstrate that there is a nodal precession variant giving a possibility to fit the data similarly to the standard relativistic precession variant, and we show that the other nodal variant can be clearly excluded.

Keywords: Dipole magnetic field – neutron star – orbiting charged matter – observed quasi-periodic oscillations

1 INTRODUCTION

Charged matter orbiting a magnetized neutron star (NS) can have frequencies of the epicyclic oscillatory motion around equatorial circular orbits, along with the orbital frequency of these circular orbits, comparable to the frequencies of the twin-peak, high-frequency quasiperiodic oscillations (HF QPOs) observed in binary systems containing magnetized NSs (Vrba et al., submitted) – a magnetized NS can be conveniently modeled by the Schwarzschild geometry and the dipole magnetic field that defines the equatorial plane of the whole background. The magnetic parameter b representing the ratio of the electromagnetic and gravitational forces acting on the charged matter must be sufficiently small for comparability to the observed frequencies and can correspond to matter with a very small

978-80-7510-576-9

specific charge so that only charged dust or plasmoids can be considered as acceptable, while protons (electrons) or ions are excluded[1].

In the standard geodesic model of the quasiperiodic oscillations, usually, the relativistic precession variants (or the epicyclic resonance variants) are considered for the explanations of the twin HF QPOs, while the nodal precession frequency is usually applied for an explanation of the low-frequency quasiperiodic oscillations (Tasheva and Stefanov, 2021). Here, we test the possibility of applying the nodal precession variants of the magnetically modified geodesic model, i.e., the variants of the relativistic precession model where the radial epicyclic frequency is substituted by the latitudinal epicyclic frequency, for charged test matter orbiting with epicyclic oscillations a magnetized NS described by the simple model considered in Vrba et al. (submitted).

We give the frequencies of the epicyclic orbital motion of the charged test matter in the equatorial plane of the magnetized NS and present the fitting curves for the nodal precession variants of the magnetically modified geodesic model to the data of the twin HF QPOs observed in binary systems containing NSs. We also give for comparison fitting of these data by the relativistic precession variants of the model.

The radius of the NS is assumed at $R = 3M$, thus, the dipole magnetic field is relevant at the range of $r > 3M$. The epicyclic oscillations around the off-equatorial circular orbits, discussed in detail in Vrba et al. (submitted), are not considered in the present paper, as they predict frequencies higher than the observed frequencies. We focus on the oscillations around the equatorial circular orbits.

Throughout this paper, we use space-like signature $(- + + +)$ and a geometric system of units in which $G = c = 1$; we restore them when we need to compare our results with observational data. Greek indices run from $0 - 3$, and Latin indices run from $1 - 3$.

2 RELATIVISTIC DIPOLE MAGNETOSPHERE OF NSS

We use the Schwarzschild geometry with line element given in the standard Schwarzschild coordinates (t, r, θ, φ) in the form

$$\mathrm{d}s^2 = -f(r)\,\mathrm{d}t^2 + f(r)^{-1}\,\mathrm{d}r^2 + r^2\left(\mathrm{d}\theta^2 + \sin^2\theta\mathrm{d}\varphi^2\right), \tag{1}$$

where

$$f(r) = 1 - \frac{2M}{r}, \tag{2}$$

M denotes the NS mass.

Around NSs with a dipole magnetic field, the motion of the charged test particles will be limited by their surface. We choose it at $R = 3M$ as this radius is the upper limit on the so-called extremely compact objects having a radius located under the photon sphere of the vacuum Schwarzschild spacetime.

---

[1] The electromagnetic Lorentz force acting on electrons or protons in the vicinity of black hole event horizon or the NS surface can lead in standard astrophysical situations to the enormous acceleration of electrons, protons, or ions (Stuchlík and Kološ, 2016a; Tursunov et al., 2020a; Stuchlík et al., 2020, 2021).

The dipole magnetic field of a considered NS can be generated by a circular current loop with radius $a \geq 2M$, located on the surface of the NS equatorial plane or by current sheet flashing on the whole NS surface. Using the Schwarzschild metric means that we can approach its horizon, but limits on the radius of realistic NSs have to be taken into consideration. The four-vector electromagnetic potential A^{μ} of the outer part of the dipole-field solution ($r > a$) in the Schwarzschild metric has only one non-zero component $-A_{\mu} = (0, 0, 0, A_{\varphi})$. The only non-zero component of the four-potential, A_{φ}, is given by Kovář et al. (2008); Petterson (1974); Preti (2004)

$$\begin{aligned} A_{\varphi} &= -\mathcal{B}\left[\ln\left(1 - \frac{2M}{r}\right) + \frac{2M}{r}\left(1 + \frac{M}{r}\right)\right] r^2 \sin^2\theta \\ &= -\mathcal{B}\, h\,(r, \theta) \end{aligned} \tag{3}$$

and the parameter governing the magnetic field is given by

$$\mathcal{B} = \frac{3\mu}{8M^3}, \tag{4}$$

where μ is the magnetic dipole moment of the NS. The Maxwell tensor, $F_{\mu\nu} = A_{\nu,\mu} - A_{\mu,\nu}$, has only two non-zero components

$$\begin{aligned} F_{r\varphi} &= \frac{\partial A_{\varphi}}{\partial r} = B^{\theta} \\ &= 2\mathcal{B} \sin^2\theta \left(\frac{2M(r-M)}{2M-r} - r \ln\frac{r-2M}{r}\right) \end{aligned} \tag{5}$$

and

$$\begin{aligned} F_{\theta\varphi} &= \frac{\partial A_{\varphi}}{\partial \theta} = B^{r} \\ &= -\mathcal{B} \sin(2\theta)\left[r^2 \ln\frac{r-2M}{r} + 2M\,(M + r)\right]. \end{aligned} \tag{6}$$

Clearly, in the equatorial plane, B^{r} vanishes, while on the symmetry axis also B^{θ} vanishes.

The magnetic field intensity $B^{\hat{\theta}}$ measured by local static observers on the NS surface enables to express the magnetic dipole moment in the form (Bakala et al., 2010)

$$\mu = \frac{4M^3 R^{3/2}\sqrt{R-2M}}{6M\,(R-M) + 3R\,(R-2M)\ln f(R)} B^{\hat{\theta}}. \tag{7}$$

Considering a magnetized NS with $R = 3M$, $M = 2M_{\odot}$[2] and $B_{\mathrm{surf}} = 10^8$ G, we obtain the magnetic dipole moment $\mu \doteq 7 \times 10^{-4}\,\mathrm{m}^2$.

---

[2] where $M_{\odot}$ is the solar mass

3 CHARGED PARTICLE DYNAMICS IN DIPOLE MAGNETIC FIELD OF NSS AND EQUATORIAL CIRCULAR ORBITS

The charged test particle motion is governed by the Lorentz equation

$$\frac{\mathrm{d}u^\mu}{\mathrm{d}\tau} + \Gamma^\mu_{\alpha\beta} u^\alpha u^\beta = \frac{q}{m} F^\mu_{\ \alpha} u^\alpha, \tag{8}$$

where u^μ is the four-velocity of the particle with the mass m and charge q, normalized by the condition $u_\alpha u^\alpha = -1$, τ is the proper time of the particle, and $F_{\mu\nu}$ is the antisymmetric tensor of the electromagnetic field. It can be deduced from the Hamiltonian formalism, see e.g. Kološ et al. (2015). The Hamiltonian H reads

$$H = \frac{1}{2} g^{\alpha\beta} (\pi_\alpha - qA_\alpha)\left(\pi_\beta - qA_\beta\right) + \frac{m^2}{2}, \tag{9}$$

where canonical four-momentum π_μ is given by the relation $\pi_\mu = mu_\mu + qA_\mu$. The test particle motion is governed by the Hamilton equations

$$\frac{\mathrm{d}x^\mu}{\mathrm{d}\zeta} = \frac{\partial H}{\partial \pi_\mu}, \quad \frac{\mathrm{d}\pi_\mu}{\mathrm{d}\zeta} = -\frac{\partial H}{\partial x^\mu}, \tag{10}$$

where $\zeta = \tau/m$. The symmetries of the Schwarzschild spacetime (1) and the dipole magnetic field (3) imply the existence of two constants of the particle motion – covariant specific energy and covariant specific axial angular momentum

$$\mathcal{E} = \frac{E}{m} = -\frac{\pi_t}{m} = -g_{tt}u^t, \quad \mathcal{L} = \frac{L}{m} = \frac{\pi_\varphi}{m} = g_{\varphi\varphi}u^\varphi + \bar{q}A_\varphi, \tag{11}$$

where $\bar{q} = q/m$ is the specific charge of the particle. The Hamiltonian (9) can be expressed in the separated form

$$\frac{H}{m^2} = \frac{1}{2} g^{rr} u_r^2 + \frac{1}{2} g^{\theta\theta} u_\theta^2 + \frac{1}{2} g^{tt} \mathcal{E}^2 + \frac{1}{2} g^{\varphi\varphi}\left(\mathcal{L} - \bar{q}A_\varphi\right)^2 + \frac{1}{2} = H_{\mathrm{D}} + H_{\mathrm{P}}, \tag{12}$$

consisting of the dynamical, H_{D}, and potential, H_{P}, parts

$$H_{\mathrm{D}} = \frac{1}{2}\left(g^{rr}u_r^2 + g^{\theta\theta}u_\theta^2\right), \tag{13}$$

$$H_{\mathrm{P}} = \frac{1}{2}\left[g^{tt}\mathcal{E}^2 + g^{\varphi\varphi}\left(\mathcal{L} - \bar{q}A_\varphi\right)^2 + 1\right]. \tag{14}$$

The motion of charged particles can be characterized by the turning points determined by the condition $H_{\mathrm{P}} = 0$, which gives the regions of the spacetime available (in the $r - \theta$ plane) for the motion of the particles with the given motion constants E, L, in dependence on the electromagnetic interaction given by the particle specific charge and intensity and character of the magnetic field.

3.1 Effective potential and equatorial circular orbits

The motion in the considered background is generally of chaotic character (Stuchlík et al., 2020), but it can be characterized by the effective potential, which represents the barrier governing the particle motion in dependence on the motion constants and the parameters of the background.

The turning points of the radial motion are determined by the equation $E = V_{\text{eff}}(r,\theta;\mathcal{L},b)$ and the effective potential reads (Kovář et al., 2008)

$$V_{\text{eff}}(r,\theta) \equiv -g_{tt}\left[g^{\varphi\varphi}\left(\mathcal{L}-\bar{q}A_{\varphi}\right)^{2}+1\right]$$
$$=\left(1-\frac{2M}{r}\right)\left[\left(\frac{\mathcal{L}}{r\sin\theta}-b\,h(r,\theta)\ r\sin\theta\right)^{2}+1\right], \tag{15}$$

being thus given by the motion constant $\mathcal{L}$ and the "magnetic parameter" b determining the intensity of the particle interaction with the given magnetic field

$$b=\bar{q}\mathcal{B}=\frac{q}{m}\frac{3\mu}{8M^{3}}. \tag{16}$$

The positive (negative) value of the magnetic parameter b corresponds to the magnetic attraction (repulsion) with inward (outward) directed electromagnetic Lorentz force.

The local extrema of the effective potential determines the circular orbits of charged particles that are stable (unstable) for local minima (maxima). The epicyclic motion is possible only around the stable circular orbits. Here, we concentrate on the equatorial circular orbits that must be considered in the regions where stability is satisfied for both radial and latitudinal (vertical) perturbations – for details, see Vrba et al. (submitted). The axial angular momentum $\mathcal{L}$ of the charged particles following the equatorial circular orbits with fixed parameter b are given by the relations (assuming in the following $M = 1$)

$$\mathcal{L}_{\text{c}}=\frac{b}{r-3}\left[r^{2}\,\mathrm{Ln}\,(r)+2r+6\right]+r\frac{\triangle(r,b)}{r-3}, \tag{17}$$

where $\triangle(r,b)=\sqrt{b^{2}\left[2\,(r-1)+(r-2)\,r\,\mathrm{Ln}\,(r)\right]^{2}+r-3}$ and $\mathrm{Ln}\,(r)=\ln\frac{r-2}{r}$. The specific energy $\mathcal{E}$ of the particles at these circular orbits reads

$$\mathcal{E}_{\text{c}}=r^{-1}\sqrt{1-\frac{2}{r}}\left\{-br^{2}+\left[r\frac{\triangle(r,b)}{r-3}\right.\right.$$
$$\left.\left.+\frac{br^{2}\,\mathrm{Ln}\,(r)+2br+6b}{r-3}-r^{2}\,\mathrm{Ln}\,(r)-2\,(r+1)\right]^{2}\right\}^{\frac{1}{2}}. \tag{18}$$

Because of the symmetry of the effective potential relative to the sign change of $\mathcal{L}$ and b, we can restrict attention to the corotating orbits. We can see that the circular orbits can exist at $r > 3$, while both the specific angular momentum and specific energy diverge if $r \to 3$; at $r = 3$, the equatorial photon circular orbit is located. The special reality condition

$$\left[2b\,(r-1)+b\,(r-2)\,r\,\mathrm{Ln}\,(r)\right]^{2}+r-3\geq 0, \tag{19}$$

governing the existence of the equatorial circular orbits at the radii $2 < r < 3$ is irrelevant here, as we assume $R = 3$.

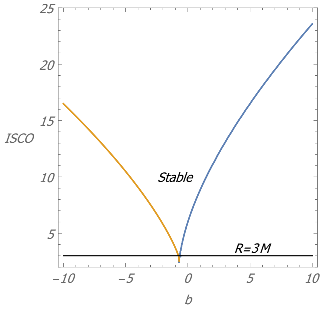

Figure 1. Dependence of ISCO position on the dipole magnetic field parameter b. The blue curve gives ISCO due to instability in the radial direction, and the orange curve gives ISCO due to instability in the latitudinal direction – relating to the off-equatorial circular orbits (Vrba et al., submitted).

The stability of the equatorial circular orbits in both radial and latitudinal directions is studied in detail in Vrba et al. (submitted) and we simply use the results of this paper, see Figure 1. We give only short summary of these results: for values of the magnetic parameter $b > b_{\mathrm{rISCO}}(r = 3) \doteq -0.654$ a marginally stable circular orbit exists at some $r > 3$ due to instability in the radial direction, while for values of $b < b_{\theta\mathrm{ISCO}}(r = 3) \doteq -0.751$, the instability at the marginally stable orbit is in the latitudinal direction – two fundamentally distinct scenarios of the instability of the equatorial circular orbits arise; in the case of $b_{\theta\mathrm{ISCO}}(r = 3) \doteq -0.751 < b < b_{\mathrm{rISCO}}(r = 3) \doteq -0.654$, the equatorial circular orbits are stable at $r > 3$ (Vrba et al., submitted).

4 FREQUENCIES OF THE EPICYCLIC EQUATORIAL ORBITAL MOTION

The locally measured epicyclic frequencies around the equatorial circular orbits are given in general axially symmetric backgrounds of the type considered here by Kološ et al. (2015)

$$\omega_{\mathrm{r}}^2(r) = \partial_{rr}^2 V_{\mathrm{eff}}, \qquad \omega_\theta^2(r) = \partial_{\theta\theta}^2 V_{\mathrm{eff}}. \tag{20}$$

The orbital frequency of the circular orbit related to the particle's proper time reads

$$\omega_\varphi = \frac{\mathrm{d}\varphi}{\mathrm{d}\tau} = \mathcal{L}(r, \theta = \pi/2)\, g^{\varphi\varphi} - bh(r, \theta = \pi/2)\,. \tag{21}$$

Since the frequencies (20) are calculated for the local comoving observer, we have to transform to the system of a static observer at infinity due to the redshift effect, using the standard SI units. The transformation for general locally measured angular frequency ω to general frequency ν measured by the distant observer can be expressed in the form

$$\nu_i = \frac{1}{2\pi}\frac{c^3}{GM}\frac{\omega_i}{-g^{tt}\mathcal{E}(r)}, \tag{22}$$

where $i = \{r, \theta, \varphi\}$.

By using the effective potential introduced above (20), we can derive the expressions for the local epicyclic frequencies of charged particles in the field of a magnetized NS with magnetic dipole field in the form (Vrba et al., submitted)

$$
\begin{aligned}
\omega_{\mathrm{r}}^2 = &-\frac{1}{r^5\,(r-2)^2}\times \\
&\Big\{b^2(r-2)\left[(r-2)^2\,r^4\mathrm{Ln}^2\,(r)+4\,(r-3)\,r^4\,\mathrm{Ln}\,(r)+4\left(r^4-2r^3-3r^2-4r+12\right)\right] \\
&+\frac{3\,(r-2)^3\left[r\triangle(r,b)+br^2\,\mathrm{Ln}\,(r)+2br+6b\right]^2}{(r-3)^2}-2\,(r-2)\,r^3 \\
&-\frac{16b\left(2r^2-7r+6\right)\left[r\triangle(r,b)+br^2\,\mathrm{Ln}\,(r)+2br+6b\right]}{r-3} \\
&-2\,(r-2)\,r^3\,\frac{\left[\triangle(r,b)+br^2\,\mathrm{Ln}\,(r)+2br-2br\,\mathrm{Ln}\,(r)-2b\right]^2}{(r-3)^2}\Bigg\}, \qquad (23)
\end{aligned}
$$

$$
\begin{aligned}
\omega_\theta^2 = &\frac{1}{r^4}\left\{\frac{\left(r\triangle(r,b)+br^2\,\mathrm{Ln}\,(r)+2br+6b\right)^2}{(r-3)^2}\right. \\
&\left.-\,b^2r^4\mathrm{Ln}^2\,(r)-4b^2r^3\,\mathrm{Ln}\,(r)-4b^2r^2-4b^2r^2\,\mathrm{Ln}\,(r)-8b^2r-4b^2\right\}, \qquad (24)
\end{aligned}
$$

$$
\omega_\varphi = \frac{\triangle(r,b)+br^2\,\mathrm{Ln}\,(r)+2br-2br\,\mathrm{Ln}\,(r)-2b}{(r-3)\,r}. \qquad (25)
$$

See also Bakala et al. (2010), where the frequencies were derived in different ways, having the same form. For a slowly rotating sphere, the frequencies were derived in Bakala et al. (2012). By applying transformation (22) to equations (23-25), we obtain the observable epicyclic frequencies. The behavior of the frequencies $\nu_r\,(r)\,, \nu_\theta\,(r)$ and $\nu_\varphi\,(r)$, as functions of the radial coordinate r in equatorial plane ($\theta = \pi/2$), is demonstrated in Figure 2.

The frequencies of epicyclic oscillations of charged particles in the field of a NS with a magnetic dipole differ in many aspects from the frequencies of uncharged particles in a Schwarzschild compact object. The most remarkable manifestation of these differences is the separation of the latitudinal and Keplerian frequencies. This occurs in the presence of any nonzero magnetic field in the case of a homogeneous magnetic field, it was studied in (in the case of a homogeneous magnetic field, it was studied in Kološ et al., 2015) and is a consequence of the disruption of spherical symmetry of the background. The strong differences in behavior of the epicyclic and orbital frequencies demonstrated in the case of the dipole magnetic field inspired the idea to apply the nodal precession variants of the magnetically modified geodesic model to the case of HF QPOs observed in the binary systems containing a NS.

Another effect that influences the behavior of the epicyclic motion is the shift in the location of the ISCO in dependence on the parameter b (see Figure 1). The last significant difference is the interchange of the profiles of the epicyclic latitudinal and radial frequencies for negative values of the parameter b due to the θ-instability – see Figure 2.

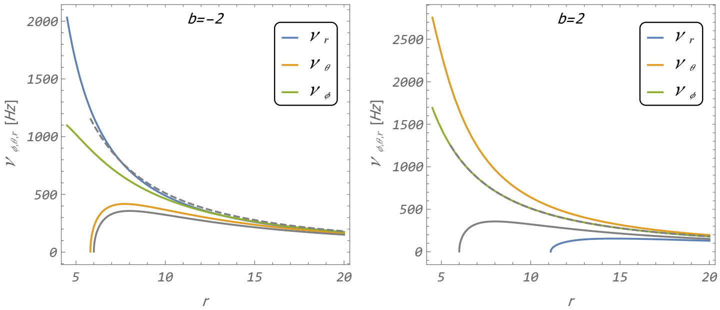

Figure 2. Epicyclic frequencies in the equatorial plane ($\theta = \pi/2$) for a NS with mass $M = 2M_\odot$ and various strengths of dipole magnetic field constructed for frequencies of the epicyclic equatorial circular motion. The colored curves represent the epicyclic frequencies in the dipole configuration. The solid black and dashed black curves represent the radial and latitudinal (Keplerian) frequencies in the Schwarzschild case, respectively.

5 FITTING TO THE HF QPOS

The HF QPOs play a crucial role in astrophysics as they provide a very solid basis for predicting the parameters of compact objects in accretion systems.

5.1 Geodesic models and their modifications

There are two main variants (and their subvariants) of the so-called geodesic model of HF QPOs using the frequencies of the epicyclic oscillations and the orbital motion in fitting the data observed in the astrophysical systems containing a black hole or a NS (Stuchlík and Kološ, 2016b): the Epicyclic Resonance (ER) model (Kluzniak and Abramowicz, 2001; Abramowicz and Kluźniak, 2001; Remillard and McClintock, 2006; Török et al., 2005) and the Relativistic Precession (RP) model (Stella et al., 1999a,b). For details of the geodesic model of HF QPOs and their applications on the situations around BHs and NSs, see Stuchlík et al. (2013); Stuchlík and Kološ (2016b).

Modification of the variants of the geodesic model by the presence of a magnetic field acting on a slightly charged orbiting matter significantly enlarges the ability of the modified model to fit the observational data because of adding a new free parameter b reflecting the electromagnetic interaction of the charged matter with the external magnetic field (Bakala et al., 2010; Kološ et al., 2017; Stuchlík et al., 2022). Here, we test in a rough way the applicability of the new variant, called nodal precession and representing a direct modification of the relativistic precession variant by substituting the radial epicyclic frequency with the latitudinal epicyclic frequency to fit the data of HF QPOs. In order to estimate the efficiency of the possibility of fitting, we compare the fitting curves of the whole set of the NS HF QPO data for the nodal precession and relativistic precession variant of the magnetically modified geodesic model.

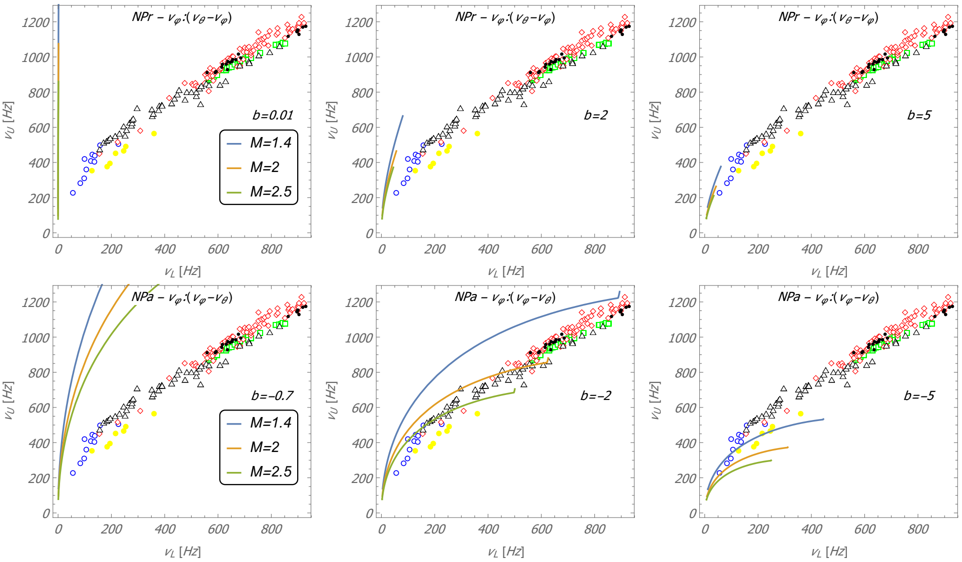

Figure 3. The NP variants of the equatorial geodesic model. HF QPOs fits for the collected data of selected sources. We variate dipole magnetic parameter b and mass of the NS.

We present only rough estimates of possible fitting to the HF QPOs observed in binary systems containing NSs using the collected data of the observed binary systems. Detailed fitting to data from individual sources is planned for future papers.

We thus use the upper (ν_{U}) and lower (ν_{L}) frequencies of the two peaks observed in the data, which are as follows for each model. The variants must differ for $b > 0$ and $b < 0$ due to the different radial profiles of the frequencies ν_r, ν_θ, ν_φ

$\underline{\mathrm{NP_a}}$: $\nu_{\mathrm{U}} = \nu_\varphi$ and $\nu_{\mathrm{L}} = \nu_\theta - \nu_\varphi$

$\underline{\mathrm{RP_a}}$: $\nu_{\mathrm{U}} = \nu_\varphi$ and $\nu_{\mathrm{L}} = \nu_\varphi - \nu_r$

$\underline{\mathrm{NP_r}}$: $\nu_{\mathrm{U}} = \nu_\varphi$ and $\nu_{\mathrm{L}} = \nu_\varphi - \nu_\theta$

$\underline{\mathrm{RP_r}}$: $\nu_{\mathrm{U}} = \nu_\varphi$ and $\nu_{\mathrm{L}} = \nu_r - \nu_\varphi$.

The fitting of the upper and lower frequency curves for each model to the astrophysical data are shown in Figure 4, where is presented the NP variants, while Figure 3 corresponds to the RP variants. It is evident that in one of the sub-variants, both the NP and RP are promising, while the other seems to be quite excluded. It is evident that both models show quite promising results for the specifically chosen values of parameter b. The RP model exhibits the best agreement with astrophysical data for low positive values $b \sim 0.01$, whereas the NP model shows the most promising results around negative values $b \sim -2$.

The charged particle within our test particle model can also represent an elementary particle (electron, proton), but the fitting to HF QPO data cannot be fulfilled for $B = 10^8 - 10^{12}$ G in strong NS magnetosphere. Our "charged test particle" more likely represents a hot spot (plasmoid, "ball lightning") in accretion flow with density lower (higher) than the surrounding plasma and with accumulated net electric charge (Ripperda et al.,

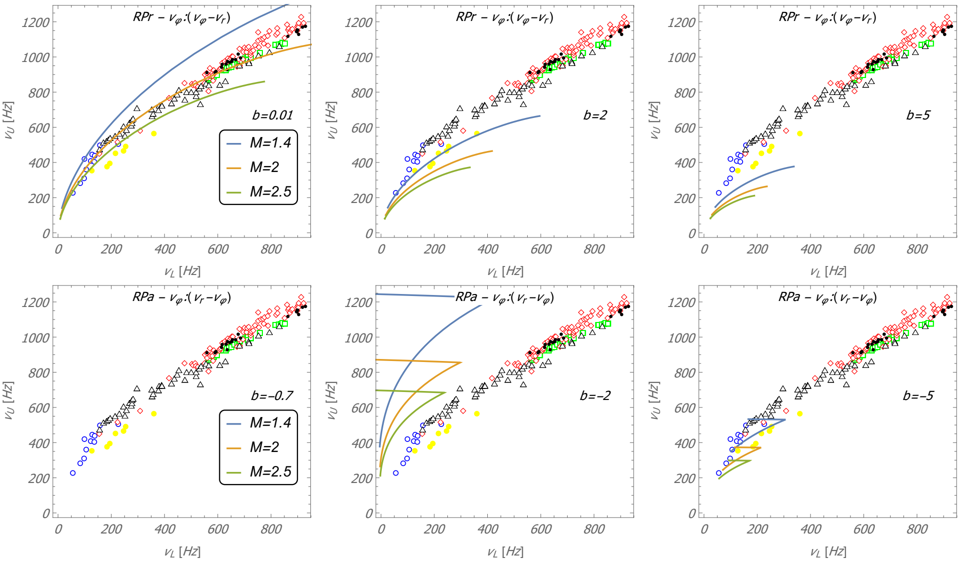

Figure 4. The RP variants of the equatorial geodesic model. HF QPOs fits for the collected data of selected sources. We variate dipole magnetic parameter b and mass of the NS.

2020; Tursunov et al., 2020b). Our HF QPOs fits can be thus used for estimates of such hot-spot (plasmoid) net specific charge. Another possible application of our "charged particle" model is that it could model magnetic field influence on quasi-neutral plasma flow. Such a connection between charged particle dynamics and plasma flow is based on the interesting finding that the fundamental frequencies of test particle dynamics could be present in the spectra of oscillating accretion disk (Mishra et al., 2019).

6 CONCLUSIONS

The presence of magnetic fields around NS is of utmost importance in numerous astrophysical contexts, as their effects can be of critical significance, even in the case of electromagnetic interaction, which is small in comparison with gravitational interaction. In fitting to data of HF QPOs from the atol sources containing NSs, the magnetically modified variants of the geodesic model based on epicyclic oscillations of orbiting charged matter can be promising. We have shown that not only the $\mathrm{PR_a}$ variant reflecting Lorentz attraction can give fits for $b \sim 0.01$, but also the $\mathrm{NP_r}$ variant with Lorentz repulsion can allow good fits for $b \sim -2$.

The fitting of the HF QPOs should be thus to slightly charged matter, e.g. to charged dust, plasmoids, or structures similar to ball lighting, if we consider the realistic magnetic field as observed in the atoll sources having NSs with magnetic field intensity ranging from 10^8G to 10^{12} G. For example, singly ionized dust grains with masses of the order of 10^{-13} g for $b \sim 0.01$ (10^{-11} g for $b \sim -2$) could be the potential contributors to this phenomenon, for the magnetic field strengths of $B = 10^{10}$ G. We can expect that the two discussed variants of the magnetically modified geodesic model of HF QPOs could improve precession of the individual data fits in some of the observed binaries containing NSs. Further improvement could be expected with the inclusion of the rotational effect of the NS that can be realized at least on the level of the Lense-Thirring term to the Schwarzschild geometry.

ACKNOWLEDGEMENTS

The authors would like to acknowledge the institutional support of the Research Centre For Theoretical Physics and Astrophysics, Institute of Physics, Silesian University in Opava.

REFERENCES

Abramowicz, M. A. and Kluźniak, W. (2001), A precise determination of black hole spin in GRO J1655-40, *Astronomy and Astrophysics*, **374**, pp. L19–L20, arXiv: `astro-ph/0105077`.

Bakala, P., Urbanec, M., Šrámková, E., Stuchlík, Z. and Török, G. (2012), On magnetic-field-induced corrections to the orbital and epicyclic frequencies: paper II. Slowly rotating magnetized neutron stars, *Classical and Quantum Gravity*, **29**(6), 065012.

Bakala, P., Šrámková, E., Stuchlík, Z. and Török, G. (2010), On magnetic-field-induced non-geodesic corrections to relativistic orbital and epicyclic frequencies, *Classical and Quantum Gravity*, **27**(4), 045001.

Kluzniak, W. and Abramowicz, M. A. (2001), Strong-Field Gravity and Orbital Resonance in Black Holes and Neutron Stars — kHz Quasi-Periodic Oscillations (QPO), *Acta Physica Polonica B*, **32**(11), p. 3605.

Kološ, M., Stuchlík, Z. and Tursunov, A. (2015), Quasi-harmonic oscillatory motion of charged particles around a Schwarzschild black hole immersed in a uniform magnetic field, *Classical and Quantum Gravity*, **32**(16), 165009, arXiv: `1506.06799`.

Kološ, M., Tursunov, A. and Stuchlík, Z. (2017), Possible signature of the magnetic fields related to quasi-periodic oscillations observed in microquasars, *European Physical Journal C*, **77**(12), 860, arXiv: `1707.02224`.

Kovář, J., Stuchlík, Z. and Karas, V. (2008), Off-equatorial orbits in strong gravitational fields near compact objects, *Classical and Quantum Gravity*, **25**(9), 095011, arXiv: `0803.3155`.

Mishra, B., Kluźniak, W. and Fragile, P. C. (2019), Breathing Oscillations in a Global Simulation of a Thin Accretion Disk, *Monthly Notices of the RAS*, **483**(4), pp. 4811–4819, arXiv: `1810.05755`.

Petterson, J. A. (1974), Magnetic field of a current loop around a Schwarzschild black hole, *Physical Review D*, **10**(10), pp. 3166–3170.

Preti, G. (2004), On charged particle orbits in dipole magnetic fields around Schwarzschild black holes, *Classical and Quantum Gravity*, **21**(14), pp. 3433–3445.

Remillard, R. A. and McClintock, J. E. (2006), X-Ray Properties of Black-Hole Binaries, *Annual Review of Astronomy & Astrophysics*, **44**(1), pp. 49–92, arXiv: `astro-ph/0606352`.

Ripperda, B., Bacchini, F. and Philippov, A. A. (2020), Magnetic Reconnection and Hot Spot Formation in Black Hole Accretion Disks, *Astrophysical Journal*, **900**(2), 100, arXiv: `2003.04330`.

Stella, L., Vietri, M. and Morsink, S. M. (1999a), Correlations in the Quasi-periodic Oscillation Frequencies of Low-Mass X-Ray Binaries and the Relativistic Precession Model, *Astrophysical Journal Letters*, **524**(1), pp. L63–L66, arXiv: `astro-ph/9907346`.

Stella, L., Vietri, M. and Morsink, S. M. (1999b), Correlations in the Quasi-periodic Oscillation Frequencies of Low-Mass X-Ray Binaries and the Relativistic Precession Model, *Astrophysical Journal Letters*, **524**(1), pp. L63–L66, arXiv: `astro-ph/9907346`.

Stuchlík, Z. and Kološ, M. (2016a), Acceleration of the charged particles due to chaotic scattering in the combined black hole gravitational field and asymptotically uniform magnetic field, *European Physical Journal C*, **76**, 32, arXiv: `1511.02936`.

Stuchlík, Z. and Kološ, M. (2016b), Models of quasi-periodic oscillations related to mass and spin of the GRO J1655-40 black hole, *Astronomy and Astrophysics*, **586**, A130, arXiv: `1603.07366`.

Stuchlík, Z., Kološ, M., Kovář, J., Slaný, P. and Tursunov, A. (2020), Influence of Cosmic Repulsion and Magnetic Fields on Accretion Disks Rotating around Kerr Black Holes, *Universe*, **6**(2), p. 26.

Stuchlík, Z., Kološ, M. and Tursunov, A. (2021), Penrose Process: Its Variants and Astrophysical Applications, *Universe*, **7**(11), p. 416.

Stuchlík, Z., Kološ, M. and Tursunov, A. (2022), Large-scale magnetic fields enabling fitting of the high-frequency QPOs observed around supermassive black holes, *Publications of the Astronomical Society of Japan*, **74**(5), pp. 1220–1233.

Stuchlík, Z., Kotrlová, A. and Török, G. (2013), Multi-resonance orbital model of high-frequency quasi-periodic oscillations: possible high-precision determination of black hole and neutron star spin, *Astronomy and Astrophysics*, **552**, A10, arXiv: `1305.3552`.

Tasheva, R. and Stefanov, I. (2021), Geodesic model complience with the frequencies of the observed X-ray quasi-period oscillations of XTE J1807-294, *Bulgarian Astronomical Journal*, **34**, p. 103, arXiv: `2305.12198`.

Török, G., Abramowicz, M. A., Kluźniak, W. and Stuchlík, Z. (2005), The orbital resonance model for twin peak kHz quasi periodic oscillations in microquasars, *Astronomy and Astrophysics*, **436**(1), pp. 1–8.

Tursunov, A., Stuchlík, Z., Kološ, M., Dadhich, N. and Ahmedov, B. (2020a), Supermassive Black Holes as Possible Sources of Ultrahigh-energy Cosmic Rays, *Astrophysical Journal*, **895**(1), 14, arXiv: `2004.07907`.

Tursunov, A., Zajaček, M., Eckart, A., Kološ, M., Britzen, S., Stuchlík, Z., Czerny, B. and Karas, V. (2020b), Effect of Electromagnetic Interaction on Galactic Center Flare Components, *Astrophysical Journal*, **897**(1), 99, arXiv: `1912.08174`.

Vrba, J., Kološ, M. and Stuchlík, Z. (submitted), Charged particles in dipole magnetosphere of neutron stars: epicyclic oscillations in and off equatorial plane.

Proceedings of *RAGtime 23–25*
Z. Stuchlík, G. Török, V. Karas and D. Lančová, editors, Silesian University in Opava, 2023, pp. 199–203

Harmonic oscillations of charged particles around weakly charged black hole

Bakhtinur Juraev[1,a] and Arman Tursunov[2,1,b]

[1]Research Centre for Theoretical Physics and Astrophysics, Institute of Physics,
Silesian University in Opava, Bezručovo nám. 13, CZ-746 01 Opava, Czech Republic
[2]Max Planck Institute for Radio Astronomy, Auf dem Hügel 69, Bonn D-53121, Germany
[a]`jur0173@slu.cz`
[b]`arman.tursunov@physics.slu.cz`

ABSTRACT
The electric charge of a black hole is frequently neglected in many astrophysical scenarios due to unrealistically large values of the charge necessary for the Reissner-Nordström spacetime metric. Nevertheless, a variety of selective accretion processes could result in a black hole having a gravitationally weak electric charge. Thus, the motion of charged particles can be influenced by a combined effect of gravitational attraction and electrostatic interaction, which can be attractive or repulsive. This can lead to the existence of certain observational patterns in the non-thermal spectra of astrophysical black holes. In the present work, we study the harmonic oscillations of charged particles around a weakly charged black hole.

Keywords: Black hole – electric charge – harmonic oscillations

1 INTRODUCTION

The *no-hair theorem* states that the spacetime around black holes can be fully described by at most three metric parameters – black hole mass, spin, and electric charge. The charge of the black hole is usually neglected in astrophysical scenarios, justified by unrealistically large values of the charge required for its visible effect on the spacetime metric. Indeed, one can compare the gravitational radius of a black hole with the characteristic length of the charge $Q_{\rm G}$ of the Reissner-Nordström black hole, which gives the maximum charge value

$$\sqrt{\frac{Q_{\rm G}^2 G}{c^4}} = \frac{2GM}{c^2}, \quad \Rightarrow \quad Q_{\rm G} = 2G^{1/2}M \approx 10^{31}\frac{M}{10M_\odot}\,\text{Fr}. \tag{1}$$

This high value of charge is not yet justifiable in astrophysically relevant scenarios. On the other hand, there exist several astrophysical mechanisms based on selective accretion, in which the black hole can be weakly charged. The reader may refer for further details to

978-80-7510-576-9

Zajaček et al. (2018); Zajacek and Tursunov (2019); Tursunov et al. (2021). Wald mechanism (Wald, 1974) is a well-known method of charging black holes. It involves the natural induction of charge by the twisting of magnetic field lines caused by the black hole's rotation's frame-dragging effect. Therefore, the black hole and the surrounding magnetosphere should both accumulate a charge of $Q \sim 10^{18}$ Fr per solar mass. Recently, it was proposed that primordial black holes (PBHs) can be charged due to Poisson fluctuation at horizon crossing or high-energy particle collisions (Araya et al., 2023), and it was reported that the range of Q for PBHs is between 10^{-22} Fr and 10^{-6} Fr per kg, respectively.

In this paper, we study harmonic oscillations of charged particles in the vicinity of , a weakly charged black hole. Harmonic oscillations of charged particles in the vicinity of weakly magnetized black holes were previously studied in Kološ et al. (2015); Tursunov et al. (2016).

We use the metric signature $(- + + +)$, and the system of geometric units, in which $G = M = c = 1$.

2 DYNAMICS OF A CHARGED PARTICLE

2.1 Equations of motion

Spherically symmetric solution of Einstein's field equations, corresponding to the Schwarzschild spacetime metric, reads

$$\mathrm{d}s^2 = -f(r)\mathrm{d}t^2 + f^{-1}(r)\mathrm{d}r^2 + r^2\left(\mathrm{d}\theta^2 + \sin^2\theta \mathrm{d}\phi^2\right), \tag{2}$$

where $f(r)$ is lapse function defined as

$$f(r) = 1 - \frac{2}{r}. \tag{3}$$

The only non-zero covariant component of the electromagnetic four-potential $A_\mu = (A_t, 0, 0, 0)$ is given by

$$A_t = -\frac{Q}{r}. \tag{4}$$

The anti-symmetric tensor of the electromagnetic field $F_{\alpha\beta} = A_{\beta,\alpha} - A_{\alpha,\beta}$ has the only one independent nonzero component

$$F_{tr} = -F_{rt} = -\frac{Q}{r^2}. \tag{5}$$

Let us now consider the motion of a charged particle of mass m and charge q in the combined background of gravitational and electric fields. The motion of a charged particle is governed by the Lorentz equation in curved spacetime

$$\frac{\mathrm{d}u^\mu}{\mathrm{d}\tau} + \Gamma^\mu_{\alpha\beta}u^\alpha u^\beta - \frac{q}{m}F^\mu{}_\nu u^\nu = 0, \tag{6}$$

where u^μ is the four-velocity of the particle, τ is the proper time of the particle and $\Gamma^\mu_{\alpha\beta}$ – Christoffel symbols.

Two integrals of motion, which correspond to the temporal and spatial components of the classical four-momentum of the charged particle, can be introduced due to the symmetries of the background Schwarzschild metric as

$$\frac{P_t}{m} = -\mathcal{E} \equiv -\frac{E}{m} = u_t - \frac{qQ}{mr}, \tag{7}$$

$$\frac{P_\phi}{m} = \mathcal{L} \equiv \frac{L}{m} = u_\phi, \tag{8}$$

where $\mathcal{E}$ and $\mathcal{L}$ denote specific energy and specific angular momentum of the charged particle.

2.2 Effective potential

Using the normalization condition for the velocity of a massive particle $u^\mu u_\mu = -1$, one can derive the effective potential for the charged particle moving around a weakly charged Schwarzschild black hole in the form

$$V_{\text{eff}}(r) = \frac{\mathcal{Q}}{r} + \sqrt{f(r)\left(1 + \frac{\mathcal{L}^2}{r^2 \sin^2\theta}\right)}, \tag{9}$$

where $\mathcal{Q} = Qq/m$ is an electric interaction parameter.

The detailed analysis dynamics of a charged particle in the vicinity of the weakly charged black hole are represented in Tursunov et al. (2021); Pugliese et al. (2011).

3 HARMONIC OSCILLATIONS

One can observe an oscillatory motion of the test particle around its equilibrium position in the form of linear harmonic oscillations if the particle is displaced from a stable equilibrium position corresponding to a circular orbit at the position r_0, which is located at the minimum of the effective potential $V_{\text{eff}}(r, \theta)$ at $r = r_0$ and $\theta = \pi/2$. The following equations govern the particle's displacement in the case of harmonic oscillations around the stable orbit: $r = r_0 + \delta r$ and $\theta = \theta_0 + \delta\theta$

$$\ddot{\delta r} + \omega_r^2 \delta r = 0, \quad \ddot{\delta\theta} + \omega_\theta^2 \delta\theta = 0, \tag{10}$$

where dot denotes $\dot{x} = \mathrm{d}x/\mathrm{d}\tau$, here τ is the proper time of the particle. Then, the locally measured angular frequencies of the harmonic oscillations of the particle are given by

$$\omega_r^2 = \frac{\partial^2 V_{\text{eff}}}{\partial r^2}, \quad \omega_\theta^2 = \frac{1}{r^2 f(r)} \frac{\partial^2 V_{\text{eff}}}{\partial \theta^2}, \quad \omega_\phi = \frac{\mathrm{d}\phi}{\mathrm{d}\tau}. \tag{11}$$

Here, ω_ϕ is an axial (Keplerian) frequency, while ω_r and ω_θ are locally measured radial and latitudinal angular frequencies of the particle's harmonical oscillations, respectively. Applying the effective potential V_{eff} from (9), the locally measured latitudinal ω_θ, radial

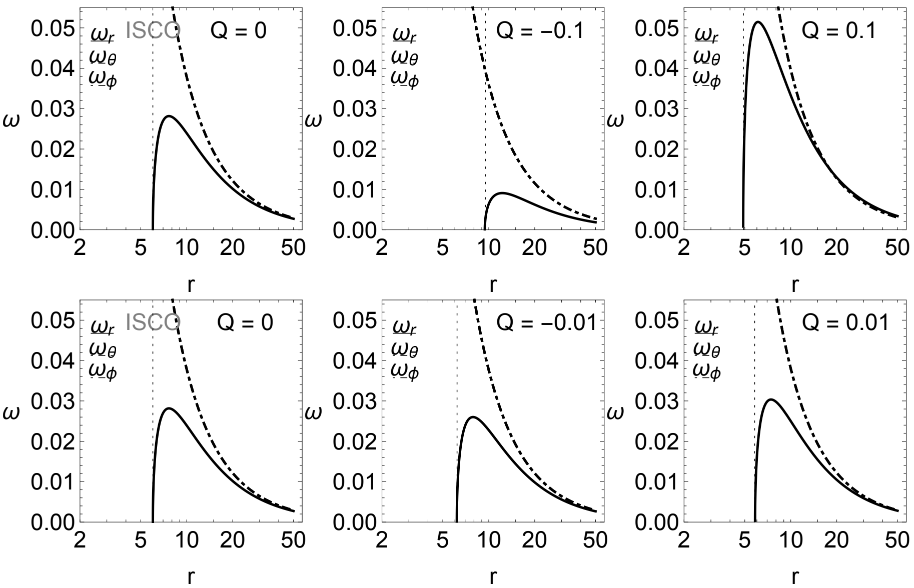

Figure 1. Dependence of locally measured frequencies ω_r, ω_θ, and ω_ϕ on radial distance from the black hole r. Due to the spherical symmetry of the fields, $\omega_\theta = \omega_\phi$. Here, we present three scenarios: the uncharged situation, where $\mathcal{Q} = 0$ (left column); the attractive electrostatic interaction, where $\mathcal{Q} < 0$ (middle column); and the repulsive electrostatic interaction, where $\mathcal{Q} > 0$ (right column).

ω_r, and axial (Keplerian) ω_ϕ frequencies of the charged particle harmonic oscillations in the field of a weakly electrically charged black hole take the explicit form

$$\omega_\theta^2 = \frac{\mathcal{L}^2}{r^4}, \tag{12}$$

$$\omega_r^2 = \frac{3\mathcal{L}^2 r^2 f^3 - 2r^3\mathcal{E}^2\left(\mathcal{E}^2 - \mathcal{Q}\right) - \mathcal{Q}^2\left(4 + 3fr^2\right)}{f^2 r^6}, \tag{13}$$

$$\omega_\phi = \frac{d\phi}{d\tau} = U^\phi = \frac{\mathcal{L}}{g_{\phi\phi}} \equiv \frac{\mathcal{L}}{r^2 \sin^2\theta}, \tag{14}$$

where $f = 1 - 2/r$ is the lapse function, $\mathcal{L}$ is the spefic angular momentum and $\mathcal{E}$ is the specific energy, which is $\mathcal{E} = V_{\rm eff}(r)$. Figure 1 illustrates the dependence of the locally measured frequencies $\omega_\theta(r)$, $\omega_r(r)$, and $\omega_\phi(r)$ on the radial coordinate r for the values of the electric interaction parameter $\mathcal{Q} = 0, \pm 0.01, \pm 0.1$. Locally measured harmonic oscillations are expressed in physical units. By factor c^3/GM, a dimensionless form can be obtained.

4 CONCLUSION

This work presents the study of harmonic oscillations of charged particles in the vicinity of a weakly charged Schwarzschild black hole. We have derived equations for the angular frequencies of the harmonic oscillations of the particle as measured by a local observer. Additionally, we have constructed the radial dependence on the locally measured angular frequencies for various values of the electric interaction parameter. The obtained results can further be applied in relation to the quasiperiodic oscillations (QPOs) phenomena observed in black hole microquasars (Kološ et al., 2017; Tursunov and Kološ, 2018).

ACKNOWLEDGEMENTS

We thank the organizers of RAGtime 2023 for providing a platform for stimulating meeting. Bakhtinur Juraev acknowledges the Silesian University in Opava grant SGS/30/2023. Arman Tursunov acknowledges the Czech Science Foundation (GAČR) grant No. 23-07043S.

REFERENCES

Araya, I. J., Padilla, N. D., Rubio, M. E., Sureda, J., Magaña, J. and Osorio, L. (2023), Dark matter from primordial black holes would hold charge, *Journal of Cosmology and Astroparticle Physics* , **2023**(2), 030, arXiv: `2207.05829`.

Kološ, M., Tursunov, A. and Stuchlík, Z. (2017), Possible signature of the magnetic fields related to quasi-periodic oscillations observed in microquasars, *European Physical Journal C*, **77**, 860, arXiv: `1707.02224`.

Kološ, M., Stuchlík, Z. and Tursunov, A. (2015), Quasi-harmonic oscillatory motion of charged particles around a Schwarzschild black hole immersed in a uniform magnetic field, *Classical and Quantum Gravity*, **32**(16), 165009, arXiv: `1506.06799`.

Pugliese, D., Quevedo, H. and Ruffini, R. (2011), Motion of charged test particles in Reissner-Nordström spacetime, *Phys. Rev. D* , **83**(10), 104052, arXiv: `1103.1807`.

Tursunov, A., Juraev, B., Stuchlík, Z. and Kološ, M. (2021), Electric Penrose process: High-energy acceleration of ionized particles by nonrotating weakly charged black hole, *Phys. Rev. D* , **104**(8), 084099, arXiv: `2109.10288`.

Tursunov, A., Stuchlík, Z. and Kološ, M. (2016), Circular orbits and related quasi-harmonic oscillatory motion of charged particles around weakly magnetized rotating black holes, *Phys. Rev. D* , **93**(8), 084012, arXiv: `1603.07264`.

Tursunov, A. A. and Kološ, M. (2018), Constraints on Mass, Spin and Magnetic Field of Microquasar H 1743-322 from Observations of QPOs, *Physics of Atomic Nuclei*, **81**(2), pp. 279–282, arXiv: `1803.08144`.

Wald, R. M. (1974), Black hole in a uniform magnetic field, *Phys. Rev. D* , **10**, pp. 1680–1685.

Zajacek, M. and Tursunov, A. (2019), The Electric Charge of Black Holes: Is It Really Always Negligible, *The Observatory*, **139**, pp. 231–236, arXiv: `1904.04654`.

Zajaček, M., Tursunov, A., Eckart, A. and Britzen, S. (2018), On the charge of the Galactic centre black hole, *Monthly Notices of the Royal Astronomical Society* , **480**(4), pp. 4408–4423, arXiv: `1808.07327`.

Proceedings of *RAGtime 23–25*
Z. Stuchlík, G. Török, V. Karas and D. Lančová, editors, Silesian University in Opava, 2023, pp. 205–211

Quasinormal spectrum in the asymptotically safe gravity

Antonina F. Zinhailo

Research Centre for Theoretical Physics and Astrophysics,
Institute of Physics, Silesian University in Opava,
Bezručovo nám. 13, CZ-746 01 Opava, Czech Republic
`F170631@fpf.slu.cz`

ABSTRACT
Asymptotically safe gravity is based on the idea of the dependence of the gravitational coupling upon the distance from the origin, approaching its classical value in the weak field regime. We consider three cases of identifying the cut-off parameter in the asymptotically safe gravity, leading to the three distinctive models for black holes. We find that the deviation of the fundamental mode from the Schwarzschild limit is a few per cent, in contrast to the higher overtones, where the deviation reaches hundreds of per cent, even when the fundamental mode almost coincides with the Schwarzschild mode. This behavior is connected with the fact that the quantum correction to the black hole spacetime is strong near the event horizon but quickly falls off with distance and is negligible near the peak of the effective potential surrounding the black hole.

Keywords: Regular spacetimes – quasinormal modes – outburst of overtones – asymptotically safe gravity

1 INTRODUCTION

The investigation of quasinormal modes (QNMs, Kokkotas and Schmidt, 1999; Nollert, 1999; Konoplya and Zhidenko, 2011) of black holes has become crucial in comprehending how black holes respond to perturbations. QNMs, representing the characteristic damped oscillations of black holes, encapsulate vital information about their fundamental properties. Their observation is facilitated by gravitational interferometer systems like LIGO and Virgo (Abbott et al., 2016). Simultaneously, the concept of asymptotically safe gravity (Bonanno and Reuter, 2000) has emerged as a theoretical framework aimed at addressing issues regarding the renormalization of gravity in the quantum domain.

This report explores the relationship between QNMs of black holes and the hypothesis of asymptotically safe gravity. We conduct an extensive examination of quasinormal modes of test fields for three black-hole models within asymptotically safe gravity, demonstrating that the overtones are considerably more sensitive to quantum corrections than the fundamental mode. This phenomenon, termed “the outburst of overtones”, is associated with the

978-80-7510-576-9

distortion of black hole geometry near its event horizon (Konoplya and Zhidenko, 2022). This report provides an overview of the primary findings concerning quasinormal spectra of black holes in asymptotically safe gravity. Further details can be explored in Konoplya et al. (2022, 2023).

2 BLACK HOLE METRICS AND WAVELIKE EQUATIONS

The metric of a spherically-symmetric black hole has the following form

$$ds^2 = -f(r)\,dt^2 + f(r)^{-1}\,dr^2 + r^2\,d\Omega^2. \tag{1}$$

In asymptotically safe gravity, Newton's coupling now depends on r. The basic constituent of the theory is the cut-off parameter. There are three known ways to identify the cut-off parameter of the theory:

(1) Identification of the cut-off parameter as a modified proper distance leads to the *Bonanno-Reuter metric* (Bonanno and Reuter, 2000). The metric function for the Bonanno-Reuter spacetime is

$$f(r) = 1 - \frac{2Mr^2}{r^3 + \frac{118}{15\pi}\left(r + \frac{9}{2}M\right)}, \tag{2}$$

where M is the black hole mass measured in units of the Planck mass.

(2) Identification of the cut-off parameter as a function of the Kretschmann scalar (Held et al., 2019) leads to the metric coinciding with the *Hayward metric* (Hayward, 2006):

$$f(r) = 1 - \frac{2r^2/M^2}{r^3/M^3 + \gamma}. \tag{3}$$

Here, the event horizon exists whenever $\gamma \leq 32/27$.

(3) Starting from a classical Schwarzschild solution, the backreaction effects produced by running Newton's coupling are taken into account iteratively. This way, a kind of coordinate independent iterative procedure for identification suggested in Platania (2019) leads to the Dymnikova black hole (Dymnikova, 1992)

$$f(r) = 1 - \frac{2M}{r}\left(1 - e^{-\dfrac{r^3}{2l_{\rm cr}^2 M}}\right). \tag{4}$$

Here, $l_{\rm cr}$ is a critical length scale below which the modifications owing to the running of Newtons constant become negligible. The maximal value of $l_{\rm cr}$ at which the event horizon still exists is

$$l_{\rm cr} \approx 1.138\,M,$$

where M is the mass measured in units of length.

The general relativistic equations for the scalar (Φ), electromagnetic (A_μ), and Dirac (Υ) fields in a curved spacetime can be cast to the wave-like form:

$$\frac{\mathrm{d}^2\Psi}{\mathrm{d}r_*^2}+\left(\omega^2-V(r)\right)\Psi=0, \tag{5}$$

where the "tortoise coordinate" r_* is:

$$\mathrm{d}r_*\equiv\frac{\mathrm{d}r}{f(r)}. \tag{6}$$

The effective potentials for the scalar ($s=0$) and electromagnetic ($s=1$) fields can be written in a unified form:

$$V(r)=f(r)\frac{\ell(\ell+1)}{r^2}+(1-s)\cdot\frac{f(r)}{r}\frac{\mathrm{d}f(r)}{\mathrm{d}r}, \tag{7}$$

where $\ell=s,s+1,s+2,\ldots$ are the multipole numbers. For the Dirac field ($s=1/2$), the problem is reduced to two iso-spectral effective potentials

$$V_\pm(r)=W^2\pm\frac{\mathrm{d}W}{\mathrm{d}r_*},\quad W\equiv\left(\ell+\frac{1}{2}\right)\frac{\sqrt{f(r)}}{r}. \tag{8}$$

The isospectral wave functions $\Psi_\pm$ can be transformed one into another by using the Darboux transformation:

$$\Psi_+=q\left(W+\frac{\mathrm{d}}{\mathrm{d}r_*}\right)\Psi_-,\quad q=const. \tag{9}$$

Therefore, it is sufficient to study only one of the iso-spectral cases.

3 QUASINORMAL MODES

Quasinormal modes represent the appropriate oscillation frequencies that govern the evolution of perturbations during the intermediate to late stages, known as the ringdown phase. These modes correspond to solutions of the master wave equation (5) subject to the following boundary conditions for the wave function $\Psi\propto e^{i\omega(r_*-t)}$:

$$\begin{aligned}\Psi &\sim \textit{pure outgoing wave},\quad r_*\to+\infty,\\ \Psi &\sim \textit{pure ingoing wave},\quad r_*\to-\infty.\end{aligned} \tag{10}$$

For finding dominant quasinormal modes, we used the 6th order WKB method (Konoplya, 2003; Konoplya et al., 2019) with the Pade approximants (Matyjasek and Opala, 2017). The WKB method has been broadly applied for finding quasinormal modes of black holes and wormholes (for example in Kodama et al., 2010; Onozawa et al., 1996; Konoplya et al., 2019; Bolokhov, 2023). In order to find precise values of modes with arbitrary relation between the multipole number and overtone, the Leaver method is used (Leaver, 1985), which is based on the convergent procedure. Another convergent technique we used is the Bernstein polynomial method (Konoplya and Zhidenko, 2023), though only several

n	ω (Bonanno-Reuter)	ω (Schwarzschild)
0	$0.066877 - 0.020549i$	$0.062066 - 0.023122i$
1	$0.059764 - 0.063499i$	$0.053629 - 0.073417i$
2	$0.047392 - 0.110619i$	$0.043693 - 0.131297i$
3	$0.030448 - 0.166115i$	$0.036544 - 0.192977i$
4	$0.019951 - 0.224263i$	$0.031639 - 0.255638i$
5	$0.012209 - 0.290487i$	$0.028063 - 0.318481i$
6	$0.000983 - 0.354117i$	$0.025304 - 0.381317i$
7	$0.000 - 0.420i$	$0.023081 - 0.444100i$

Table 1. Dominant quasinormal modes for the electromagnetic perturbations ($\ell = 1$) of the Bonanno-Reuter black hole ($M = 4$) and the corresponding modes for the Schwarzschild black hole, according to Konoplya et al. (2022).

first overtones can be found during reasonable computing time. Finally, in order to see the evolution of perturbations in time, the time-domain integration developed in Gundlach et al. (1994) has been applied. This method was also used in a great number of publications (see, for example, Konoplya and Fontana, 2008; Churilova and Stuchlik, 2020; Bronnikov and Konoplya, 2020 and references therein) with a very good concordance with other methods for the fundamental mode.

3.1 Bonanno-Reuter metric

Using the first-order WKB formula, we can obtain quasinormal modes in the high multipole number $\ell \to \infty$ regime in analytic form. For this, we will use the expression for the position of the peak of the effective potential, which for the Bonanno-Reuter metric is located at:

$$r_{\max} \approx 3M - \frac{1652}{135\pi M} - \frac{5071817}{54675\pi^2 M^3} - \frac{28261793432}{22143375\pi^3 M^5}. \tag{11}$$

Then, the WKB formula yields

$$Im(\omega) = \frac{\left(n + \frac{1}{2}\right)}{3\sqrt{3}M}\left(1 - \frac{1298}{405\pi M^2} + O\left(\frac{1}{M^4}\right)\right), \tag{12}$$

$$Re(\omega) = \frac{\left(\ell + \frac{1}{2}\right)}{3\sqrt{3}M}\left(1 + \frac{59}{27\pi M^2} + O\left(\frac{1}{M^4}\right)\right). \tag{13}$$

Observing table 1, it becomes evident that as n increases, the deviation of the overtones amplifies, while the fundamental mode only exhibits a slight deviation from the Schwarzschild limit. Additionally, at $n = 7$, a purely imaginary (non-oscillatory) mode emerges in the spectrum, which is not an algebraically special one.

n	ωM (Hayward)	ωM (Schwarzschild)
0	$0.113494 - 0.089160i$	$0.110455 - 0.104896i$
1	$0.066731 - 0.319873i$	$0.086117 - 0.348053i$
2	$0.041068 - 0.576924i$	$0.075742 - 0.601079i$
3	$0.021679 - 0.833067i$	$0.070410 - 0.853678i$
4	$0.000000 - 1.082236i$	$0.067074 - 1.105630i$
5	$0.001449 - 1.317232i$	$0.064742 - 1.357140i$

Table 2. Quasinormal modes for the $\ell = 0$ scalar perturbations of the Hayward black hole ($\gamma = 1$) and the corresponding modes for the Schwarzschild black hole, according to Konoplya et al. (2022).

3.2 Hayward metric

In a similar fashion, we obtain the following expressions for the Hayward metric for the location of the peak of the effective potential,

$$r_{\max} \approx 3M - \frac{2\gamma M}{9} - \frac{\gamma^2 M}{27} - \frac{70\gamma^3 M}{6561} - \frac{665\gamma^4 M}{177147}, \tag{14}$$

and the eikonal quasinormal frequencies,

$$Im\,(\omega) = \frac{\left(n + \frac{1}{2}\right)}{3\sqrt{3}M}\left(1 - \frac{2}{27}\gamma + O\left(\gamma^2\right)\right), \tag{15}$$

$$Re\,(\omega) = \frac{\left(\ell + \frac{1}{2}\right)}{3\sqrt{3}M}\left(1 - \frac{2}{54}\gamma + O\left(\gamma^2\right)\right). \tag{16}$$

According to observations in Cardoso et al. (2009), there exists a correspondence between the eikonal quasinormal modes and characteristics of null geodesics: The real and imaginary parts of ω are multiples of the frequency and instability timescale of the circular null geodesics, respectively. While we confirm this observation for the specific case considered in asymptotically safe gravity, generally, this correspondence does not hold for modes with $\ell \gg n$ that cannot be accurately reproduced by the WKB formula (Konoplya and Stuchlík, 2017; Konoplya, 2023).

Table 2 shows that there is an outburst of overtones for the Hayward metric as well.

3.3 Dymnikova black hole

As can be seen from Table 3, the overtones deviate at a stronger rate from their Schwarzschild values when n is increased. For all three types of metrics, the deformation of the geometry occurs mainly near the event horizon, while in the far zone, the metrics merge with the Schwarzschild one. The overtones are highly sensitive to these near-horizon deformations.

l_{cr}	$n = 0$	$n = 1$	$n = 2$	$n = 3$
0	$0.24826 - 0.09249i$	$0.2145 - 0.2937i$	$0.175 - 0.525i$	$0.146 - 0.772i$
0.7	$0.24823 - 0.09247i$	$0.2141 - 0.2935i$	$0.173 - 0.525i$	$0.140 - 0.772i$
0.75	$0.24814 - 0.09239i$	$0.2135 - 0.2930i$	$0.170 - 0.523i$	$0.135 - 0.768i$
0.8	$0.24804 - 0.09226i$	$0.2125 - 0.2922i$	$0.166 - 0.521i$	$0.123 - 0.765i$
0.85	$0.24790 - 0.09200i$	$0.2112 - 0.2909i$	$0.160 - 0.518i$	$0.103 - 0.762i$
0.9	$0.24766 - 0.09159i$	$0.2088 - 0.2886i$	$0.149 - 0.512i$	$0.06 - 0.74i$
0.95	$0.2473 - 0.09085i$	$0.206 - 0.2849i$	$0.13 - 0.50i$	$0.06 - 0.81i$
1.0	$0.2468 - 0.08986i$	$0.201 - 0.280i$	$0.107 - 0.508i$	$0.05 - 0.8i$
1.05	$0.24614 - 0.08855i$	$0.195 - 0.276i$	$0.107 - 0.514i$	$0.04 - 0.8i$
1.1	$0.24516 - 0.08699i$	$0.1892 - 0.2731i$	$0.091 - 0.519i$	$0.05 - 0.87i$

Table 3. Quasinormal modes found by the Leaver method for $\ell = 1$, electromagnetic perturbations; $M = 1$. The metric is approximated by the 17th-order parametrization in Konoplya et al. (2023). The Schwarzschild limit corresponds to $l_{\mathrm{cr}} = 0$.

4 CONCLUSIONS

We have reviewed recent results obtained in Konoplya et al. (2023, 2022) regarding the behavior of overtones in various black hole models within asymptotically safe gravity. Despite different approaches to identifying the cutoff parameters, a qualitatively similar feature is observed in all three cases: an outburst of overtones that convey information about the geometry of the event horizon.

ACKNOWLEDGEMENTS

I would like to thank Roman Konoplya for the most useful discussions. I also thank the internal grant of Silesian University, SGS/30/2023.

REFERENCES

Abbott, B. P. et al. (LIGO Scientific, Virgo) (2016), Observation of Gravitational Waves from a Binary Black Hole Merger, *Phys. Rev. Lett.*, **116**(6), p. 061102, arXiv: `1602.03837`.

Bolokhov, S. V. (2023), Long lived quasinormal modes and telling oscillatory tails of the Bardeen spacetime, 10.20944/preprints202310.0517.v1.

Bonanno, A. and Reuter, M. (2000), Renormalization group improved black hole space-times, *Phys. Rev.*, **D62**, p. 043008, arXiv: `hep-th/0002196`.

Bronnikov, K. A. and Konoplya, R. A. (2020), Echoes in brane worlds: ringing at a black hole–wormhole transition, *Phys. Rev. D*, **101**(6), p. 064004, arXiv: `1912.05315`.

Cardoso, V., Miranda, A. S., Berti, E., Witek, H. and Zanchin, V. T. (2009), Geodesic stability, Lyapunov exponents and quasinormal modes, *Phys. Rev. D*, **79**(6), p. 064016, arXiv: `0812.1806`.

Churilova, M. S. and Stuchlik, Z. (2020), Ringing of the regular black-hole/wormhole transition, *Class. Quant. Grav.*, **37**(7), p. 075014, arXiv: `1911.11823`.

Dymnikova, I. (1992), Vacuum nonsingular black hole, *Gen. Rel. Grav.*, **24**, pp. 235–242.

Gundlach, C., Price, R. H. and Pullin, J. (1994), Late time behavior of stellar collapse and explosions: 1. Linearized perturbations, *Phys. Rev. D*, **49**, pp. 883–889, arXiv: `gr-qc/9307009`.

Hayward, S. A. (2006), Formation and evaporation of regular black holes, *Phys. Rev. Lett.*, **96**, p. 031103, arXiv: `gr-qc/0506126`.

Held, A., Gold, R. and Eichhorn, A. (2019), Asymptotic safety casts its shadow, *JCAP*, **06**, p. 029, arXiv: `1904.07133`.

Kodama, H., Konoplya, R. A. and Zhidenko, A. (2010), Gravitational stability of simply rotating Myers-Perry black holes: Tensorial perturbations, *Phys. Rev. D*, **81**, p. 044007, arXiv: `0904.2154`.

Kokkotas, K. D. and Schmidt, B. G. (1999), Quasinormal modes of stars and black holes, *Living Rev. Rel.*, **2**, p. 2, arXiv: `gr-qc/9909058`.

Konoplya, R. A. (2003), Quasinormal behavior of the d-dimensional Schwarzschild black hole and higher order WKB approach, *Phys. Rev. D*, **68**, p. 024018, arXiv: `gr-qc/0303052`.

Konoplya, R. A. (2023), Further clarification on quasinormal modes/circular null geodesics correspondence, *Phys. Lett. B*, **838**, p. 137674, arXiv: `2210.08373`.

Konoplya, R. A. and Fontana, R. D. B. (2008), Quasinormal modes of black holes immersed in a strong magnetic field, *Phys. Lett. B*, **659**, pp. 375–379, arXiv: `0707.1156`.

Konoplya, R. A. and Stuchlík, Z. (2017), Are eikonal quasinormal modes linked to the unstable circular null geodesics?, *Phys. Lett. B*, **771**, pp. 597–602, arXiv: `1705.05928`.

Konoplya, R. A., Stuchlik, Z., Zhidenko, A. and Zinhailo, A. F. (2023), Quasinormal modes of renormalization group improved Dymnikova regular black holes, *Phys. Rev. D*, **107**(10), p. 104050, arXiv: `2303.01987`.

Konoplya, R. A. and Zhidenko, A. (2011), Quasinormal modes of black holes: From astrophysics to string theory, *Rev. Mod. Phys.*, **83**, pp. 793–836, arXiv: `1102.4014`.

Konoplya, R. A. and Zhidenko, A. (2022), First few overtones probe the event horizon geometry, arXiv: `2209.00679`.

Konoplya, R. A. and Zhidenko, A. (2023), Bernstein spectral method for quasinormal modes of a generic black hole spacetime and application to instability of dilaton–de Sitter solution, *Phys. Rev. D*, **107**(4), p. 044009, arXiv: `2211.02997`.

Konoplya, R. A., Zhidenko, A. and Zinhailo, A. F. (2019), Higher order WKB formula for quasinormal modes and grey-body factors: recipes for quick and accurate calculations, *Class. Quant. Grav.*, **36**, p. 155002, arXiv: `1904.10333`.

Konoplya, R. A., Zinhailo, A. F., Kunz, J., Stuchlik, Z. and Zhidenko, A. (2022), Quasinormal ringing of regular black holes in asymptotically safe gravity: the importance of overtones, *JCAP*, **10**, p. 091, arXiv: `2206.14714`.

Leaver, E. W. (1985), An Analytic representation for the quasi normal modes of Kerr black holes, *Proc. Roy. Soc. Lond. A*, **402**, pp. 285–298.

Matyjasek, J. and Opala, M. (2017), Quasinormal modes of black holes. The improved semianalytic approach, *Phys. Rev. D*, **96**(2), p. 024011, arXiv: `1704.00361`.

Nollert, H.-P. (1999), TOPICAL REVIEW: Quasinormal modes: the characteristic 'sound' of black holes and neutron stars, *Class. Quant. Grav.*, **16**, pp. R159–R216.

Onozawa, H., Mishima, T., Okamura, T. and Ishihara, H. (1996), Quasinormal modes of maximally charged black holes, *Phys. Rev. D*, **53**, pp. 7033–7040, arXiv: `gr-qc/9603021`.

Platania, A. (2019), Dynamical renormalization of black-hole spacetimes, *Eur. Phys. J. C*, **79**(6), p. 470, arXiv: `1903.10411`.

Title: **Proceedings of RAGtime 23–25:**
Workshops on black holes and neutron stars,
6–10 Sep., 10–14 Oct., 27 Nov.–1 Dec. 2021/2022/2023,
Opava, Czech Republic

Published by: Silesian University in Opava
Institute of Physics
Bezručovo nám. 13
CZ-746 01 Opava, Czech Republic

Editors: Z. Stuchlík, G. Török, V. Karas and D. Lančová

Cover design: Otakar Karlas

1st edition

Printed by: Printo, spol. s r. o.,
Jelínkova 1379/13,
CZ-721 00 Ostrava Svinov, Czech Republic

Published in December 2023

EVROPSKÁ UNIE
Evropské strukturální a investiční fondy
Operační program Výzkum, vývoj a vzdělávání
MINISTERSTVO ŠKOLSTVÍ, MLÁDEŽE A TĚLOVÝCHOVY
INTER-EXCELLENCE
SLEZSKÁ UNIVERZITA
FYZIKÁLNÍ ÚSTAV V OPAVĚ

The publication was supported by the INTER-EXCELLENCE project No. LTI17018, the ESF projects No. CZ.02.2.69/0.0/0.0/18_058/0010238, CZ.02.2.69/0.0/0.0/18_056/0013 364, and CZ.02.2.69/0.0/0.0/18_054/0014696, and the internal grants of the Silesian University in Opava.

ISBN 978-80-7510-576-9 (Print)
ISBN 978-80-7510-577-6 (Online)
ISSN 2336-5668 (Print)
ISSN 2336-5676 (Online)

Typeset in LaTeX

Název: **Proceedings of RAGtime 23–25:**
Workshops on black holes and neutron stars,
6–10 Sep., 10–14 Oct., 27 Nov.–1 Dec. 2021/2022/2023,
Opava, Czech Republic

Nakladatel: Slezská univerzita v Opavě
Fyzikální ústav v Opavě
Bezručovo nám. 13
CZ-746 01Opava, Česká republika

Editoři: Z. Stuchlík, G. Török, V. Karas a D. Lančová

Obálka: Otakar Karlas

První vydání

Tisk: Printo, spol. s r. o.,
Jelínkova 1379/13
CZ-721 00 Ostrava Svinov, Česká republika

Vydáno v prosinci 2023

EUROPEAN UNION
European Structural and Investment Funds
Operational Programme Research,
Development and Education

MINISTRY OF EDUCATION,
YOUTH AND SPORTS

INTER-EXCELLENCE

SILESIAN
UNIVERSITY
INSTITUTE OF PHYSICS
IN OPAVA

Vydání publikace bylo podpořeno projektem INTER-EXCELLENCE č. LTI17018, ESF projekty s reg. čísly CZ.02.2.69/0.0/0.0/18_058/0010238, CZ.02.2.69/0.0/0.0/18_056/0013364 a CZ.02.2.69/0.0/0.0/18_054/0014696, a interními projekty Slezské univerzity v Opavě.

ISBN 978-80-7510-576-9 (Print)
ISBN 978-80-7510-577-6 (Online)
ISSN 2336-5668 (Print)
ISSN 2336-5676 (Online)

Vysázeno systémem LaTeX